

---

The relevance of aerosol in the retrieval  
of tropospheric NO<sub>2</sub> from satellite  
- a study of model data applicability

---



The relevance of aerosol in the retrieval of  
tropospheric NO<sub>2</sub> from satellite - a study  
of model data applicability

Vom Fachbereich für Physik und Elektrotechnik  
der Universität Bremen

zur Erlangung des akademischen Grades  
**Doktor der Naturwissenschaften (Dr. rer. nat.)**  
genehmigte Dissertation

von

M.Sc. Joana Leitão Alexandre  
aus Lisboa

---

Dissertation eingereicht am: 15.08.2011

Tag des Promotionskolloquiums: 13.10.2011

1. Gutachter: Prof. Dr. John P. Burrows

2. Gutachter: Prof. Dr. Otto Schrems

*Para a minha avózita.*



# Abstract

Nitrogen dioxide (NO<sub>2</sub>) is a key pollutant in the troposphere, being one of the main precursors of tropospheric ozone, and source of nitric acid, as well as contributing to global climate change. Tropospheric NO<sub>2</sub> vertical columns can be determined from satellite observations, although some uncertainties are still associated with the retrieval process. The conversion from measured slant columns to vertical columns is accomplished with air mass factors (AMFs) that are determined by radiative transfer (RT) models. While the measurement (instrumental) conditions are well assessed, improvement is still needed regarding the *a priori* information of atmospheric characteristics required for the estimation of AMFs (e.g., vertical distribution of the gas, aerosol loading and clouds).

This thesis presents a sensitivity study focused on the impact of aerosol on the tropospheric NO<sub>2</sub> AMF. Optical properties, size distribution, and vertical distribution of the aerosol were varied within several scenarios. Overall, the results show a tendency for two main opposite effects. On the one hand, enhancement of the measurement sensitivity occurs by means of multiple scattering, when aerosol is mixed with the trace gas. On the other hand, a shielding effect by an aerosol layer located above the NO<sub>2</sub> is also verified. The identified pivotal factors for the AMF calculations were the relative vertical distribution of aerosol and NO<sub>2</sub>, the aerosol optical depth and the single scattering albedo, as well as the surface reflectance. A case study was developed, focusing on the impact on the NO<sub>2</sub> measurements of volcanic ash emitted from Eyjafjallajökull during the spring of 2010. Aerosol and NO<sub>2</sub> data from the EURAD chemical transport model (CTM) were used to design scenarios for the RT calculations. A small variation of AMFs was found, revealing that, in the days and region analysed, the satellite observations of NO<sub>2</sub> were not significantly affected by the mentioned eruption. Nonetheless, it was verified that the conclusions of the study are dependent on the accuracy of the CTM data, and on the approach employed to account for (and determine) aerosol optical properties. Such findings highlight the potential challenges that can be faced in the future if model data are used in satellite retrievals.

In addition, a model evaluation performed within the GEMS project is described, where global stratospheric and tropospheric NO<sub>2</sub> columns predicted by two chemical transport models – MOZART and TM5 – are compared with SCIAMACHY observations. The evaluation exercise allowed for the identification of flaws in the model systems, showing problems with the prediction of high levels of pollution in some regions (e.g., East-Asia), and with the simulation of NO<sub>2</sub> concentrations during biomass burning events.



# Publications

## Journal Articles

Boersma, K. F., et al.: *An improved tropospheric NO<sub>2</sub> column retrieval algorithm for the Ozone Monitoring Instrument*, Atmos. Meas. Tech. Discuss., 4, 2329-2388, 2011

Leitão, J., et al.: *On the improvement of NO<sub>2</sub> satellite retrievals – aerosol impact on the airmass factors*, Atmos. Meas. Tech., 3, 475-493, 2010

Leitão, J., et al.: *Sensitivity Study of the Airmass Factors used for Satellite Retrievals of tropospheric NO<sub>2</sub>*, CURRENT PROBLEMS IN ATMOSPHERIC RADIATION (IRS 2008): Proceedings of the International Radiation Symposium (IRC/IAMAS). AIP Conference Proceedings, Volume 1100, pp. 279-282, 2009

## Conference contributions (selection, only as first author)

J. Leitão, A. Richter, J.P. Burrows, V. Huijen, O. Stein, J. Flemming, A. Inness, and the MACC GRG team, Validation of global NO<sub>2</sub> MACC products with SCIAMACHY measurements, MACC Conference on Monitoring and Forecasting Atmospheric Composition, Utrecht, 23-27 May 2011

J. Leitão, A. Richter, M. Vrekoussis, A. Kokhanovsky, and J.P. Burrows, How satellite retrievals of NO<sub>2</sub> vertical columns can be improved using aerosol measurements, European Aerosol Conference (EAC2009), Karlsruhe, 6-11 Sept. 2009

J. Leitão, A. Richter, A. Kokhanovsky, and J.P. Burrows; On the improvement of satellite retrievals of NO<sub>2</sub> using aerosol measurements, Accent Aerosol Workshop, Bad Honnef, 17-19 Aug. 2009

---

J. Leitão, A. Richter, J.P. Burrows, and the GEMS GRG team; Evaluation of global NO<sub>2</sub> GEMS products using IUP-Bremen SCIAMACHY measurements, GEMS General Assembly, Jülich, April 2009

J. Leitão, A. Heckel, A. Richter, A. Kokhanovsky, and J.P. Burrows; Sensitivity Study of the Airmass Factors used for Satellite Retrievals of tropospheric NO<sub>2</sub>, IRS2008, Foz do Iguaçu, 3-8 Aug. 2008

J. Leitao, A. Richter, A. Heckel, and J.P. Burrows; Impact of aerosol on the NO<sub>2</sub> airmass factors used for satellite retrievals, EGU – General Assembly, Vienna, 13-19 April 2008

J. Leitão, A. Heckel, A. Richter, A. Kokhanovsky, and J.P. Burrows; Sensitivity of satellite NO<sub>2</sub> retrievals to aerosols, 4th DOAS International Workshop 2008 for Environmental Research and Monitoring Hefei, 31 Mar - 2 April 2008

J. Leitão, A. Heckel, A. Richter, T. Dinter, W. von Hoyningen-Huene, A. Kokhanovsky, and J.P. Burrows; Using MERIS data in the calculation of NO<sub>2</sub> airmass factors, Accent Workshop - Tropospheric NO<sub>2</sub> measured by satellites, Utrecht, 10-12 Sept. 2007

# Table of contents

Table of contents.....	i
List of Figures.....	iii
List of Tables.....	vi
List of chemical species.....	vii
List of acronyms and abbreviations.....	viii
1 Introduction and motivation.....	1
2 Fundamentals.....	5
2.1 Earth's atmosphere.....	6
2.2 Atmospheric pollution.....	10
2.2.1 Climate change.....	11
2.2.2 Stratospheric ozone.....	12
2.2.3 Tropospheric ozone.....	16
2.3 Nitrogen dioxide (NO <sub>2</sub> ).....	18
2.4 Atmospheric aerosol.....	24
2.5 Radiative transfer.....	35
2.5.1 Radiation in the atmosphere.....	35
2.5.2 Radiative transfer equation.....	38
2.5.3 SCIATRAN – radiative transfer model.....	39
2.6 NO <sub>2</sub> retrieval.....	40
2.6.1 DOAS method.....	40
2.6.2 Airmass factor.....	42
2.6.3 Retrieval of tropospheric NO <sub>2</sub> .....	43
2.7 Satellite instruments.....	47
2.7.1 SCIAMACHY.....	48
2.7.2 GOME-2.....	49
2.8 Atmospheric models.....	50
3 Influence of aerosol on NO <sub>2</sub> airmass factors.....	53
3.1 Impact of aerosol on satellite remote sensing.....	54
3.2 Radiative transfer settings.....	56
3.2.1 Definition of NO <sub>2</sub> vertical distribution.....	58

---

3.2.2	Definition of aerosol properties and vertical distribution .....	60
3.3	Sensitivity study .....	66
3.3.1	Influence of surface reflectance .....	67
3.3.2	Influence NO <sub>2</sub> profile .....	68
3.3.3	Influence of different aerosol characteristics .....	72
3.4	Summary .....	85
4	Case study – Eyjafjallajökull eruption .....	89
4.1	The EURAD model .....	90
4.1.1	General overview of the CTM .....	90
4.1.2	CTM settings for the volcanic ash simulations .....	92
4.2	EURAD data for SCIATRAN input .....	93
4.3	Impact of volcanic ash on NO <sub>2</sub> AMFs .....	102
4.3.1	AMF variation for different scenarios .....	103
4.3.2	Scenarios and results for specific locations .....	105
4.3.3	Aerosol mixing state assumptions .....	112
4.4	Summary .....	118
5	Validation of NO <sub>2</sub> model output .....	121
5.1	The GEMS project .....	122
5.2	Chemical Transport Models (CTMs) .....	124
5.2.1	MOZART .....	125
5.2.2	TM5 .....	126
5.3	Description of evaluation method .....	128
5.3.1	Data treatment .....	128
5.3.2	Data comparison - methods .....	133
5.4	Results: Comparison with independent satellite data .....	135
5.4.1	MOZART .....	136
5.4.2	TM5 .....	144
5.5	Quantitative analysis .....	154
5.6	Summary .....	155
6	Conclusions and outlook .....	161
6.1	Appendix .....	167
7	References .....	169
	Acknowledgements .....	189

# List of Figures

Figure 2.1 Vertical temperature profile after the US Standard Atmosphere .....	9
Figure 2.2 Temperature vertical profiles in the tropopause region for different latitudes .....	9
Figure 2.3 Global average radiative forcing .....	13
Figure 2.4 NO <sub>x</sub> emissions for anthropogenic sources, for the year 2005, from EDGAR.....	19
Figure 2.5 Fire pixel counts for the year 2005, from MODIS .....	19
Figure 2.6 Annual average of NO <sub>2</sub> tropospheric columns for the year 2005, from SCIAMACHY .....	20
Figure 2.7 Schematic representation of main daytime chemical processes of NO <sub>x</sub> species.....	21
Figure 2.8 Typical daily cycle of NO <sub>x</sub> , PAN and O <sub>3</sub> concentrations .....	23
Figure 2.9 Images from scanning electron microscope showing different aerosol shapes .....	24
Figure 2.10 Global mean distribution of aerosol optical thickness, from MERIS.....	26
Figure 2.11 Idealised scheme of an atmospheric aerosol size distribution.....	27
Figure 2.12 Solar flux outside the atmosphere, at sea level, and emission of a blackbody at 6000 K ..	35
Figure 2.13 Scattering phase functions for particles in the Mie and Rayleigh regime .....	38
Figure 2.14 NO <sub>2</sub> block AMF (BAMF) for 3 scenarios.....	43
Figure 2.15 Three main steps of the NO <sub>2</sub> data analysis .....	46
Figure 2.16 SCIAMACHY observation modes.....	49
Figure 3.1 Schematic representation of possible interactions between sunlight and particles.....	54
Figure 3.2 NO <sub>2</sub> profiles from surface to 10.0 km used in the SCIATRAN.....	59
Figure 3.3 Phase functions at 440 nm for fine and coarse aerosol .....	62
Figure 3.4 Aerosol extinction profiles used in the SCIATRAN.....	64
Figure 3.5 NO <sub>2</sub> AMF for simulations with different SR values (no aerosol) .....	68
Figure 3.6 NO <sub>2</sub> AMF for simulations with different SR values (Sc. C, AOD 0.1 and 0.9).....	69
Figure 3.7 NO <sub>2</sub> AMF for simulations with different SR values (Sc. C, different AOD, SZA 50°).....	69
Figure 3.8 NO <sub>2</sub> AMF for simulations with different SR values (Sc. C, different SSA, AOD 0.5) .....	70
Figure 3.9 NO <sub>2</sub> AMF for simulations with different NO <sub>2</sub> profiles (different BL height, no aerosol) ...	70
Figure 3.10 NO <sub>2</sub> AMF for simulations with different NO <sub>2</sub> profiles (Sc. A, C and H, different AOD). 71	
Figure 3.11 NO <sub>2</sub> AMF for simulations with different NO <sub>2</sub> profiles (different AOD).....	73
Figure 3.12 NO <sub>2</sub> AMF for simulations with different phase functions (Sc. C) .....	74
Figure 3.13 NO <sub>2</sub> AMF for simulations with different aerosol layers (Sc. B, C and F, different AOD) 77	
Figure 3.14 NO <sub>2</sub> AMF for simulations with different aerosol layers (Sc. B, C and F, SZA 50°) .....	78

---

Figure 3.15 NO <sub>2</sub> AMF for simulations with different aerosol layers (Sc. I, J and K).....	78
Figure 3.16 NO <sub>2</sub> AMF for simulations with different aerosol layers (Sc. D and E, different AOD)....	80
Figure 3.17 NO <sub>2</sub> AMF for simulations with different aerosol layers (Sc. L to P).....	81
Figure 3.18 NO <sub>2</sub> AMF for simulations with different SSA (Sc. B and D, different AOD) .....	83
Figure 3.19 NO <sub>2</sub> AMF for simulations with different SSA (Sc. C and F).....	84
Figure 3.20 NO <sub>2</sub> AMF for simulations with different SSA (Sc. J and O) .....	85
Figure 4.1 RGB images from MODIS and MERIS of ash plume from Eyjafjallajökull .....	90
Figure 4.2 NO <sub>2</sub> concentrations from the model EURAD .....	95
Figure 4.3 Volcanic ash AOD, at 437.5 nm, derived from EURAD model data .....	95
Figure 4.4 Used tropospheric NO <sub>2</sub> vertical columns derived from EURAD model data .....	96
Figure 4.5 AOD (437.5 nm) of total aerosol and volcanic ash, derived from EURAD model data....	99
Figure 4.6 Phase functions determined for each aerosol type, at 437.5 nm .....	100
Figure 4.7 Comparison between the phase function of ash used and the one derived from measurements performed at IUP - Bremen.....	101
Figure 4.8 Phase functions used for the mixture of all aerosol types and without ash .....	102
Figure 4.9 NO <sub>2</sub> AMF for the 16 <sup>th</sup> of April 2010 calculated for 3 scenarios .....	106
Figure 4.10 NO <sub>2</sub> AMF for the 17 <sup>th</sup> of April 2010 calculated for 3 scenarios .....	106
Figure 4.11 NO <sub>2</sub> AMF for the 18 <sup>th</sup> of April 2010 calculated for 3 scenarios .....	107
Figure 4.12 Ratio of NO <sub>2</sub> AMF of calculations with no aerosol and total aerosol.....	107
Figure 4.13 Ratio of NO <sub>2</sub> AMF of calculations with no aerosol and all aerosol except ash .....	108
Figure 4.14 Ratio of NO <sub>2</sub> AMF of calculations with no ash and total aerosol .....	108
Figure 4.15 Selected locations for a detailed analysis of the effect of ash on the NO <sub>2</sub> AMFs. ....	109
Figure 4.16 NO <sub>2</sub> and aerosol vertical profiles for selected locations, on the 16 <sup>th</sup> April 2010. ....	111
Figure 4.17 NO <sub>2</sub> and aerosol vertical profiles for selected locations, on the 17 <sup>th</sup> April 2010. ....	111
Figure 4.18 NO <sub>2</sub> and aerosol vertical profiles for selected locations, on the 18 <sup>th</sup> April 2010. ....	112
Figure 5.1 Scheme of different MOZART versions analysed and their changes.....	126
Figure 5.2 Scheme of different TM5 versions analysed and their changes .....	128
Figure 5.3 NO <sub>2</sub> model data separated into stratospheric and tropospheric columns.....	129
Figure 5.4 Tropospheric NO <sub>2</sub> VC from SCIAMACHY, at different spatial resolutions .....	131
Figure 5.5 Tropospheric NO <sub>2</sub> VC from model output before and after the masking with SCIAMACHY available measurements .....	132
Figure 5.6 Regions selected for the evaluation of NO <sub>2</sub> .....	133
Figure 5.7 3-month averages of strat. NO <sub>2</sub> from SCIAMACHY and MOZART V1, V7 and V10....	137
Figure 5.8 3-month averages of strat. NO <sub>2</sub> from SCIAMACHY and MOZART V9 and V10 .....	138
Figure 5.9 Seasonality curves of strat. NO <sub>2</sub> from SCIAMACHY and MOZART V1, V7 and V10...	139
Figure 5.10 Seasonality curves of strat. NO <sub>2</sub> from SCIAMACHY and MOZART V9 and V10 .....	140
Figure 5.11 3-month averages of trop. NO <sub>2</sub> from SCIAMACHY and MOZART V1, V7 and V10. .	141

Figure 5.12 3-month averages of trop. NO <sub>2</sub> from SCIAMACHY and MOZART V9 and V10.....	142
Figure 5.13 Monthly averages of trop. NO <sub>2</sub> from SCIAMACHY and MOZART V10 for Siberia and Alaska fires .....	143
Figure 5.14 Seasonality curves of trop. NO <sub>2</sub> from SCIAMACHY and MOZART V1, V7 and V10 .	145
Figure 5.15 Seasonality curves of trop. NO <sub>2</sub> from SCIAMACHY and MOZART V9 and V10.....	146
Figure 5.16 3-month averages of strat. NO <sub>2</sub> from SCIAMACHY and TM5 V7 .....	147
Figure 5.17 3-month averages of strat. NO <sub>2</sub> from SCIAMACHY and TM5 V9 and V10 .....	148
Figure 5.18 Seasonality curves of strat. NO <sub>2</sub> from SCIAMACHY and TM5 V7 and V9 .....	149
Figure 5.19 3-month averages of trop. NO <sub>2</sub> from SCIAMACHY and TM5 V7 .....	150
Figure 5.20 3-month averages of trop. NO <sub>2</sub> from SCIAMACHY and TM5 V9 and V10.....	151
Figure 5.21 Monthly averages of trop. NO <sub>2</sub> from SCIAMACHY and TM5 V7 and V10 .....	152
Figure 5.22 Seasonality curves of trop. NO <sub>2</sub> from SCIAMACHY and TM5 V7, V9 and V10 .....	153

---

# List of Tables

Table 2.1	Volume mixing ratios of the permanent and some variable atmospheric gases .....	7
Table 3.1	Size distribution parameters and refractive indices from 12 AERONET stations. ....	61
Table 3.2	Scenarios considered for the SCIATRAN runs, NO <sub>2</sub> and aerosol layers .....	64
Table 3.3	Aerosol parameters used to define the aerosol vertical profile in SCIATRAN scenarios.....	65
Table 3.4	Source references used of the extra aerosol vertical profiles .....	66
Table 4.1	Density ( $\rho$ ) for different aerosol species .....	97
Table 4.2	Size distribution parameters ( $r$ and $\sigma$ ) for the different aerosol modes used .....	98
Table 4.3	Refractive indices for the different aerosol species .....	98
Table 4.4	Optical characteristics of aerosol layers and results for 16 <sup>th</sup> April, 2010.....	113
Table 4.5	Optical characteristics of aerosol layers and results, for 17 <sup>th</sup> April, 2010.....	114
Table 4.6	Optical characteristics of aerosol layers and results, for 18 <sup>th</sup> April, 2010.....	115
Table 5.1	Monthly correlation coefficients of trop. NO <sub>2</sub> from SCIAMACHY and MOZART V1....	156
Table 5.2	Monthly correlation coefficients of trop. NO <sub>2</sub> from SCIAMACHY and MOZART V10..	156
Table 5.3	Monthly correlation coefficients of trop. NO <sub>2</sub> from SCIAMACHY and TM5 V7 .....	157
Table 5.4	Monthly correlation coefficients of trop. NO <sub>2</sub> from SCIAMACHY and MOZART V10..	157
Table 5.5	Monthly correlation coefficients of trop. NO <sub>2</sub> from SCIAMACHY and TM5 V10.....	158
Table A.1	Monthly correlation coefficients of trop. NO <sub>2</sub> from SCIAMACHY and MOZART V7... 167	
Table A.2	Monthly correlation coefficients of trop. NO <sub>2</sub> from SCIAMACHY and MOZART V9... 168	
Table A.3	Monthly correlation coefficients of trop. NO <sub>2</sub> from SCIAMACHY and TM5 V9.....	168

# List of chemical species

Ar – Argon	IO – Iodine monoxide
BrO – Bromine monoxide	N <sub>2</sub> – Nitrogen
CFCl <sub>3</sub> – Trichlorofluoromethane (also known as CFC-11)	N <sub>2</sub> O – Nitrous oxide
CF <sub>2</sub> Cl <sub>2</sub> – Dichlorodifluoromethane (also known as CFC-12)	N <sub>2</sub> O <sub>5</sub> – Dinitrogen pentoxide
CH <sub>3</sub> O <sub>2</sub> – Methyl peroxide radical	NaCl – Sodium chloride
CH <sub>3</sub> OOH – Methyl hydroperoxide	NaNO <sub>3</sub> – Sodium nitrate
CH <sub>4</sub> – Methane	NH <sub>3</sub> – Ammonia
CHOCHO – Glyoxal	NH <sub>4</sub> <sup>+</sup> – Ammonium ion
Cl/Cl <sub>2</sub> – Chlorine atom/molecular	NO – Nitric oxide
ClNO <sub>2</sub> – Chlorine nitrite	NO <sub>2</sub> – Nitrogen dioxide
ClONO <sub>2</sub> – Chlorine nitrate	NO <sub>3</sub> – Nitrate radical
ClO – Chlorine monoxide	NO <sub>3</sub> <sup>-</sup> – Nitrate ion
(ClO) <sub>2</sub> – Chlorine monoxide dimer	NO <sub>x</sub> – Nitrogen oxides (=NO+NO <sub>2</sub> )
CO – Carbon monoxide	NO <sub>y</sub> – Nitrogen species
CO <sub>2</sub> – Carbon dioxide	O/O <sub>2</sub> – Oxygen atom/molecule
CH <sub>3</sub> SCH <sub>3</sub> (DMS) – Dimethyl sulfide	O( <sup>1</sup> D) – Oxygen atom (first excited state)
H/H <sub>2</sub> – Hydrogen atom/molecule	O( <sup>3</sup> P) – Oxygen atom (ground state)
H <sup>+</sup> – Hydron	O <sub>3</sub> – Ozone
H <sub>2</sub> O – Water	OCIO – Chlorine dioxide
HCl – Hydrogen chloride	OH – Hydroxyl radical
HCHO – Formaldehyde	PAN – Peroxyacetyl nitrate
HNO <sub>3</sub> – Nitric acid	PM <sub>2.5</sub> – Particulate matter with size ≤ 2.5 μm
HNO <sub>4</sub> – Peroxynitric acid	PM <sub>10</sub> – Particulate matter with size ≤ 10 μm
HO <sub>2</sub> – Hydroperoxyl radical	SO <sub>2</sub> – Sulphur dioxide
HOCl – Hypochlorous acid	SO <sub>4</sub> <sup>-2</sup> – Sulphate ion
	VOCs – Volatile organic compounds

---

# List of acronyms and abbreviations

AD-net – Asia Dust Network	CLTRAP – Convention on Long-Range Transboundary Air Pollution
AeroCom – Aerosol Comparisons between Observations and Models	CNRS – Centre National de la Recherche Scientifique
AERONET – Aerosol Robotic Network	CTM – Chemical Transport Model
AMF – Airmass Factor	
AL – Aerosol Layer	
AOD – Aerosol Optical Depth (also known as Aerosol Optical Thickness, AOT)	DOAS – Differential Optical Absorption Spectroscopy
AR4 – Fourth Assessment Report	DANDELIONS – Dutch Aerosol and Nitrogen Dioxide Experiments for Validation of OMI and SCIAMACHY
AVHRR - Advanced Very High Resolution Radiometer	
AWI – Alfred Wegener Institute	
	EARLINET – European Aerosol Research Lidar Network
BASCOE - Belgian Assimilation System for Chemical Observations	ECMWF – European Centre for Medium- Range Weather Forecasts
BAMF – Block Airmass Factor	EDGAR – Emission Database for Global Atmospheric Research (2, V3 – version 3, and F72000 - Fast Track 2000)
BL – Boundary Layer	EEA – European Environment Agency
BRDF – Bidirectional Reflectance Distribution Function	EEM – EURAD Emission Module
	EMEP – European Monitoring and Evaluation Programme
CAFE – Clean Air for Europe	ENVISAT – Environmental Satellite
CALIPSO – Cloud-Aerosol Lidar and Infrared Pathfinder Satellite Observation	ERS-2 – European Remote Sensing Satellite 2
CBM-IV – Carbon Bond Mechanism IV	ESA – European Space Agency
CCN – Cloud Condensation Nuclei	EURAD – European Air Pollution Dispersion
CFCs – Chlorofluorocarbons	EUROTRAC – European Experiment on the Transport and Transformation of
CINDI – Cabauw Intercomparison Campaign of Nitrogen Dioxide Measuring Instruments	

Environmentally Relevant Trace Constituents in the Troposphere over Europe	KNMI – Koninklijk Nederlands Meteorologisch Instituut
FRESCO – Fast Retrieval Scheme for Cloud Observables	LOA-PHOTONS – Laboratoire d'Optique Atmospherique - PHOTONS national observatory
GAW – Global Atmospheric Watch	LOWTRAN – Low Spectral Resolution Atmospheric Transmittance
GEIA – Global Emission Inventories Activity	LT – Local Time
GEMS – Global and Regional Earth-System (Atmosphere) Monitoring Using Satellite and In-situ Data	LRTAP – Convention on Long-range Transboundary Air Pollution
GFEDv2 – Global Fire Emission Database version 2	MACC – Monitoring Atmospheric Composition and Climate
GHG – Greenhouse Gases	MADE – Modal Aerosol Dynamics Model for EURAD
GMES – Global Monitoring for Environment and Security	MAX-DOAS – Multi Axis Differential Optical Absorption Spectroscopy
GOCART – Goddard Chemistry Aerosol Radiation and Transport	MetOp – Meteorological Operational
GOME(-2) – Global Ozone Monitoring Experiment (2)	MERIS – Medium Resolution Imaging Spectrometer
GOMETRAN – radiative transfer model for GOME	MISR – Multi-angle Imaging Spectrometer
IFS – Integrated Forecasting System	MM5 – Meteorological Model Version 5
IR – Infrared	MOCAGE - Model of Atmospheric Chemistry at Large Scale
IPCC – Intergovernmental Panel on Climate Change	MODIS – Moderate Resolution Imaging Spectroradiometer
IUGG – International Union of Geodesy and Geophysics	MODTRAN – Moderate Resolution Transmittance Model
IUP – Institute für UmweltPhysik (Institute of Environmental Physics)	MOPITT - Measurements of Pollution in the Troposphere
JPL (97, 03, and 06) – chemical kinetics and photochemical data for use in atmospheric studies published by the Jet Propulsion Laboratory in 1997, 2003, or 2006	MOZAIC – Measurements of Ozone, Water Vapour, Carbon Monoxide and Nitrogen Oxides by In-service Airbus Aircraft
	MOZART – Model for Ozone and Related Chemical Tracers

NASA – National Aeronautics and Space Administration

NDVI – Normalized Difference Vegetation Index

OASIS 4 - Ocean Atmosphere Sea Ice Soil Coupling Software 4

OMI – Ozone Monitoring Instrument

ORCHIDEE – Organizing Carbon and Hydrology in Dynamic Ecosystems

POPs – Persistent Organic Pollutants

PROMOTE – Protocol Monitoring for the GMES Service Element: Atmosphere

RACM – Regional Atmospheric Chemistry Mechanism

RADM2 – Regional Acid Deposition Model, version 2

REAS – Regional Emission Inventory in Asia

RETRO – Reanalysis of the Tropospheric Chemical Composition over the Past 40 years

RF – Radiative Forcing

RGB – Red, Green, Blue

RIU – Rheinisches Institut für Umweltforschung

RT – Radiative Transfer

RTM – Radiative Transfer Model

SAP – Scientific Assessment Panel

SBUV – Solar Backscatter Ultraviolet

SC – Slant Column

SCIAMACHY – Scanning Imaging Absorption Spectrometer for Atmospheric Chartography

SCIATRAN – radiative transfer model for SCIAMACHY

SOA – Secondary Organic Aerosol

SORGAM – Secondary Organic Aerosol Module

SR – Surface Reflectance

SSA – Single Scattering Albedo

SWIR – Short Wave Infrared

SZA – Solar Zenith Angle

TAR – Third Assessment Report

TM3, TM4, TM5 – Tracer Model 3, 4, 5

TNO – Toegepast-Natuurwetenschappelijk Onderzoek

TOA – Top of Atmosphere

TOMS – Total Ozone Mapping Spectrometer

UN – United Nations

UNECE – United Nations Economic Commission for Europe

UNFCCC – United Nations Framework Convention on Climate Change

US – United States

UTC – Coordinate Universal Time

UV – Ultraviolet

VAAC – Volcanic Ash Advisory Centre

VC – Vertical Column

vis – Visible

WHO – World Health Organization

WMO – World Meteorological Organization

# 1

## Introduction and motivation

The Industrial Revolution that took place in the 18<sup>th</sup> century was a historical turning point for the equilibrium previously found between humans and natural ecosystems. Since then, a heavier burden has developed, which we cannot yet fully control: pollution. Human activities have already affected and damaged the Earth's ecosphere (atmosphere, biosphere, hydrosphere and lithosphere) in many ways, with partly irreversible consequences. The effects of pollution have aggravated severely with the intensification of production and the increase of fossil fuel consumption, which resulted in large amounts of harmful compounds being released to the ecosystems. The rapid growth of human population has led to changes in land use and agricultural practices, resulting in additional pollution, in many different forms, and on a global level. Remote regions are no longer pristine as they once were. According to the Gaia hypothesis suggested by Lovelock, any man-made atmospheric pollution will not only affect the atmosphere but will, eventually, force the biosphere to adapt as well. Biogeochemical processes (e.g., water cycle, carbon cycle) are links between the different Earth systems and are severely disturbed by human activities. Smog and high concentrations of ozone in the troposphere, acid rain, particulate pollution, depletion of stratospheric ozone, and intensification of the greenhouse effect that leads to global climate change, are only a few examples of the human-induced environmental problems caused in the atmosphere.

The atmosphere encloses the Earth and is essential for the existence of life. This layer absorbs harmful UV solar radiation before it reaches the surface, and also keeps the surface temperature fairly constant, at a suitable level for life to be able to exist. Atmospheric constituents (gases, aerosol and

## Introduction and motivation

---

clouds) play a crucial role in the Earth's energy balance, absorbing and emitting incoming and outgoing radiation. A close look into current air quality levels brought to attention, not only to the scientific community but also to the general public, the extent of environmental problems and how these are directly linked to human activities. The depletion of the Antarctic ozone layer came as a warning of how important it is to keep the stratosphere intact, so that UV radiation is screened. In spite of the success of the Montreal Protocol, recently, in the spring of 2011, this problem was no longer limited to remote areas of the South Pole, but also verified above highly populated regions in the Northern hemisphere (AWI, 2011). Monitoring air quality is already a long established practice, together with assessing pollution levels and establishing strategies to reduce anthropogenic pollution and its consequences. To better understand these processes, it is also important to analyse their sources and how the biogeochemical cycles are affected.

Remarkable progress has been achieved in atmospheric (chemistry) science over the past years. The number of observational platforms has grown, and technological developments have allowed for new and improved instrumental methods to measure atmospheric composition. Ground-based observation techniques have evolved greatly, with measurements being performed from airborne platforms as well (e.g., balloon or aircraft). However, a fundamental breakthrough in global observations took place with the launch of satellites and the possibility of performing space-based measurements. Remote sensing techniques have reached a level that atmospheric composition can now be measured from space and assessed on a global scale. The resulting maps help the study of atmospheric processes involved in the formation and transport of, e.g., chemical compounds and aerosol. In addition, pollution trends can be derived from the long-term observations, and the efficiency of measures implemented to reduce emissions can be assessed. At the same time, atmospheric models, such as global circulation models (GCMs) together with chemical transport models (CTMs), became essential tools to facilitate the interpretation of measurements. The integration of observations with meteorological data and known chemical mechanisms in these models empowers the prediction of pollution events, so that the population may be warned and prepared.

Nitrogen dioxide ( $\text{NO}_2$ ) is a key pollutant in the troposphere, harmful for living beings, and one of the main precursors of tropospheric ozone (e.g., Wayne, 2006). It can form nitric acid, which is responsible for acid rain (e.g., Wallace and Hobbs, 2006), and contributes to global climate change by interfering, directly and indirectly, with the Earth's radiative budget (e.g., IPCC, 2007). Nitrogen oxides ( $\text{NO}_x = \text{NO} + \text{NO}_2$ ) are mainly emitted from fossil fuel combustion and are, therefore, linked to anthropogenic pollution in urban and industrial areas. In addition,  $\text{NO}_x$  (mostly  $\text{NO}$ ) is emitted from biomass burning events, microbial activity in soils, and lightning. The good knowledge of emission processes and chemical mechanisms involving this compound is crucial when analysing atmospheric pollution. With the goal of improving air quality, environmental regulations were implemented in

many countries, and close monitoring of atmospheric composition became compulsory. Since  $\text{NO}_2$  is a good proxy for pollution levels in urban and industrial environments, satellite observations can also be used for that purpose. These datasets are not only useful to monitor pollution and determine emission trends (e.g., Richter et al., 2005; Kim et al., 2006), but also important for the study of transport processes in the atmosphere (Mora et al., 2007). Satellite measurements have been used to estimate global  $\text{NO}_x$  emissions (e.g., Martin et al., 2003) and, on a more detailed level, the contributions from specific source categories, such as fuel combustion, biomass burning and soils (e.g., Jaeglé et al., 2005), lightning (e.g., Beirle et al., 2010a), and ships (e.g., Beirle et al., 2004). Furthermore, as it will be demonstrated in this thesis, and was also done by van Noije et al. (2006) and Huijnen et al. (2010b), satellite data are often useful, as an independent dataset, to validate CTMs. In this way, inaccuracies can be identified and the model schemes revised, so that the simulation output will get closer to reality.

Satellite observations employing the DOAS (Differential Optical Absorption Spectroscopy) method yield slant columns, i.e., the absorber concentration integrated along the light path. These slant columns are converted into vertical columns with the use of air mass factors (AMFs) that are computed with radiative transfer models. The AMFs are dependent on many aspects such as: geometry and wavelength of measurement, vertical distribution of the chemical species, surface reflectance, aerosol loading, and clouds. While some of these factors are well known, others are highly uncertain and variable. The main goal of this work was to understand how atmospheric aerosol influences satellite observations of trace gases, with focus on  $\text{NO}_2$ , and, consequently, the retrieved tropospheric vertical columns. The assessment of this impact is essential given that anthropogenic sources of aerosol and other pollutants are often collocated. This is of particular importance if long-term trends of, for example, tropospheric  $\text{NO}_2$  are studied in regions where large changes were also verified in the aerosol loading. The presence of aerosol and its influence is not always accounted for in the retrieval of satellite measurements. Those retrievals that do include aerosol, address this issue in different ways, e.g., using information from static climatologies, or applying simplified model predictions. Here, a case study was developed where detailed model output for  $\text{NO}_2$  and aerosol was used in the calculations of AMFs. The investigation focused on the impact of volcanic ash, selecting the eruption of the Icelandic volcano Eyjafjallajökull in the spring of 2010 as the event to analyse. The implementation of this method to a large dataset turned out to be more complex than anticipated. On the one hand, aerosol is highly variable in time and space, and global data on high resolution is not readily available. In addition, the simplification of the complex processes of interaction between particles and radiation is not yet mastered so that it can be applied online to large satellite datasets.

### **Structure of the thesis**

This thesis starts with the introduction of the fundamental concepts relevant for the presented investigation. The basic concepts of the Earth's atmosphere and its composition are covered, with more detail for NO<sub>2</sub> and aerosol. Furthermore, radiative transfer principles are explained, with focus on atmospheric scattering processes. Following that, a description of the DOAS method and the satellite retrieval of tropospheric NO<sub>2</sub> is provided.

In chapter 3, results from a sensitivity study are presented, where key factors were identified for the radiative transfer calculations representing the aerosol effects on satellite observations. This study illustrates how atmospheric aerosol can affect the satellite retrieval of tropospheric NO<sub>2</sub> columns. The conclusions reached are based on the changes of airmass factors determined with the radiative transfer model SCIATRAN (Rozanov et al., 2005).

The outcome of the sensitivity study was then taken further. Chapter 4 deals with a case study focussing on the impact of volcanic ash on satellite observations. For this analysis the scenario chosen was the eruption of the Icelandic volcano Eyjafjallajökull in the spring of 2010. Aerosol and NO<sub>2</sub> data were provided by the RIU group working with the EURAD CTM. With these data, a set of scenarios were defined for conditions during the volcanic eruption and then used in the radiative transfer model. In this chapter, the variation of AMFs could be attributed to the presence of ash, demonstrating how it affects the satellite observations.

Proceeding to chapter 5, a model evaluation performed within the GEMS project is described. Global stratospheric and tropospheric NO<sub>2</sub> columns predicted by two chemical transport models – MOZART and TM5 – are compared with observations from the satellite instrument SCIAMACHY. This analysis emphasises the importance of satellite data to identify flaws in the modelling systems, contributing to the development and improvement of their capabilities.

Finally, chapter 6 summarises the major conclusions of this thesis and provides an outlook on future work. In addition, the potential for application of the findings of this work is contemplated, so that improvements of the current methods employed for the retrieval of trace gas columns measured from satellite instruments can be achieved in the near future.

# 2

## Fundamentals

At the centre of the Solar System lies the Sun, a star with a diameter that is approximately 109 times larger than the Earth. The planet Earth was formed approximately 4.5 billion years ago (much later than the Sun), from the collision of large solid elements rotating in the solar nebula. Sunlight takes a little more than 8 minutes to reach the Earth. This energy is essential for life (e.g., for photosynthesis) and drives the climate and weather of the planet. The Sun is quite a dynamic celestial body that consists mostly of hydrogen, helium, and other plasma, and has a surface temperature of about 5770 K. The variable solar activity occurs because of its differential rotation and also due to changes in magnetic fields that interact with the plasma. The Sun is rotating with a synodic period which is faster at the equator (~25 days) than at the poles (~35 days), the differential rotation (27-day cycle). Furthermore, approximately every 11 years the magnetic fields in the sunspot groups reverses itself, meaning that the dipole changes polarity. After approximately 22 years the polarity has gone through a full cycle (22 year magnetic cycle). Due to an increased activity during changing phases of the magnetic cycle and an enhanced output in electromagnetic radiation and particle emissions, this cycle and the 27-day cycle eventually affect the Earth's ecosystems and our climate.

The following sections introduce the main aspects related to the Earth's atmosphere, approaching topics from its structure to the chemical composition, focussing more on the nitrogen dioxide (NO<sub>2</sub>), the trace gas analysed in this work, and aerosol, which have an important impact on satellite observations. In addition, also basic concepts of radiative transfer will be reviewed. The fundamentals explained here are based on information available in several publications, such as Brasseur (2003),

Jacobson (2005), Seinfeld and Pandis (2006), Wallace and Hobbs (2006), Wayne (2006), Hewitt and Jackson (2009), and Burrows et al. (2011) and further references cited accordingly.

## 2.1 Earth's atmosphere

According to Merriam-Webster (<http://www.merriam-webster.com/dictionary/>) the word *atmosphere* (from 1677) comes from the new Latin *atmosphæra*, with origins in the Greek *atmos*, vapour + Latin *sphaera*, sphere. Earth's atmosphere as we know it today is the result of many changes since the origin of the planet. This evolution was significantly linked to the biosphere as, for example, the oxygen content of the atmosphere is mostly owed to the photosynthesis done by primary life forms some million years ago. In fact, Lovelock and co-workers conjectured, in the Gaia theory, that the atmosphere was a “construction maintained by the biosphere” (Hewitt and Jackson, 2009, and references therein), i.e., in a single system the biosphere can maintain the Earth in homeostasis. The atmosphere is a thin layer of gas surrounding the planet and kept in place by gravitation. It protects the Earth from the harmful UV solar radiation and maintains its temperature at a suitable level for life to be able to exist. The chemical composition of the atmosphere can be divided into two different categories: primary and trace gases. The permanent compounds are those gases with fairly constant volume mixing ratios both in time and space, i.e., well mixed throughout the atmosphere. These are argon (Ar), molecular nitrogen (N<sub>2</sub>) and oxygen (O<sub>2</sub>), which together account for more than 99.96% of the atmosphere by volume. In Table 2.1, their contributions to atmosphere composition are described, together with some of the trace gases belonging to the remaining 0.04%. These so-called variable gases include a vast variety of species and, in this table, only a few most relevant are mentioned, e.g., water vapour, CO<sub>2</sub>, CH<sub>4</sub>, O<sub>3</sub>, among others. Nevertheless, the atmosphere is not composed only of gases but contains also aerosol (atmospheric solid and/or liquid particles) and clouds which are highly variable in space and time.

Already back in 1960, the International Union of Geodesy and Geophysics (IUGG) defined that the atmosphere (up to about 120 km) is divided into four distinct layers according to the vertical profile of temperature: troposphere, stratosphere, mesosphere, and thermosphere (Liou, 2002). In Figure 2.1, the commonly referred US standard atmosphere (1976) is portrayed, with the identification of the layers and the interfaces: tropopause, stratopause, and mesopause. Furthermore, the region closest to the surface is called planetary boundary layer (BL). This region is different from the remaining free troposphere because of the strong and significant interactions of atmosphere with the surface. While the upper part of the troposphere is influenced by the surface only on longer time scales, the boundary

## Fundamentals

---

layer responds immediately to surface forcing, i.e., within an hour or less (Stull, 1988). Close to the surface, variations of temperature are registered from day to night, which will influence the dynamics within this layer and, consequently, its vertical extent. At these altitudes a rapid vertical mixing of pollutants is often observed, depending on temperature profile.

Table 2.1 Fractional concentrations by volume (volume mixing ratios) of the permanent atmospheric compounds (in percentage) and some of the variable gases (in ppmv). The values are provided for dry air (values reported by Wallace and Hobbs (2006))

Compound	Volume Mixing Ratio	Main Source
Nitrogen (N <sub>2</sub> )	78.08%	Biological
Oxygen (O <sub>2</sub> )	20.95%	Biological
Argon (Ar)	0.93%	Radiogenic
Water Vapour (H <sub>2</sub> O)	0 - 5%	Evaporation, Biological
Carbon Dioxide (CO <sub>2</sub> )	379 ppmv	Biological, Oceanic, Combustion
Methane (CH <sub>4</sub> )	1.75 ppmv	Biological, Anthropogenic
Hydrogen (H <sub>2</sub> )	0.5 ppmv	Biological, Anthropogenic
Nitrous Oxide (N <sub>2</sub> O)	0.3 ppmv	Biological, Anthropogenic
Carbon Monoxide (CO)	0.04 – 0.2 ppmv	Photochemical, Combustion, Anthropogenic
Ozone (O <sub>3</sub> )	0.01 - 0.1 ppmv	Photochemical
Nitrogen species (NO <sub>y</sub> )	0.00001 – 1 ppmv	Biological, Anthropogenic, Lightning

The troposphere (from the Greek turning or changing) is the lowest layer and, therefore, more directly influenced by human activities and the resulting emissions. Most of the total mass of the atmosphere (~80%) is confined to this region. In fact, nearly all of the water vapour, clouds, and precipitation are in this layer, which are active mechanisms to clean great part of the pollutants from the atmosphere. This mass distribution is related to the variation of atmospheric pressure ( $p$ ) with altitude ( $z$ ) that follows the hydrostatic equation:

$$\frac{dp}{dz} = -g \rho \quad (2.1),$$

where  $g$  is the acceleration due to gravity ( $9.807 \text{ m.s}^{-2}$  on average) and  $\rho$  the air density. Assuming that the atmosphere can be treated as an ideal gas and, thus, follows the equation of state, it is possible to come to the following relation that describes an exponential decrease of the air pressure:

$$p(z) \approx p_0 e^{-z/H} \quad (2.2),$$

where  $H$  is the scale height parameter which is assumed to be 7 – 8 km at the lowest 100 km of the atmosphere, and  $p_0$  the surface pressure. A decrease of the temperature with increasing altitude is also observed in the troposphere with a typical lapse rate of  $6.5 \text{ K.m}^{-1}$  (starting at 288 K at the surface level). The troposphere extends to the tropopause which has a latitude dependent altitude. While at the poles the typical height for the tropopause is 8 km, this can increase to 15 km or more in the equatorial region (see the example in Figure 2.2). This variation is related to the amount of incident solar light that reaches the Earth. More light will result in higher temperatures which drive the dynamics and expansion of the tropospheric layer. Therefore, a slight seasonal variation in some regions is also expected. In Figure 2.2 the temperature profiles in the tropopause region are represented for different locations: tropical ( $15^\circ\text{N}$ ), mid-latitude ( $45^\circ\text{N}$ ) and sub-arctic ( $60^\circ\text{N}$ ). These profiles were taken from the database of the MODTRAN model (the MODerate resolution TRANsmittance model for LOWTRAN model, Berk et al., 1989) and are based on a subset of the 1966 Atmospheric Supplements (Kneizys et al., 1996). While the transition from the stratosphere to the troposphere is quite sudden in the tropics, an isothermal layer can be differentiated for the remaining locations. Furthermore, the altitude of the tropopause, i.e., the height where the inversion of the tropospheric temperature profile occurs, presents a seasonal variation and also depends on latitude.

The temperature profile in the stratosphere (from the Latin *stratum* layer) starts with the isothermal layer above mentioned that extends from the tropopause to an average altitude of 20 km. Then, the temperature will increase up to the stratopause that is situated at approximately 50 km. The stratosphere is mostly characterised by high concentrations of  $\text{O}_3$  (~90% of Earth's ozone). Ozone absorbs UV radiation heating up the atmosphere, causing an inversion of the temperature profile. As stated before, this process is essential for life on Earth since the UV radiation is extremely harmful for living organisms. Because of this stable temperature profile, vertical mixing in this layer is strongly reduced which, in the event of high emissions directly at this altitude (as in the Mount Pinatubo eruption (e.g., Dahlback et al., 1994)), results in long lasting layers of pollutants.

In the mesosphere (from the Greek in between) the amount of ozone is much less and the temperature decreases once more to the altitude of approximately 85 km. This reduction can also be explained by radiative cooling from  $\text{CO}_2$ . In this layer the photochemistry is reduced but still quite important, as most of the energy is absorbed by molecular oxygen and ozone (e.g., Allen et al., 1984). Above this layer lies the thermosphere (from the Greek heated) that extends to an altitude of several hundred kilometres, where the air density is quite low and very few molecules exist at this height. The temperatures here increase once more (from 500 K to 2000 K) mostly because of absorption of short

## Fundamentals

wavelength solar radiation by atoms and molecules, the dissociation of atomic nitrogen and oxygen molecules, and the stripping of electrons from atoms. The mesopause is therefore the coldest place on Earth, with temperatures as low as 173 K.

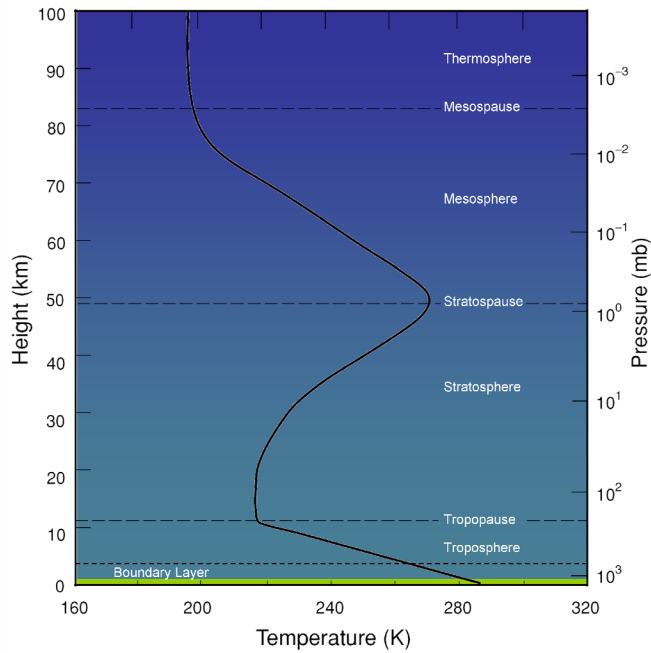


Figure 2.1 Vertical temperature profile after the US Standard Atmosphere and definitions of atmospheric nomenclature. (Source: adapted from Liou, 2002)

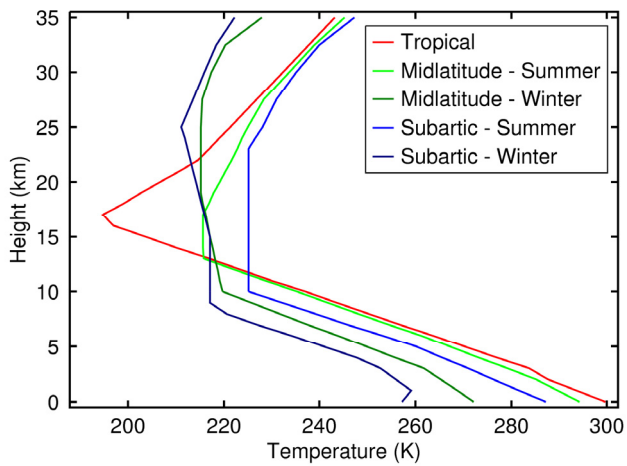


Figure 2.2 Temperature vertical profiles in the tropopause region for different latitudes: tropical (15°N), mid-latitude (45°N) and sub-arctic (60°N); at different seasons (summer and winter, except for tropical).

## 2.2 Atmospheric pollution

The first known use of the word pollution dates back to the 14<sup>th</sup> century (<http://www.merriam-webster.com>). This term is defined in many online dictionaries as: “the action of polluting especially by environmental contamination with man-made waste” or, in other words, the introduction of harmful substances or contaminants into the environment (water, air, or soil). Natural air pollution has been around since the beginning of the Earth with fires, volcanic eruptions, and meteorite impacts that kept introducing chemical compounds into the planet's ecosystem. However, currently, the type of pollution requiring closer attention from the scientific community is the one caused by mankind. Anthropogenic air pollution results mostly from fuel combustion in industry, vehicles and households. Moreover, these are not the only sources of harmful emissions, as there are also other human activities releasing dangerous chemical compounds into the atmosphere. This is, for example, the case of CFCs (chlorofluorocarbons) that are nowadays banned from use because of their destructive effect on the ozone layer. Nevertheless, these were, for many years, utilised in refrigerating and air conditioner apparatus, as solvents and cleaning agents, or even blowing agents for foams. Furthermore, the rapid growth of population and high demand for food led to the intensification of agricultural practices that prompted the use of fertilisers and pesticides on massive scale. All these pollutants resulted in what are, nowadays, well known environmental problems: smog and high concentrations of ozone in the troposphere, acid rain, particulate pollution, depletion of stratospheric ozone, and intensification of the greenhouse effect that leads to global climate change. It is in this context that the word Anthropocene emerges (Crutzen and Stoermer, 2000), to describe this new era that started, most probably, with industrial revolution. The attempt to control air pollution and reduce the negative effects of anthropogenic emissions started already long ago in London with the banning of coal burning. With the spread of affected areas and recognition of transport of emissions outside of national borders, it became essential to define common universal strategies of control. In 1979, the Convention on Long-Range Transboundary Air Pollution (LRTAP) was created to address some of the major environmental problems of the UNECE (United Nations Economic Commission for Europe) region. The scientific collaboration and policy negotiations between the current 51 Parties made possible the creation of eight protocols to reduce emissions of air pollutants, such as sulphur, NO<sub>x</sub> (nitrogen oxides) or POPs (Persistent Organic Pollutants). Furthermore, a mechanism for regional monitoring of pollution was implemented – the European Monitoring and Evaluation Programme (EMEP). Also in Europe, the CAFE (Clean Air for Europe) programme started in 2001 with the goal of establishing long-term and integrated strategies to tackle air pollution. Another important international treaty is the Montreal Protocol which focuses on the protection of the stratospheric ozone layer by limiting the production of CFCs and their emissions into the atmosphere. After some years of negotiations in the United Nations Environment Program, the protocol was

opened for signature in 1987 and entered into force in 1989. The protocol was ratified by all nations belonging to the UN, and has been revised to adjust the measures stipulated for the controlled substances listed in the annexes of the protocol. The United Nations Framework Convention on Climate Change (UNFCCC) was created to deliberate the possibilities to embrace the challenge posed by climate change and minimise the impacts on the globe. The Intergovernmental Panel on Climate Change (IPCC) was established by UNEP and the World Meteorological Organization (WMO), so that a clear scientific view of the current understanding on climate change could be offered to policymakers. This scientific body reviews also technical and socio-economic information, and produces reports that are fundamental for the UNFCCC. The Kyoto Protocol was adopted in 1997 and entered into force in 2005, introducing binding targets for 37 industrialised countries and the European community for reducing anthropogenic emissions of relevant GHGs. Environmental legislation has been commonly debated in many European, Asian and American countries. Universal agreement on what the needs are in terms of air quality assurance is not easily achieved but progress has been made in the past decades and collaboration towards a common goal has been slowly accomplished.

### 2.2.1 Climate change

In this context, climate change refers to the alterations observed due to rapid global warming, resulting from an increased greenhouse effect. The definition however is not the same for every convention or organisation. While at the IPCC the climate change topic deals with all impacts caused by both natural and anthropogenic emissions, for the UNFCCC this refers mostly to the consequences of human activities (directly or indirectly). The greenhouse effect is in fact a natural effect that avoids that the temperature of the planet to become below the freezing point. Part of the short-wavelength sunlight that reaches the Earth's surface is absorbed and emitted back to space in the range of IR wavelength. Much of this radiation is then absorbed and re-emitted by gases, aerosol, and clouds in the atmosphere. As this emission is in all directions, part of the energy is radiated back towards the surface thereby increasing the temperature. However, this natural radiative forcing has been intensified in the past decades (or even centuries) partly because of human activities that change the atmospheric composition.

The main greenhouse gases (GHGs) are CO<sub>2</sub>, CH<sub>4</sub>, water vapour, O<sub>3</sub> and N<sub>2</sub>O. The intensification of CO<sub>2</sub> emissions (by 80% from 1970 to 2004, according to the most recent report of IPCC (2007)) is mainly the outcome of the rapidly increasing fossil fuel combustion needed to power a fast growing urban and industrial society. In addition, massive deforestation carried out in many countries led to the increase of emissions, partly from the burning of the forests, but also from the release of carbon

that was stored in the vegetation and soils. The trend of CO<sub>2</sub> measured in Mauna Loa, Hawaii, is a quite famous chart known as the Keeling curve (Keeling et al., 2010). These measurements are one of the evidences of fast increasing CO<sub>2</sub> in the past decades. Still, while CO<sub>2</sub> atmospheric mixing ratios have grown by ~36% over the last 250 years, CH<sub>4</sub> abundance levels have increased by ~30% in the past 25 years alone (IPCC, 2007). However, this increase is not yet taken as most worrying because, according to the latest estimations in the IPCC report (see Figure 2.3), the combined positive radiative forcing, i.e., warming effect, due to CH<sub>4</sub>, N<sub>2</sub>O and CFCs and tropospheric ozone (1.33 W.m<sup>-2</sup>) is still less than that of CO<sub>2</sub> (1.66 W.m<sup>-2</sup>).

The importance attributed to the role of N<sub>2</sub>O in the radiative forcing balance has been intensified in the past years. In the IPCC report from 2001, N<sub>2</sub>O was considered to be the fourth (from the long-lived GHGs) largest contributor to positive radiative forcing, while, in 2009, Wuebbles referred to it as "the third most important gas directly affecting climate". Although the N<sub>2</sub>O is contemplated in the Kyoto Protocol, the emissions of this important GHG have been increasing by ~20% since pre-industrial times (Wuebbles, 2009). The main problem in the implementation of control policies and effectiveness of reduction of N<sub>2</sub>O concentrations is related to its sources and its long lifetime (about 114 years (e.g., IPCC, 2001)). The emissions of N<sub>2</sub>O from natural and anthropogenic sources are of similar magnitude (IPCC, 2007). The largest fraction of the latter derives from agriculture related sources, namely the intensive use of fertilisers needed to sustain the high demand of food worldwide (Jacob, 1999). Additional sources of N<sub>2</sub>O are microbial process occurring in the soil and oceans.

The negative radiative forcing of ozone in the stratosphere is related to the depletion observed in the recent years. From Figure 2.3 it is also possible to observe that aerosol has an active role on the climate change effects, although the exact extent of this influence is still not fully understood (note the large range of values indicated by the horizontal lines). Global dimming has counterbalanced the greenhouse effect by reducing the amount of direct solar radiation that reaches the Earth's surface. This is mostly done by the highly reflecting particles of sulphate aerosol, whereas soot particles will essentially absorb the radiation. The contribution of aerosol to this estimation of radiative forcing balance is now simplified into direct and indirect effects. The latter refers to the aerosol influence when particles change cloud properties, which is nowadays better understood when compared to the findings from the previous TAR report (IPCC, 2001). More on this topic is discussed in section 2.4.

### 2.2.2 Stratospheric ozone

Most of the ozone of the atmosphere is present in the stratosphere in altitudes from 15 to 50 km, approximately. As it was already mentioned, the ozone layer is vital for life on Earth because it filters

## Fundamentals

the dangerous UV radiation from the sunlight before it reaches the surface. There are three main absorption bands in the O<sub>3</sub> spectrum (Brasseur and Solomon, 2005):

1. the Hartley-band from 200 to 310 nm,
2. the Huggins-band from 310 to 400 nm,
3. the Chappuis-band from 400 to 850 nm.

In the past decades, the ozone layer has been severely depleted mostly due to the high emission of CFCs before the 1990s. Chlorofluorocarbons were used, for example, in refrigerating systems and aerosol propellants and most of them were released directly to the atmosphere. These compounds are chemically inert and, therefore, very resistant and with long lifetimes (e.g., 45 years for CFC<sub>13</sub> or 100 years for CF<sub>2</sub>Cl<sub>2</sub>). As dry and wet deposition are not mechanisms that affect the CFCs, these were often transported to the stratosphere where, *via* photodissociation by UV radiation, these compounds would be transformed into chlorine atoms that are responsible for the destruction of ozone, as it will be explained shortly.

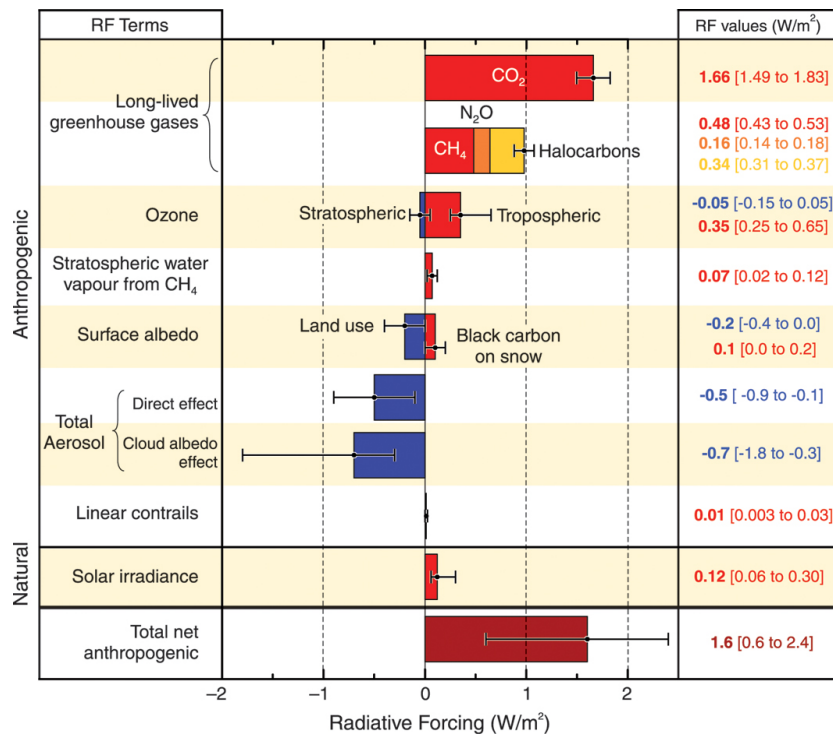
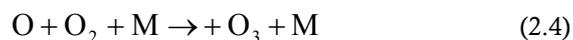


Figure 2.3 Global average radiative forcing (RF, in W.m<sup>-2</sup>), in 2005 with respect to 1750, for different agents and mechanisms. The natural and net anthropogenic radiative forcing are also shown. (Source: adapted from IPCC, 2007)

The mechanisms of formation and destruction of ozone were first explained by Chapman (1930). It includes 4 main reactions as follows (e.g., Wallace and Hobbs, 2006):



Ozone is formed in reaction (2.4) from the photodissociation of molecular oxygen by UV (< 242 nm) radiation. The ozone molecule itself will also photodissociate when absorbing UV radiation. Different products can result from this reaction (2.5):  $\text{O}({}^1\text{D})$  for wavelength  $\lambda < 310$  nm (Hartley-band), and  $\text{O}({}^3\text{P})$  for  $\lambda > 310$  nm (Huggins band). In the reactions above, M is a third body, normally  $\text{N}_2$  or  $\text{O}_2$ , which absorbs the excess of energy from the collision of the three compounds. Ozone is not equally distributed in the stratosphere and its profile explains the increase of temperature observed for this layer. At high altitudes there is less  $\text{O}_2$  in the atmosphere that is needed to initiate the formation of ozone and, hence, its concentration decreases. On the other hand, closer to the tropopause, the  $\text{O}_3$  concentration is more influenced by the reduction in the flux of photons that, at the UV wavelengths, will dissociate  $\text{O}_2$ . Measurements of ozone in the stratosphere revealed that reaction (2.6) was too slow to explain the observed  $\text{O}_3$  amounts in the atmosphere. Therefore, different mechanisms were proposed where species from the families  $\text{ClOx}$ ,  $\text{BrOx}$ ,  $\text{NOx}$ , and  $\text{HOx}$  would be involved, promoting a catalytic cycle as follows:



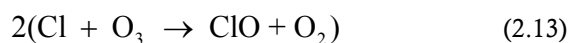
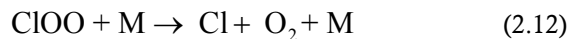
Including these catalytic cycles into models brings predicted and measured ozone distributions into good agreement. Because X is a catalyst agent in these reactions, i.e., not consumed in the cycle, it does not necessarily need to be present in high concentrations to destroy many  $\text{O}_3$  molecules. One of the catalyst agents can be Cl. In the stratosphere, the main sources of Cl, nowadays, are the anthropogenic CFCs (Wayne, 2006) that, when existing at these altitudes will have a strong destructive effect on the ozone layer. Regarding the  $\text{NOx}$ , their main source in the high atmosphere is  $\text{N}_2\text{O}$ , a rather stable compound in the troposphere. When reaching the stratosphere it can be photolysed into  $\text{N}_2$  and the remaining fraction reacts with the excited oxygen atom  $\text{O}({}^1\text{D})$  yielding two molecules of  $\text{NO}$  (Brasseur and Solomon, 2005). As mentioned on the previous section, nitrous oxide has a significant impact on climate. In addition to this effect, this compound has an important indirect influence on stratospheric ozone depletion by contributing to the formation of extra  $\text{NO}$ . This increase of nitric oxide will not only result in the intensification of the natural catalytic cycle of ozone destruction, but also counterbalance the importance of  $\text{ClONO}_2$  as a reservoir species. From the main ozone depleting substances,  $\text{N}_2\text{O}$  is not yet one of the chemical species under control of the Montreal

## Fundamentals

---

Protocol, although its emissions values are the highest and it is predicted to be, in the 21<sup>st</sup> century, the most damaging compound to the ozone layer (Ravishankara et al., 2009).

The chemical cycles above mentioned are the general picture for what happens in the stratosphere. It is also important to mention that the peak of production of stratospheric ozone occurs in tropical regions because of increased incident light. This will then be transported to the mid-latitude and Polar regions *via* the Brewer-Dobson circulation. The ozone depletion phenomenon is more severe at the poles, mostly in Antarctica, and this is caused by the combination of different factors. During the local dark winter, the stratospheric air develops a westerly circulation pattern and a vortex is created, separating these air masses from the remaining atmosphere at lower latitudes. In this region, temperatures drop to about -80°C and polar stratospheric clouds are formed. On the surface of these cloud ice particles, heterogeneous chemical reactions take place, converting inert substances, as for example HCl or ClONO<sub>2</sub>, to easily photolysable species, such as Cl<sub>2</sub>, HOCl and ClNO<sub>2</sub>. When in spring the Sun illuminates the Polar regions again, intensive destruction of the O<sub>3</sub> is provoked by reactions similar to those described above. However, the most efficient mechanism of ozone depletion in the stratosphere takes place *via* a different cycle (e.g., Wayne, 2006):



The result is then the well-known ozone hole. In addition, other compounds (e.g., BrO) will also contribute to the destruction of the ozone layer in the stratosphere (see e.g., Wayne, 2006, for more details on halogens chemistry). According to the recent SAP report (WMO, 2010b), every year the ozone is almost completely depleted in Antarctica during the Austral summer. The levels of ozone have reached a minimum in the mid-1990s and, while the ozone hole has not aggravated in the recent years, it also does not show clear signs of recovery yet. In fact, the last bulletin from WMO reports that, in 2010, although the ozone hole initially appeared to be recovering, larger areas of ozone depletion were observed in the end of the year (WMO, 2010a). The very cold recent winter (2010/2011) had also negative consequences for the ozone layer in the Arctic, causing a massive ozone depletion never before observed in this region (e.g., AWI, 2011). This event shows how this issue is not only relevant for remote regions like Antarctica. In addition, a recent study by Kang et al. (2011) demonstrates how polar ozone depletion can affect the lower latitudes, namely, contributing to the change of precipitation patterns in subtropical areas.

### 2.2.3 Tropospheric ozone

In the troposphere, ozone is a secondary pollutant formed through photochemical reactions of trace gases like NO<sub>x</sub> and VOCs, for example. Ozone is essential for life on Earth when existing at the higher altitudes in the stratosphere. Additionally, it also controls the oxidizing capacity of the troposphere, by producing OH, a key oxidising agent of the atmosphere (i.e., it cleans the air from chemical pollutants). On the other hand, it is rather harmful to humans, causing respiratory illnesses, and to the remaining biosphere when concentrated close to the surface. The World Health Organization (WHO) guideline for concentrations of this pollutant, close to the surface, is 100 µg/m<sup>3</sup> 8-hour mean (WHO, 2006a). The range of O<sub>3</sub> levels close to the surface is highly variable in polluted regions and even more when compared to remote areas. Reported to WHO, annual averages from measurements performed in Europe during 2001 show a variation from 40 to 80 µg/m<sup>3</sup>, though these values can be much higher on hourly basis, e.g., 600 µg/m<sup>3</sup> measured in Mexico City (WHO, 2006b). The summer of 2003 was a good example of such events, a period that was particularly difficult for several European countries, with very high temperatures and hourly ozone concentration values reaching 300 µg/m<sup>3</sup> in many places. Ozone concentrations in the troposphere were not always this high. According to Wallace and Hobbs (2006), the values had more than doubled back in the year 2000. Ozone trends were analysed in detail by Oltmans et al. (2006), who found different patterns around the globe. Nowadays, decreasing trends are found in some areas due to restraints in emissions from anthropogenic activities (IPCC, 2007, and references therein). This high increasing trend, since the industrial revolution, is mostly associated to the rapid increase of NO<sub>x</sub> emissions from fossil fuel combustion, but also from other precursors (Evans et al., 2000). In the recent IPCC report (IPCC, 2007), it was acknowledged that over Europe, ozone levels in the free troposphere have finally levelled off after the precedent continuous increase until the late 1980s.

Generally, urban smog can be defined as local high concentrations of pollutants, both gases and particles that are emitted mainly from anthropogenic sources, e.g., fossil fuel combustion, vehicles, etc. One of the first serious events of smog that was registered happened in London in the beginning of the nineteenth century. This was described as a combination of intense fog and smoke (and hence the derivation of the name) mostly from coal and chemical combustion, and occurred in the winter periods. Later, in the early twentieth century, for the first time in Los Angeles, severe pollution events that took place mostly in the summer months were attributed to another type of smog - the photochemical smog. As the name indicates, this type of smog arises from photochemical reactions. The full chemical scheme involved in the ozone production is quite complex and involves many different chemical species. The main precursors of ozone in the troposphere are NO<sub>x</sub> and VOCs, as the process of formation is initialised by the reaction of OH with organic compounds. Furthermore,

peroxy radicals will allow the conversion of NO into NO<sub>2</sub> without consuming ozone, thereby resulting in an increase of the concentrations of this pollutant. More on these cycles is explained in the following section. Although photochemical smog is mostly related to pollutants emitted in urban environments, at high concentrations, this sort of events can also occur in remote areas. Crutzen (1973) suggested that reactions of OH with CH<sub>4</sub> and hydrocarbons with longer lifetime are the origin of ozone in less polluted regions. Additionally, during the night, ozone can be transported over large distances into remote clean areas. Episodes of high ozone concentrations are frequently associated with specific meteorological conditions, such as inversion layers (e.g., Evans et al., 2000; Carvalho et al., 2010). In this way, the dispersion of the polluted air by convective mixing towards the free troposphere is limited. High-pressure systems often lead to this capping inversion behaviour from the upper part of the BL, and the concentrations of pollutants rise close to the surface, often to dangerous levels for humans and nature. Good examples of such events are the frequent summer episodes verified over the Iberian Peninsula that are often associated with the presence of the Azores anticyclone, which is responsible for the subsidence of dry air (e.g., Leitão and Soares, 2004; Kulkarni et al., 2011, and references therein). This weather system associated with clear sky periods, high values of solar radiation and air rich in ozone precursors are perfect conditions for photochemical production of tropospheric ozone.

The removal of ozone from the troposphere can occur by uptake of this compound by foliage or soils. In addition, the main photochemical sink of ozone in the troposphere is the reaction with HO<sub>2</sub>, producing OH and oxygen. Furthermore, another process of ozone destruction is the denominated NO<sub>x</sub> titration, where the ozone reacts with NO to form NO<sub>2</sub>. Overall, the ozone lifetime can be quite short, on the order of a few hours, in urban areas. Therefore, in such locations large diurnal differences of the O<sub>3</sub> levels are usually registered (see the next section), which are in part related to the emission peaks and depletion of the precursors. Moreover, the variation of O<sub>3</sub> concentrations is dependent on the availability of radiation to start the essential photochemical cycle, the vertical mixing and dry deposition processes. Throughout the year also the variation of UV radiation is going to have an impact on the amount of ozone that is produced. On the other hand, the low production rate in the winter and some spring months (Harrison, 1999), is partly compensated by a longer lifetime in this period. This leads to accumulation of ozone and explains the some higher levels registered in those seasons. Furthermore, the seasonal cycle and latitudinal variation is also related to the water vapour present in the atmosphere that is involved in the destruction of this chemical species.

## 2.3 Nitrogen dioxide (NO<sub>2</sub>)

When dealing with atmospheric chemistry or air pollution, normally NO and NO<sub>2</sub> are treated as nitrogen oxides (NO<sub>x</sub>) because of their rapid interconversion. The main sources of NO<sub>x</sub> in the boundary layer are fossil fuel combustion (in industrial processes, energy production, automobile vehicles, etc), biomass burning events, and soils (*via* nitrification and denitrification processes accomplished by microorganisms). The main hot-spots of NO<sub>x</sub> emissions are located in the Northern hemisphere close to large urban and industrial areas where the main anthropogenic sources are situated. This is illustrated in Figure 2.4 where NO<sub>x</sub> emission values as provided by EDGAR emission inventory are shown (EDGAR-EU, 2009). A significant fraction of the NO<sub>x</sub> emissions also originates from biomass burning events which, sometimes, are occurring naturally, but often are caused by human intervention with the purpose of clearing forest areas or old crop fields. The determination of NO<sub>x</sub> emitted from fires is a complex process because of the difficult estimation of burnt area. Additionally, high uncertainties are still associated with the complex chemistry that takes place in these situations and the emission factors of different chemical species that are highly dependent on fire type, e.g., fuel, injection height, temperature and duration. Nevertheless, the main regions typical for this source are well known and can be clearly identified in Figure 2.5 where fire pixel counts from measurements of the MODIS instrument, flying on the Terra satellite, are plotted. This is also confirmed on maps of NO<sub>2</sub> from satellite measurements (see Figure 2.6) where, clearly, high tropospheric columns coincide with the main areas of elevated fire occurrence. The main sources of NO<sub>x</sub> at higher altitudes of the troposphere are lightning storms, aircraft and subsiding injections from the stratosphere. Nitrogen oxides from combustion processes are mostly emitted as NO and only a smaller amount (values of ~5% of the total) is primarily emitted as NO<sub>2</sub> (WHO, 2006b). It is for this chemical species that columns can be retrieved from satellite measurements, as those exemplified for the year 2005 in Figure 2.6. From this map it becomes obvious the great difference from values in urban areas (and biomass burning regions) to those measured in remote locations.

The fast increasing trends of NO<sub>x</sub> emissions since pre-industrial times (Evans et al., 2000; IPCC, 2007) have recently reverted in some countries, in response to stricter environmental policies that demanded the implementation of emission reduction measures and use of cleaner fuels (e.g., Konovalov et al., 2008; van der A et al., 2008). Nevertheless, Lamarque and co-workers (2005) forecast that NO<sub>x</sub> will continue to rise until the year 2100. NO<sub>x</sub> emissions in the rapidly developing economies in Asia are expected to continue to rise. In the mid-1990s NO<sub>x</sub> emission rates for Asia were reported by Akimoto (2003) to exceed the amount emitted in North America and Europe, and Zhang et al. (2010) reported an increase of 70% in China in the period from 1995 to 2004. These were attributed mainly to emissions from vehicles and the cement industry before the year 2000 and after

## Fundamentals

that from power plant emissions. This high enhancement of emissions in China was also observed in trends of tropospheric  $\text{NO}_2$  columns determined from measurements of GOME and SCIAMACHY (Richter et al., 2005).

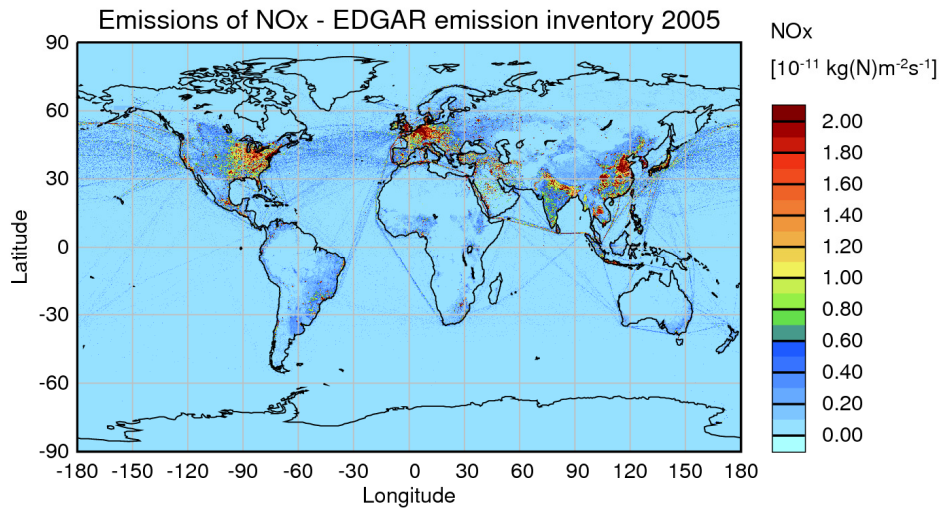


Figure 2.4 NO<sub>x</sub> emissions for anthropogenic sources, for the year 2005, according to the sectors defined in EDGAR: agriculture, aviation, energy, fuel production, ground transport, industry combustion and process emissions, residential and other combustion, ships, solid waste, and other. Biomass burning emissions are not included. (Source: data from EDGAR-EU, 2009)

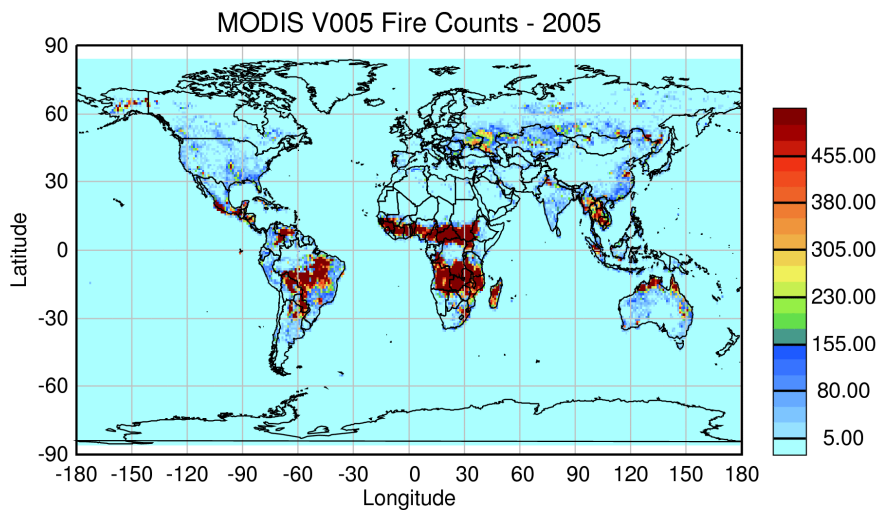


Figure 2.5 Fire pixel counts for the year 2005 (corrected for overpass and clouds), determined from measurements of MODIS instrument flying on Terra satellite. The dataset V005 used was available at 1 degree spatial resolution for monthly averages at <http://disc.sci.gsfc.nasa.gov/neespi/data-holdings/mod14cm1.shtml> (NASA, 2011).

## Nitrogen dioxide (NO<sub>2</sub>)

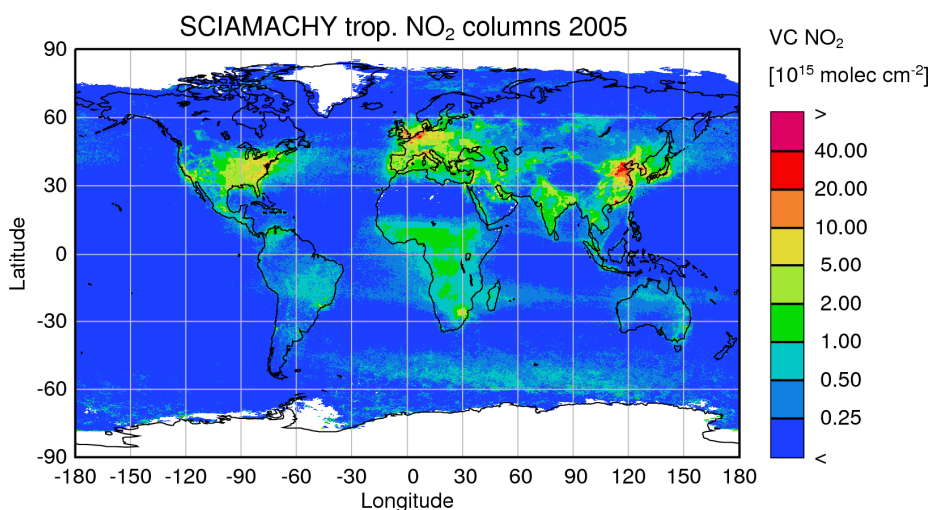


Figure 2.6 Annual average of NO<sub>2</sub> tropospheric columns for the year 2005, measured by SCIAMACHY instrument flying on ENVISAT.

NO<sub>2</sub> is a reddish brown gas with a characteristic pungent odour, and, more importantly, a key pollutant in the troposphere and adverse for human health. It is one of the main precursors from ozone and also generates harmful compounds, as nitric acid responsible for acid rain. Furthermore, because NO<sub>2</sub> absorbs radiation on the visible wavelength range, it can contribute to global climate change by interfering, directly and indirectly, with the Earth's radiative budget (Solomon et al., 1999; IPCC, 2007; Vasilkov et al., 2009). According to WHO (2006b), NO<sub>2</sub> concentrations in the range of 15 to 30 µg/m<sup>3</sup> have been measured in the remote areas of industrialised countries. The values reported in the literature consulted differ over a large range, which reflects the high variability of the concentration of this trace gas in the atmosphere and its short atmospheric lifetime. Often, in big cities, and not necessarily megacities, these values exceed the 40 µg/m<sup>3</sup> annual mean guideline for air quality proposed by WHO (2006a), and the recommended hourly mean value of 200 µg/m<sup>3</sup>. The atmospheric processes involving NO<sub>2</sub> are complex incorporating several different chemical species. Here, only a summary of the most important features is described. In the presence of sunlight (with  $\lambda < 420$  nm) NO<sub>2</sub> will be photolysed, yielding O<sub>3</sub> according to the following reactions:



The (null) cycle is then completed with the re-formation of NO<sub>2</sub> by

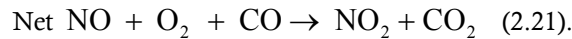
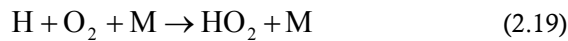


This reaction has a significant activation energy ( $\sim 13$  kJ.mol<sup>-1</sup>), which explains the variation in altitude of the ratio between NO and NO<sub>2</sub> concentrations. As the temperature in the troposphere

## Fundamentals

---

decreases with height, the production of  $\text{NO}_2$  decreases with altitude. In addition to reaction (2.17),  $\text{NO}_2$  is also formed in the presence of hydrocarbons ( $\text{CO}$ ,  $\text{CH}_4$  and other VOCs) that provide the necessary peroxy radicals (e.g.,  $\text{HO}_2$ ,  $\text{CH}_3\text{O}_2$ ) to start reaction (2.20). This results in enhanced production of ozone. The detailed chemistry involving all the possible pathways for the interaction between VOCs, OH and the  $\text{NO}_x$  family can be found for example in Warneck (2000) and Wayne (2006). A simplified chemistry scheme is presented in Figure 2.7, and here an example is given for the reactions with  $\text{CO}$ :



This cycle illustrates how ozone concentrations can increase in the presence of  $\text{NO}_x$ , since the  $\text{NO}_2$  formed from reaction (2.20) will lead to the production of ozone *via* reactions (2.15) and (2.16). On the other hand, in remote areas where  $\text{NO}_x$  concentrations are low, the  $\text{HO}_2$  will react with  $\text{O}_3$  to reform OH. In the presence of  $\text{O}_2$ , reaction (2.18) may turn differently, with  $\text{CO}_2$  being formed together with  $\text{HO}_2$  as second product. Similar processes take place with  $\text{CH}_4$  but the product of the reaction is  $\text{CH}_3\text{O}_2$ , able, on the one hand, to react with  $\text{HO}_2$  and form  $\text{CH}_3\text{OOH}$ , but also with  $\text{NO}$  to form  $\text{NO}_2$ .

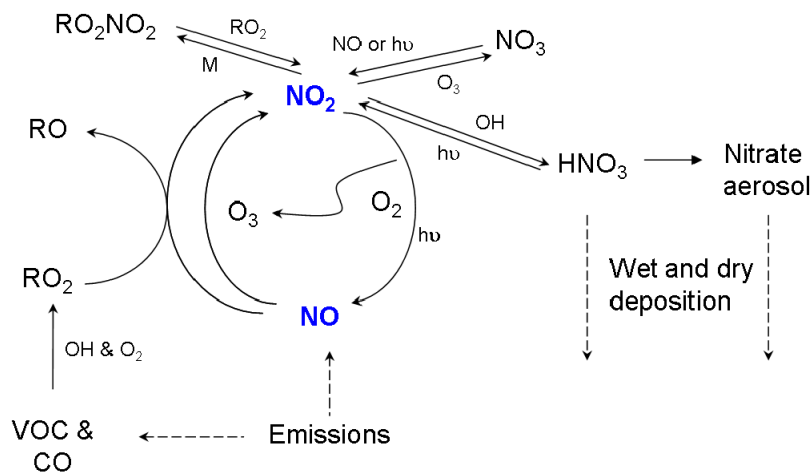


Figure 2.7 Schematic representation of main daytime chemical processes of  $\text{NO}_x$  species. (Source: adapted from Jenkin and Clemitshaw, 2000; Wayne, 2006)

Another significant reaction of  $\text{NO}_2$  is the formation of nitric acid, a key pollutant responsible for acid rain that severely affects the ecosystems:



This reaction is in fact one of the main processes for loss of NO<sub>x</sub> since HNO<sub>3</sub> (together with nitrate aerosol) will be removed from the atmosphere by wet or dry deposition. On the other hand, an important reservoir of NO<sub>x</sub> is peroxyacetylnitrate (PAN, Seinfeld and Pandis, 2006). The lifetime of this compound is highly dependent on temperature, varying from less than one hour at high temperatures, to days when above the BL at colder temperatures. Thus, PAN has a major role in the long-range transport of the nitrogen oxides, especially in the winter months.

The nighttime oxidation chemistry is quite different from the processes occurring during the day. The nitrate radical is formed by the following reaction (Wayne et al., 1991):



This radical is the main sink for VOCs during the nighttime and, in addition, can react with NO<sub>2</sub> and form, in the equilibrium, N<sub>2</sub>O<sub>5</sub>, which is a source of HNO<sub>3</sub> and nitrate ions. The nitrate radical is an important oxidant of the atmosphere, however, unlike OH, it does not act as a catalyst but only initiates the removal of organic compounds. During the day, this radical will be quickly photolysed producing both NO and NO<sub>2</sub>.

From the chemistry described it becomes obvious that the concentrations of NO<sub>x</sub> and, consequently, ozone depend not only on the emission load but also on sunlight. The amount of these chemical species presents a clear daily cycle and also seasonal variations throughout the year. A typical diurnal variation, in urban scenes, is illustrated in Figure 2.8. The peak of NO in the early hours of the day is related to the usual traffic rush hours in cities characterised by high emissions from motor vehicles. Often a second peak in beginning of the night is also observed. The high NO values gradually decrease as this species is converted to NO<sub>2</sub> and the ozone formed accumulates with concentrations rising in the early afternoon. After sunset, the NO<sub>2</sub> is quite stable in the atmosphere, its concentrations increase, and the ozone decreases once more. Satellite measurements performed at different times of the day provide, theoretically, a good option to observe this diurnal variation on the global scale. Boersma et al. (2008) have shown that the morning tropospheric NO<sub>2</sub> columns measured by SCIAMACHY in the morning are, in most industrial regions of northern mid-latitudes, up to 40% higher than those of OMI, observed in the afternoon. On the other hand, when looking at the biomass burning regions, the afternoon values are the higher ones, with a maximum difference of 35%, which can be explained by enhanced fire activity. One other interesting aspect is that the seasonal variation of NO<sub>2</sub> is different for each source type. This was presented, for example, by van der A and co-workers (2008) that have analysed seasonal changes seen from satellite measurements of GOME and SCIAMACHY for a time series of 10 years, compiling, as well, information from previous studies. The fuel combustion emissions are mostly constant throughout the year, but the values of NO<sub>2</sub> are higher in winter due to the longer lifetime (less sunlight for photolysis) and changes in available OH.

On the other hand, biomass burning emissions vary according to wet and dry season, the latter with obvious higher fire occurrences and, therefore, enhanced emissions. Soil emissions are an even more complex source and the main conclusion from that study was that the maximum of  $\text{NO}_2$  emitted from this source occurs in summer season.

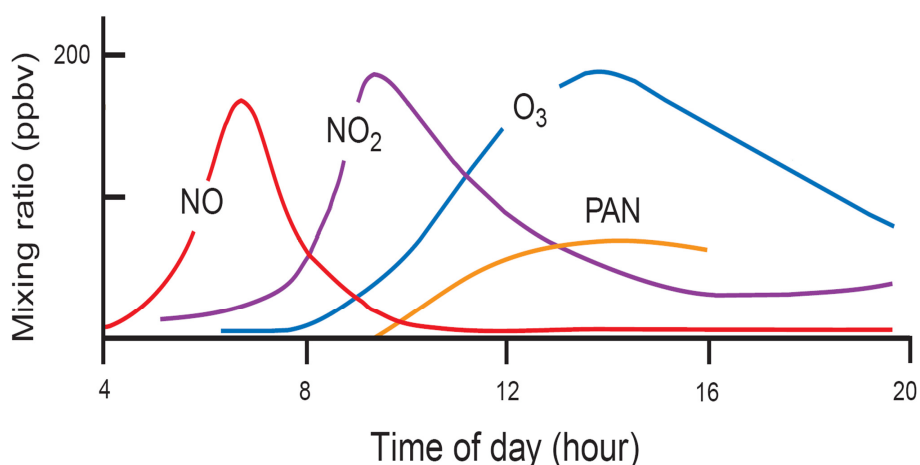


Figure 2.8 Typical daily cycle of  $\text{NO}_x$ , PAN and  $\text{O}_3$  concentrations in urban polluted environments, here illustrated from photochemical smog of Los Angeles. (Source: adapted from Wallace and Hobbs, 2006)

The topics described above refer to what occurs in the troposphere, the region where the  $\text{NO}_2$  affects more directly the human life and also the ecosystems. However,  $\text{NO}_2$  also exists in the stratosphere (together with  $\text{NO}$ ), and, in fact, just like for ozone, most of the atmospheric  $\text{NO}_2$  is located in the stratosphere (Noxon, 1978; Noxon, 1979). As illustrated above, stratospheric  $\text{NO}_2$  partially controls the amount ozone in this layer acting both as catalytic agent on its destruction but also avoiding it when it forms chlorine and bromine nitrates. The destruction of ozone by  $\text{NO}_x$  compounds occurs *via* reactions (2.7) to (2.9), the catalyst agent X being  $\text{NO}$ . This cycle would be similar to the null cycle that occurs in the troposphere if the  $\text{NO}_2$  did not react with oxygen atoms to form extra  $\text{NO}$  (Jacob, 1999). The main source of  $\text{NO}_x$  in the stratosphere was already identified in previous sections as  $\text{N}_2\text{O}$ . An increasing trend of  $\text{N}_2\text{O}$  has been observed in the past decades leading to the aggravation of the problem of stratospheric ozone depletion.  $\text{NO}_2$  increases in altitude to about 35 km and then the tendency reverts (Brasseur and Solomon, 2005). The variation with latitude has been measured and it was found that in the summer the  $\text{NO}_2$  is higher polewards and the opposite is found for winter months. This variation is related to dynamics and chemistry, i.e., the balance between the amount of  $\text{NO}_x$  produced and what is kept in reservoir species in this layer:  $\text{N}_2\text{O}_5$ ,  $\text{HNO}_3$  and others.

## 2.4 Atmospheric aerosol

In simple terms, aerosol is a suspension of atmospheric solid and/or liquid particles. However, their definition is much more complex and, depending on the scientific community or area of research, aerosol can refer to different types of suspended particles. According to the American Meteorology Society (<http://amsglossary.allenpress.com/glossary>), aerosol term should be used when referring to colloidal system composed of either solid or liquid particles dispersed in gas, and not to designate cloud particles or single dispersed particles. In addition, suspended solid or liquid water particles (haze, fog, liquid precipitation or snow, as a few examples) are known as hydrometeors. In practice, for scientific research, aerosol often refers only to solid particles that may or not contain water (this definition is assumed in the present thesis). The size of these particles is highly variable with diameters ranging from a few nanometres to micrometres (suspended particles with 0.1 mm in diameter also exist but their residence time is very short). The characterisation of size using the diameter implies that particles would be spherical, however, as it is possible to see by examples in Figure 2.9, this is not the case for the great fraction of aerosol (e.g., Adachi et al., 2010). The chemical composition of the aerosol present in the troposphere is quite variable, including species like sulphate, ammonium, nitrate, sodium and chloride from sea-salt, and carbonaceous material (elemental carbon and organic matter). In addition, also some trace metals, minerals and water are found in particles.

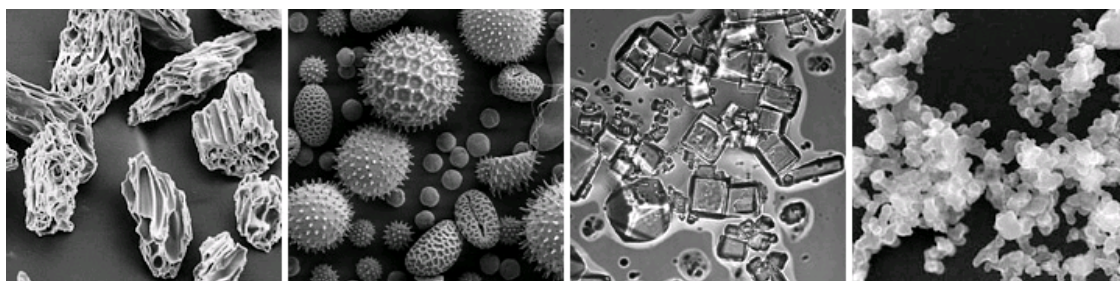


Figure 2.9 Images from scanning electron microscope showing different aerosol shapes: volcanic ash, pollen, sea-salt, and soot (from left to right). (Source: <http://earthobservatory.nasa.gov/Features/Aerosols/>, courtesy of USGS, UMBC (Chere Petty), and Arizona State University (Peter Buseck))

### Physicochemical properties of aerosol

Aerosol can be either directly emitted from different sources or formed in the atmosphere through chemical and physical processes (secondary aerosols). The estimations of total emitted particles and the contribution from each source is quite uncertain and very different values are presented in the literature reviewed. Nevertheless, the common agreement is that, on global level, particles from

natural sources outweigh the anthropogenic aerosol by far in terms of mass, although on urban and industrial regions the contrary is more frequently observed. This is the case of dust, which can be from mineral origin (windblown), e.g., desert dust and other soil particles, or from volcanic ash. According to Han et al. (2007, and references therein) mineral aerosol is estimated to be ~50% of total tropospheric aerosol. The main source regions are the Sahara, Taklimakan and Gobi deserts. Large volcanic eruptions (like the one in 1991 from Mount Pinatubo) release a huge amount of particles, often directly into the stratosphere, where they will have an important role on climate change. Volcanic aerosol will be mostly sulphate which is highly reflective. Stratospheric aerosol is also important for the ozone depletion processes since it serves as surface for the reactions to take place. However, not all eruptions have such high injection heights and most of them will in fact remain in the troposphere with higher impact on human health and ecosystems. Emitted from the oceans, sea-salt is also a key contributor to atmospheric particles, although these are often too big to last long in the atmosphere. Smaller fractions of natural aerosol include pollens and many other tiny particles from plants and bacteria. Smoke from biomass burning events (organic compounds and black carbon) is also a relevant source of particulate matter. As it happens for NO<sub>2</sub>, the emission of aerosol from fires is related to its characteristics, i.e., the type of material burnt, the combustion temperature and its efficiency. The black carbon is mostly emitted from processes occurring at higher temperatures and the opposite is verified for organic particles. As mentioned above, large wildfires take place every year in the tropics, i.e., central Africa, Southern America and South-East Asia. Furthermore, many other human activities contribute to the concentration of atmospheric aerosol. These sources include major anthropogenic sources for air pollution such as fuel combustion, traffic and industrial processes, but other less obvious mechanisms, like re-suspension of dust from roads or wind erosion of cultivated land, also contribute for atmospheric aerosol. Global observations of aerosol are achieved with, for example, satellite instruments (see text below). Maps like the one presented in Figure 2.10 allow for a clear identification of hot-spots for emission of particulate matter.

Gas-to-particle processes are responsible for the formation of secondary aerosols, and these include condensation of low vapour pressure organic compounds, inorganic aerosol produced from chemical reactions and conversion of gaseous organics into particulate matter. The exact amount of aerosol that is formed *via* gas-to-particle conversion is not well known, however, WHO (2006a) reported that this could be up to 50% of all the particles in the air. Sulphur compounds can oxidise (reacting with OH) or condensate onto primary particles to produce sulphate aerosol. These are also formed, at a faster rate, in reactions that occur in the cloud droplets. Essentially, sulphuric acid is neutralised by ammonia and the resulting compounds will condensate into particles. The main sources of SO<sub>2</sub> are fossil fuel combustion processes and volcanoes. Sulphate aerosol is also formed from DMS emitted by marine phytoplankton. These particles are highly scattering particles that will influence the radiative balance from Earth-atmosphere system, as explained below. Nitrogen species are also involved in the

## Atmospheric aerosol

formation of nitrates as secondary particles. If ammonia is in excess, after the reaction with the sulphates, reaction will take place with  $\text{HNO}_3$  and the resultant aerosol will be ammonium nitrate. In addition, reaction with  $\text{NaCl}$  will form  $\text{NaNO}_3$ . This type of aerosol is also non-absorbing. The deposition to the surface of ammonium compounds is responsible for acidification and eutrophication problems in ecosystems. Organic aerosols are emitted as primary aerosol particles but can also be formed from condensation of some (semi-)volatile organic compounds (VOCs), designated by secondary organic aerosols (SOA). This process is rather complex and not yet fully understood. The main sources of these particles are biogenic emissions, biofuel combustion and fire events.

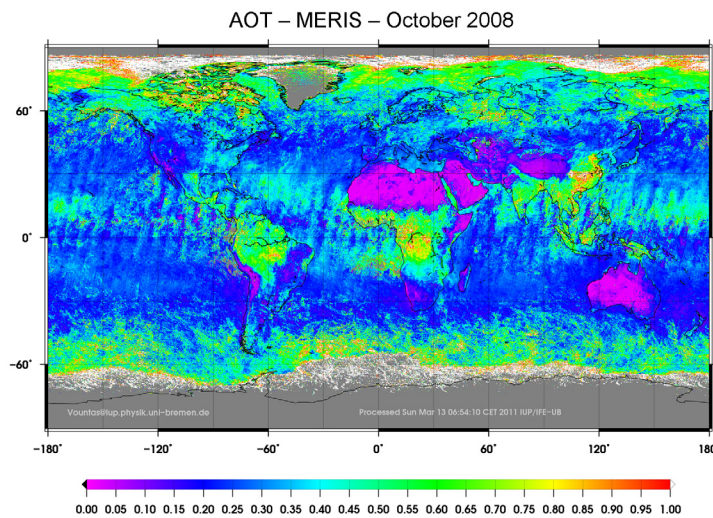


Figure 2.10 Global mean distribution of aerosol optical thickness retrieved from MERIS data, at 440 nm, for September of 2008. (Courtesy: Marco Vountas from IUP – Bremen)

The size and shape of airborne particles vary significantly and are dependent on several aspects. For simplicity, aerosol is often distinguished between fine and coarse particles, i.e., particles with diameter smaller and bigger than  $2.5 \mu\text{m}$ , respectively. An ultrafine category, particles smaller than  $0.01 \mu\text{m}$ , is also sometimes found in literature. Fine particles are mostly emitted from combustion processes and include sulphates, ammonium and carbonaceous material. Bigger particles are those created by mechanical processes like windblown dust, ash and sea-salt. The size of nitrate aerosol encloses both fine and coarse mode. The smallest particles are usually found in industrialised areas resulting from the reaction of  $\text{HNO}_3$  with ammonia, and the coarse nitrate is a product of the reaction of  $\text{HNO}_3$  with sea-salt particles or with soil particles containing calcium or magnesium carbonates. Refractive carbon species (methodologically defined as black or elemental carbon), but also referred to as soot, to which category some authors also classify brown carbon, is an important pollutant from anthropogenic sources as it is mainly emitted from high temperature combustion processes, when the fuel is not fully

## Fundamentals

oxidised. On the other hand, organic carbon can be both emitted directly from vehicles or industrial processes, or, as mentioned above, can be a secondary product from the condensation of VOCs. The ratio of these two carbonaceous elements varies for different environments. As mentioned above, the aerosol originating from biomass burning varies according to different factors, and changes of sizes within smoke are often registered normally related to differences in fuels burned, combustion phase, and aging (Eck et al., 2003). The aerosol emitted from smouldering combustion is generally composed by larger particles than those from smoke of flaming fires. Most of the larger particles are only found in aged smoke and have, therefore, grown during transport (Eck et al., 2003; 2009).

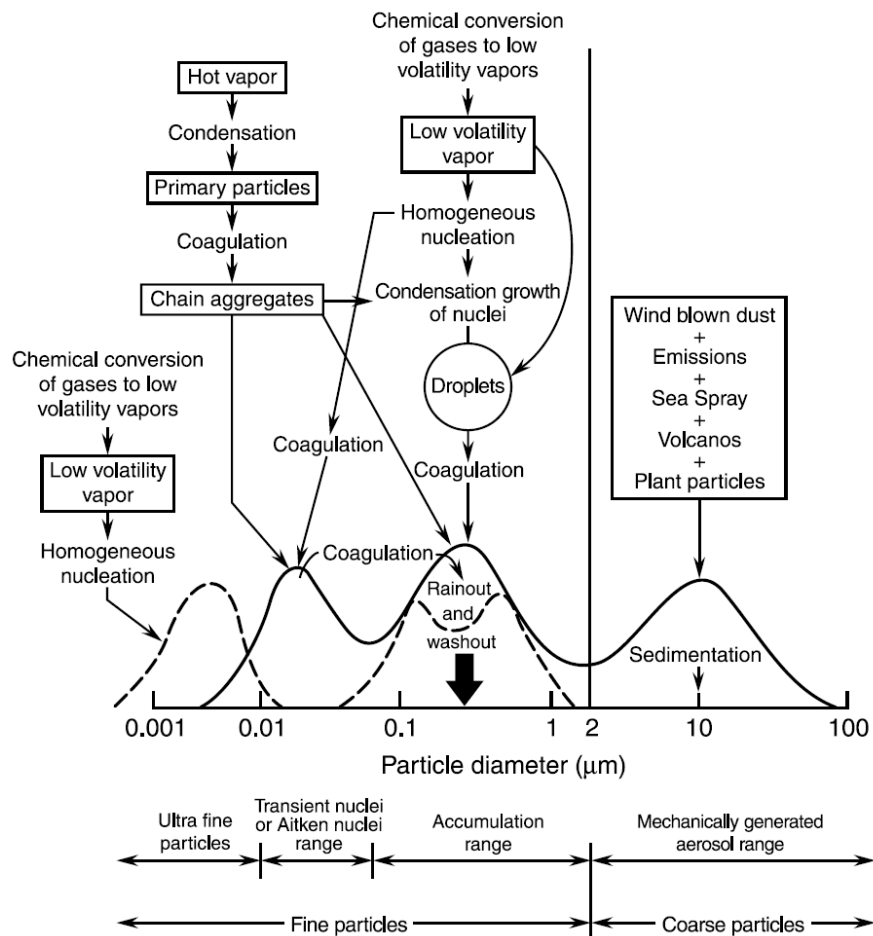


Figure 2.11 Idealised scheme of an atmospheric aerosol size distribution illustrating the original hypothesis of Whitby and co-workers of three modes (nuclei, accumulation and coarse) and also in dashed the ultrafine particle mode. Detail for the possible variations of the accumulation mode is also exemplified. (Source: Pitts and Finlayson-Pitts, 2000)

Such a simplistic division between fine and coarse aerosol is not always enough to distinguish the large range of aerosols present in the atmosphere, especially when the behaviour of fine particles vary

much according to their size. When analysing typical size distributions (like that presented in Figure 2.11) three distinct modes appear: nuclei (or Aitken), accumulation, and coarse. As the name indicates, the first mode includes mostly particles originating from nucleation processes. In addition, also aerosol emitted from combustion or formed by condensation are within this size range. These particles are normally too small to be quickly deposited and will coagulate with larger particles, integrating then the accumulation mode. The denomination of this mode illustrates the considerable accumulation of particles within this size range (diameter of 0.1 to 2.5  $\mu\text{m}$ ) which happens due to inefficient removal by either dry or wet deposition. In addition to those formed by coagulation, also particles grown by condensation of vapours belong to this category. Larger particles are mostly primary aerosol and their sources were already enumerated above. Due to their large size, the sedimentation velocity is high and, consequently, their residence time is short. Although their contribution in number for the total aerosol is small, this fraction accounts for the greater part of aerosol mass. The log-normal distribution suggested by Aitchison and Brown (1957) is the most frequent mathematical function used to describe the aerosol size distribution according to the following equation:

$$f(r) = \frac{1}{\sqrt{2\pi} r \ln \sigma} \exp \left[ -\frac{(\ln r - \ln r_0)^2}{2(\ln \sigma)^2} \right] \quad (2.24)$$

where  $r$  is the mode radius of the distribution,  $r_0$  and  $\sigma$  the mean radius and the width of the size distribution, respectively. This equation can then be written in function of the number, area, volume or mass of particles.

The residence times of particles in the troposphere vary from very short periods of less than an hour to a few weeks time (Wallace and Hobbs, 2006). The main sinks of aerosol are related to physical processes such as wet and dry deposition. The latter refers to those particles that simply deposit by gravitational fallout or a sequence of turbulent diffusion and Brownian diffusion with final uptake at the surface (Brasseur, 2003). Scavenging is in fact the more relevant process of removal, where particulate matter is either incorporated into cloud droplets during cloud formation and rained out, or washed out directly by precipitation.

A more extensive explanation of this topic is available at, for example, Pitts and Finlayson-Pitts (2000) and Seinfeld and Pandis (2006).

### **Vertical distribution and transport**

The aerosol distribution in the troposphere is highly variable and influenced by sources, emission mechanisms, removal processes and meteorological conditions. A distinction between profiles in the

boundary layer and free troposphere is necessary since they are governed by different physical processes. Most of the aerosol is emitted directly into the BL and stays in this layer during the day. A vertical distribution that follows an exponential decrease has been frequently reported in the literature. However, in highly polluted regions and with complete development of the BL, the particles can be homogeneously mixed throughout the full extension of the layer. Yet, it is important to note that such distributions are altered during the day. Aerosol does not always follow the diurnal evolution of the mixing layer and, as the boundary layer height decreases during the night, the particulate matter can remain above. Measurements have shown that a residual layer of aerosol is often observed after the collapse of the BL (e.g., Hodzic et al., 2004). Furthermore, the presence of aerosol in the free troposphere is not a rare phenomenon as aerosol plumes are frequently transported over large distances in this region. This transport can be on smaller regional scales, but also between continents or around the hemisphere when the plumes are caught in easterly jet streams. Such events explain why dust from the Gobi desert is sometimes found on the American continent (Arimoto et al., 2006), or Saharan dust in Southern America (Ansmann et al., 2009) and Europe (Ansmann et al., 2003; Gerasopoulos et al., 2003). Hamonou et al. (1999) explained that the dust outbreaks transported across the Mediterranean region were related to synoptic uplift phenomena from the warm Saharan air mass that come close to the cooler air mass above the sea. Alternatively, because the Asian deserts are located more than 2 km above sea level, the dust lifted from the surface is directly emitted and transported at higher altitudes, above the BL of cities located at lower altitudes. Nevertheless, cases have been registered of dust present in the lower atmosphere causing extraordinary pollution events with highly decreased visibility. In addition, also smoke from biomass burning can be transported hundreds of kilometres away from its source. Measurements of smoke plumes have evidenced transport from Northern America boreal forests into Europe. The pyroconvective power from fires can inject the fire plumes directly in the free troposphere, i.e., at heights above 3 km (e.g., Kahn et al., 2007), facilitating long-range transport. However, injections of burnt material in the mixing layer are not sporadic. Labonne and co-workers (2007) have identified, from CALIPSO measurements, several cases where the top of aerosol layer is below the top of the boundary layer.

### **Optical properties of aerosol**

In addition to the physicochemical properties and the distribution in the atmosphere, the interaction of aerosol with the radiation is mediated by their optical properties. When sunlight comes across a particle in the atmosphere this radiation can be absorbed or scattered. The combined effect of these two phenomena is denominated by **extinction**. **Absorption** is the process by which electromagnetic energy of radiation is converted into thermal energy. This is not the most relevant process in the visible wavelength range because most of the particles are in fact weak absorbers. The main absorbing aerosol type is soot resulting from combustion processes (e.g., VanCuren, 2003). Absorption by

aerosol will result in increased temperature of the particles' surroundings, changing, therefore, the relative humidity of the air. Consequently, circulation and stability of the atmosphere is altered and the process of cloud formation as well. **Scattering** of light by aerosol consists basically in the redistribution of the radiation in directions different from the initial line of propagation. To represent such process one needs to introduce the concept of **phase function**, which is the angular distribution of scattered light for a given local volume of an aerosol medium, or in other words, the probability of light to be scattered in a certain direction of angle  $\theta$ . When assuming spherical particles, the phase function can be determined by:

$$\int_0^{2\pi} \int_0^{\pi} P(\theta, x, m) \sin \theta d\theta d\varphi = 4\pi \quad (2.25),$$

where  $m$  is the complex refractive index,  $\theta$  the scattering angle and  $x$  the size parameter equal to  $\pi d/\lambda$ , where  $d$  is the particle's diameter and  $\lambda$  the wavelength. This explains the dependence with wavelength of this fundamental property of the particles. Consequently, the phase function depends only on aerosol size distribution, particle shape, and chemical composition, but not on its load or spatial distribution. Examples of aerosol phase functions are presented in Figure 2.13.

The **complex refractive index** is the optical property of the particle in regard to its surrounding medium, i.e., the air when referring to atmospheric aerosol (Seinfeld and Pandis, 2006). This index  $m$  is represented by:  $m = n + ik$ , where  $n$  and  $k$  are the real and imaginary parts, respectively. These vary with wavelength and represent the non-absorbing ( $n$ ) and absorbing components ( $k$ ).

The optical thickness of the atmosphere is the combination of Rayleigh scattering, molecular gaseous absorption, and aerosol's absorption and scattering. Based on the Beer-Lambert's law (further discussed later in section 2.5.1), **aerosol optical depth** (AOD,  $\tau$ ) of a layer, also designated by optical thickness (AOT), represents the extinction of sunlight that passes through this layer of height  $h$ , and can be expressed by:

$$\tau(\lambda) = \int_0^h k_{ext}(\lambda, z) dz \quad (2.26),$$

where  $k_{ext}$  is the extinction coefficient with units  $(\text{length})^{-1}$  and  $z$  the height above ground level. For an ensemble of particles, this coefficient (and also the absorption and scattering ones) can be determined by:

$$k_{ext} = N \sigma_{ext} \quad (2.27),$$

where  $N$  is the number (density) of particles in a unit volume, and the  $\sigma_{ext}$  the extinction cross section defined by:

$$\sigma_{ext} = Q_{ext} A \quad (2.28),$$

with  $Q_{ext}$  the extinction efficiency and  $A$  the geometrical (projected) area of a spherical particle. Still, as the cross section will be representative for the aerosol ensemble, when dealing with non-identical particles this parameter can be determined in function of the size distribution.

From what was explained above it can be deduced that  $Q_{ext} = Q_{abs} + Q_{scat}$  (the sum of the efficiencies for absorption and scattering, respectively), and the same is valid for the coefficients or cross sections. The **single scattering albedo** (SSA,  $\omega_0$ ) describes the absorption properties of the aerosol by the probability that a photon which interacts with a volume element will be scattered rather than absorbed (e.g., Burrows et al., 2011). This parameter is determined by:

$$\omega_0(\lambda) = \frac{k_{scat}(\lambda)}{k_{ext}(\lambda)} = \frac{Q_{scat}(\lambda)}{Q_{ext}(\lambda)} \quad (2.29).$$

For non-absorbing particles this value equals 1, although that is not found for atmospheric aerosol. Nevertheless, distinction can (and should) be made between aerosol with high and low SSA, where soot, for example, is reported to have the lowest values and desert dust (or sulphates) are on the highest range. The lower SSA values are found mostly in polluted environments and biomass burning plumes.

The spectral dependence of the extinction coefficient and, consequently, also AOD can be determined from the **Ångström coefficient** ( $\alpha$ ):

$$\alpha = -\frac{\ln k_{ext \lambda_1} - \ln k_{ext \lambda_2}}{\ln \lambda_1 - \ln \lambda_2} = -\frac{\ln \tau_{\lambda_1} - \ln \tau_{\lambda_2}}{\ln \lambda_1 - \ln \lambda_2} \quad (2.30).$$

This parameter is inversely proportional to the particle size, which means that the AOD of larger particles is less spectrally dependent (Hamonou et al., 1999).

## Aerosol pollution

Although a great fraction of aerosol is part of the natural components of the Earth's atmosphere, it can still be harmful for human health and ecosystems (e.g., *via* acid rain), and contribute to visibility degradation when present in high amounts (Chang et al., 2009 and references therein; Wang et al., 2009). In addition to their relevance as pollutants in the boundary layer, atmospheric particles play a major role in climate change by their direct and indirect impacts on radiative forcing (see below for more details). In terms of air quality, aerosol amounts are usually classified into PM<sub>10</sub> and PM<sub>2.5</sub>, which is the particulate matter with an atmospheric equivalent diameter below 10 and 2.5  $\mu\text{m}$ , respectively. Such particles can be inhaled by humans and severely affect the respiratory and cardiovascular systems. For that reason, the WHO guidelines are quite strict with a 10  $\mu\text{g}/\text{m}^3$  annual mean and 25  $\mu\text{g}/\text{m}^3$  daily average for the smallest particles, and 20  $\mu\text{g}/\text{m}^3$  annual mean and 50  $\mu\text{g}/\text{m}^3$  daily average for PM<sub>10</sub>. From measurements reported by WHO (2006b), the annual average PM<sub>10</sub>

concentrations are found to be much higher than the recommend values in most cities considered from around the world. Measurements vary from a minimum of  $15 \mu\text{g}/\text{m}^3$  in Europe to a maximum concentration of  $220 \mu\text{g}/\text{m}^3$  in Latin America ( $60 \mu\text{g}/\text{m}^3$  for Europe). The amount of particles in rural areas is normally lower than in urban locations, although the difference is not significant. Air pollution control measures have been implemented in many developed countries and aerosol concentrations have shown a decreasing trend in the past years. Nevertheless, these policies were only implemented after a fast increase of anthropogenic emissions over the past century (IPCC, 2007). Particulate matter is still a major problem in developing countries, especially in Asia (WHO, 2006b). The rapid expansion of Chinese economy has led to the growth of industry and the number of cars which resulted in a dramatic increase of national emissions in recent years. Heavy pollution events in Beijing are widely known with hazy skies and very reduced visibility (Cheng and Tsai, 2000).

### **Influence on radiative forcing**

Aerosol's feedback on climate change occurs *via* several direct and indirect processes that can result both in warming and cooling of the Earth's atmosphere. The direct effect happens through the reflection and absorption of incoming solar light and outgoing IR radiation. The net direct effect depends on the underlying surface. Backscatter of an aerosol layer above dark surfaces results in a negative contribution to radiative forcing. On the other hand, for very bright surfaces, the net reflection might be reduced, meaning that the probability of absorption increases and the overall effect is a positive contribution to the radiative forcing. Indirect forcing is related to the modification of cloud properties. Particles act as cloud condensation nuclei (CCN), and, in this way, changing the clouds' albedo (from CCN amount) and their lifetime (linked to reduced precipitation). More details on the effects of aerosol in climate change can be found in the recent AR4 report (IPCC, 2007). Additionally, aerosol changes ice and snow cover because deposited absorbing aerosol will decrease the values of surface reflectance, which would otherwise be higher, leading to increase melting.

Typically, soot is the only highly absorbing aerosol emitted from anthropogenic sources, while the remaining ones (e.g., sulphate) consist mainly of scattering particles. The overall estimation of aerosol radiative forcing is a cooling effect, both directly and indirectly (IPCC, 2007). However, as mentioned above (see Figure 2.3), some uncertainties remain related to the magnitude of aerosol's impact on climate change. These are mostly related to the strong variability of aerosol properties (particularly the radiative ones) and complex formation processes, unknowns regarding the exact amount present in the atmosphere and, ultimately, the overall feedback of aerosol in cloud properties. Yet, it is important to highlight that great progress has been made since the first IPCC report and the radiative forcing of each aerosol types are nowadays better understood and estimated.

Within the context of this report, aerosol interaction with radiation will interfere with the satellite measurements of trace gases in the atmosphere. As it will later be demonstrated, depending on the particles' optical properties, the amount of aerosol and its vertical distribution relative to that of the trace gas of interest, the sensitivity of the satellite measurements can either be increased or decreased.

### Measurements

The detailed and precise characterisation of aerosol is still a challenge although great progress has been made in the past decade(s). The difficulty lies in the high geographic, seasonal and diurnal variability of size and composition of aerosol. Furthermore, precise estimation of sources and amount emitted is hampered by complex formation and transformation processes that occur all the time in the atmosphere. Several options exist for measurements of aerosol and its properties: in-situ, passive ground-based remote sensing and lidar instruments, or aircraft and space-borne instruments. Each of them has advantages but also some caveats. A combination of different datasets is the best alternative to get hold of a complete dataset with accurate information on several aerosol properties. While in-situ measurements provide good information on local aerosol, such observations cannot always be extrapolated for more distant regions or different altitudes. Observations by passive remote sensing techniques solve partially this problem, but, by providing an average for a column, do not offer the possibility of gaining information at different heights. Furthermore, the retrieval of aerosol amount with this method is limited by the presence of clouds. Lidar, on the other hand, is exceptional on providing vertical distribution of aerosol and its optical and microphysical properties. Additionally, aerosol can also be measured below thin clouds or over bright surfaces. Aerosol from both local and remote origin is observed with high resolution at different altitudes. Still, because of the small measurement volume, these datasets are not representative for a large area and serve mostly to characterise local conditions. Also, the interference of sunlight reduces the quality of data from measurements performed during the day. Aircraft instruments are also a possibility to measure aerosol properties (with different methods) at selected layers, but this is done according to the flight plan and not simultaneously for different altitudes.

The Aerosol Robotic Network (AERONET, Holben et al., 1998) is a worldwide network that was established by NASA and LOA-PHOTONS (CNRS) and started its regular observations in 2003. Currently, the many ground-based remote sensing Sun photometers provide long-term and continuous measurements of aerosol optical, microphysical and radiative properties, such as AOD. Data is freely available online on AERONET's website: <http://aeronet.gsfc.nasa.gov/>. This network has been crucial to better characterise the aerosol and reduce the current uncertainties on the definition of aerosol optical properties. Data collected from these stations (and reported by Dubovik et al., 2002) was essential for the realisation of the sensitivity study presented in chapter 3 of the current

manuscript. Many lidar networks have been established in different continents, such as the European Aerosol Research Lidar Network (EARLINET, Mattis et al., 2002) with currently 30 stations operating in 15 different European countries, or the Asian Dust network (AD-net, Murayama et al., 2001) with a few stations in Japan, Korea and China that mainly focus on the study of dust from the Asian deserts being transported into the cities. A recent space-borne lidar is flying on Cloud-Aerosol Lidar and Infrared Pathfinder Satellite Observations (CALIPSO) satellite, the Cloud-Aerosol Lidar with Orthogonal Polarisation (Winker et al., 2003). This two-wavelength polarisation-sensitive instrument is a unique tool that offers the possibility to access information on the aerosol vertical distribution from space and also qualitative classification of aerosol size (Poole et al., 2002). Other satellite instruments probing atmospheric aerosol are, for example, the two MODIS instruments (Salomonson et al., 1989; King et al., 1992) flying on Terra and Aqua, providing global AOD maps for the morning and the afternoon in the time span of 1 to 2 days; MERIS (Bézy et al., 2000) flying in the ENVISAT that was built mainly to observe the ocean colour, but also provides AOD among other parameters (see Figure 2.10 above); and MISR (Martonchik et al., 2002) that offers the possibility to retrieve information on both aerosol load, particle size and composition from a multi-angle viewpoint (nine to be more precise), but has global coverage of only every nine days. These are only a few examples among the many instruments providing frequent data on different aerosol characteristics. More information on the instruments and the retrieval methods can be found, for example, at Kokhanovsky (2008) and Burrows et al. (2011). Further on, many field campaigns held (e.g., ACE, ACE-ASIA, SAFARI, SAMUM, etc) have provided key information regarding the physical and chemical constitution of particulate matter in different environments and offered a closer look into short-term variations of, for example, concentration and vertical distribution (e.g., injection heights in fire events or evolution of typical layer elevation in desert dust storms). Global aerosol models are also essential tools to understand atmospheric composition and describe global distributions of aerosol. The AeroCom initiative (<http://dataips1.ips1.jussieu.fr/AEROCOM/>), created in 2003, joins several scientists working towards a common goal of improving the current state of the art in regard to modelling of global aerosol, by combining satellite and ground-based observations with results from more than 14 global models.

Data from several networks above mentioned were used in the analysis presented in chapter 3. Information on aerosol vertical distribution was taken from lidar measurements performed not only at ground-based stations, but also from CALIPSO observations. In addition, AERONET datasets provided essential figures for optical properties of particles and aerosol size distributions.

## 2.5 Radiative transfer

### 2.5.1 Radiation in the atmosphere

Sunlight is essential for maintaining life on Earth. The Sun radiates over all wavelengths, but most of the energy is concentrated in the IR and visible range, with a small fraction in the UV (Bohren and Clothiaux, 2006). At the top of the atmosphere, the solar flux resembles a blackbody emitting at 5770 K (see Figure 2.12), with a peak in the visible range. The Earth spectrum, on the other hand, can be approximated by a blackbody emission at 300 K. Radiation traversing the atmosphere will be changed due to absorption and scattering by gases, particles and clouds.

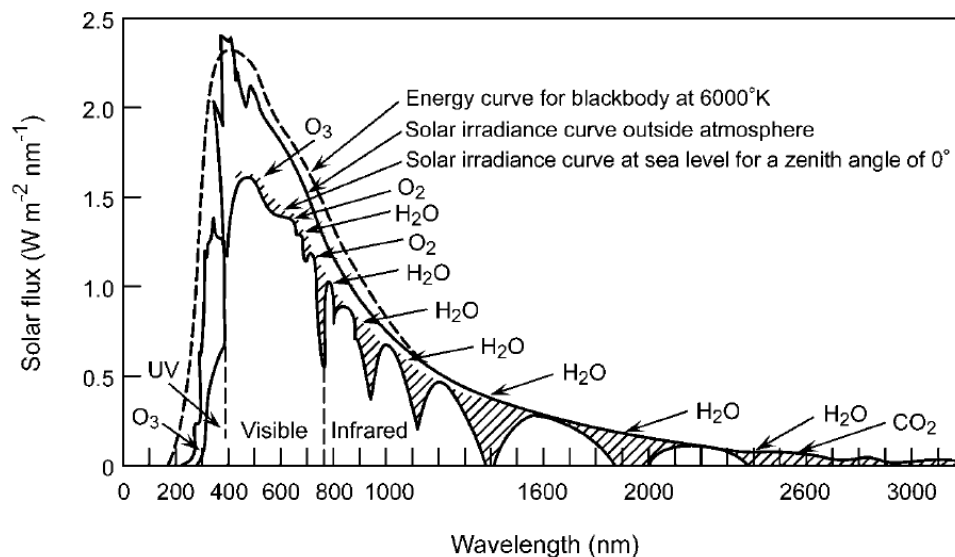


Figure 2.12 Solar flux outside the atmosphere and at sea level, together with the simulated emission of a blackbody at 6000 K. The light absorption of the atmospheric gases  $O_3$ ,  $O_2$ ,  $H_2O$  and  $CO_2$  is also shown. (Source: Pitts and Finlayson-Pitts, 2000)

Following the analogy of Bohren and Clothiaux (2006) when introducing the basic concepts of atmospheric radiation, life (scattering) and death (absorption) of photons will be reviewed in this manuscript, as these are the most relevant processes for the study presented.

In the atmosphere, absorption of sunlight occurs by atoms, molecules and aerosol. The main difference between what happens to molecules and to particles (in terms of absorption) is the apparent size, given that, in theory, molecules occupy a space but do not have dimensions. As mentioned above, the electromagnetic radiation absorbed is transformed into thermal energy. Molecules can absorb photons having the same energy as the difference between their energy levels. When this

process takes place, molecules turn into an excited state. These transitions can be classified into electronic, vibrational or rotational. Due to their structure, each molecule (and atom) will have specific spectral absorption bands that can be used to characterise the chemical species with spectroscopic methods. The reverse process of absorption of radiation will, evidently, result in emission of photons. The molecule is photolysed when the energy of the absorbed photon is high enough to compensate the energy balance from initial state and end product.

Important examples of atmospheric absorption of radiation were already acknowledged: UV sunlight absorbed by ozone; NO<sub>2</sub> being photolysed by sunlight; greenhouse gases absorbing shortwave and IR radiation contributing to climate change.

### Beer–Lambert’s law

Beer-Lambert’s law (also known as Beer’s law or Beer–Lambert–Bouguer law) states that light passing through a layer of thickness  $l$  will be partially absorbed and the intensity  $I_0$  reduced to  $I$ . Such a decline of intensity is proportional to the absorption cross section  $\sigma$  (units of cm<sup>2</sup>/molecule), the number density  $N$  (units of molecules/cm<sup>3</sup>) and  $s$  the path length (units of cm). This can be represented by the following equation:

$$I = I_0 \exp(-\sigma N s) \quad (2.31).$$

According to Beer-Lambert’s law, the effect of light absorption by atmospheric constituents on the intensity and wavelength distribution of sunlight at the Earth’s surface depends on the nature and concentration of the gases and particles present, as well as the path length. The latter is a function of solar zenith angle (SZA), which can be understood as the angle between the local zenith and the line of sight to the Sun. Larger SZAs correspond to longer paths and, hence, the reduction in solar intensity by absorption and scattering processes will be larger.

In section 2.4 scattering by particulate matter was introduced. This redistribution of the radiation depends on several properties of the particles (size, composition, and amount) and can be represented by phase functions. Light scattering can be divided into two types: inelastic - where the energy of the photon changes; or elastic - where the energy remains unchanged. Raman scattering (rotational or vibrational) is an example of the first, where scattering will change the state of excitation of the molecule that absorbed the photon. For the elastic scattering, three domains can be defined depending on the size (diameter  $d$ ) of the scatterer relative to the wavelength:  $d \ll \lambda$ , Rayleigh scattering;  $d \approx \lambda$ , Mie scattering; and  $d \gg \lambda$ , geometric scattering. Within the visible wavelength range, the size of the majority of atmospheric aerosol corresponds to the Mie scattering regime, while for gases this will be Rayleigh scattering. This last category describes the scattering on very large particles that can be described by classical optics, based on the principles for reflection, refraction and diffraction.

### Rayleigh scattering

Named after Lord Rayleigh (Rayleigh, 1899), this solution addresses the (elastic) scattering of radiation by molecules much smaller than the wavelength of incident light. The shape of the scattering object can be neglected in the calculations, which will then result in a relatively simple phase function ( $P_{Ray}$ ) for unpolarised light, with  $\theta$  as scattering angle:

$$P_{Ray}(\theta) = \frac{3}{4}(1 + \cos^2(\theta)) \quad (2.32).$$

Since the scatterers that follow this regime are relatively small, the scattering of radiation in forward and backwards directions is symmetric (see Figure 2.13). The cross section of Rayleigh particles can be described by the following equation:

$$\sigma_{Ray} = \frac{128\pi^5}{3} \frac{x^2}{\lambda^4} \quad (2.33),$$

where,  $x$  is the size parameter as defined above. This equation highlights the inverse relation between the Rayleigh scattering efficiency with the fourth power of  $\lambda$ , which implies that shorter wavelengths will be scattered more efficiently. This relation is the explanation for the blue (shorter wavelength) skies and reddish sunsets (longer light path through the air and increased scattering). In an ideal case, an atmosphere clear of particles would be the perfect example for Rayleigh scattering.

### Mie theory

The Mie theory (Mie, 1908), also called Lorenz-Mie theory, provides a solution to Maxwell's equations, describing the optics of homogenous spherical particles, i.e., determines the scattering and absorption of light by spheres at different wavelengths. Often, for simplicity of calculations and reduction of computation time, this theory is used for all species of aerosol although it is known that particulate matter is usually non-spherical (see Figure 2.9). Still, adaptations have been developed for other shapes, such as, spheroids or layered concentric spheres, among others. Experimental results have shown that errors arise when this theory is used for non-spherical particles (Mishchenko et al., 1995). The full derivation of equations for the Mie theory is quite extensive and a more complete explanation of the mathematical details and descriptions of Mie scattering can be found at Bohren and Huffman (1983) and van de Hulst (1981). Relevant to mention are some of the differences with regard to the scattering of small particles. The phase functions for Mie scattering (equation (2.25)) do not correspond to symmetric scattering (as for Rayleigh), but suggest a predominant forward scattering, i.e., more radiation scattered in the direction of smallest scattering angles (see some examples in Figure 2.13). Nevertheless, the Mie scattering will match the Rayleigh regime for smallest particles. This is an indication of the stronger dependence of the Mie scattering on the size of the particles. In addition, for an ensemble of particles, the amount of total radiation scattered is not linearly proportional to the amount of particles but rather dependent on the size distribution of the aerosol.

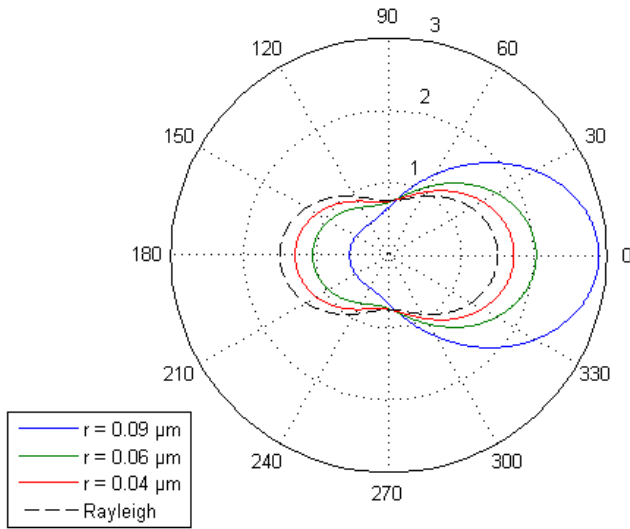


Figure 2.13 Scattering phase functions for particles in the Mie regime (spherical) with different radii ( $r$ ). For comparison also the phase function in the Rayleigh regime is presented (black dashed line).

## 2.5.2 Radiative transfer equation

Atmospheric radiative transfer (RT) is a relevant process for many scientific questions. Radiative transfer models (RTMs, that solve the RT equations) determine what happens to radiation when it is traversing the atmosphere (or another medium), accounting for absorption, scattering and emission by all atmospheric constituents and the surface. Basically, information is provided regarding the gain and loss of radiation at a certain point in the atmosphere. Several examples were given above that depend on this computation, e.g., quantification of greenhouse effect and the changes of the radiative balance of the Earth-atmosphere system by aerosol, an important process for climate change. Furthermore, a practical application of this estimation, especially within the scope of the study presented here, is that it simulates the light path in the atmosphere, essential information for the retrieval of trace gases and aerosol columns from measurements performed with remote sensing techniques. In a way, Beer-Lambert's law provides a very simplified solution for the radiative transfer equation, for a highly simplified scenario. With that in mind, the general form of the equation can be written as

$$\frac{dI(\lambda)}{ds} = -k_{ext}(\lambda)[I(\lambda) - J(\lambda)] \quad (2.34),$$

where  $I$  is the intensity,  $s$  the length of the light path,  $J$  represents the gain and  $k_{ext}$  (extinction coefficient) the loss of radiation, for a given wavelength  $\lambda$ . These terms can be further specified in different contributions:

- the increase from elastic and inelastic scattering processes;

- the loss from either absorbing or scattering processes, i.e., extinction.

Combining all, the overall RT equation is

$$\frac{dI(\lambda)}{ds} = -[k_{abs}(\lambda) + k_{scat}(\lambda)] \cdot I(\lambda) + I_{th}(\lambda, T) + I_s(\lambda) \quad (2.35),$$

where  $k_{abs}$  and  $k_{scat}$  are the absorption and scattering coefficients, respectively, and the last terms represent the intensities  $I_{th}$  from thermal emission, and  $I_s$  from incoming radiation.

In addition, it is important to remember that the radiation arriving at a certain point (say, a molecule of gas) is not only coming from the direct source (the Sun for example) but also from diffuse radiation. The full explanation of the solution for the radiative transfer equation can be found, for example, in Liou (2002).

### 2.5.3 SCIATRAN – radiative transfer model

The radiative transfer model used for the calculations of the work presented in this thesis was the SCIATRAN model (Rozanov et al., 2005; Rozanov et al., to be submitted, 2011). SCIATRAN developed at IUP-Bremen is in fact a follow up of GOMETRAN (Rozanov et al., 1997) that simulated the radiation measured by GOME in the 240 – 800 nm wavelength range, in nadir viewing geometry. With the launch of SCIAMACHY satellite instrument it became necessary to include a broader range of wavelengths (0.2 – 40  $\mu\text{m}$  in the latest version) and other viewing geometries (limb, occultation) in such simulations, and, hence, SCIATRAN was created. Several versions have existed in the past decades as frequent improvements are implemented incorporating more features and broaden the potential applications, as it is the case of different viewing geometries: limb, nadir, off-nadir, zenith, or off-axis measured by space-, air- and balloon-borne, or ground-based instruments. The analysis presented here was carried out with different versions of the model: 2.2 for the sensitivity study performed in chapter 3, and version 3.1 for the case study introduced in chapter 4. The main differences between these two consist of (A. Rozanov, personal communication, Feb. 2011):

- a new option to solve the RT equation in vector mode;
- polarised radiative transfer with the discrete ordinate method;
- further extension of spectral range to 40  $\mu\text{m}$ ;
- rotational Raman scattering included;
- surface reflection, previously considered as Lambertian surface, can now be described by the bidirectional reflectance distribution function (BRDF);
- a coupled mode for ocean-atmosphere system was implemented, including some underwater calculations.

None of the additional features was used in this research but some bug fixes and additions to the user interface were also performed in between versions. This RT code resolves the equation and principles mentioned in the previous section(s) providing radiances at the top-of-atmosphere (TOA) or ground but also other quantities such as weighting functions and airmass factors (AMFs), which is this the most relevant output for the work of the present thesis. The mathematical solving of the RT equation can be done in several manners, from more basic assumptions to rather complex and complete scenarios. Calculations in the plane-parallel mode do not consider the spherical shape of the Earth's atmosphere and the equation can be solved with both the discrete-ordinates method and the finite differences. This method is limited to SZAs smaller than  $90^\circ$ . The pseudo-spherical mode, on the other hand, determines the light paths for the direct solar beam in a spherical atmosphere, but solves the RT equation for diffuse radiation in plane-parallel mode. Finally, a fully spherical atmosphere can also be considered. It is also important to mention that SCIATRAN vertical profiles of trace gas, pressure, temperature, and aerosol parameters are defined for a certain altitude grid but these will be linearly interpolated in between the levels. Furthermore, when using the Legendre expansion coefficients to define the aerosol phase functions, a delta-M approximation is used to accelerate the performance. According to Rozanov et al. (to be submitted, 2011), when determining the intensity at the TOA with a RT model, the highest levels of accuracy are obtained when this approximation is combined with the single scattering correction technique. In the case study presented in chapter 4, this set-up was essential to achieve results in reasonable computational time and compatible to the available resources. Some of the phase functions used for that analysis had more than 500 Legendre coefficients in the phase matrix requiring an extremely high number of streams to be used. This would have severely slowed down the performance of the model. Therefore, it was necessary to use less streams in the RT calculations. The resulting error on the AMFs from this approximation is rather small, in the order of 0.03%.

A more detailed description of SCIATRAN can be found at Rozanov et al. (to be submitted, 2011).

## 2.6 NO<sub>2</sub> retrieval

### 2.6.1 DOAS method

The Differential Optical Absorption Spectroscopy (DOAS) method is employed in the retrieval of trace gas columns from measurements of the sunlight in the UV-vis-NIR range. This remote sensing

method is based on the absorption of light by trace gases, and consequent reduction of intensity along a path of light that goes from a source to the instrument. Hence, it is possible to derive the concentration of a certain species of interest integrated along the atmospheric light path. In reality, as there will not be only one light beam with a specific path reaching the instrument, this amount is an average over all contributing light paths, which can be determined by radiative transfer models. The DOAS method is based on Beer-Lambert's law described earlier. However, when measuring radiation crossing the Earth's atmosphere ( $I$ ), it is necessary to account for the many absorbers ( $i$ ) that are present at different abundances along the path ( $s$ ) and have individual cross sections ( $\sigma_i$ , variable with wavelength  $\lambda$ ). Therefore, equation (2.31) can be re-written into:

$$\frac{dI(\lambda)}{ds} = -I_0(\lambda) \left\{ \sum_i \sigma_i(\lambda, s) \rho_i(s) \right\} \quad (2.36),$$

where  $I_0$  is the reference spectrum without absorption of the trace gas of interest and  $\rho$  the concentration of the absorber. For satellite measurements,  $I_0$  can be used from the direct observations of the Sun that are made without looking into the Earth's atmosphere. The absorption cross sections of trace gases are measured in the laboratory and usually depend on temperature and pressure, which, for the atmosphere, results in a variation with altitude. To account for this variability, more than one cross section is needed in principle, although, in the UV-vis range, this can (often) be neglected. As it has been described above, extinction of light in the atmosphere occurs also due to Rayleigh and Mie scattering. Thus, considering the contribution of those processes, the earlier equation becomes:

$$\frac{dI(\lambda)}{ds} = -I_0(\lambda) \left\{ \sum_i \sigma_i(\lambda) \rho_i(s) + \sigma_{Ray}(\lambda) \rho_{Ray}(s) + \sigma_{Mie}(\lambda) \rho_{Mie}(s) \right\} \quad (2.37).$$

When considering atmospheric particles, the aerosol's extinction cross sections can be approximated as part of Mie regime. From the measured spectrum, low frequency structures (as those of aerosol) will be eliminated with a high pass filter and, in this way, not mistaken for molecular absorption features of trace gases. Moreover, the absorption cross sections of a single trace gas can be separated into the contribution from the highly structured differential part ( $\sigma'$ ) and that coming from broadband absorption. In the retrieval, the latter is combined with the Rayleigh and Mie contributions. Through this process, all structures that are not from the absorber of interest are treated as a closure term and approximated by a polynomial of order  $p$ . The quantity desired is in fact the slant column density (SC), i.e., the amount of absorber present along the average light path through the atmosphere to the satellite instrument:  $SC = \int \rho(s) ds$ . Hence, equation (2.37) used for the retrieval becomes:

$$I(\lambda) = I_0(\lambda) \exp \left\{ - \sum_i \sigma'_i(\lambda) SC_i - \sum_p a_p \lambda^p \right\} \quad (2.38),$$

where the second term of the exponent is the polynomial. From this equation it is also possible to derive the optical depth ( $\tau$ ) according to:

$$\tau(\lambda) = -\ln \left\{ \frac{I(\lambda)}{I_0(\lambda)} \right\} \quad (2.39).$$

The SC will be obtained using a least squares fitting procedure, where the difference between the fitted and observed optical depths is minimised.

A more detailed explanation of the DOAS method and the accuracy of measurements is available, for example, at Platt and Stutz (2008) and Burrows et al. (2011).

## 2.6.2 Airmass factor

The previous section describes how slant columns can be obtained from measured radiances. However, vertical columns (VC) representing the amount of trace gas integrated vertically from the surface to the TOA are quantities more easily interpreted. Similar to the equation for slant column, a VC for a certain height  $h$  can be calculated with:

$$VC = \int_0^{TOA} \rho(h) dh \quad (2.40).$$

From remote sensing measurements of the SCs, this amount can be derived by applying an airmass factor (AMF):  $AMF = SC/VC$ , which is a parameter computed by radiative transfer models. As it was mentioned above, SCIATRAN was the radiative transfer model used for the analysis presented in this thesis. The determination of AMFs by this model is based on the difference of intensity simulated at the TOA (for satellite measurements) with and without the absorber, which is divided by the cross section and vertical column (Rozanov and Rozanov, 2010). Since the AMF translates the effect of the light path on the measured trace gas amount, information on measurement conditions (such as observation geometry and wavelength) and atmospheric characteristics (e.g., vertical distribution of the chemical species, surface reflectance, aerosol loading and clouds) is needed. The appropriate selection of such *a priori* assumptions is essential to obtain the correct values of the AMF and, thus, accurate VCs of the trace gases. AMFs are also useful to express the measurement sensitivity: the larger the airmass factor, the higher the sensitivity of the measurement. Applying an AMF that is too high will result in an underestimation of the VC. Likewise, the determined trace gas VC will be too large if the value of the AMF used for the conversion of the SC is too small. The possible effects of atmospheric particles in satellite measurements were announced earlier in the text. Aerosol does not only affect the spectral distribution of the intensity measured, but also changes the light path of scattered light. This effect will also be accounted for when computing the airmass factors and chapters 3 and 4 are focused on the impact of aerosol on satellite observations of tropospheric trace gases.

It is also important to point out that the definition of the AMF mentioned above can be generalised by applying it to discrete layers in different altitudes. This corresponds to a block airmass factor (BAMF)

for a layer  $i$ :  $BAMF_i = SC_i / VC_i$ , which quantifies the change of airmass factor with altitude. When weighting the BAMF with the atmospheric absorber profile one obtains the total AMF:

$$AMF_i = \frac{\sum_i^N (BAMF_i \cdot VC_i)}{\sum_i^N VC_i} \quad (2.41),$$

where  $VC_i$  is the vertical column of the absorber in layer  $i$  and  $N$  is the total number of layers. The BAMF values determined for different altitudes, illustrate how the sensitivity of measurements varies with height. In Figure 2.14  $NO_2$  BAMFs are presented as function of altitude for three different scenarios, the first without aerosol and the last two with the trace gas mixed with different amounts of aerosol in that same layer. This figure highlights the increased sensitivity for  $NO_2$  detection in the presence of aerosol in the upper part of the layer and above it, as well as the reduced sensitivity close to the surface.

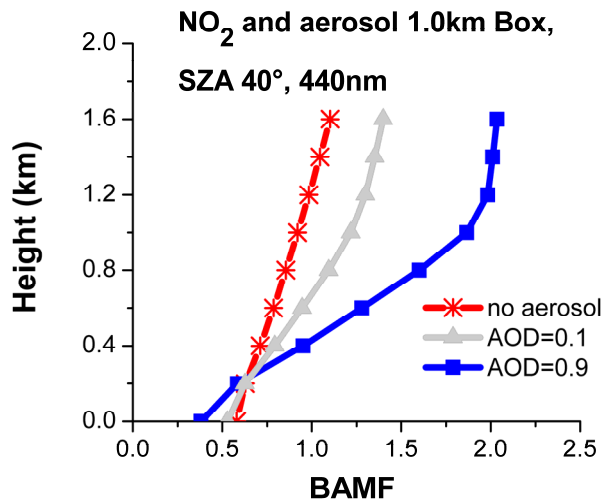


Figure 2.14  $NO_2$  block airmass factor (BAMF) for 3 scenarios: no aerosol (red), and an aerosol layer extending from the surface to 1.0 km with an optical depth (AOD) of 0.1 (grey) and 0.9 (blue). AMFs determined at 440 nm, with surface reflectance = 0.03,  $\omega_0 = 0.93$  and solar zenith angle (SZA)  $40^\circ$ .

More detailed discussions of the airmass factor concept can be found in Wagner et al. (2007), Leitão et al. (2010), Rozanov and Rozanov (2010) and Burrows et al. (2011).

### 2.6.3 Retrieval of tropospheric $NO_2$

The retrieval of tropospheric  $NO_2$  columns from space-based observations is performed in several steps. First,  $NO_2$  slant column densities are retrieved with the DOAS technique (described above),

usually in the wavelength window of 425 – 450 nm. Though, more recently, for GOME-2 data this has been extended to 497 nm (Richter et al., 2011). A larger fitting window is also used for OMI measurements, where NO<sub>2</sub> is fitted in the range of 405 - 465 nm (Boersma et al., 2011), so that the moderate signal-to-noise ratio is compensated for. In fact, the selection of fitting window follows several criteria to assure that in this wavelength range strong differential structures of the NO<sub>2</sub> absorption spectra are included, and that overlap with other spectral features is avoided as these interfere with the fitting process.

The tropospheric SC is calculated by eliminating the stratospheric contribution from the retrieved total columns. One frequent procedure applied is the commonly called reference sector method, also referred to as tropospheric residual method (Velders et al., 2001; Martin et al., 2002; Richter and Burrows, 2002). This approach is rather simple and based on the assumption that over clean tropospheric regions, such as the Pacific, the measured slant column of NO<sub>2</sub> corresponds only to stratospheric amounts. Assuming that this concentration does not vary with longitude, the stratospheric NO<sub>2</sub> can be directly subtracted from the total slant columns around the globe resulting then in tropospheric slant columns. This is a very practical and simple method that does not require the knowledge of NO<sub>2</sub> vertical profiles. However, the assumption of no NO<sub>2</sub> in the troposphere over the Pacific and the homogenous longitudinal variation might introduce errors because of variations in NO<sub>2</sub>. This can be clearly identified by the occurrence of negative tropospheric values, especially in the regions of the polar vortex (Richter and Burrows, 2002; Boersma et al., 2004; Beirle et al., 2010b). To solve this issue, adaptations have been made, mostly for GOME and OMI datasets, where the selection of the clean areas is improved, and regions classified as unpolluted, based on the absence of known tropospheric sources (Leue et al., 2001; Wenig et al., 2004; Bucsela et al., 2006). Still, although these attempts might correct the signal over highly polluted locations, they do not completely solve the problem of longitudinal variations. The satellite instrument SCIAMACHY (see section 2.7), measures both in nadir and limb viewing geometries and offers a unique solution for this challenge. A combination (matching, to be more precise) of these two measurements provides information regarding the amount of NO<sub>2</sub> present at altitudes where simultaneous observations (within minutes) are performed. In this way, the stratospheric NO<sub>2</sub> columns can be determined and subtracted from the total columns measured in nadir viewing geometry. Sioris et al. (2004) and Sierk et al. (2006) have explored the potential of this approach to derive tropospheric NO<sub>2</sub> and recent progress has been achieved by Beirle et al. (2010b) and Hilboll et al. (2011, to be submitted). The limitations of this method are related to the resolution of the measurements (3 km vertical step), and the reduced sensitivity of limb observations to the lower stratosphere, leading to somewhat high uncertainties of the stratospheric column densities. In addition, uncertainties are often associated with the definition of tropopause height which is necessary when determining the height and extension of the stratosphere. Furthermore, the use of this method cannot be straightforwardly implemented for the

data of the remaining satellite instruments. An alternative to these two methods is the synergistic use of model simulations (Richter et al., 2005; Boersma et al., 2007). Chemical transport models are able to predict global amounts of stratospheric NO<sub>2</sub>, and these simulations collocated with the satellite measurements allow for a subtraction of stratospheric columns. For the retrieval of tropospheric NO<sub>2</sub> columns from OMI measurements, total columns from this same instrument are assimilated in the TM4 model, and the output data are then used to eliminate the stratospheric fraction (Boersma et al., 2007). A similar approach had already been used by Richter et al. (2005), with daily stratospheric NO<sub>2</sub> column data from the SLIMCAT model that was scaled to the GOME data over an unpolluted region. The drawback of using such datasets is obviously related to model uncertainties that, in some cases, can be quite high (see chapter 5 with the validation of CTM output).

As explained above, when dividing the tropospheric SC by an appropriate airmass factor a tropospheric NO<sub>2</sub> vertical column is obtained. In the current retrieval method used at IUP-Bremen, an AMF lookup table is employed (Nüß, 2005) to derive the daily NO<sub>2</sub> tropospheric vertical columns from the measurements. The vertical distribution of tropospheric NO<sub>2</sub> was taken from MOZART-2 model simulations (Horowitz et al., 2003), for 1997, on a 2.8125° x 2.8125° grid. The surface reflectance values used are from the database of Lambert-equivalent reflectivity created by Koelemeijer (2006), based on GOME observations of the reflectivity at the top of the atmosphere. In the current approach, the information for aerosol settings is based on a static map derived from CO<sub>2</sub> emissions which attributes urban aerosol to polluted regions, rural aerosol elsewhere over continents, and maritime aerosol over the oceans. These three aerosol models are then combined in scenarios (defining abundance and vertical distribution) built with the LOWTRAN model (see details, e.g., Nüß, 2005). All this information is then used to determine monthly averaged airmass factors. This methodology does not capture the full spatial and temporal variability of aerosol nor its characteristics. Therefore, the study presented here investigates a way of improving the current approach. Alternative methods are currently applied to different products: some retrieval processes do not explicitly correct for aerosol impact, arguing that the cloud correction scheme also accounts for a large part of the aerosol effect (Boersma et al., 2004; 2007; 2011); others include full aerosol treatment in the radiative transfer calculations using aerosol fields from models (Martin et al., 2003; Lee et al., 2009). Another important aspect in the retrieval is the presence of clouds in the field of view of the satellite instrument. The pixels most affected by clouds are removed from the data through several methods. For the near-real-time dataset (standard operational product), screening of data is performed according to radiation intensity, where anything above a certain limit is classified as being cloud covered. On the other hand, for other analyses (like the one presented in chapter 5), a different method can be applied, using the FRESCO product (Koelemeijer et al., 2001, 2002), and considering a cloud filter of 0.2 which corresponds to maximum cloud coverage of 20%.

## NO<sub>2</sub> retrieval

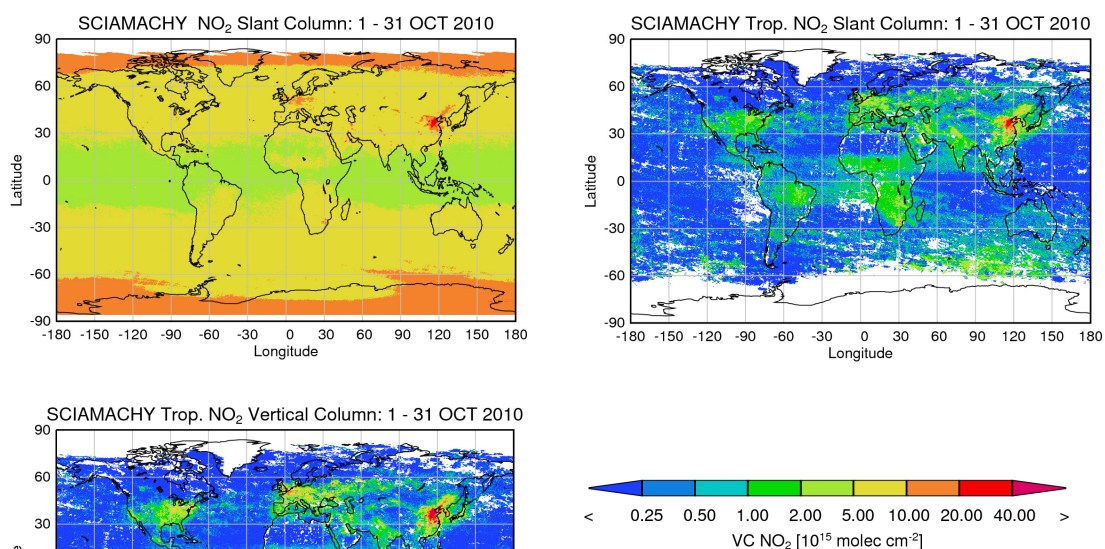


Figure 2.15 Three main steps of the NO<sub>2</sub> data analysis as described in the text, starting with the initial total slant column density (top left), going through tropospheric slant column with cloud screened data (top right), to finally achieve the tropospheric vertical column density (bottom).

Several sources of errors are associated with the retrieval of tropospheric NO<sub>2</sub> vertical columns from satellite measurements. These can be both random and systematic. While averaging the data will reduce the first, the latter are more difficult to quantify (Burrows et al., 2011). As it is the case for all remote sensing measurements, the recorded radiation intensity is the basis for all retrieved quantities and also for the measurement quality. Instrument noise and polarisation sensitivity of the optical components are also error sources for the radiance values collected. For the slant columns, accuracy of the absorption cross sections used (see DOAS method description above) influences the quality of the retrieval. In addition, their temperature dependence should be accounted for in the analysis when measuring trace gases, to resolve the variation for the different temperatures within the atmosphere column. For the computation of the tropospheric SCs, the stratospheric correction mentioned above is the relevant step, and for the tropospheric VCs, the uncertainty of the results is mostly related to the assumptions made in the calculation of the light path. As it was already explained, the AMFs used to convert slant to vertical columns are determined with a radiative transfer model, and a computation that requires several *a priori* assumptions as, for example, surface spectral reflectance, aerosol optical and physical properties, the vertical distribution of particles and absorber, and on clouds. Since all this information is not always available with a high level of accuracy, and cannot reproduce the spatial variability found in a typical satellite field of view, high uncertainties can result from wrong *a priori* settings. These are only a few of the uncertainties associated with the retrieved tropospheric vertical

columns. A complete list and a detailed discussion on this aspect is beyond the focus of this thesis. The analysis presented here (chapter 3 and 4) focuses on the aerosol assumptions made in the determination of the air mass factors and how these can be related to the accuracy of the final tropospheric NO<sub>2</sub> vertical columns.

Further details regarding the several methods utilised to retrieve tropospheric NO<sub>2</sub> columns from satellite measurements and its related uncertainties can be found, e.g., in Leue et al. (2001), Richter and Burrows (2002), Martin et al. (2002), Boersma et al. (2004; 2011) and Burrows et al. (2011).

## 2.7 Satellite instruments

When mankind was able to reach the space an opportunity was created to explore and study the atmosphere from a different perspective. Probing the Earth from above allows a better observation point to assess global atmospheric composition. The Soviet Union started measuring ozone and aerosol from space already back in the 1960s. A decade later, in the United States of America, progress was also made in regards to space observations, and a series of satellites has been launched since then. Among those, it is important to highlight two instruments measuring since 1978, providing long time series of ozone and sulphur dioxide (among other species): the two Solar Backscatter Ultraviolet (SBUV), and the three Total Ozone Mapping Spectrometer (TOMS). Nonetheless, in Europe, the potential of remote sensing observations of tropospheric trace gases (and other constituents) from space was initially not fully explored. Instruments onboard the first polar orbiting European Research Satellite (ERS-1) performed measurements mainly with the purpose of assessing meteorological parameters. Launched in 1995 on ERS-2, GOME (Burrows et al., 1999) was the first satellite to perform measurements of tropospheric trace gases and also provide valuable information on ozone in the stratosphere. Such observations were essential to improve knowledge on the O<sub>3</sub> chemistry and the depletion process occurring at high altitudes. Nowadays there are several instruments flying on satellites that provide global data of atmospheric composition from which information of air pollution can be inferred. Furthermore, interpretation of climate change effects is also possible with such observations, as well as the study of many other aspects in different layers of the atmosphere.

## 2.7.1 SCIAMACHY

The ENVironmental SATellite (ENVISAT) of the European Space Agency (ESA) hosts ten remote sensing instruments; including SCIAMACHY (SCanning Imaging Absorption spectroMeter for Atmospheric CHartography) as part of the atmospheric chemistry mission onboard this satellite. Launched in March 2002 into a Sun-synchronous near-polar orbit, this satellite crosses the equator at 10:00 solar local time (LT) in descending node. With an orbital period of 100.6 minutes, which corresponds to 14 orbits per day, global coverage at the equator is achieved by SCIAMACHY after 6 days. The general goal of ENVISAT is to better comprehend the environmental processes at different levels of the Earth's system, i.e., not only the atmosphere but the whole biosphere, including also the lithosphere, hydrosphere and cryosphere. SCIAMACHY (Goede et al., 1991; Burrows et al., 1995; Bovensmann et al., 1999; Gottwald and Bovensmann, 2011), on the other hand, is mainly focused in measuring the atmospheric constituents so that current understanding on global atmospheric composition and processes can be improved. Furthermore, it is (and has been for the past 8 years) an essential tool to determine trends of air pollution and effects related to the intensification of the greenhouse effect. Apart from information on trace gases, the inversion of measured radiance and irradiance provides insight also on aerosol and clouds. This passive imaging spectrometer observes Earth's atmosphere (all its layers), in several modes: nadir (looking downwards), limb (looking forward in flight direction), and solar and lunar occultation (see Figure 2.16); and measures radiation in wavelength ranges from UV to SWIR: 214 - 1773 nm (channels 1 to 6), 1934 - 2044 nm and 2259 - 2386 nm (channels 7 and 8). All of these viewing geometries are done in a systematic sequence for each orbit. The measurements performed on the illuminated side of the orbit are mostly for scientific needs, while those executed on the night side (when the atmosphere appears to be dark) are mainly done for calibration purposes and some eclipse interest. A distinct feature of this instrument is that, with the limb and nadir viewing geometries, it is possible to measure overlapping air masses in different modes. This is then useful to derive coincident information, mainly from stratospheric constituents, for vertical profiles and concentrations. Direct sunlight is measured in solar occultation mode while sunlight reflected at the moon's surface is recorded in the lunar occultation state. For nadir observations, a series of forward/backward scans will cover a ground scene of typically 400 km along track with individual ground pixels between 26 km x 30 km and 32 km x 930 km, depending on the integration time. At IUP-Bremen, the current SCIAMACHY nadir products available include both reactive gases (such as, O<sub>3</sub>, NO<sub>2</sub>, BrO, HCHO, CHOCHO, SO<sub>2</sub>, IO, CO, OCIO) and greenhouse gases (water vapour, CH<sub>4</sub>, CO<sub>2</sub>), as well as cloud and aerosol properties.

NO<sub>2</sub> vertical columns retrieved from SCIAMACHY's nadir measurements are used in chapter 5 to evaluate results of chemical transport models: MOZART and TM5.

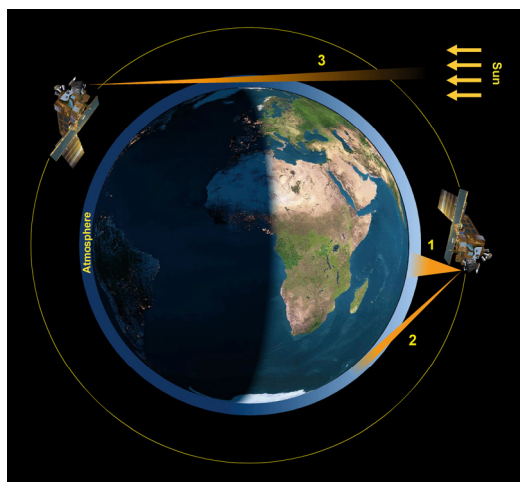


Figure 2.16 SCIAMACHY observation modes: 1) nadir, 2) limb, 3) occultation. (Courtesy of: DLR-IMF)

## 2.7.2 GOME-2

The Meteorological Operational satellite programme (MetOp) embraces a series of three satellites that will provide not only global measurements of atmospheric composition, but also weather data services that can be used to monitor climate and improve weather forecasts. This programme has been set up by ESA and the European organisation for the exploitation of METeorological SATellites (EUMETSAT). MetOp-A was launched in October 2006 with more than ten instruments onboard, one of those being the Global Ozone Monitoring Experiment-2 (GOME-2, Callies et al., 2000; Munro et al., 2006). The satellite flies on a Sun-synchronous orbit that crosses the equator at 09:30 solar LT in descending node. GOME-2 measurements achieve global coverage within 1.5 days, with the default swath width of 1920 km. This spectrometer is a follow-up of the first GOME on ERS-2 (that itself is a smaller version of SCIAMACHY) which started the long-term monitoring of atmospheric ozone by ESA. As its predecessors, measurements from this instrument allow an improved monitoring of ozone fields, providing also vertical distribution of this compound. Additionally, from the measured radiation, total columns of  $\text{NO}_2$ ,  $\text{SO}_2$ , BrO, HCHO and OCIO can be retrieved together with information on cloud parameters (e.g., cloud fraction, its optical thickness and cloud top height), aerosol properties (e.g., aerosol optical thickness and absorbing index) and UV fields (UV index). One of the upgrades of this instrument with respect to GOME is its higher spatial resolution with ground pixels of 80 km x 40 km, with field of view ( $0.286^\circ \times 2.75^\circ$ ) at nearly daily global coverage. In addition, the calibration processes have been improved and GOME-2 contains now two spectrometers, one for polarised and the other for unpolarised light. However, in comparison to SCIAMACHY this instrument presents some limitations as it can only perform measurements in nadir viewing and sideways viewing for polar coverage. Furthermore, the four main optical channels

measure only in the wavelength range of 240 - 790 nm, i.e., UV and visible light, at a high spectral resolution between 0.2 - 0.5 nm.

## 2.8 Atmospheric models

The atmosphere is a complex system that is not yet fully understood as a whole, although deep knowledge exists for individual atmospheric processes (Seinfeld and Pandis, 2006). Models are powerful tools that offer the possibility to simultaneously describe physical and chemical atmospheric mechanisms, reproducing the behaviour of pollutants, assessing the influence of emissions on atmospheric composition, and, ultimately, the impact on human health and ecosystems. Air quality models simulate the spatial distribution and temporal variation of atmospheric components, and can be used with different goals, focusing on problems such as urban smog, stratospheric ozone depletion, and/or global climate change. Since models are able to relate the pollutant's emissions with air quality levels, these are a functional source of information regarding the effectiveness of strategies to reduce air pollution. Thus, this is one of the reasons why policymakers often base their decisions on model data.

Models vary in temporal and spatial resolution, input data used, chemical processes included and dynamics considered. Several types of air quality models exist, and they are often divided into two classes: empirical and diagnostic models (Russell and Milford, 2000). While the former focus on a statistical analysis of historical air quality data, the others are able to represent, with more detail, the physical phenomena and chemistry of the atmosphere, simulating the life cycle of pollutants from their emissions to a final state. Deterministic models describe transport and chemical transformation of atmospheric compounds with analytical or numerical expressions based on the conservation-of-mass principle (Russell and Milford, 2000). The changes in pollutants' concentrations are dependent on meteorology, topography, chemical transformations, surface deposition and source emission characteristics. These input data will control the transport and chemical reaction rates, the diffusion and deposition processes, and will define initial and boundary conditions. Models that focus on atmospheric particulate matter need to account for different processes. These are formulated according to the fundamental equation of aerosol dynamics, describing aerosol transport, growth, coagulation and sedimentation (Russell and Milford, 2000). When simulating atmospheric particulate matter, the key variables are size and chemical composition of aerosol which are controlled by condensation, coagulation, sedimentation, and nucleation processes. The full description of different

model types and their schemes is beyond the scope of this work, however further information can be found at Russell and Milford (2000) and Seinfeld and Pandis (2006).

One of the main drivers of the models is the meteorological processes, which can be accounted for in many different ways. Recent air quality models use dynamic, or prognostic, meteorological models that solve a set of partial differential equations: the Navier-Stokes equations (Russell and Milford, 2000). These describe the conservation mass momentum combined with energy conservation and thermodynamics in a moving fluid. Such approach will improve the accuracy of the meteorological inputs. In most of the model schemes, the equations describing atmospheric composition are usually not linked to those governing air motion. While this assumption would be correct for some cases of tropospheric pollution, it does not represent the general atmospheric behaviour where, often, the concentrations of pollutants can affect the meteorology processes (and vice-versa). Examples of climate being altered due to change in atmospheric chemical composition have been mentioned in previous sections, where it was explained that greenhouse gases and aerosol can warm the atmosphere and that the particulate matter also influences the cloud formation. Hence, a new category of models has been developed in the recent years focusing on the simulation of chemical weather, i.e., the short-term variability of atmospheric chemical composition (Lawrence et al., 2005). Atmospheric chemical transport models (CTMs) can, nowadays, be coupled with numerical weather predictions models, offering the possibility for feedback mechanisms between meteorology and pollutants. This is commonly called chemical weather forecasting (Baklanov, 2010; Kukkonen et al., 2011). The two modelling components can be integrated in one model system with offline or online methods.

In this thesis models were used in two different analyses. CTM output data for NO<sub>2</sub> and aerosol was used as source of *a priori* information for the calculation of AMFs applied in the retrieval of tropospheric NO<sub>2</sub> vertical columns. In addition, in chapter 5, satellite data was proven to be essential in the model development, by validating stratospheric and tropospheric columns simulated by two different CTMs (MOZART and TM5) against satellite observations made by SCIAMACHY. This work has been developed within the GEMS project (and the follow up MACC), a novel initiative that addressed the chemical weather forecasting thematic and attempting to improve the current use of this modelling approach.



# 3

## Influence of aerosol on NO<sub>2</sub> airmass factors<sup>1</sup>

The improvement on the retrieval process of trace gas columns from satellite measurements is a continuous work in progress. Accurate vertical columns are important to better understand atmospheric processes, assess trends of air pollution and efficiently allocate efforts to mitigate pollution. Several aspects contribute to uncertainties in the calculated values. The calculation of airmass factors (AMFs, used to convert the slant to vertical columns) is based on many *a priori* assumptions where further development is still required. An appropriate selection of these definitions used is crucial to obtain the correct values of the AMFs and, thus, reduce the uncertainties of the NO<sub>2</sub> columns. For such undertaking it is necessary to prioritise efforts and resources. Thus, the solution is to establish key factors by performing sensitivity studies. Here, the focus was to determine the influence of aerosol on the tropospheric NO<sub>2</sub> airmass factor. As the anthropogenic sources of aerosol and other pollutants, like NO<sub>2</sub>, are often collocated, a proper characterisation of the aerosol's impact on the retrieval is essential. This is of particular importance if long-term trends of, for example, tropospheric NO<sub>2</sub> are studied which are accompanied by large changes also in the aerosol loading. Both particulate matter and NO<sub>2</sub> are highly variable in time and space, which is a result of many different aspects related to their sources, lifetime and atmospheric conditions. Therefore, a wide

---

<sup>1</sup> Based on the paper: Leitão et al. (2010), On the improvement of NO<sub>2</sub> satellite retrievals – aerosol impact on the airmass factors.

variety of scenarios was needed to understand as much as possible the variation of the AMF for different combinations of aerosol and trace gas characteristics.

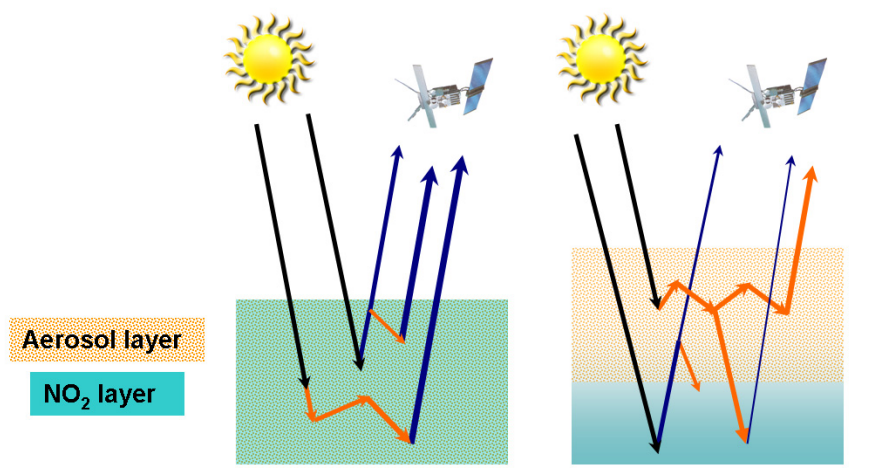


Figure 3.1 Schematic representation of possible interactions between sunlight and particles, resulting in different amount radiation that reaches the satellite instrument

### 3.1 Impact of aerosol on satellite remote sensing

Particles present in the atmosphere interact with radiation, consequently, influencing the remote sensing measurements of atmospheric trace gases (see Figure 3.1). This effect is related to the fact that satellite measurements of tropospheric trace gases use scattered solar light to retrieve information on the atmospheric composition. These observations are based on the detection of the absorption along the light path from the Sun through the atmosphere to the instrument. For an ensemble of photons, scattering is regarded as a statistical process, where many different light paths contribute to the signal observed at the top of the atmosphere. For an optically thin absorber, the overall absorption signal is determined by the amount of absorption along the individual light paths weighted with their relative contributions to the total radiance measured. In comparison to a pure Rayleigh atmosphere, the presence of aerosol can change both the individual light path lengths and their contributions to total radiance observed at the satellite. This influence is mostly associated with the aerosol optical properties, its amount and vertical distribution relative to that of the trace gas of interest. In addition, also surface reflectance, solar zenith angle (SZA) and satellite viewing angle influence the

observations. The conjugation of these factors can lead to either increase or decrease of the sensitivity of the satellite measurements. Moreover, qualitatively, the effects of an aerosol layer on tropospheric measurements using scattered sunlight can be separated into four groups:

- light path enhancement within the aerosol layer as result of multiple scattering, leading to an increase in absorption signal from the path between scattering events;
- increased sensitivity within and above the aerosol layer as result of larger scattering probability and, hence, larger contributions of these paths to the radiance observed at the satellite (albedo effect);
- decreased sensitivity below the aerosol layer as more photons are scattered back to the satellite before they can reach these altitudes (shielding effect);
- decreased sensitivity within and below the aerosol layer in cases of strongly absorbing particles as the number of photons returning from this region is reduced.

With the exception of the last point, the effects of aerosol listed above are very similar to the considerations made for clouds (e.g., Hild et al., 2002; Boersma et al., 2004; Beirle et al., 2009; Kokhanovsky and Rozanov, 2009; Boersma et al., 2011). The present study assesses the importance of aerosol for the retrieval of tropospheric NO<sub>2</sub> columns from satellite observations in clear sky cases, i.e., the impact of clouds was not taken into account. The effects of clouds in the retrieval were already analysed in detail in many previous studies such as Boersma et al. (2004), Wang et al. (2005) and Kokhanovsky and Rozanov (2009). The first study demonstrated that the correction for the aerosol impact cannot be simply separated from the effect of clouds and, therefore, if a cloud retrieval scheme is adopted, it will account for a large part of the aerosol effect by retrieving a different cloud fraction and height. More recently, Boersma et al. (2011) shows empirical evidence that the cloud retrievals with the algorithm for OMI are sensitive to the presence of scattering aerosol, therefore correcting its effects through aerosol-induced cloud parameters. An analysis focussed on clear sky scenes shows that non-zero O<sub>2</sub>-O<sub>2</sub> cloud fractions coincide with aerosol plumes retrieved from MODIS.

Different studies have also analysed the aerosol impact on the airmass factor applied in the retrieval process. Boersma and co-workers (2004) focussed on the overall uncertainties of the retrieval of tropospheric NO<sub>2</sub> columns from satellite measurements. They reported that including realistic aerosol in the radiative transfer calculations would increase the airmass factors by up to 40% depending on aerosol type and aerosol optical depth. The vertical profile of the aerosol was assumed to be exponential with a scale height of 2.0 km and the vertical NO<sub>2</sub> profile was not specified. Monthly aerosol properties derived with the GOCART model were used for another study performed by Martin et al. (2003). The authors found that biomass burning and desert dust aerosols would reduce the AMFs by 10–20% while over industrial regions an increase of 5–10% was observed. A comparable sensitivity study to the one presented here was carried out by Gloudemans et al. (2008) to analyse,

among other aspects, the impact of aerosol in the retrieval of CH<sub>4</sub> and CO (in the IR region) from the SCIAMACHY instrument. One of the main findings from this study was that, depending on the location of the plume and type of particulate matter, the omission of aerosol influence in the retrieval process can lead to significant errors in the total column of CH<sub>4</sub>. Thomas et al. (2005), with a similar study for SO<sub>2</sub> (retrieved in the UV region) concluded that aerosol is relevant mainly for optical depth above 0.3 and in the presence of desert dust plumes in the boundary layer (BL). If these two conditions were realised at the same time the authors estimated that the column would be underestimated by 5–10%. For the TOMS SO<sub>2</sub> retrieval, Krueger et al. (1995) showed that neglecting a rather thin aerosol layer may result in a systematic overestimation of the retrieved total SO<sub>2</sub> content. Focusing on HCHO retrieval, Fu et al. (2007) have also analysed the sensitivity of the AMFs to aerosol definitions. From the results, the relative vertical distribution of the trace gas and aerosol was identified as major factor influencing the AMFs. A strong enhancement of the AMFs was observed for the case of an aerosol layer standing below the HCHO. Furthermore, the aerosol impact on ground-based zenith-sky DOAS measurements was also investigated by Chen et al. (2009). The aerosol effect was studied by changing the vertical distribution of the aerosol and NO<sub>2</sub> layers, together and independently of each other, and varying also the single scattering albedo (SSA). From this analysis an error of 10% was determined. Nevertheless, for these measurements, the uncertainties caused by unknown aerosol properties and vertical profiles of both aerosol and NO<sub>2</sub> tended to cancel each other.

The investigation carried out included a broad set of scenarios, accounting for both hypothetical and realistic cases, with, for example, different atmospheric profiles of trace gas and aerosol. Several datasets available were used as source for the required input settings of the radiative transfer model. Trace gas profiles were taken from model simulations, and lidar and Sun photometer measurements were used to define the vertical profiles of aerosol and its properties. The results presented in this thesis show to which parameters the measurements are most sensitive and to which extent the modification of aerosol properties (physical and optical) affects the results.

## 3.2 Radiative transfer settings

As described earlier in the introductory chapters (section 2.6), the measured slant columns ( $SC$ ) are converted to vertical columns ( $VC$ ) according to:

$$VC = \frac{SC(\lambda, \Theta, \dots)}{AMF} \quad (3.1),$$

where the airmass factor (*AMF*) expresses the sensitivity of the measurement based on information of different parameters for measurement conditions (such as observation geometry and wavelength), and for atmospheric characteristics (e.g., vertical distribution of the chemical species, surface reflectance, aerosol loading and clouds). This factor is normally determined with radiative transfer models and incorrect assumptions in the modelling will ultimately lead to inaccurate NO<sub>2</sub> columns. Vertical columns can be underestimated with too high AMFs, and vice-versa. As described in section 2.6, the AMFs currently used are based on limited datasets and quality has to be improved. It is, therefore, important to understand the main source of uncertainties and the spread of values. As mentioned above, some studies have been performed to identify potential source of errors. In the AMF determination it is important to consider the influence of particles present in the atmosphere. The sensitivity study presented here focuses mainly on the aerosol load and its characteristics (size distribution, optical properties, and vertical distribution). With this analysis, it was demonstrated how much the AMF values can vary for different aerosol settings, and consequently, the retrieved NO<sub>2</sub> columns. In addition, the effect of variations in the surface reflectance value and the NO<sub>2</sub> vertical profile were also analysed.

The airmass factors analysed in this chapter were calculated with the radiative transfer model SCIATRAN 2.2 (Rozanov et al., 2005). The computations were performed on a vertical grid of 200 m from surface to the top of the trace gas and aerosol layers, at four different wavelengths (425, 437.5, 440 and 450 nm), in nadir observation, and at six solar zenith angles (SZA, from 20° to 70° in steps of 10°). SCIATRAN was operated using the discrete ordinate method for solution of the radiative transfer equation, in plane-parallel geometry, accounting for full multiple scattering effects, but without including polarisation. At the viewing geometry used here, the effects of Earth's curvature and refraction can be neglected. As atmospheric scenario, the US standard (1976) atmospheric pressure and temperature were used.

The surface reflectance is defined as the ratio of incoming radiation to the reflected one, i.e., for the Earth case, it is the percentage of sunlight that is reflected by the Earth surface. The range of possible values is from zero for dark (black) surfaces that absorb all the incoming light, to unity, i.e., 100%, for bright (white) surfaces that reflect all the incident radiation. Fresh snow has typically very high surface reflectance close to 1 (in the visible wavelengths) while the oceans (seen from space) have low ones. Other examples of contrasts are the forests which in general appear to be dark surfaces and the desert areas that are very good reflecting areas. Still, it is important to highlight that many of these values change greatly from season to season. The surface reflectance, derived from MERIS measurements (Popp et al., 2011), presents values close to an average of 0.03 in regions distinctive for its anthropogenic pollution, like Europe, US or China. On the other hand, for the same regions, the database compiled by Koelemeijer et al. (2003) often shows higher values, around 0.05. In addition,

Kleipool and co-authors (2008) have produced global maps of the Earth's surface Lambertian equivalent reflectance, from OMI measurements, for the period of October 2004 to October 2007. The values of this dataset are, on average, 0.005 lower than the Koelemeijer values, and 0.02 higher than the black sky albedo derived from MERIS, at 470 nm. This illustrates the high variability of this surface's property and how difficult it can be to select a single value for a broader region. This parameter showed to be very relevant for the retrieval of trace gas, which confirmed previous findings from Richter and Burrows (2002) or Boersma et al. (2004). For the majority of scenarios considered, this parameter was set to 0.03 assuming that this is, for the spectral range used, an average value for urban areas. Nevertheless, to ensure completeness, the value of surface reflectance in the radiative transfer calculations was also varied to 0.01, 0.07 and 0.1 (for a limited number of scenarios) so that the effect of this property on the AMF could be determined.

### 3.2.1 Definition of NO<sub>2</sub> vertical distribution

As illustrated before, tropospheric NO<sub>2</sub> presents a clear daily cycle and its concentrations are highly variable in space. Likewise, its vertical distribution is dependent on many different aspects, and often hard to predict. Normally, for simplicity, it is assumed that the vertical distribution of this pollutant follows the evolution of the boundary layer, being well mixed in this height. However, such a homogenous profile might not always be the correct representation of what happens in reality. The usual short lifetime of NO<sub>2</sub> is also a reason why one would expect distinct distributions in urban and background environments. Data from campaigns like DANDELIONS or CINDI held in Cabauw, Netherlands, have been quite helpful to better understand how the distribution of this chemical species occurs in the atmosphere. Measurements from MAX-DOAS instruments (Wagner et al., 2004; Wittrock et al., 2004), from lidar (Volten et al., 2009) and, more recently available, from sonde (Sluis et al., 2010), offer the possibility to assess vertical distribution of NO<sub>2</sub>. Such information provided on larger datasets (high spatial and temporal coverage) is highly promising to be a source for satellite retrievals.

For this study, different cases were selected starting with basic NO<sub>2</sub> profiles where the gas was homogeneously distributed within a BL of 0.6, 1.0 or 2.0 km height (hereafter referred to as box profiles). Then, a second set of scenarios was simulated where two different profiles of tropospheric NO<sub>2</sub> (from surface to 5.5 km) were used: average urban and rural (see Figure 3.2). These profiles are an average from CHIMERE (Schmidt et al., 2001; Honoré et al., 2008) model runs with a 9.0 km x 9.0 km resolution, at 10:00 LT and for the period from 23<sup>rd</sup> May to 11<sup>th</sup> June 2007 (which was randomly selected). The NO<sub>2</sub> volume mixing ratio above 5.5 km (the top of model simulations) was set to decrease slowly to a value of 0.0015 ppt at 100 km (the top of radiative transfer calculations).

The model results are based on simulations for three different locations: Paris downtown; 15 km East of Paris; and 100 km East of Paris, a rural region. Since the first two sites are very similar, and, considering that the typical size of a satellite pixel would include both of these locations, their average is defined as average urban – “Avg Urb”. In Figure 3.2, the different NO<sub>2</sub> mixing ratio profiles are shown from surface level up to 10 km. From this figure it becomes clear that the NO<sub>2</sub> profile determined by the model for the urban conditions is not at all similar to a homogenous distribution over a BL of 1.0 km or even 600 m. This has a significant impact on the results, as it will be further discussed. In addition, the large difference between the urban and rural profiles illustrates how the NO<sub>2</sub> vertical distribution can show significant variations over a short distance. This might be a crucial point for satellite retrievals where, at the spatial resolution of the currently used *a priori* data, both urban and rural scenes are often contained in one model grid cell. In the study of Heckel et al. (2011), it has been shown how the AMFs can differ in a region where both ocean and land areas exist. Differences of up to a factor of two were found when highly resolved AMFs were determined instead of a single one for a large domain. Such a variation of values needs to be taken carefully in consideration given that it will have a direct impact on the retrieved VCs and their accuracy.

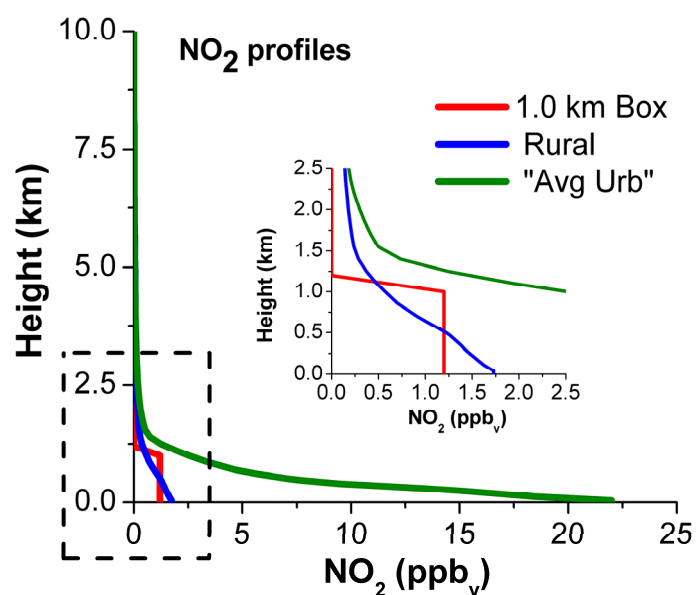


Figure 3.2 NO<sub>2</sub> profiles from surface to 10.0 km used in the SCIATRAN settings for the airmass calculations: box profile of 1.0 km (red); average urban (“Avg Urb”) (green) and rural (blue) based on CHIMERE model results.

### 3.2.2 Definition of aerosol properties and vertical distribution

The role of the aerosol in the atmospheric radiative processes was already explained in detail in chapter 2. The influence of aerosol on the retrieval of tropospheric NO<sub>2</sub> from satellite measurements is not only relevant for urban scenes, which are major sources for those two components, but also for biomass burning events (although these cases are out of the scope of this study). Furthermore, it is important to consider, as well, cases of aerosol (like desert dust) that is often transported far away from its origin to source regions of NO<sub>2</sub>. These plumes are often found at high altitudes in the atmosphere but, sometimes, are also at lower altitudes mixed with boundary layer pollution.

For the radiative transfer calculations, information on different aerosol characteristics is required, namely, the size distribution parameters, optical properties, its amount and vertical distribution. Currently, datasets of aerosol attributes are available from records from both ground-based measurements and space-borne instruments.

#### a) Phase functions

Within the radiative transfer model, angular distributions of scattered light are required to simulate the interaction of particles and light. The phase function varies with the aerosol composition, the size of the particles relative to the wavelength of the radiation, and it also depends on particle shape and internal structure (see section 2.4 for more details). The optical properties and size distributions, at 440 nm, these were mainly taken from records of 12 worldwide AERONET stations presented in Dubovik et al. (2002). This dataset is representative of the usual classification of four different aerosol types that have distinctive physicochemical, optical and radiative properties: urban/industrial, biomass burning, desert dust and oceanic. In Table 3.1 the parameters for the different size distributions considered are given, together with the refractive index. The phase functions were determined with the program *spher.f* (FORTRAN program) developed by Michael Mishchenko and freely available at <http://www.giss.nasa.gov/staff/mmishchenko/brf/>. For each of the aerosol types, from the 12 locations considered, the phase functions (see Figure 3.3) for both fine and coarse particles were determined and used separately in each of the scenarios. A clear distinction between phase functions of fine and coarse aerosol is found, with the bigger particles showing a stronger peak in forward direction. In reality, a mixture of both sizes is normally found, but for the sensitivity study performed here a clear separation of particle sizes facilitated the interpretation of results. Nevertheless, it is important to keep in mind that coarse aerosol is mostly found in desert dust scenario or from the ocean, e.g., sea-salt. On the other hand, the aerosol emitted in urban areas and from open vegetation fires are, on average, dominated by small particles (Seinfeld and Pandis, 2006).

## Influence of aerosol on NO<sub>2</sub> airmass factors

Table 3.1 Size distribution parameters (radius and sigma) and refractive indices taken from 12 AERONET stations (Dubovik et al., 2002): Urban (Urb), Biomass Burning (BB), Desert Dust (DD) and Oceanic. Data from measurements performed at 12 AERONET stations (Dubovik et al., 2002): Paris/Creteil – France (Urb), GSFC/Maryland – USA (Urb), Maldives (Urb), Mexico city – Mexico (Urb), Amazonia forest – Brazil (BB), South American cerrado – Brazil (BB), African savannah – Zambia (BB), Boreal forest – USA and Canada (BB), Cape Verde (DD), Persian Gulf (DD), Saudi Arabia (DD) and Lanai (Oceanic).

<b>Location (Urban)</b>	<b>Paris</b>	<b>Maryland</b>	<b>Maldives</b>	<b>Mexico city</b>
r (μm), σ (fine)	0.06, 0.43	0.07, 0.38	0.09, 0.46	0.06, 0.43
r (μm), σ (coarse)	0.31, 0.79	0.42, 0.75	0.35, 0.76	0.68, 0.63
Refractive index	1.4 – <i>i</i> 0.009	1.41 – <i>i</i> 0.003	1.44 – <i>i</i> 0.011	1.47 – <i>i</i> 0.014
<b>Location (Biomass burning)</b>	<b>Amazonia forest</b>	<b>S. American cerrado</b>	<b>African savannah</b>	<b>Boreal forest</b>
r (μm), σ (fine)	0.08, 0.40	0.06, 0.40	0.07, 0.40	0.08, 0.43
r (μm), σ (coarse)	0.37, 0.79	0.37, 0.79	0.50, 0.73	0.32, 0.81
Refractive index	1.47 – <i>i</i> 9.30E-4	1.52 – <i>i</i> 0.015	1.51 – <i>i</i> 0.021	1.5 – <i>i</i> 9.4E-3
<b>Location (desert dust + oceanic)</b>	<b>Cape Verde</b>	<b>Persian Gulf</b>	<b>Saudi Arabia</b>	<b>Lanai</b>
r (μm), σ (fine)	0.05, 0.49	0.08, 0.42	0.07, 0.40	0.07, 0.48
r (μm), σ (coarse)	0.47, 0.63	0.69, 0.61	0.66, 0.60	0.53, 0.68
Refractive index	1.48 – <i>i</i> 2.5E-3	1.55 – <i>i</i> 2.5E-3	1.56 – <i>i</i> 2.9E-3	1.36 – <i>i</i> 1.5E-3

### b) Vertical distribution

For remote sensing applications, the total amount of aerosol present in the atmosphere is often specified by an aerosol optical depth (AOD) which is the vertical integral of the extinction by aerosol from the top of the atmosphere to the ground (see section 2.4 for more details). As mentioned above, different aerosol vertical distributions were considered for the several scenarios. In the first phase of the study, the aerosol profile was defined as a box shaped profile, i.e., layers with homogeneously distributed aerosol, which had variable top height for each setup considered. Three cases were set with extinction coefficients representative for three aerosol loads: 0.1 (low pollution level), 0.5 (moderate pollution) and 0.9 (polluted scene) aerosol optical depths. Next, the aerosol profile was defined in different ways relative to the trace gas: following the NO<sub>2</sub> box profile; starting at surface level and with the top of the layer lower or higher than that of the NO<sub>2</sub> profile; and, discrete elevated aerosol layers above the NO<sub>2</sub> layer (assumed to be in the BL). These scenarios (A to H in Table 3.2) were selected as

simplified representations of potential occurrences. Normally, the urban aerosol is assumed to be either in homogenous layers extending from the surface to the top of BL or, often, following an exponential decrease with height (e.g., scenario K). In general, one can assume that the majority of anthropogenic sources are the same for both  $\text{NO}_2$  and aerosol and, therefore, they would have similar spatial distributions (e.g., scenarios C and J). However, depending on the source location and transport processes, the aerosol layer can extend to a higher altitude (e.g., scenarios F and I), whereas  $\text{NO}_2$  will be in general more concentrated closer to the emission site and at lower levels, due to a shorter lifetime. In addition, measurements have already shown that a residual layer of aerosol can remain at higher altitudes above the boundary layer after this one has reduced its extension (Hodzic et al., 2004; 2006). For that reason, the extension of each layer was also varied independently so that different scenarios could be analysed. The scenarios with elevated discrete aerosol layers (e.g., scenarios D and M) are mostly adequate to illustrate plumes of biomass burning smoke and desert dust that are transported several hundreds to thousands of kilometres away from the source and which

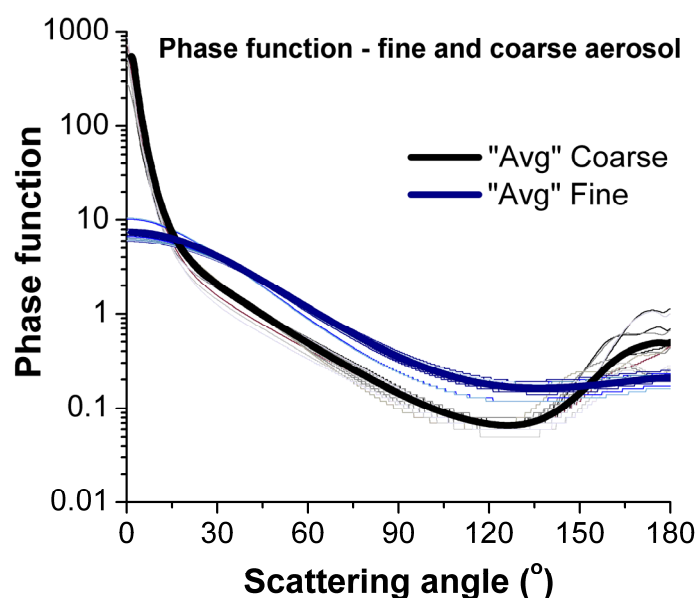


Figure 3.3 Phase functions, at 440 nm, for fine (blue) and coarse (grey) aerosol determined for 4 distinct aerosol types: Urban (Urb), Biomass Burning (BB), Desert Dust (DD) and Oceanic. Optical properties taken from 12 AERONET stations (Dubovik et al., 2002): Paris/Creteil – France (Urb), GSFC/Maryland – USA (Urb), Maldives (Urb), Mexico city – Mexico (Urb), Amazonia forest – Brazil (BB), South American cerrado – Brazil (BB), African savannah – Zambia (BB), Boreal forest – USA and Canada (BB), Cape Verde (DD), Persian Gulf (DD), Saudi Arabia (DD) and Lanai (Oceanic). Average of phase functions for each of the aerosol sizes considered is presented in thick lines (blue for fine and black for coarse aerosol).

can be lifted to higher altitudes during transport (Damoah et al., 2004). These events can happen not only on a continental scale (e.g., smoke from fires in the African savannah that is transported across the Atlantic Ocean as shown by Husar et al. (1997)), but also on a regional scale, as transport within Europe (Balis et al., 2003; Hodzic et al., 2006; Arola et al., 2007). These aerosol plumes often occur in the free troposphere, but they can also be part of the boundary layer either by intrusion processes or due to the low initial injection height (e.g., scenarios L and P). Good examples of this case are the dust outbreaks from deserts that often can mix with urban type aerosol emitted within European or Asian cities (e.g., Zhou et al., 2002).

On a second stage of the research, the vertical aerosol profiles used in the calculations were based on different studies resulting from lidar measurements made at ground-based stations, such as those that are part of the European Aerosol Research LIdar NETwork (EARLINET, Mattis et al., 2002) or the Asian Dust network (AD-net, Murayama et al., 2001) (see Table 3.3 and Table 3.4). In this way, specific situations, as those suggested above, could be simulated in more realistic scenarios. The studies considered here are from different locations around the world and representative of different times of the year. Figure 3.4 shows the vertical profiles of extinction coefficients for all the cases investigated. This extensive selection of scenarios was designed to assure that many different possible cases would be considered and the conclusions drawn from this study could be generalised. However, the detailed analysis of all these examples would be too extensive and often repetitive as many of the results led to similar conclusions. Therefore, in the current manuscript, focus is given only to a few scenarios: I to P (represented in the top graphs of Figure 3.4). Further details of assumptions made for scenarios I to P are presented in Table 3.3, and the literature source references for the remaining cases are provided in Table 3.4.

The size distribution and corresponding phase functions, for both fine and coarse aerosol, were maintained from the initial stage. It is important to mention that the profiles considered in this study are not the exact representation of the original ones. Often adjustments were required in order to obtain a profile from surface to the top of atmosphere. Moreover, as these are meant to be examples for case studies their accuracy is not a subject of this analysis and does not influence the conclusions drawn. Since lidar measurements (both satellite and ground-based) are usually performed at 355 nm and/or 532 nm, an Ångström exponent (Ångström, 1929), also taken from the literature, was necessary to convert these values to the corresponding ones at 440 nm (within the wavelength region where NO<sub>2</sub> is retrieved).

Cases for oceanic aerosol type were not included at this stage because this aerosol is normally only observed in very low concentrations at polluted sites and is usually mixed with other types of aerosol.

## Sensitivity study

Therefore, for simplicity of the analysis, it was assumed that its influence in the NO<sub>2</sub> retrieval is similar to that of the other types considered.

Table 3.2 Scenarios considered for the SCIATRAN runs, defined by the combination of a NO<sub>2</sub> and an aerosol layer, as in box profiles (e.g., Scen.B: NO<sub>2</sub> layer 0.0 - 1.0 km and aerosol layer 0.0 - 0.6 km).

Scenario	A	B	C	D	E	F	G	H
NO <sub>2</sub> layer (km)	0.0 – 0.6				0.0 – 1.0			0.0 – 2.0
Aerosol layer (km)	0.0 – 0.6	0.0 – 0.6	0.0 – 1.0	0.6 – 1.0	1.0 – 2.0	0.0 – 2.0	2.0 – 3.0	0.0 – 2.0

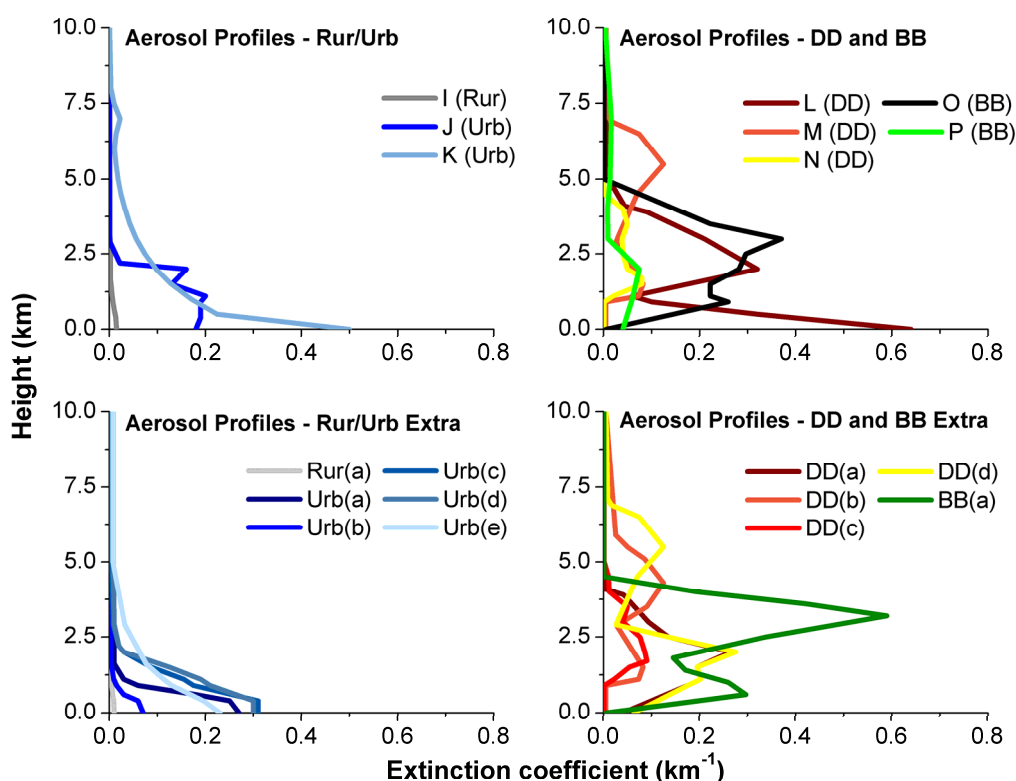


Figure 3.4 Aerosol extinction profiles from surface level to 10.0 km used in the SCIATRAN settings for the AMF calculations for: (left) rural (Rur) and urban (Urb) locations; and (right) desert dust (DD) events and biomass burning (BB) plumes. These profiles are based on measurements as it is explained in Table 3.2 for scenarios I to P (top) and in Table 3.3 for the extra ones (bottom).

## Influence of aerosol on NO<sub>2</sub> airmass factors

Table 3.3 Aerosol parameters (single scattering albedo ( $\omega_0$ ), Ångström exponent ( $\alpha$ ) and aerosol optical depth (AOD)) taken from each of the references mentioned, these were used to define the aerosol vertical profile (with extinction coefficients) for the SCIATRAN scenarios. These are representative of different aerosol types: Urban (Urb), Desert Dust (DD), and Biomass Burning (BB) scenes.

Scenario and Reference for aerosol ext. profile	Aerosol type	$\omega_0$	$\alpha$	AOD	Further notes
<b>I</b> based on CALIPSO records <sup>a</sup>	Urb	0.93 <sup>b</sup>	1.4 <sup>c</sup>	0.07	Background conditions
<b>J</b> Chazette et al. (2005)	Urb	0.87	2.1	0.40	19 July 2000 in Paris (FR)
<b>K</b> Amiridis et al. (2005)	Urb	0.93 <sup>b</sup>	1.4 <sup>c</sup>	0.62	4yr average over Thessaloniki (GR)
<b>L</b> Zhou et al.(2002)	DD	0.92 <sup>b</sup>	0.19	1.05	12 May 2000 in Heifei (CN)
<b>M</b> Murayama et al. (2003)	DD	Altitude dependent values – 0.8 to 0.95	Altitude dependent values – 0.01 to 1.1	0.66	23 April 2001 in Tokyo (JP)
<b>N</b> Pérez et al. (2006)	DD	0.93	0.19 <sup>d</sup>	0.16	18 June 2003 in Barcelona (SP)
<b>O</b> Balis et al. (2003)	BB	0.92 <sup>b</sup>	1.4 <sup>c</sup>	1.05	9 August 2001 in Thessaloniki (GR)
<b>P</b> Müller et al. (2005)	BB	0.92 <sup>b</sup>	Altitude dependent values – 0.0 to 1.1	0.42	26 June 2003 in Leipzig (DE)

- a) Data provided by Chieko Kittaka and David Winker from NASA - Goddard Space Flight Center.  
b) Average of the respective aerosol type based on Dubovik et al. (2002).  
c) Average for urban aerosol in Mattis et al. (2004).  
d) Same as Zhou et al. (2002).  
e) From Müller et al. (2005) and references therein.

### c) Single Scattering Albedo (SSA)

The SSA differs according to the type and source of aerosol and, thus, is in part dependent on the location of measurement (see for example Hu et al., 2007). For the majority of the scenarios considered in this analysis, the impact of aerosol absorption was investigated by comparing the AMFs determined with runs where  $\omega_0$  was set to 0.93 (average from all the SSA values given at 440 nm in

Dubovik et al. (2002)) and others where  $\omega_0$  was assumed to be 1.0 (i.e., non-absorbing aerosol). This allowed determining the maximum effect on the results when reducing the absorbing ability of aerosol. However, for a limited number of cases, this variation was analysed with further detail by setting  $\omega_0$  to 0.80 and 0.95. Furthermore, in the last stage of the analysis, when considering measurements of aerosol profiles, the  $\omega_0$  values varied from scenario to scenario: either taken from the corresponding records or based on typical values for the aerosol types (see Table 3.3).

Table 3.4 Source references used of the extra aerosol vertical profiles and further required information.

Scenario/Aerosol type	Reference for aerosol ext. profile
Rur(a)	based on CALIPSO records <sup>a</sup>
Urb(a)	based on CALIPSO records <sup>a</sup>
Urb(b)	based on CALIPSO records <sup>a</sup>
Urb(c)	He et al. (2008)
Urb(d)	He et al. (2008)
Urb(e)	Mattis et al. (2004)
DD(a)	Müller et al. (2003)
DD(b)	Murayama et al. (2003)
DD(c)	Pérez et al. (2006)
DD(d)	Müller et al. (2003) and Murayama et al. (2003)
BB(a)	Murayama et al. (2004)

a) Data provided by Chieko Kittaka and David Winker from NASA - Goddard Space Flight Center.

### 3.3 Sensitivity study

A comprehensive analysis was performed with air mass factors of  $\text{NO}_2$  determined for many different case studies where diverse settings of the radiative transfer calculations were changed. More than 1700 scenarios were created and, for each of them, AMFs were determined for four different wavelengths and six solar zenith angles (SZA). The amount of results obtained was immense and here only a selection of those will be presented, offering an overview of the main observations made and key conclusions reached. The contribution exerted by aerosol in the results can be analysed by comparing these scenarios with a reference scenario where no aerosol is considered in the radiative transfer

calculations. Therefore, in the following sections reference is often made to such scenario. The selection of results presented follows the cases which are more representative of the aerosol type in consideration. Also, only the results obtained for 440 nm are shown as this is the wavelength for which the AERONET aerosol optical properties are given. An extension of the calculations to the wavelength range often used for NO<sub>2</sub> retrieval revealed an average increase of AMF by 10% from 425 to 450 nm. For different SZA, the general trend showed that the AMF increases for lower Sun, but for specific cases, this tendency was also reverted. In some circumstances (see for example Figure 3.17), when considering fine aerosol, a decrease could be observed with high Sun, and in other cases, with coarse particles, a small increase was then followed by decay after 50° or 60°.

### 3.3.1 Influence of surface reflectance

The surface reflectance (SR) selected for all scenarios included in this sensitivity study was 0.03. NO<sub>2</sub> is not measured only over urban areas but also in remote locations where the albedo can vary according to the different type of soil and vegetation. Knowing that the surface reflectance is influencing the sensitivity of the satellite measurements, the impact of changes in this parameter was also analysed. This value was set to 0.01 (typical for example for forests), 0.07 and 0.1 (values found in desert scenes) for a few scenarios: a) NO<sub>2</sub> box profile of 1.0 km layer; b) NO<sub>2</sub> and aerosol box profiles of 1.0 km layer (scenario C); and c) NO<sub>2</sub> box profile of 1.0 km layer and aerosol with elevated box from 1.0 to 2.0 km high (scenario E) (not shown).

The results presented in Figure 3.5, Figure 3.6 and Figure 3.7 highlight the impact of the surface reflectance, which can be quite large, in the AMF calculations. An increase of this value resulted always in an increase of the AMF. Brighter surfaces will more efficiently reflect the sunlight back to the satellite and, therefore, contribute to the enhancement of the measured NO<sub>2</sub> columns. From Figure 3.5 it is possible to see that this effect is independent on the aerosol presence. Changing from dark (SR = 0.01) to bright surface (SR = 0.10) led to an enhancement of about 200% of the AMF. However, when the NO<sub>2</sub> and aerosol are mixed in the same layer, the increase of the AMF was, on average, 90% for the different AODs considered (Figure 3.6). The maximum value obtained was in fact, much higher and changes by a factor of 2.8 were registered for the case of high Sun (SZA of 20° and 30°), with coarse particles mixed with the trace gas and AOD = 0.1. The dependence of this change on the amount of aerosol present in the atmosphere is illustrated also in Figure 3.7 where the AMFs are plotted as a function of surface reflectance, for one SZA (50°) and different AODs. The impact of aerosol is largest over dark surfaces and rapidly decreases as surface reflectance increases. This indicates that the increase in reflectivity resulting from aerosol has less effect if the surface is already bright. However, the situation changes when considering absorbing aerosol (Figure 3.8). In

that case, a decrease of the AMF is observed when a dark layer of aerosol (mixed with the trace gas) stands on top of a bright surface, i.e., surface reflectance of 0.1 and above. In a last scenario, the influence of different surface reflectance values for an elevated aerosol layer (from 1.0 to 2.0 km) was also investigated. This layer was selected because (as it will be shown later in section 3.3.3) these circumstances normally generate a decrease of the AMF due to the shielding of the trace gas by the particles standing above it. It was therefore important to understand how these two effects would interplay. The main difference from the results for this scenario and the previous one were found when high aerosol optical depth was considered. The surface reflectance has a higher impact on the scenario with elevated layer because the decrease of AMF, resulting from an aerosol shielding layer standing above the  $\text{NO}_2$ , is now reduced by enhanced reflectivity of the brighter surface. In this scenario, the increase of surface reflectance changed the AMF up to a factor of 3.8.

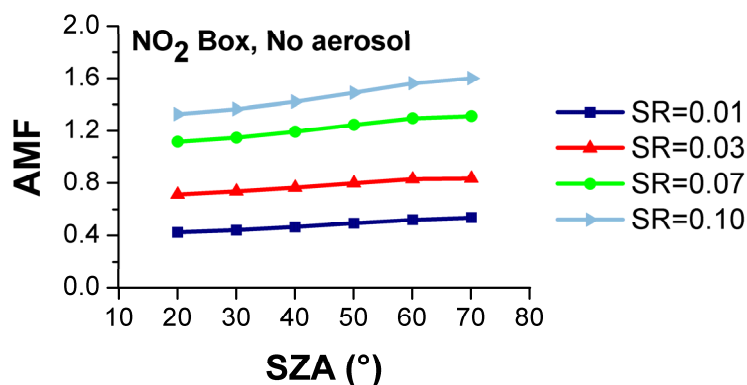


Figure 3.5  $\text{NO}_2$  air mass factors for simulations with different surface reflectance (SR) values (0.01 (dark blue), 0.03 (red), 0.07 (green) and 0.10 (light blue)). The 1.0 km box profile was considered for  $\text{NO}_2$  and no aerosol was included in the calculations. AMFs determined at 440 nm.

### 3.3.2 Influence $\text{NO}_2$ profile

As mentioned above, the  $\text{NO}_2$  vertical distribution is often assumed to be homogeneously distributed in the BL and to follow its evolution throughout the day. To test the impact of the  $\text{NO}_2$  profile in the radiative transfer calculations, a set of scenarios was created for different BL heights: 0.6, 1.0, and 2.0 km. In addition, the results for these cases were also compared to the scenarios where the model profiles were used.

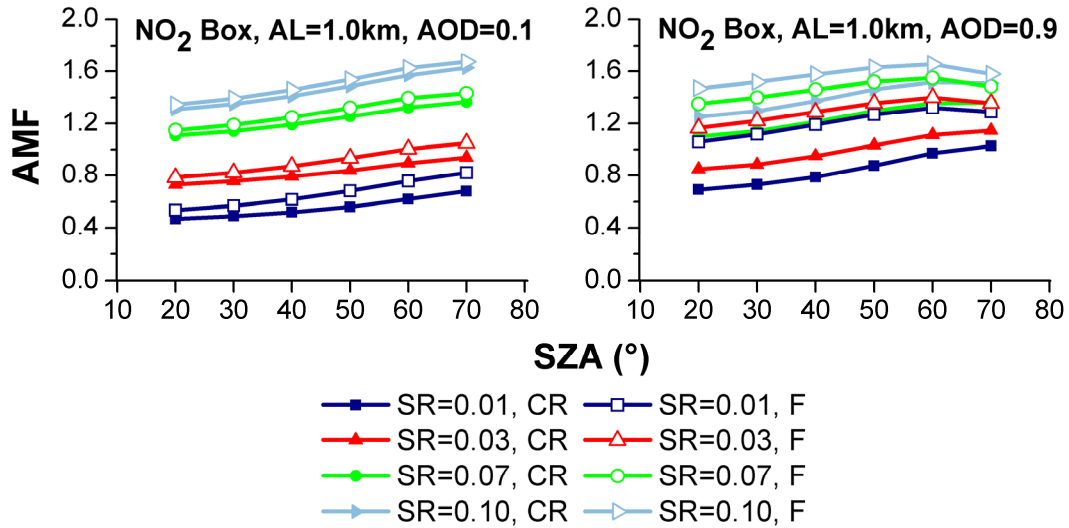


Figure 3.6 NO<sub>2</sub> air mass factors for simulations with different surface reflectance (SR) values (0.01 (dark blue), 0.03 (red), 0.07 (green) and 0.10 (light blue)). Scenario C (NO<sub>2</sub> and aerosol layer – 1.0 km box profile) was used with the phase functions determined for coarse (CR) and fine (F) particles (optical properties taken from Creteil/Paris AERONET station). AMFs determined at 440 nm, with  $\omega_0 = 0.93$  and different AODs: 0.1 (left), and 0.9 (right).

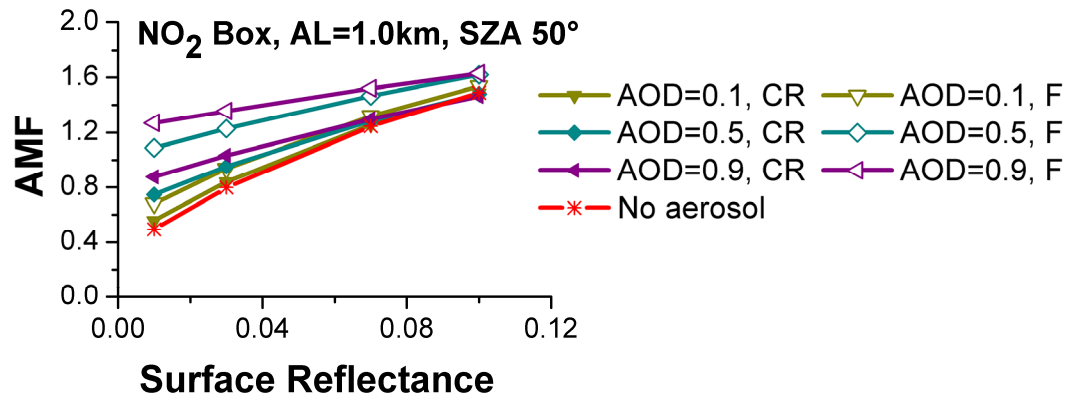


Figure 3.7 NO<sub>2</sub> air mass factors for simulations with different surface reflectance (SR) values. Scenario C (NO<sub>2</sub> and aerosol layer – 1.0 km box profile) was used with the phase functions determined for coarse (CR) and fine (F) particles (optical properties taken from Creteil/Paris AERONET station). AMFs determined at 440 nm, with  $\omega_0 = 0.93$ , SZA = 50° and different AODs: 0.1 (green), 0.5 (blue), and 0.9 (purple), and, in addition, for the scenario without aerosol (red).

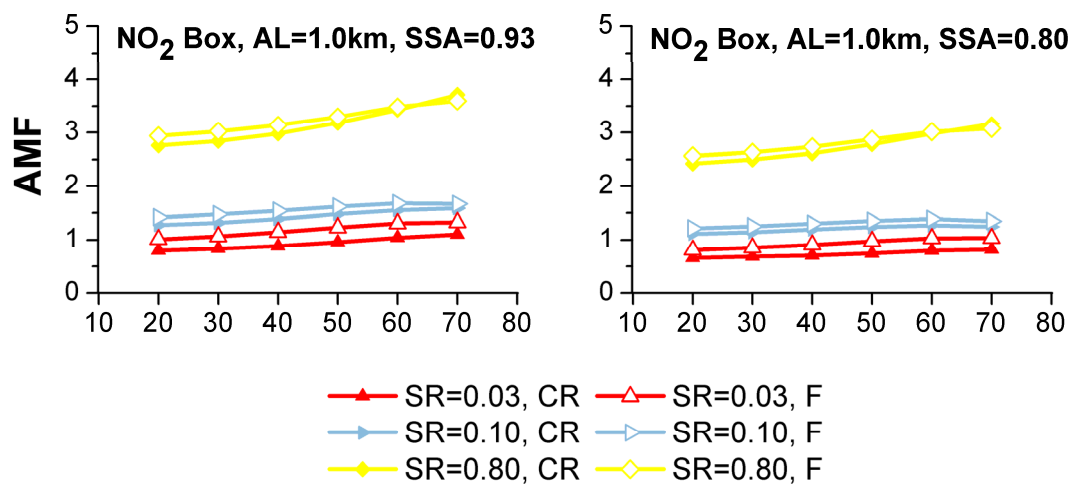


Figure 3.8 NO<sub>2</sub> air mass factors for simulations with different surface reflectance (SR) values (0.03 (red), 0.10 (blue), and 0.80 (yellow)). Scenario C (NO<sub>2</sub> and aerosol layer – 1.0 km box profile) was used with the phase functions determined for coarse (CR) and fine (F) particles (optical properties taken from Creteil/Paris AERONET station). AMFs determined at 440 nm, with AOD = 0.5 and different  $\omega_0$ : 0.93 (left) and 0.80 (right).

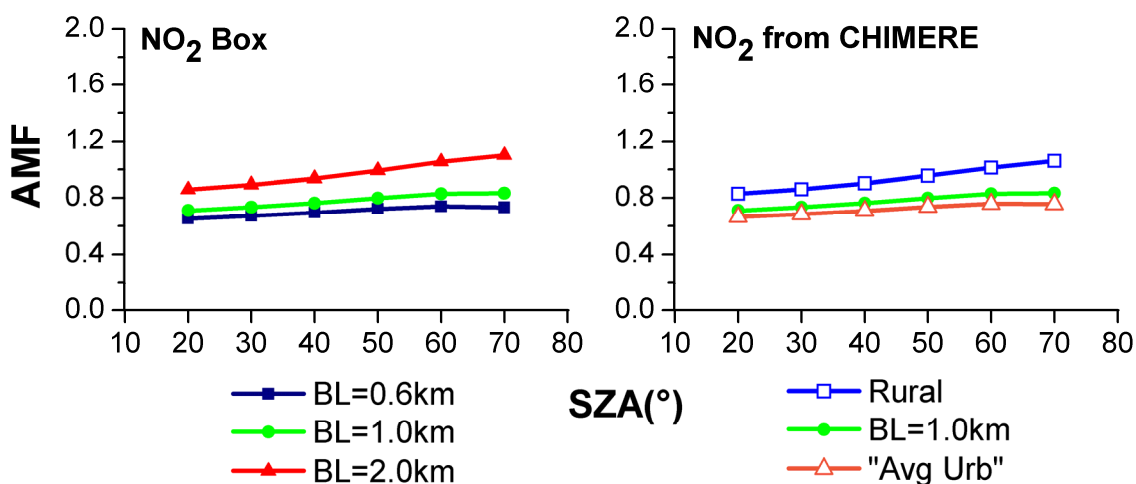


Figure 3.9 NO<sub>2</sub> air mass factors for scenarios with different NO<sub>2</sub> profiles and no aerosol included. Changing boundary layer (BL) height of 0.6, 1.0 and 2.0 km (left). Profiles from the CHIMERE model: rural – Rur – and urban – "Avg Urb" (right). AMFs determined at 440 nm.

## Influence of aerosol on NO<sub>2</sub> airmass factors

Before discussing the impact of the boundary layer height with trace gas and aerosol mixed in the atmosphere, it is important to mention that the variations of the boundary layer alone will influence the AMF calculations, i.e., even when considering only a layer of NO<sub>2</sub> without aerosol present (Figure 3.9). When the top of the NO<sub>2</sub> layer was expanded from 0.6 km to 2.0 km the AMFs increased on average by a factor of 1.4. This is related to the fact that the sensitivity of the measurements is smaller closer to the surface. The same can be concluded when comparing the results of simulations with the 1.0 km box profile to those using the modelled profiles. The “Avg Urb” profile places the NO<sub>2</sub> mostly concentrated near the surface and, therefore, leads to smaller AMFs due to the shielding effect related to Rayleigh scattering (e.g., at 440 nm and SZA = 40°, the AMF decreased from 0.77 to 0.71). On the other hand, the “Rural” profile illustrates a distribution more similar to the box profiles and its AMF was higher than any of the polluted cases (e.g., at 440 nm and SZA = 40°, AMF value is now 0.90).

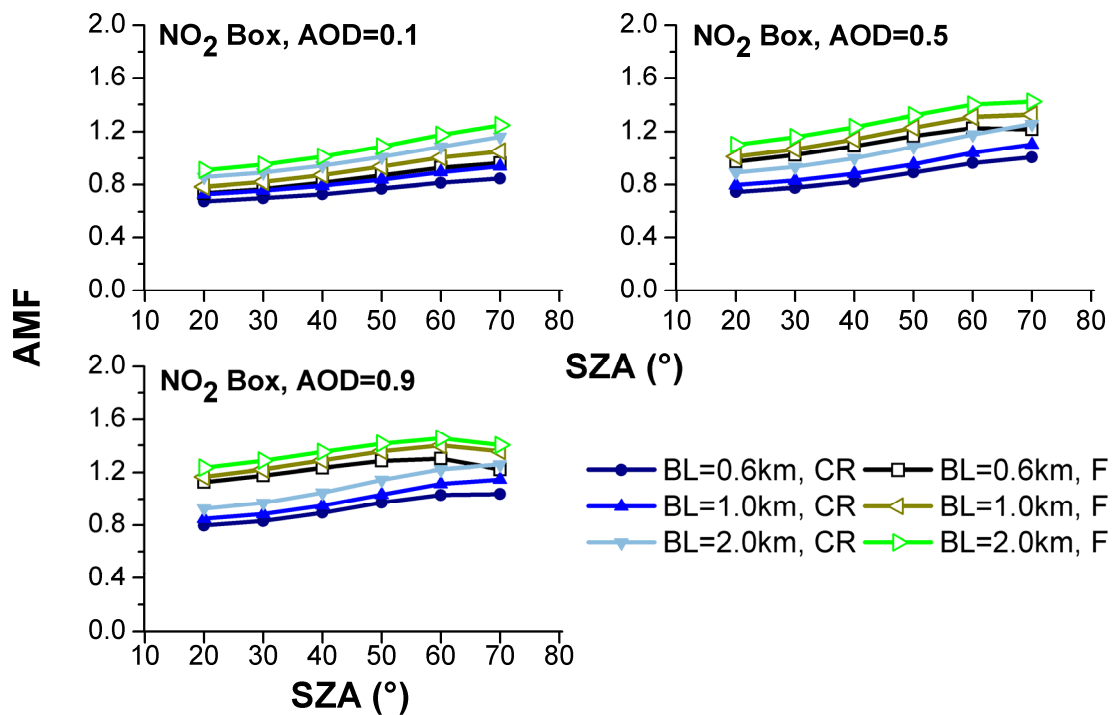


Figure 3.10 NO<sub>2</sub> air mass factors for different boundary layer heights. Scenarios A, C and H (well mixed NO<sub>2</sub> and aerosol layers in boundary layer (BL) extending to: 0.6, 1.0 and 2.0 km, respectively) were used with the phase functions determined for coarse (CR) and fine (F) particles (optical properties taken from Creteil/Paris AERONET station). AMFs determined at 440 nm, with surface reflectance = 0.03,  $\omega_0 = 0.93$ , and different AODs: 0.1 (top left), 0.5 (top right), and 0.9 (bottom).

Following that, the  $\text{NO}_2$  and aerosol were considered to be well mixed and homogeneously distributed in layers of the same height (scenarios A, C and H, respectively). For each one of these cases it was found that the smallest AMFs were determined for the conditions without aerosol. Thus, one can conclude that, in these scenarios, the presence of aerosol originates an increase of the sensitivity of the measurements, even if quite small for coarse particles and low aerosol load. In practice, this indicates that, for the cases exemplified here, if the effect of aerosol scattering is not accounted for in the retrieval, the  $\text{NO}_2$  VC will be overestimated. Furthermore, comparing the findings for different boundary layer heights, the results for  $\text{NO}_2$  mixed with aerosol (Figure 3.10) followed the same pattern as in the calculations performed without aerosol. If a too low BL height is assumed in the retrieval, the tropospheric columns of  $\text{NO}_2$  will be overestimated. However, the changes in the AMF are smaller in this case than for the scenarios without aerosol. Yet, the spread of values obtained is higher for the simulations with aerosol, with AMFs ranging from 0.85 to 1.40, at 440 nm, while without aerosol the values vary between 0.85 and 1.10. The AMF increased, on average, by about 20% when the boundary layer's top changed from 0.6 to 2.0 km. The largest effect, at 440 nm, was found for the simulation with coarse aerosol and optical depth of 0.1 with 37% variation. Interestingly, the effect seems to decrease with growing aerosol load. Such a variation is possibly a result of the increase in scattering (and, therefore, the effective albedo) which will improve the sensitivity of the satellite measurements of the lower atmosphere.

In a last test, the results with the modelled profiles were compared to those obtained with the  $\text{NO}_2$  box profiles. In Figure 3.11, AMFs obtained for the case of a box profile of 1.0 km, are compared to those determined for the modelled "Avg Urb", both mixed with an aerosol layer of 1.0 km. These results confirm what was also observed for the case without aerosol: the satellite measurements will be less sensitive to the modelled  $\text{NO}_2$  since this is closer to the surface. This reduction in the AMFs was more evident when more aerosol was mixed with the trace gas.

### 3.3.3 Influence of different aerosol characteristics

As mentioned above, the main focus of this sensitivity study was, in fact, to learn exactly how the aerosol influences the retrieval of  $\text{NO}_2$  vertical columns from satellite measurements, by changing the AMFs. Since these AMFs are not only dependent on the aerosol parameterisation, in the previous sections the effect of surface reflectance and  $\text{NO}_2$  profile was investigated so that this could be compared (and weighted) to the following results.

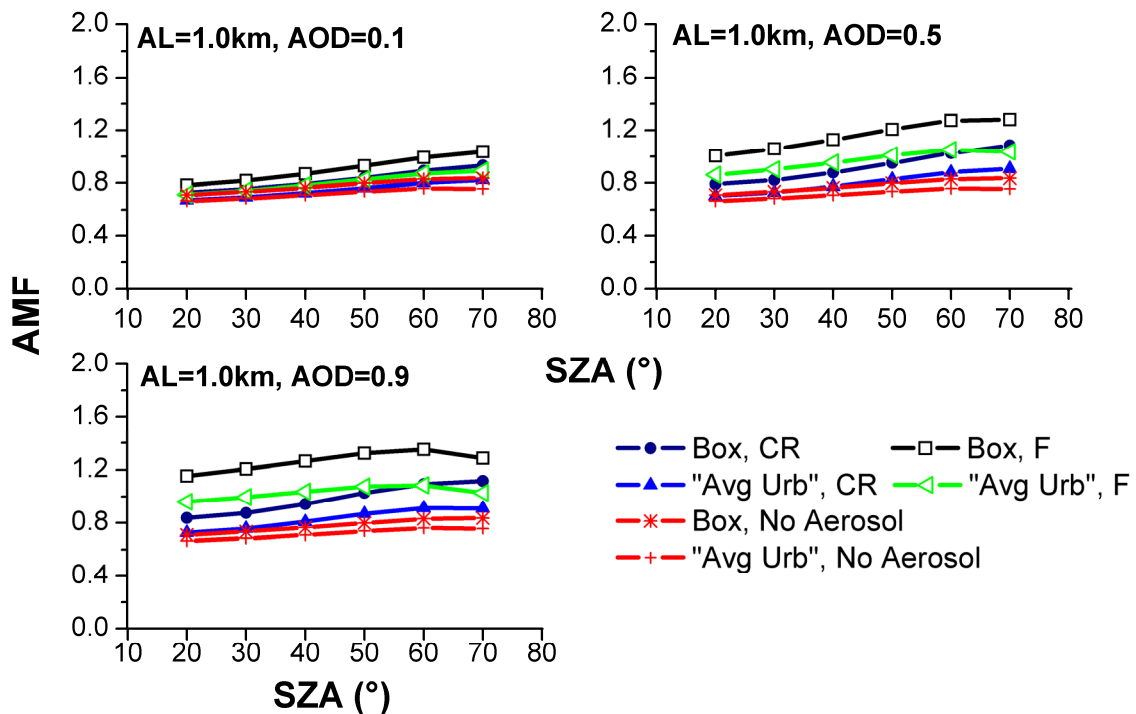


Figure 3.11 NO<sub>2</sub> airmass factors for different NO<sub>2</sub> profiles: box of 1.0 km and "Avg Urb" from the CHIMERE model. Aerosol layer (AL) of 1.0 km was considered with the phase functions determined for coarse (CR) and fine (F) particles (optical properties taken from Creteil/Paris AERONET station). AMFs determined at 440 nm, with surface reflectance = 0.03,  $\omega_0 = 0.93$ , and different AODs: 0.1 (top left), 0.5 (top right), and 0.9 (bottom).

### a) Size distribution and phase function

The variation in the size parameters for different aerosol types representative of the locations (AERONET stations) considered in this study was rather small. The similarity in values resulted in nearly identical phase functions with noticeable differences only between the two general size distributions considered: fine and coarse. In Figure 3.12 the AMFs are plotted for the case where NO<sub>2</sub> and aerosol are homogeneously mixed in a 1.0 km layer. The aerosol optical depth is 0.1 and the phase functions used correspond to different locations. The examples given were selected as those with the smallest and highest radii from the aerosol types considered, i.e., the highest range of values is represented. It is possible to see that the NO<sub>2</sub> AMFs determined within the various scenarios with fine particles are very similar, and the same occurs for those with coarse aerosol (notice the different scale in the y-axis from the previously presented figures). From the overall results it was found that fine particles have a higher impact on intensifying the changes of the AMF (in both directions) than

the coarse ones. However, this effect depends on several factors, such as the vertical distribution or Sun position (e.g., very low Sun can favour the enhancement of signal by the coarse particles standing in a discrete layer above the trace gas). An example of this behaviour can be observed in the previous Figure 3.9. The AMFs resulting from the simulations with fine aerosol mixed with the trace gas were higher than in the cases accounting for coarse particles. This means that, at the same AOD, fine aerosol increases the sensitivity to the  $\text{NO}_2$  more than coarse particles, and this difference of results increases with AOD. This is most likely related to the less pronounced forward peak in scattering for fine particles (see phase function in Figure 3.3) which increases the ratio of photons scattered towards the satellite under this observation geometry and, hence, improves the sensitivity.

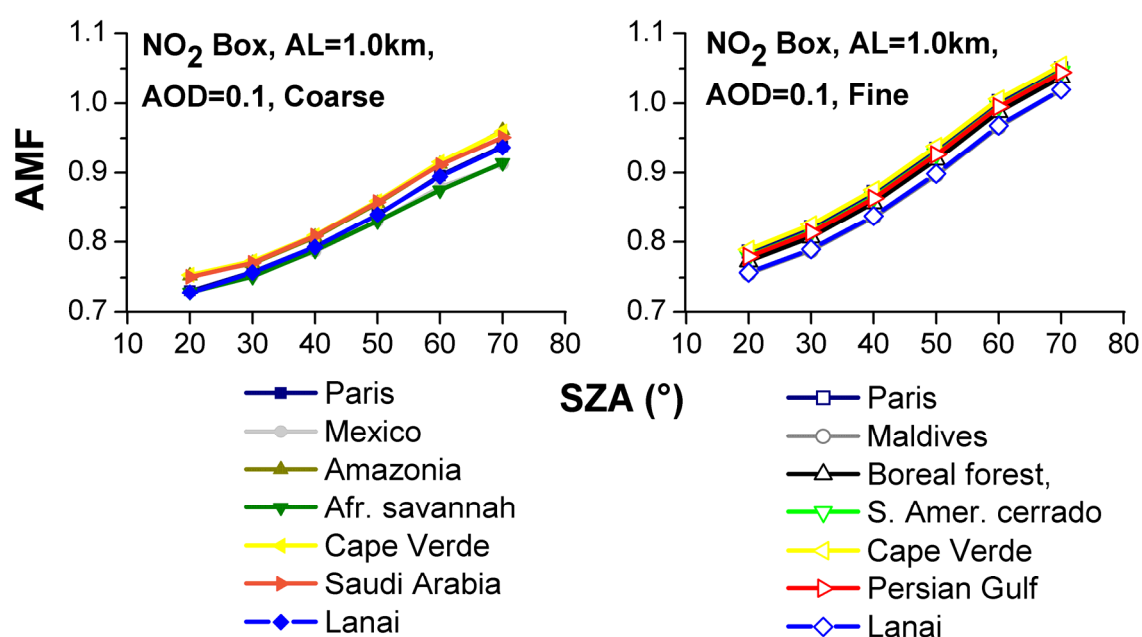


Figure 3.12  $\text{NO}_2$  air mass factors for Scenario C ( $\text{NO}_2$  and aerosol layer – 1.0 km box profile). AMFs determined at 440 nm, with surface reflectance = 0.03,  $\omega_0 = 0.93$ , and AOD = 0.1. Phase functions for coarse particles with optical properties and size distributions taken from: Paris/Creteil – France (Urb), Mexico city – Mexico (Urb), Amazonia forest – Brazil (BB), African savannah – Zambia (BB), Cape Verde (DD), Saudi Arabia (DD) and Lanai (Oceanic) (left). Phase functions for fine particles with optical properties and size distributions taken from: Paris/Creteil – France (Urb), Maldives (Urb), Boreal forest – USA and Canada (BB), South American cerrado – Brazil (BB), Cape Verde (DD), Persian Gulf (DD) and Lanai (Oceanic) (right).

## b) Vertical distribution

The vertical distribution of aerosol was defined to be representative of typical scenarios for each aerosol type, i.e., urban, desert dust and biomass burning. Therefore, it makes sense to separate the

analysis of results into different cases: a) aerosol layer extending from surface, the classic case of urban pollution; and b) elevated aerosol layers which are normally originated from windblown dust and fire smoke transported far in the high atmosphere (although, extraordinary cases have been registered with these plumes extending down to the surface). The main objective of the study was to understand how the retrieval would change over polluted regions (where most of the NO<sub>2</sub> is measured) characterised by a majority of anthropogenic emissions, i.e., urban areas. The satellite measurements of NO<sub>2</sub> emitted from fires are important as well, but also a more complex case as the distribution of the gas is hard to predict and varies much from fire to fire (as it was already explained in the previous chapter).

### Urban

The case where NO<sub>2</sub> and aerosol had the same vertical profiles, representing a situation where both are well mixed, was already presented. In the following scenarios, the vertical extension of the aerosol layer was varied to 0.6 and 2.0 km (scenarios B and F respectively) while the NO<sub>2</sub> profile was kept constant. This was done for two NO<sub>2</sub> profiles, a simple 1.0 km box profile and the more realistic urban profile as modelled by CHIMERE (“Avg Urb”). Figure 3.13 shows the results side by side for different AODs.

As it can be observed, in general, any aerosol mixed with the trace gas tends to enhance the NO<sub>2</sub> signal, indicating that an overestimation of the NO<sub>2</sub> VC will likely occur when effects caused by aerosol presence are neglected in the retrieval. However, the magnitude of the influence does vary as it depends on the relative position of trace gas and aerosol, in particular the aerosol load above the trace gas. In addition, the size of the particles plays a more relevant role in the calculations of the cases considered here. As for the previously discussed scenarios, at the same AOD, fine particles have a larger influence on the airmass factors, due to the generally higher backscattering (see Figure 3.3). In the simulations with box profiles, the interplay between reduction and enhancement of sensitivity can explain the observed variations: if the aerosol layer is close to the surface, i.e., with its top at 600 m, below the top of the trace gas layer, the sensitivity will be enhanced due to higher reflectivity and multiple scattering. An increase of the AMFs by 11% on average was found when the top of aerosol layer was lowered from 1.0 km to the 600 m and, in the case of highly polluted scenes with AOD of 0.9, the difference between the values was as high as 25%. Compared to the simulation without aerosol, the sensitivity was enhanced by up to a factor of two. On the other hand, when the aerosol layer extended higher than the layer of NO<sub>2</sub>, the AMF was lower (by 5 to 45%) than in the case when both aerosol and NO<sub>2</sub> had the top layer at 1.0 km. This was the outcome of the elevated part of the aerosol layer that acted as a shield and, thereby, partly cancelled the enhancement of sensitivity in the lower section. Yet, compared to the AMF values obtained without aerosol, the fine particles slightly increased the NO<sub>2</sub> signal, with the exception of high solar zenith angles. In comparison, the coarse

particles had smaller influence on the measurements. In Figure 3.14 the dependence of the AMFs on the AOD is clearly depicted. The differences found in the AMFs calculated with AOD = 0.1 and higher values highlight the importance of using the right AOD in the retrieval. An underestimation of the AOD will lead to an overestimation of the VCs. Scenario F (aerosol layer extending to 2.0 km) is an exception to this statement as the AMF values do not vary much for different AODs.

In qualitative terms, the interpretation of the scenarios with the urban NO<sub>2</sub> profiles is quite similar. However, for the latter, the AMF values are smaller as the NO<sub>2</sub> is more concentrated at the surface where the satellite sensitivity is the smallest. This has already been illustrated in section 3.2.1. The shielding effect of aerosol is also more pronounced for the NO<sub>2</sub> urban profile than for the 1.0 km box, leading to an overall reduced effect of aerosol. Thus, the importance of atmospheric particulate matter is reduced if a more realistic NO<sub>2</sub> profile is assumed.

In section 3.3.2 results were presented for the scenarios where NO<sub>2</sub> and aerosol were well mixed in the same box layer. For such cases it was found that the aerosol enhanced the sensitivity of the measurements. When comparing those to the results obtained for the case with NO<sub>2</sub> simulated by the model and different aerosol layers, large differences were found. The measurement sensitivity was found to be high when the NO<sub>2</sub> and particles were lofted to an altitude of 2.0 km (AMFs from 0.81 to 1.50). On the other hand, if only the aerosol was at high altitudes and the NO<sub>2</sub> was kept close to the surface as in the “Avg Urb” profile, the resultant AMFs were much smaller (~50%). As it would be expected, because the modelled profile resembles the box profile of 600 m, the results were more similar, i.e., maximum difference found was of 7% (AOD 0.9 and SZA 70°), where the AMF for the first case is actually higher.

Clearly, in these particular circumstances, the aerosol effect is much smaller than before, and very close to zero in the case of typical background profiles for both the NO<sub>2</sub> and aerosol. Independently of its detailed shape, the presence of an aerosol layer tends to cover the NO<sub>2</sub> layer below thereby decreasing the sensitivity of the measurements to trace gas amounts close to the surface. Depending on the Sun position and the aerosol profile, small enhancements as well as reductions in sensitivity can occur. This emphasises the fact that the sensitivity of the measurements does not only depend on the vertical distribution or total load of the aerosol but the combined effect of both aerosol and NO<sub>2</sub> distribution. For coarse particles all the AMFs were smaller than for the case without aerosol, indicating that the aerosol might be preventing light from reaching down lower into the NO<sub>2</sub> layer close to the surface (or back from this layer to the satellite instrument).

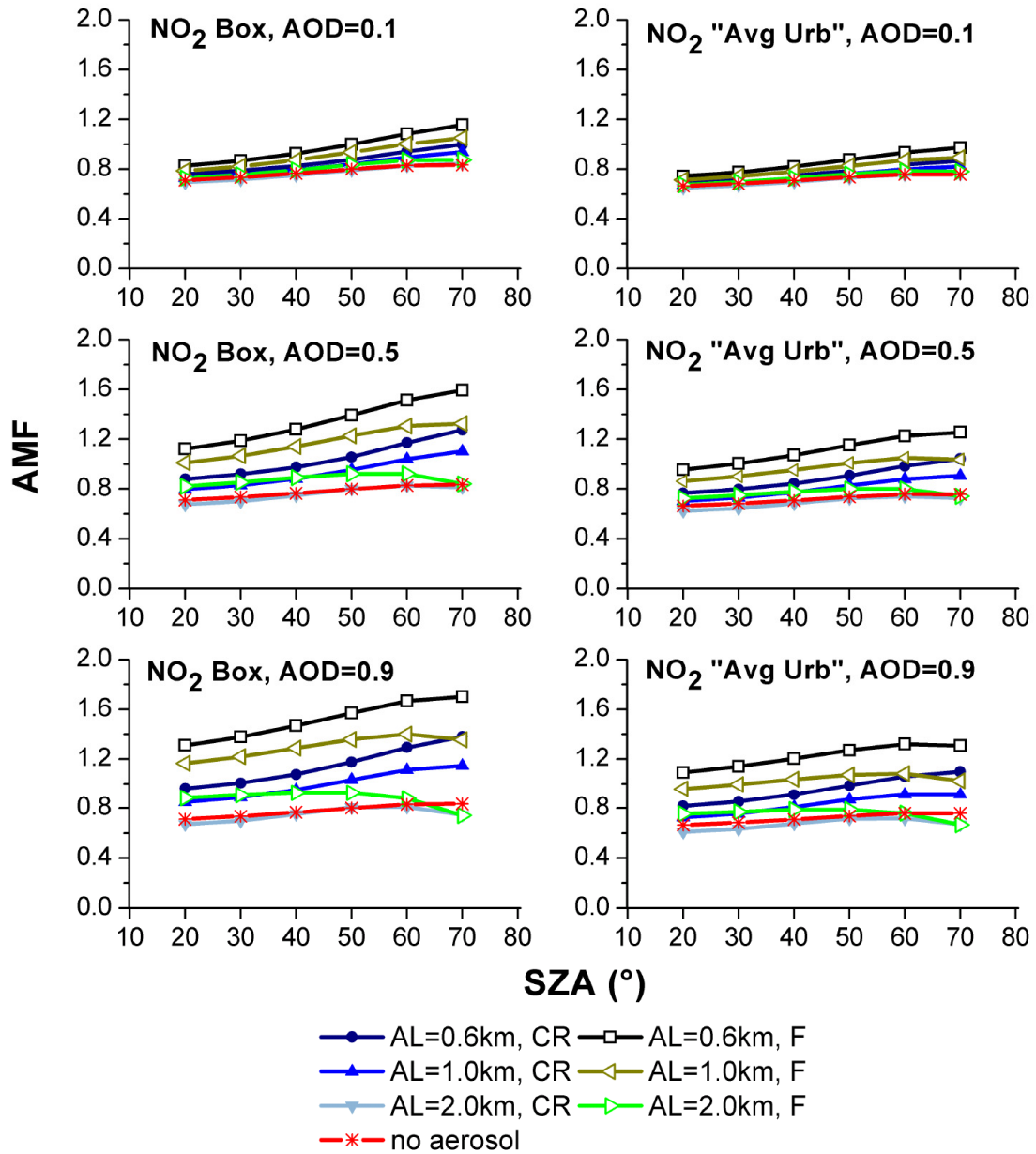


Figure 3.13 NO<sub>2</sub> air mass factors for a 1.0 km box NO<sub>2</sub> profile using no aerosol (red) and for the scenarios B, C and F (extension of aerosol layer (AL) from surface to 0.6, 1.0 and 2.0 km, respectively) calculated with the phase functions determined for coarse (CR) and fine (F) particles (optical properties taken from Creteil/Paris AERONET station) (left). AMFs determined at 440 nm, with surface reflectance = 0.03,  $\omega_0 = 0.93$  and different AODs: 0.1 (top), 0.5 (middle) and 0.9 (bottom). Same as before for the aerosol settings but using the average of modelled urban NO<sub>2</sub> profile ("Avg Urb") (right).

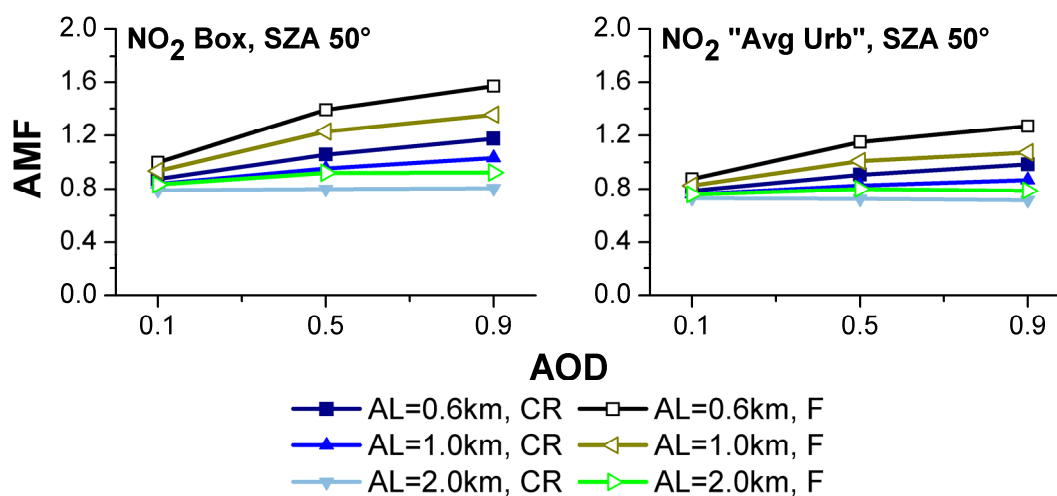


Figure 3.14  $\text{NO}_2$  air mass factors for a 1.0 km box  $\text{NO}_2$  profile using no aerosol (red) and for the scenarios B, C and F (extension of aerosol layer (AL) from surface to 0.6, 1.0 and 2.0 km, respectively), calculated with the phase functions determined for coarse (CR) and fine (F) particles (optical properties taken from Creteil/Paris AERONET station) (left). AMFs determined at 440 nm,  $\text{SZA} = 50^\circ$ , with surface reflectance = 0.03,  $\omega_0 = 0.93$  and different AODs: 0.1, 0.5 and 0.9. Same as before for the aerosol settings but using the average of modelled urban  $\text{NO}_2$  profile ("Avg Urb") (right).

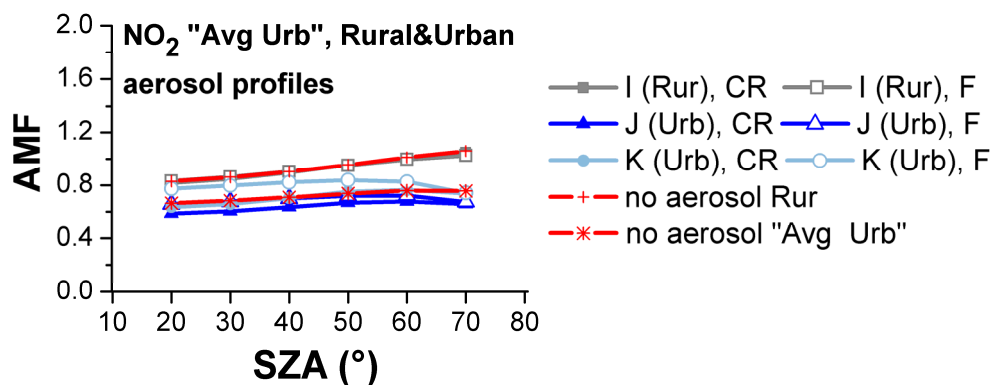


Figure 3.15  $\text{NO}_2$  air mass factors for no aerosol (red) cases (rural – Rur - and urban – "Avg Urb" –  $\text{NO}_2$  profiles from CHIMERE) and for the scenarios I (background – Rur –  $\text{NO}_2$  and aerosol vertical profiles), J and K (urban – Urb –  $\text{NO}_2$  and aerosol vertical profiles) calculated with the phase functions determined for coarse (CR) and fine (F) particles (optical properties taken from Creteil/Paris AERONET station). AMFs determined at 440 nm, with surface reflectance = 0.03,  $\omega_0 = 0.93$  (I, K) and 0.87 (J), and AOD = 0.07 (I), 0.40 (J) and 0.62 (K) (see Table 3.3).

In addition to what was described above, the model NO<sub>2</sub> profiles were also combined with aerosol profiles derived from measurements in rural areas (scenario I) and urban environments (scenarios J and K). The results are shown in Figure 3.15 for calculations assuming fine and coarse particles separately.

### **Desert dust and biomass burning**

The transport of dust and smoke plumes into European and certain Asian cities is not a rare event. These plumes are not only observed in the free troposphere but can, sporadically, also make a large contribution to the aerosol load measured in the boundary layer. Scenarios D, E and G (elevated aerosol layers from 0.6 to 1.0 km, 1.0 to 2.0 km and 2.0 to 3.0 km, respectively) are simplified representations of such events with aerosol being mostly concentrated at higher altitudes.

The results from these runs led to the same conclusions as before, i.e., an aerosol layer standing above the trace gas obstructs the observations from space (see Figure 3.16). A decrease of 6% to ~70% was observed when comparing the AMFs obtained for the scenario without aerosol to that with aerosol distributed from 1.0 to 2.0 km. This reduction was higher for larger aerosol load, i.e., optical depth of 0.9. If such plumes, standing in high altitudes, are not accounted for in the retrieval process, the tropospheric vertical columns are underestimated. The differences of the results for the cases with layers 1.0 to 2.0 km and 2.0 to 3.0 km (not presented here) were not significant. This indicates that the height of the aerosol layer is not so relevant for the sensitivity of the measurements when there is no overlap of the trace gas and aerosol layers. Contrary to this, in the case of aerosol mixed with NO<sub>2</sub> at the top of the layer (from 0.6 to 1.0 km), it was possible to notice that the particles do not interfere much with the measurements of the trace gas (cancelling of albedo and shielding effects). In fact, a slight enhancement (~10% maximum for 440 nm) of the columns is registered only when small particles are present. It should be noted however, that this is not the case for lower single scattering albedo (see next section). In the presence of highly absorbing aerosol, the shielding effect was dominant and a decrease of the AMF was found. Therefore, the cancelling between the two effects verified for these circumstances is naturally related to the definition of the aerosol properties. Furthermore, it is important to point out once more that the effect of aerosol on measurements of NO<sub>2</sub> present within a biomass burning plume can be quite different than in the case of NO<sub>2</sub> located in a boundary layer of 1.0 km height, as discussed here.

In a more realistic scenario, aerosol is also present close to the surface in urban areas. Therefore, profiles have been defined to include both the local plumes and those of long-range transport from biomass burning smoke or desert dust (e.g., scenarios L and P from Table 3.3). An example of these

## Sensitivity study

results is presented in Figure 3.17 for desert dust layers and fire plumes measured over different cities across the globe.

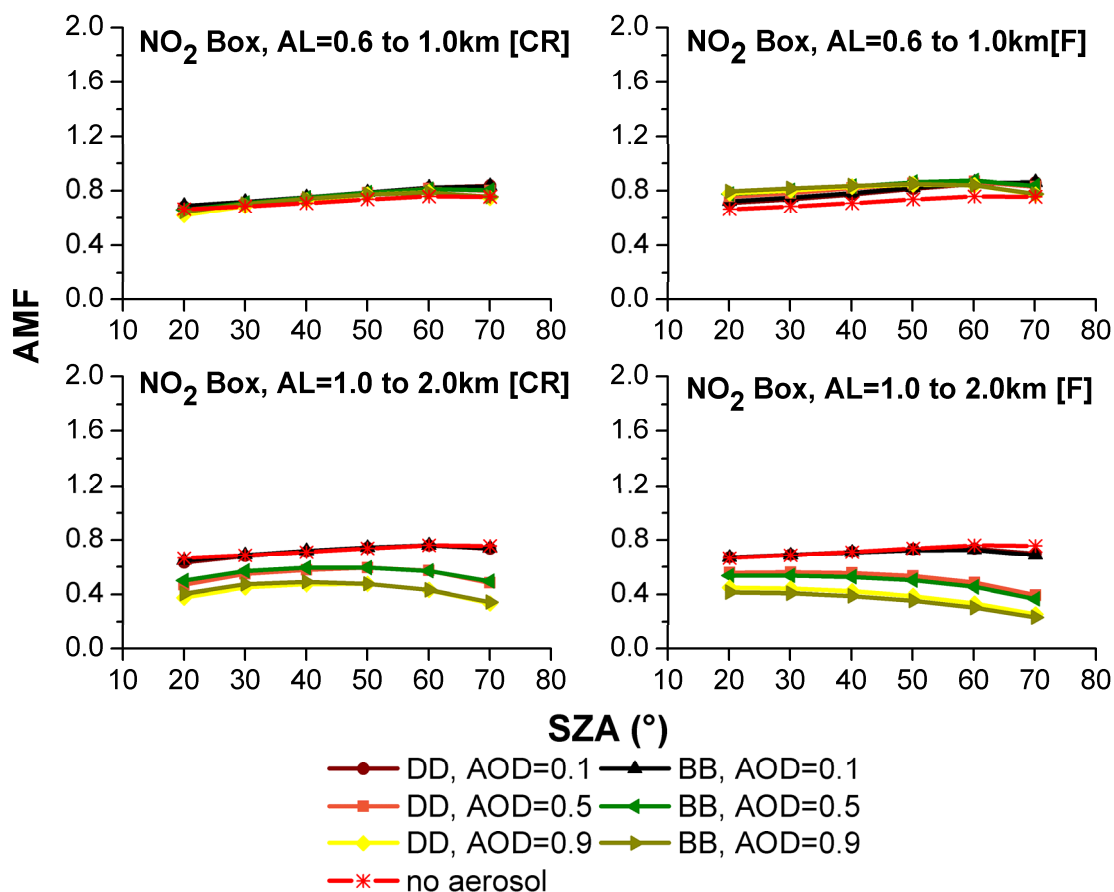


Figure 3.16 NO<sub>2</sub> air mass factors for a 1.0 km box NO<sub>2</sub> profile using no aerosol (red) and also for scenarios D (top) and E (bottom) (elevated aerosol layers (AL) from 0.6 to 1.0 km and 1.0 to 2.0 km, respectively) calculated with the phase functions determined for coarse (CR, left) and fine (F, right) particles (optical properties taken from Amazonian Forest/Brazil and from Saudi Arabia AERONET stations, respectively for the biomass burning (BB) and desert dust (DD) cases). AMFs determined at 440 nm, with surface reflectance = 0.03,  $\omega_0 = 0.93$  and different AODs: 0.1, 0.5, and 0.9.

As it can be seen from these findings, the effect of the aerosol layers transported above polluted areas can be quite different. Once more, the reduction in the sensitivity of the measurements, when compared with the “no aerosol” case, can be negligible or as large as ~62% (for scenario O). This pronounced reduction is caused by the combination of several factors: the large aerosol optical depth (AOD = 1.05); its absorbing nature ( $\omega_0 = 0.92$ ); and the small fraction of particles that are mixed with

the trace gas. This distribution of aerosol is the main difference between scenario L and O. The aerosol close to the surface present in scenario L may have contributed to the cancelling of the shielding effect and, therefore, explain the large disparity between the results of the scenarios. In the case of simulations M, N and P the AMFs are not so reduced mainly because of the lower aerosol loads. For the desert dust cases, only coarse aerosol was considered in the radiative transfer calculations but both fine and coarse (not presented here) particles were used for the biomass burning situations. The difference in the AMF, calculated with each of the aerosol types, is in the order of 20 - 25% with the higher values obtained for the runs with fine aerosol.

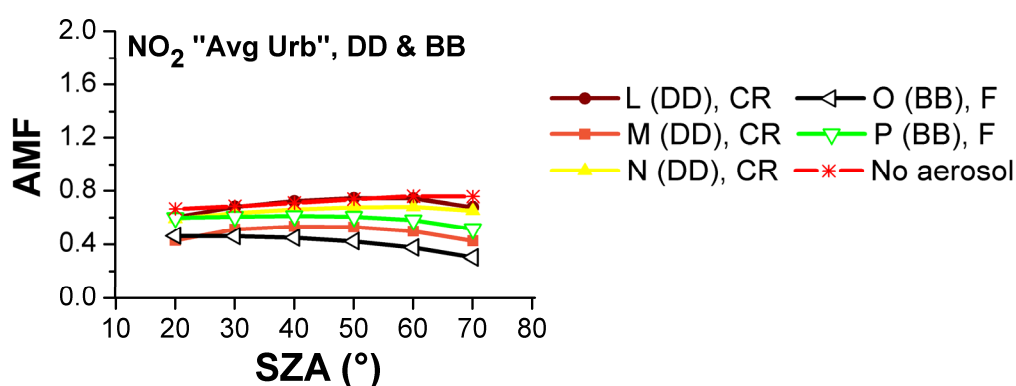


Figure 3.17 NO<sub>2</sub> airmass factors for urban NO<sub>2</sub> profile from CHIMERE using no aerosol (red) and also for scenarios L to P (measured aerosol profiles) calculated with the phase functions determined for desert dust (DD) coarse (CR) particles (optical properties taken from Saudi Arabia AERONET station) and for biomass burning (BB) fine (F) particles (optical properties taken from Amazonian Forest/Brazil AERONET station). AMFs determined at 440 nm, with surface reflectance = 0.03, and  $\omega_0 = 0.92$  (L, O, P) and 0.93 (N) (in scenario M  $\omega_0$  varies in height from 0.80 to 0.95), and AOD = 1.05 (L, O), 0.66 (M), 0.16 (N) and 0.42 (P) (see Table 3.3).

### c) Single Scattering Albedo (SSA)

After determining that the relative position of trace gas and aerosol was relevant for the AMF values, it was necessary to determine how much the assumption on the particle absorption property was influencing the calculations. The SSA assumed for most of the cases presented in the previous sections was fixed to 0.93, with exception for some of the scenarios with measured profiles. However, in reality, this particle property can vary quite a lot within the aerosol plume, or for different aerosol types (e.g., values given by Dubovik et al. (2002) fluctuated from 0.88 to 0.98). Therefore, the following section analysis the results obtained when this variable was altered in the radiative transfer

calculations to 0.80 and 0.95, the minimum and maximum of the values measured by Murayama et al. (2003) in scenario M.

As mentioned above, for all the scenarios including box profiles, the AMFs were calculated both for a single scattering albedo (SSA) of 0.93 and 1.0. As expected the values of AMF determined with non-absorbing aerosol were the highest. The lower values of AMFs for the scenarios with absorbing aerosol were an effect of the reduction of available light when such aerosol is present in the atmosphere. As illustrated above, highly absorbing aerosol can change the effective albedo and, consequently, decrease the measurement sensitivity, i.e., decrease the value of slant columns although, in reality, the  $\text{NO}_2$  does not change. The results for the calculations with different SSA values are first presented for simulations performed with the box profiles in scenarios B and D (Figure 3.18), C and F (Figure 3.19), followed by scenarios J and O (Figure 3.20). In the latter, the  $\text{NO}_2$  modelled profiles and measured aerosol vertical distribution were considered and further details on the settings can be found in Table 3.3.

As expected, the SSA can have a great impact on the calculation of the AMF. An increase in the absorbing properties of the aerosol (SSA decreases from 0.95 to 0.80) induced a general reduction of the AMF. While, for low aerosol load (in the scenarios with box profiles) this variation of SSA values resulted in a difference of the AMFs in the order of 5-12%, in a more polluted atmosphere with AOD of 0.9, the effect of SSA on the AMF was as high as 75%. Still, as it can be observed from the several graphs, the variation of the AMF values is, not only dependent on the aerosol amount, but also on the profiles considered. The changes of absorption by the particles distributed in lower layers (AL = 0.6 and 1.0 km) registered higher differences for the measurement sensitivity. On the other hand, the variation of AMFs for different SSA was smaller when considering higher aerosol plumes (AL = 0.6 to 1.0 km, and AL = 2.0 km). However, this small variation is quite important for these circumstances, because the presence of aerosol can contribute either to a reduction or enhancement of the measurement sensitivity, depending on how absorbing the particles are. While in the previous calculations, with  $\omega_0 = 0.93$ , no changes were noticed between the computations with or without aerosol, in this case, for  $\omega_0 = 0.80$ , the AMFs are smaller than the “no aerosol” case by ~28%. On the other hand, for the cases with  $\omega_0 = 0.95$  (not shown in the figures), the AMFs increase by a max. of 17% (scenario D) and 32% (scenario F). This suggests once more a competition of multiple scattering enhancements and shielding effect. These findings could be also observed for the results of scenarios J and O. Although for the latter, the aerosol present above the trace gas is so much that not even full scattering of light (by non-absorbing particles) would improve the sensitivity of the measurements.

Influence of aerosol on NO<sub>2</sub> air mass factors

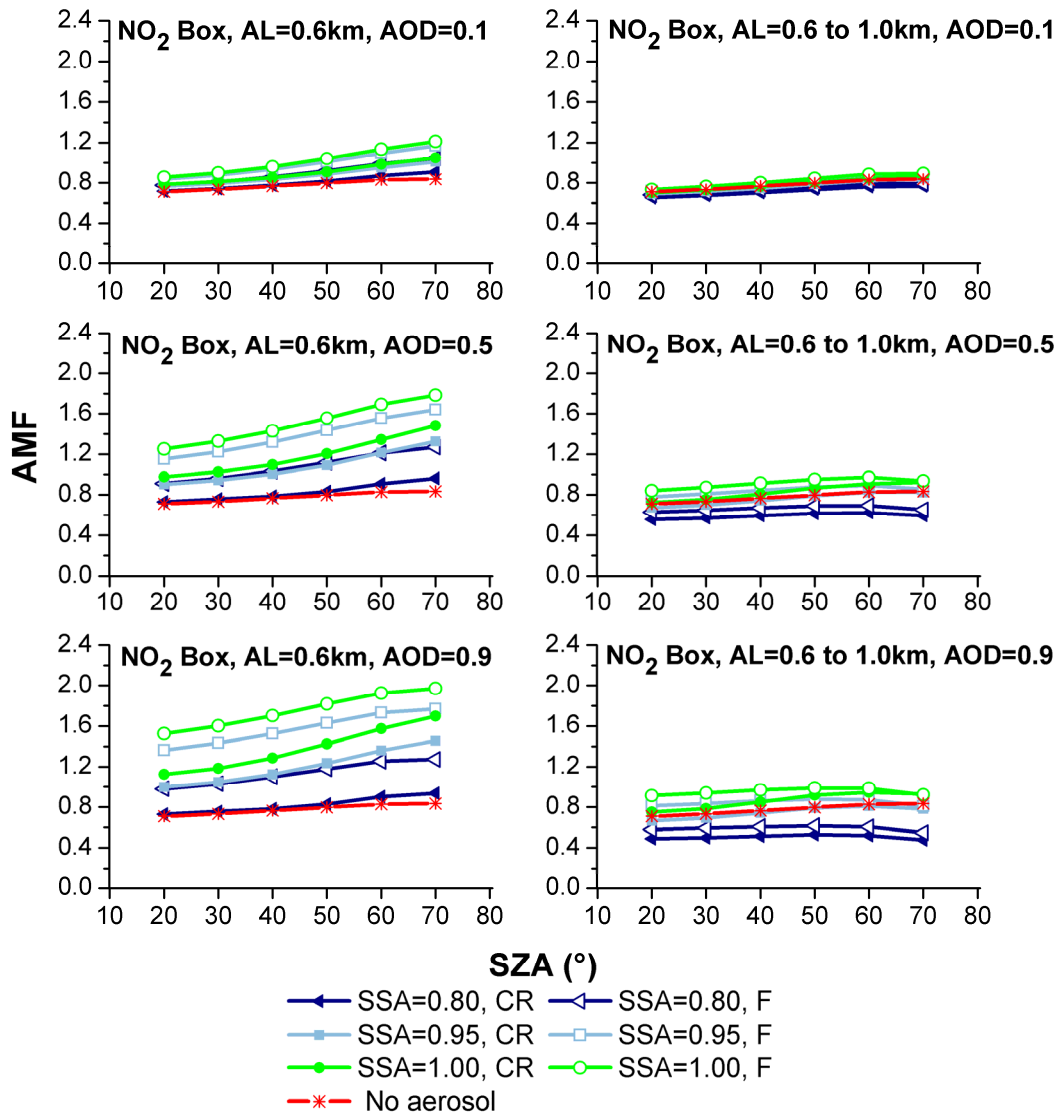


Figure 3.18 NO<sub>2</sub> air mass factors for simulations with different single scattering albedo (SSA,  $\omega_0 = 0.80, 0.95$  and  $1.00$ ) for (left) scenario B (NO<sub>2</sub> - 1.0 km box; aerosol layer (AL) - 0.6 km box) and (right) scenario D (NO<sub>2</sub> - 1.0 km box; aerosol layer (AL) – box from 0.6 to 1.0 km), calculated with the phase functions determined for coarse (CR) and fine (F) particles (optical properties taken from Creteil/Paris AERONET station). AMFs determined at 440 nm, with surface reflectance = 0.03, and different AODs: 0.1 (top), 0.5 (middle), and 0.9 (bottom).

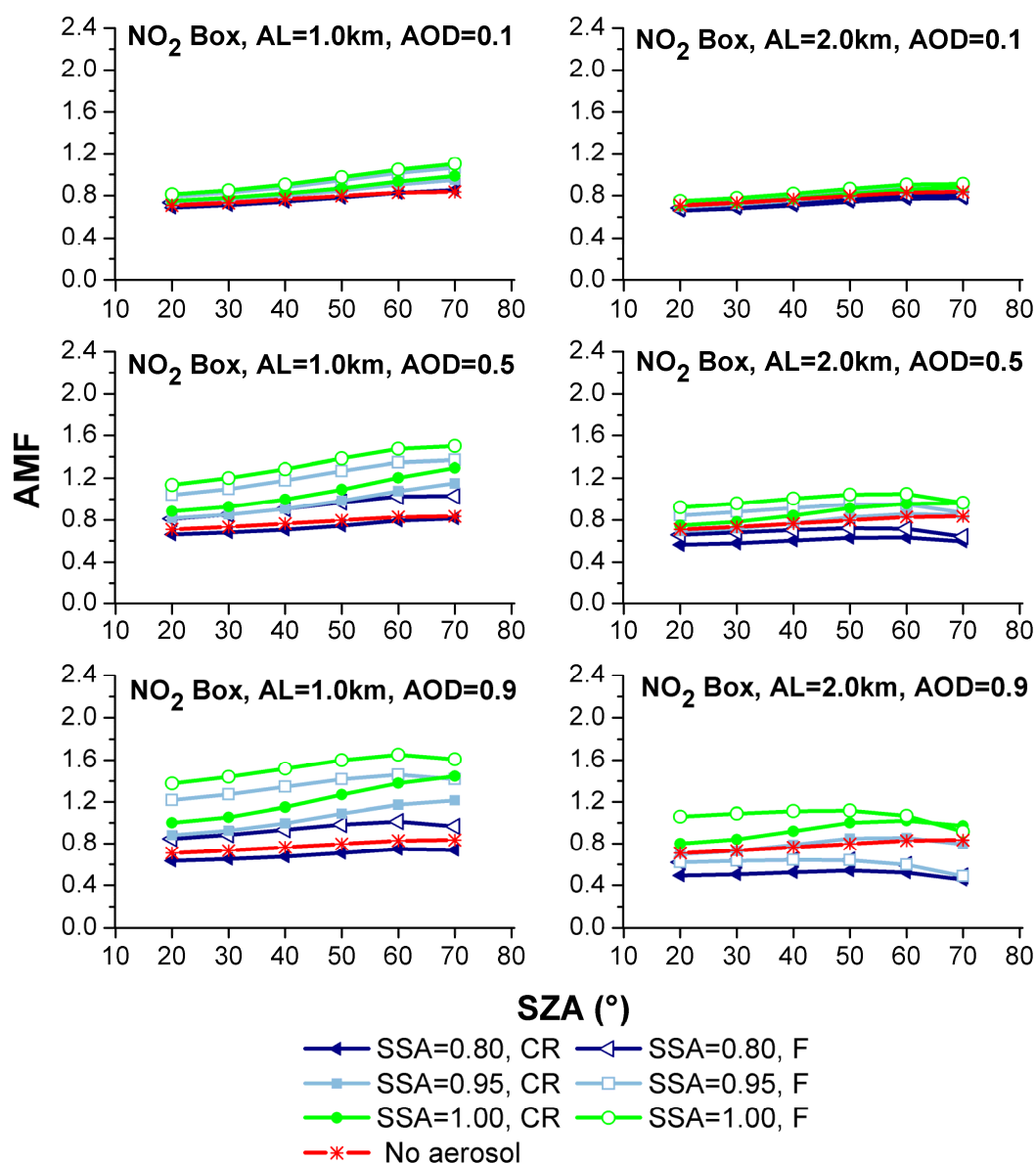


Figure 3.19  $\text{NO}_2$  air mass factors for simulations with different single scattering albedo (SSA,  $\omega_0 = 0.80, 0.95$  and  $1.00$ ) for (left) scenario C ( $\text{NO}_2$  and aerosol layer (AL) – 1.0 km box) and (right) scenario F ( $\text{NO}_2$  - 1.0 km box; aerosol layer (AL) – 2.0 km box), calculated with the phase functions determined for coarse (CR) and fine (F) particles (optical properties taken from Creteil/Paris AERONET station). AMFs determined at 440 nm, with surface reflectance = 0.03, and different AODs: 0.1 (top), 0.5 (middle), and 0.9 (bottom).

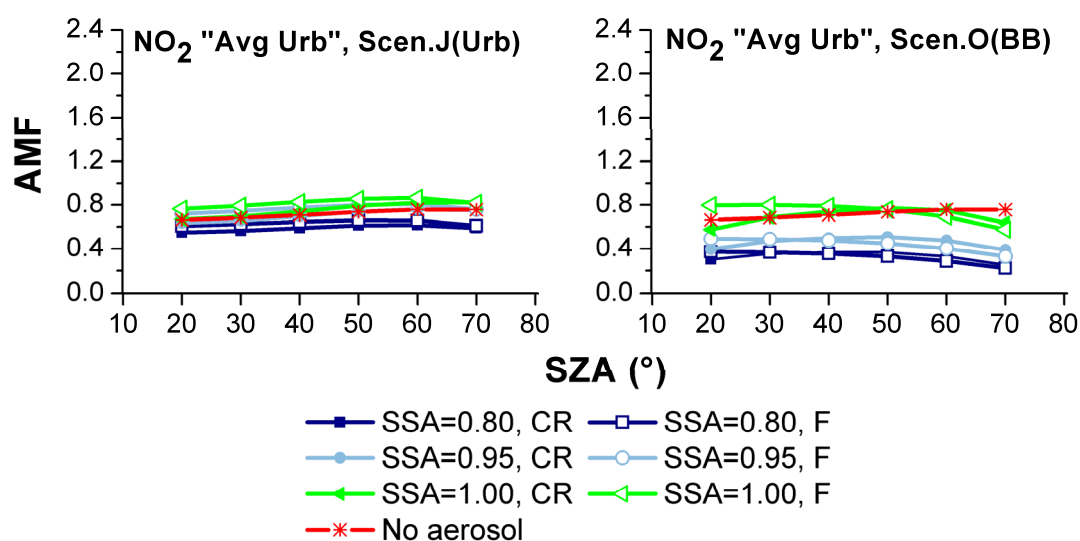


Figure 3.20 NO<sub>2</sub> air mass factors for different single scattering albedo (SSA,  $\omega_0 = 0.80, 0.95$  and  $1.00$ ) for scenario J (left) and O (right) (urban NO<sub>2</sub> profile from CHIMERE with urban (Urb) and biomass burning (BB) aerosol, respectively) calculated with the phase functions determined for coarse (CR) and fine (F) particles (optical properties taken from Creteil/Paris and Amazonian Forest/Brazil AERONET stations for scenario J and O, respectively). AMFs determined at 440 nm, with surface reflectance = 0.03, and the AOD = 0.40 (J) and 1.05 (O).

### 3.4 Summary

The interaction of atmospheric particles with the radiation will cause interference in the satellite observations. In fact, this study has shown that aerosol can have a significant impact on the retrieval of tropospheric trace gases using nadir measurements of backscatter radiation in the UV/visible range from space. In order to identify and quantify this influence, the effects of different aerosol parameters were investigated using both idealised and realistic scenarios, where the characteristics of particulate matter were change together with the vertical profile of NO<sub>2</sub>. Overall, a large variability in the results was observed with examples of both increasing and decreasing measurement sensitivity.

The most important factors for the satellite sensitivity are not only related to aerosol assumptions (physical and optical properties, and vertical profile), but also with the definition of NO<sub>2</sub> vertical distribution and surface reflectance. For the latter, changes of 90% on the AMF values were registered when this value was increased from 0.01 to 0.1 (and the presence of aerosol was included in the

## Summary

---

simulations). This influence becomes even more noteworthy in other scenarios where higher impact on the AMF was found. This illustrates how important it is to have accurate knowledge of the surface properties.

Regarding the aerosol properties, the factors identified as pivotal for the determination of tropospheric NO<sub>2</sub> vertical columns were the relative vertical distribution of aerosol and NO<sub>2</sub>, the AOD and the SSA. In addition, differences in the AMFs were found when applying either coarse or fine aerosol size distributions, with higher values for the latter. However, large differences were not evident when considering small variations of those main types.

The results indicate that, if, in the radiative transfer calculations, the NO<sub>2</sub> profile is based on an underestimated boundary layer height, then the tropospheric NO<sub>2</sub> column will be overestimated (and vice-versa). Variations of the vertical extension of a well-mixed layer can result in large differences, especially when the aerosol load is modest and in low Sun conditions. When the top height of trace gas and aerosol layers were increased from 1.0 to 2.0 km, a maximum difference of 26% of the airmass factors was found. However, even larger effects (up to 55%) were found in the case without aerosol, although the scenarios of clean atmosphere result in lower AMFs.

Aerosol mixed with the trace gas, even if not at the full extension of the layer, will, by means of increased effective albedo and multiple scattering, enhance the NO<sub>2</sub> signal. In contrast, any aerosol layer that lies above the trace gas will act as a shield, decreasing the sensitivity of the measurements. If an elevated aerosol layer is not accounted for, the computed NO<sub>2</sub> columns will be too small, and this underestimation can be quite large. Still, it is important to mention that these findings hold only for the SSA considered here (0.93), and that a dominant shielding effect is found in the event of highly absorbing aerosol mixed with the NO<sub>2</sub>. In any case, the magnitude of these effects will be determined by the relative vertical distribution of aerosol and NO<sub>2</sub>. A balance between enhancement and reduction of the signal will occur when the aerosol is both mixed with and above the NO<sub>2</sub> layer as might often be the case. As two examples, the AMF for a 1.0 km layer of NO<sub>2</sub> increases by a factor of two when mixed with an aerosol layer (600 m high from the surface - Scenario B) of AOD 0.9, while for the case with an aerosol layer of the same optical depth between 2.0 and 3.0 km (Scenario G) the AMF is reduced by ~78%.

Throughout the scenarios considered a high diversity of AMFs determined with different AODs can be perceived. From the results presented in the current thesis, it was possible to see that the variations of AODs are more relevant for the cases where low layers of NO<sub>2</sub> and aerosol (600 m) were considered. In contrast, a small effect was verified for scenario F where the aerosol layer has its top at 2.0 km, higher than the NO<sub>2</sub>.

The absorption properties of the particles also play an important role in the retrieval of the trace gas. The largest airmass factors were always obtained for the purely scattering aerosol ( $\omega_0 = 1.0$ ). A decreasing SSA always reduces the measurement sensitivity. For highly polluted scenes (AOD > 0.9) the airmass factor was increased by, on average, a factor of 1.5 when the single scattering albedo is modified from 0.80 to 0.95.

In a second stage of the sensitivity study, more realistic vertical profiles were applied: NO<sub>2</sub> vertical distribution was based on CHIMERE model simulations for Paris and surroundings, and aerosol characteristics taken from measurements, mostly performed at ground-based lidar stations. In these conditions, a much smaller effect of aerosol was observed, especially in the urban cases (scenarios I to K), where the AMFs vary only by ~7% on average. Nonetheless, it is important to highlight that this moderate impact does not correspond to situations of highly polluted scenes, as those of megacities, where AOD can be much higher than 0.9. Large decreases of the sensitivity of the measurements were found only for aerosol layers that are elevated or expand from surface to higher altitudes in the atmosphere. These situations usually correspond to aerosol plumes from biomass burning events, desert dust storms (scenarios L to P), or volcanic eruptions (as it will be seen in the following chapter).

This study shows that, in order to use satellite measurements of trace gases, namely NO<sub>2</sub>, to analyse atmospheric composition, improved knowledge of the aerosol properties is required. These include the vertical profile, AOD, size distribution and also the scattering/absorption properties of the particles. In addition, not only aerosol data is required for an upgrade of the tropospheric columns retrieved from satellite measurements. As it was demonstrated in this analysis, assumptions on the NO<sub>2</sub> vertical distribution also have an impact on the calculations. The exact shape of the NO<sub>2</sub> profile in different locations is still rather unknown, which makes the use of typical profiles as *a priori* assumptions a complex approach. The solution might be a conjugation between measurements and data from model simulations that can provide information to define *a priori* datasets for the radiative transfer calculations. Static climatological assumptions that are often applied can be replaced by more up-to-date data that is more suitable to describe the measurement conditions. Through this method, spatial and temporal variability can be accounted for, improving the retrieval algorithm for tropospheric NO<sub>2</sub> columns.



# 4

## Case study – Eyjafjallajökull eruption

On the 14<sup>th</sup> of April 2010, the eruption of the Icelandic volcano Eyjafjallajökull, also known as Eyjafjalla or Eyjafjöll, which had started in March 2010, entered a second phase. At this stage, a large amount of ash was released, and this cloud was transported towards Central Europe by north-westerly winds (see Figure 4.1). The consequences of this were unprecedented, causing the shutdown of most of Europe's airspace from the following day onwards until the 20<sup>th</sup> of April. This disruption of flights resulted in worldwide disturbances and had major impact on many aspects, mostly on the financial level. For this reason, and because of its rarity, this event was widely covered by the scientific community that followed closely the evolution of the eruption with the objective to characterise the ash plume and its transport. This detailed description of the event provided sufficient data to also analyse in detail what happened to the satellite observations during this period where ash was dispersed above the polluted regions in Europe. The sensitivity study presented in the previous chapter showed that tropospheric NO<sub>2</sub> airmass factors vary much depending on aerosol properties and atmospheric distribution. These changes of AMFs represent how the trace gas columns measured by satellite instruments are affected by the presence of aerosol at the time of the measurement. In this chapter, the impact of the Eyjafjallajökull's ash cloud on the NO<sub>2</sub> measurements will be studied, using data from a simulation done at the Rhenish Institute for Environmental Research (RIU) with the EURAD model. This model run was performed specially to reproduce this event, i.e., the advection

and properties of the ash cloud. These results were, therefore, ideal to study the mentioned event in particular, since chemical transport models do not usually account for volcanic eruptions in the standard runs.

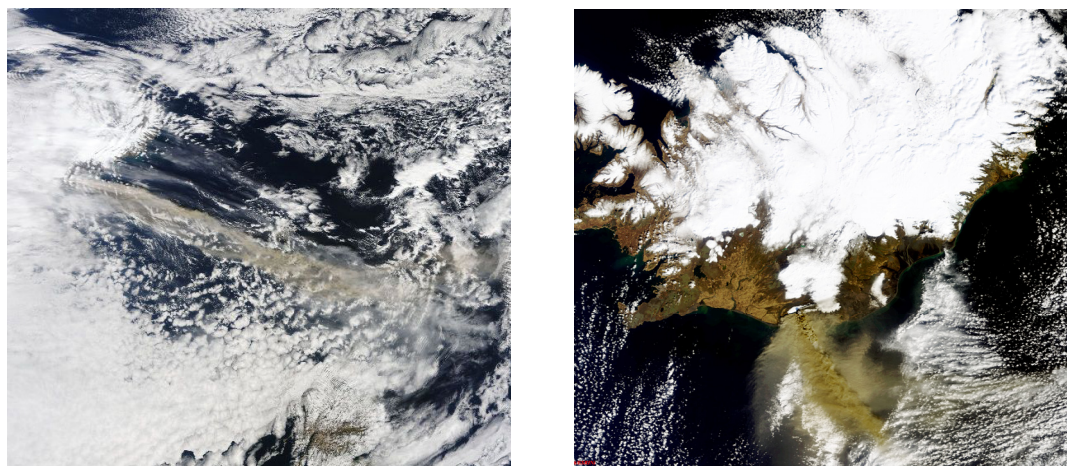


Figure 4.1 RGB images captured by the MODIS instrument on NASA's Terra satellite (left) and observed by the MERIS instrument on ESA's ENVISAT satellite (right), for the 15<sup>th</sup> and 17<sup>th</sup> April 2010, respectively. The ash plume from Eyjafjallajökull volcano is clearly identified in the direction to Europe. (Source: MODIS image created by NASA/MODIS Rapid Response Team (Gutro, 2010), and MERIS provided by ESA (2010).)

## 4.1 The EURAD model

### 4.1.1 General overview of the CTM

The EUROpean Air pollution Dispersion (EURAD) model is a 3D chemical transport model (CTM) that serves mostly the scientific community, but also provides information for the general public. Developed by the group at RIU, at the University of Cologne, it is mainly designed to assess air quality conditions and can be used for policy support in subjects related to smog and acidification. In addition, chemical and nuclear emergencies are also simulated by EURAD, as it happened for the recent event of radioactive vapour emitted from the nuclear accident at the Fukushima power plant north-east of Tokyo. Regular model simulations are performed for Europe (at different spatial resolutions) and output of concentrations, deposition fluxes and exposure is produced for the troposphere (up to 100 hPa). Chemical species simulated include, among others, sulphur dioxide, nitric oxide, nitrogen dioxide, ozone and volatile organic compounds. In addition, particulate matter is predicted as total suspended particles or particulate matter of different sizes, e.g.,  $PM_{2.5}$  or  $PM_{10}$ .

Several physical, chemical and dynamical processes that influence atmospheric composition are simulated, including emission, transport, diffusion, chemical transformations and deposition (wet and dry) of trace gases and aerosol (Hass, 1991; Ackermann et al., 1998; M. et al., 2004). The model system is composed of three modules: EEM (EURAD Emission Module); MM5 (Meteorological Model Version 5, <http://www.mmm.ucar.edu/mm5/mm5-home.html>) and EURAD-CTM. The MM5 uses initial and boundary conditions from ECMWF-data. EMEP data is normally the basis for emission values, but data from different sources can also be included in the emission database. In the case of nitrogen oxides, emission data of different sources are provided in the form of NO<sub>x</sub> which is then split into NO and NO<sub>2</sub>. These compounds are then included in the transport and chemistry schemes of the model. NO<sub>2</sub> is considered to be emitted from two different sources: traffic and other mobile sources, with amounts that correspond to 20% and 10%, respectively, of NO<sub>x</sub> emission values. To improve the model performance, data from several sources are assimilated, and for the NO<sub>2</sub>, this includes in-situ data from the EEA and various national environmental protection agencies, and also satellite observations from SCIAMACHY. More details on the emission definitions can be found at Memmesheimer et al. (1991). The chemical mechanisms employed are the RADM2, its successor RACM (Geiger et al., 2003), and the aerosol mechanism MADE (Modal Aerosol Dynamics model for EURAD/Europe, Ackermann et al., 1998). The chemical mechanism contains 105 reactive species (including intermediates and oxidation products needed for production of secondary organic aerosol) treated in 275 chemical reactions.

MADE provides aerosol properties, e.g., size distribution, number concentration, volume, and chemical composition in mass. In the simulations, several processes influence the atmospheric particles, including, for example, the generation of primary aerosol and its aging, as well as the formation of secondary aerosol *via* aerosol and gas phase interactions. The latter is treated by the module Secondary ORGanic Aerosol Module (SORGAM, Schell et al., 2001). The transformation processes considered are nucleation, coagulation, condensation and evaporation. Particulate matter is divided into three lognormal modes: Aitken and accumulation modes that belong to the category of fine particles, and the coarse aerosol. Coagulation controls the relation between the two smaller modes, but growth *via* condensation may occur for each mode. The two smaller modes are secondary non-organic and organic (anthropogenic and biogenic) aerosols, and primary organic and elemental carbon (Schell et al., 2001). Unspecified material of anthropogenic origin is accounted for in all three modes. The sources for coarse particles also include sea-salt (Monahan et al., 1986; Mårtensson et al., 2003) and mineral dust (Nickovic et al., 2001). The thermodynamic model used to solve the particle chemistry in the equilibrium of the H<sup>+</sup> – NH<sub>4</sub><sup>+</sup> – NO<sub>3</sub><sup>-</sup> – SO<sub>4</sub><sup>2-</sup> – H<sub>2</sub>O system is described by Friese and Ebel (2010). The dry deposition of aerosol species and their gravitational settling velocity are different for each of the modes considered, and this is parameterised using a resistance model (Ackermann et

al., 1998). Wet deposition, on the other hand, is considered in different ways and is proportional to the wet removal of sulphate. Particles belonging to the accumulation mode are 100% absorbed into the cloud water, while cloud droplets will scavenge the Aitken particles that formed interstitial aerosol. Data from this model were produced specifically for the volcanic eruption of Eyjafjallajökull whose ash affected the atmosphere above Europe. Further details on the data used are provided in the following section.

A permanent model evaluation of chemical and meteorology data is performed with offline observations and data assimilation techniques, for the boundary layer, free troposphere and lower stratosphere (Elbern et al., 1997; M. et al., 2004). The model has supported several field campaigns by forecasting and analysing the distribution of chemical species in the boundary layer. In addition, the EURAD group has been involved in various previous and ongoing activities of the European environmental project EUROTRAC (Hass et al., 2003), GEMS and MACC which account for model intercomparison exercises.

Additional information on the model system can be found at the model's website <http://www.eurad.uni-koeln.de/>.

### 4.1.2 CTM settings for the volcanic ash simulations

The EURAD (version 4.6) model provides hourly output data and, for this analysis, the simulation results for the hours 09:00, 10:00 and 11:00 UTC, for the days 16, 17 and 18 of April 2010 were used. The data<sup>2</sup> were generated for Europe, on a Lambert conformal projection with a spatial resolution of 15 km. Values were given for 23 vertical layers, following sigma coordinates, up to an altitude of 100 hPa. The lowest kilometres of the atmosphere, including the boundary layer, are well represented by roughly 15 layers. For this study, the relevant output were the volume mixing ratios of NO<sub>2</sub> (see example in Figure 4.2) and the aerosol mass concentrations for the species described above, with the exception of mineral dust that was replaced by volcanic ash in this particular model run.

This simulation was performed especially to reproduce the volcanic ash emitted during the eruption of the Icelandic volcano Eyjafjallajökull that had a peak of emissions in the period of 14<sup>th</sup> to 20<sup>th</sup> of April 2010. For these computations, emission data from the TNO inventory was used, with base year of

---

<sup>2</sup> Information regarding the special model settings was provided by E. Friese, personal communication.

2005, on a  $0.125^\circ \times 0.0625^\circ$  resolution. The order of magnitude of volcanic ash emission strength was estimated with the volcanic plume model Plumeria (Mastin, 2007) and later adjusted, by poor man's inversion, with measurements from Mount Zugspitze/Hohenpeissenberg, a GAW station, to an initial value of  $2.5 \times 10^6$  g/s. The injection height of the plume was taken from VAAC reports (London Volcanic Ash Advisory Centre), available for every 6 hours, and from daily reports on volcanic activity of the Icelandic Meteorological Office (Petersen, 2010). These were also the sources for coarse estimations of emission reduction during periods of lower volcanic activity. Approximately 70% of the volcanic ash emissions were distributed over the upper three model layers of vertical plume extension. In this particular run, all the particles of the volcanic ash were assumed to have a size within the range of coarse mode. The volcanic ash was treated as an inert species, i.e., with similar behaviour as mineral dust, being subject to advection, vertical diffusion, dry deposition and cloud interaction processes, such as wet deposition and vertical redistribution within clouds, but no chemical changes.

## 4.2 EURAD data for SCIATRAN input

The purpose of this study was to analyse how the presence of volcanic ash in the atmosphere affected the observations of tropospheric trace gases by satellite instruments. The analysis was focussed on the retrieval of  $\text{NO}_2$  and on the particular event of April 2010, when a plume of volcanic ash from the Eyjafjallajökull Icelandic volcano was transported above Europe. Similar to what was done in the previous chapter,  $\text{NO}_2$  tropospheric AMFs were calculated with the latest version of the radiative transfer (RT) model SCIATRAN 3.1 (Rozanov et al., to be submitted, 2011). The computations were performed on a vertical grid of 95 layers from surface to the top of atmosphere defined as 100 km. A very fine grid, from sea level up to  $\sim 13$  km, was used to assure that the vertical profiles of trace gas and aerosol were well described. Higher accuracy of the radiative transfer calculations is obtained when a finer grid is used because the profiles of trace and aerosol are better described. Calculations were performed for the wavelengths 437.5 and 461 nm, in nadir observation, and at seven solar zenith angles (SZA, from  $10^\circ$  to  $70^\circ$  in steps of  $10^\circ$ ). SCIATRAN was operated using the discrete ordinate method for solution of the RT equation, in plane-parallel geometry, accounting for full multiple scattering effects, but without including polarisation. As atmospheric scenario, the pressure and temperature of the model layers were used in the lowest kilometres. However, above the model top, scaled US standard (1976) atmospheric pressure and temperature profiles were considered. The surface reflectance was set to 0.05. This was kept constant to assure that changes in the AMFs were not resulting from different surface properties.

As mentioned in the previous sections, for this study, the NO<sub>2</sub> and aerosol description in the RT model were based on results from a particular simulation from the EURAD model, with special focus on the mentioned volcanic eruption. The data available on an hourly basis (per model cell) were interpolated to the overpass time of GOME-2 to better reproduce the measurement conditions. The determination of the overpass time is based on the assumption that the model grid box is at the centre of GOME-2's swath.

The model data had to be adapted to be used as input for SCIATRAN. This process is described in the following sections. It is important to highlight that the results presented in this chapter do not correspond to the full model domain, as illustrated in Figure 4.2 and Figure 4.3, but only to the region of {40°N-60°N 10°W-20°E}. The reason for this area restriction was mainly related to the computation time required to perform calculations for the full domain. Furthermore, as the goal of the study was to examine the impact on NO<sub>2</sub> measurements, it was mostly relevant to determine AMFs for polluted regions where measured vertical columns of NO<sub>2</sub> might be affected by the presence of ash.

### a) Adaptation of NO<sub>2</sub> profiles

The NO<sub>2</sub> vertical profiles used in this study were adapted from the EURAD model output. The volume mixing ratios provided for the various model layers (see example for the lowest layer in Figure 4.2) were then used to define the trace gas profile in the RT model. Although the values were provided to the top of the model, only the values up to 7 km, above surface, were considered. This step was necessary to assure that only tropospheric NO<sub>2</sub> was being considered in the RT calculations. This profile was then interpolated to the finer altitude grid used in the SCIATRAN model. The resulting vertical columns for the domain of interest in this analysis are presented in Figure 4.4. From this figure, the high resolution of the model where isolated sources of pollution are visible, as it is the case for the Spanish cities Madrid and Barcelona, as well as Milan and the Po-valley in Italy. In addition, also the cleaner and high regions, like the Alps and Pyrenees, can be identified, providing further confidence to the model simulations. The NO<sub>2</sub> patterns are very different on the three days analysed not only in regard to vertical columns but also in respect to its vertical distribution (see examples in Figure 4.16, Figure 4.17 and Figure 4.18). As it was illustrated in the previous chapter, this is an important factor for the analysis of the results

### b) Compilation of aerosol components

To reproduce the interaction between atmospheric particles and radiation it is important to describe the optical properties of the particulate matter present in the atmosphere at different heights. In the

## Case study – Eyjafjallajökull eruption

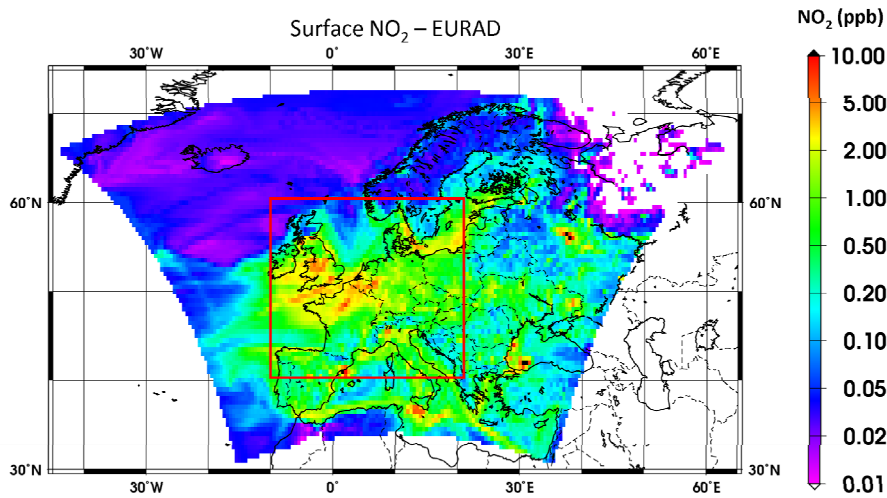


Figure 4.2 NO<sub>2</sub> concentrations from the model EURAD, at surface level, on 16<sup>th</sup> of April 2010, at 10:00 UTC. The results are presented for the full domain of the model. The region used for the presented study is illustrated with the red square.

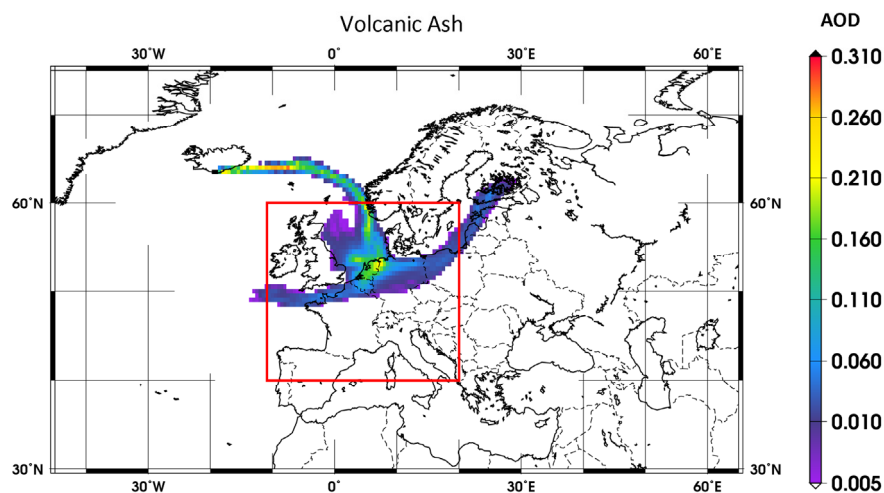


Figure 4.3 Volcanic ash AOD, at 437.5 nm, derived from aerosol mass concentrations from the model EURAD, on 16<sup>th</sup> of April 2010, at the time of GOME-2 overpass. The results are presented for the full domain of the model. The region used for the case study is illustrated with the red square.

SCIATRAN model this can be done in several ways and the method selected was to use extinction coefficients and single scattering albedo values for individual layers. In addition, specific phase functions were determined for the plume at different heights. The aerosol optical properties were described according to the aerosol modes of a certain aerosol species (hereafter referred to as aerosol types). It is important to point out that, although mass concentrations were available for SOA from different sources (anthropogenic and biogenic), the optical properties and particle characteristics of

## EURAD data for SCIATRAN input

these two aerosol groups were considered to be similar. Likewise, the same approach was taken for primary organic aerosol, elemental carbon and other primary aerosol from anthropogenic sources. Properties of the species denoted as "primary", in the following sections, were attributed to the aerosol from these three sources. In addition, marine aerosol was considered to be mainly sea-salt.

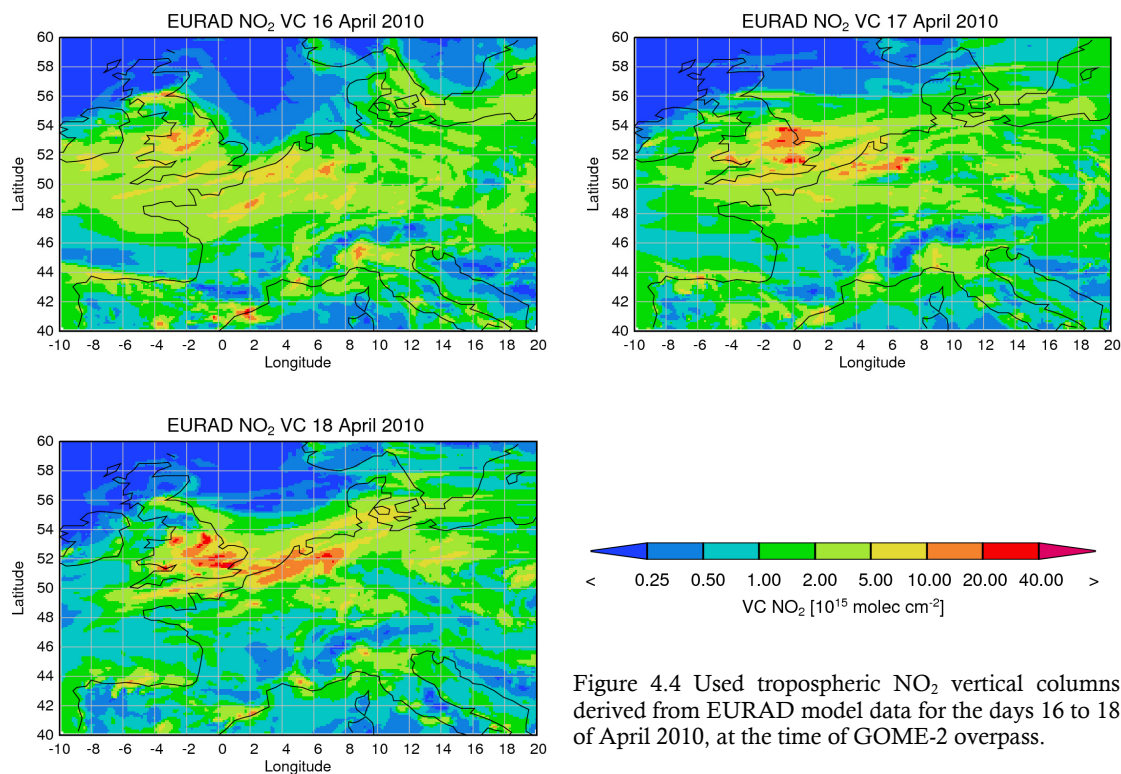


Figure 4.4 Used tropospheric NO<sub>2</sub> vertical columns derived from EURAD model data for the days 16 to 18 of April 2010, at the time of GOME-2 overpass.

The extinction coefficients ( $k_{ext}$ ) were determined for each aerosol type, at the 23 model layers, according to the equation introduced in chapter 2, and analogously for the scattering coefficient ( $k_{scat}$ ):

$$k_{ext} = N \sigma_{ext} \quad \text{and} \quad k_{scat} = N \sigma_{scat} .$$

The number density  $N$  was determined by:  $N = \frac{m}{\rho \bar{V}}$ , where

$m$  is the mass of the correspondent aerosol type provided in the model output (for a specific layer),  $\rho$  the density (see Table 4.1) and  $\bar{V}$  the volume of the aerosol type averaged with respect to its size distribution. The latter was determined with the program *spher.f* developed by M. Mishchenko and freely available at <http://www.giss.nasa.gov/staff/mmishchenko/brf/>. This software is based on the Mie theory and computes light scattering providing the corresponding phase functions, as well as the extinction and scattering cross sections for the different aerosol types. The assumed size distribution parameters of the three aerosol modes were taken from the EURAD definitions and are presented in Table 4.2. In addition, the refractive indices for the different species were based on several sources as explained in Table 4.3. Although these properties were described for 440 nm, the extinction and

scattering coefficients (and phase functions described below) of the various aerosol types were determined for 437.5 and 461 nm, assuming that the variation of the optical properties at this wavelength range is negligible.

The total extinction and scattering coefficients of the aerosol layer correspond to the sum of the coefficients for each aerosol type. With these values it was possible to compute single scattering

albedo (SSA,  $\omega_0$ ) values for a specific layer (equation (2.29) from intro):  $\omega_0 = \frac{k_{scat}}{k_{ext}}$ .

Finally, the last step of the preparation of input settings was the interpolation of the total extinction coefficients and SSA into the finer layering grid used for the RT calculations.

A simple picture of the plume and aerosol amount is provided by the aerosol optical depth as shown in Figure 4.5. AOD for total aerosol and for ash alone is presented to highlight the contribution of the volcanic ash to the total optical depth of the atmospheric particles. This parameter is calculated by:

$$\tau(\lambda) = \int_0^h k_{ext}(\lambda, z) dz \text{ (see section 2.4), where } h \text{ is the height at the considered top of atmosphere.}$$

Table 4.1 Density ( $\rho$ ) for the different aerosol species used in the conversion of mass concentrations to extinction coefficients. The values for all the species were taken from Péré et al. (2010) and references therein, with exception of the value for the ash that was based on measurements of ash from this volcano reported by Schumann et al. (2011). The density for primary aerosol species was taken as an average of values reported for organic and black carbon.

Aerosol Species	Density (g/cm <sup>3</sup> )
NH <sub>4</sub> <sup>+</sup>	1.70
NO <sub>3</sub> <sup>-</sup>	1.70
SO <sub>4</sub> <sup>2-</sup>	1.84
SOA	1.50
Primary	1.50
Sea-salt	2.10
Ash	2.60

## EURAD data for SCIATRAN input

---

Table 4.2 Size distribution parameters ( $r$  and  $\sigma$ ) for the different aerosol modes used in the *spher.f* program. These values were taken according to the definitions of the EURAD model.

Aerosol mode	$r$ ( $\mu\text{m}$ ), $\sigma$
Aitken	0.005, 1.7
Accumulation	0.035, 2.0
Coarse	0.5, 2.2

Table 4.3 Refractive indices for the different aerosol species considered in the *spher.f* program. The values for all the species were taken from Péré et al. (2010) and references therein, with exception of the value for the ash that was based on measurements of ash from this volcano reported by Schumann et al. (2011). The refractive index for primary aerosol species was taken as an average of organic and black carbon.

Aerosol Species	Refractive index (440 nm)
NH <sub>4</sub> <sup>+</sup>	1.52 - <i>i</i> 0.0005
NO <sub>3</sub> <sup>-</sup>	1.53 - <i>i</i> 0.006
SO <sub>4</sub> <sup>2-</sup>	1.44 - <i>i</i> 1.0E-8
SOA	1.45 - <i>i</i> 0.001
Primary	1.66 - <i>i</i> 0.285
Sea-salt	1.45 - <i>i</i> 0.0056
Ash	1.59 - <i>i</i> 0.004

Light scattering distribution is described by phase functions. In this study these were determined for each of the aerosol types available from EURAD output (Figure 4.6). As already mentioned, the *spher.f* program from M. Mishchenko (<http://www.giss.nasa.gov/staff/mmishchenko/brf/>) was used to determine the Legendre expansion coefficients required as input in the RT model SCIATRAN.

From Figure 4.6 below, it is evident how scattering by the extremely small particles (phase functions are all identical and not differentiable) is similar to Rayleigh scattering. The aerosol belonging to the accumulation mode presents a stronger forward peak, with a minimum within  $\sim 127^\circ$  scattering angle. An exception to this behaviour is the shape of the phase function of primary aerosol that does increase at large scattering angles. Coarse particles also have very unique phase functions in comparison to

## Case study – Eyjafjallajökull eruption

those of the smallest size ranges. The phase function for primary aerosol is, once more, the most distinctive one, while particles of ash and sea-salt tend to scatter light in a more comparable way, most probably because of the more similar refractive indices. For those, likewise to what occurs for the accumulation mode, the phase functions show a minimum at  $125^\circ$  and  $129^\circ$  for sea-salt and ash, respectively, which indicates the strong forward scattering of light by particles of this type.

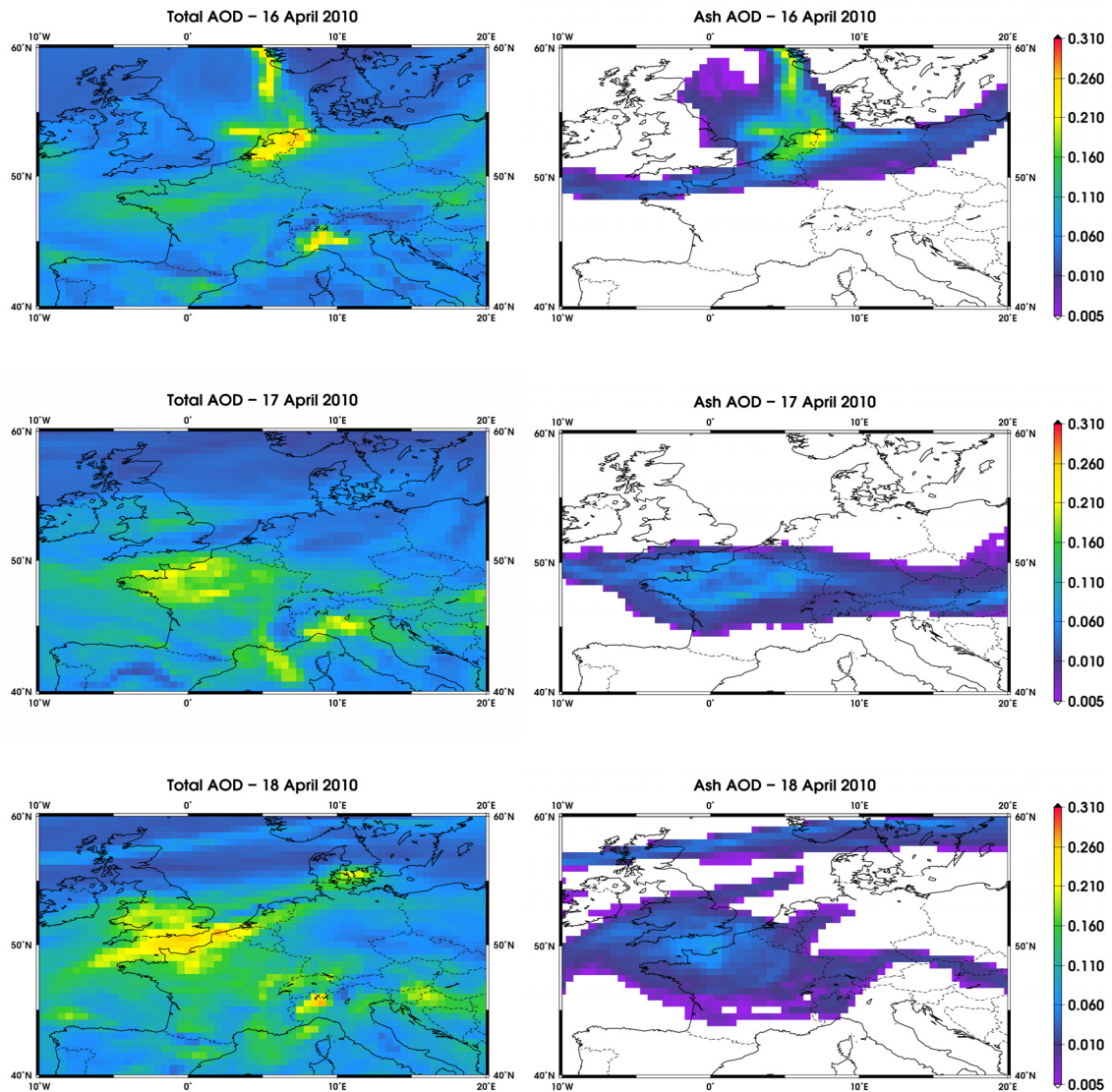


Figure 4.5 AOD, at 437.5 nm, for total aerosol (left) and volcanic ash (right) derived from the aerosol mass concentrations simulated by the EURAD model, for the period of 16<sup>th</sup> to 18<sup>th</sup> (top to bottom) of April 2010, in Europe (in the region of interest for this study).

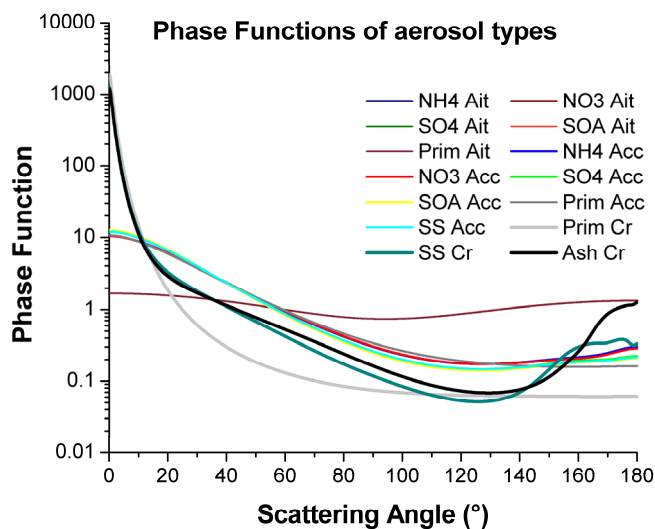


Figure 4.6 Phase functions determined for each aerosol type, at 437.5 nm: the different size modes (Aitken (Ait), accumulation (Acc) and coarse (Cr)) for the various aerosol species (ammonium ( $\text{NH}_4^+$ ), nitrate ( $\text{NO}_3^-$ ), sulphate ( $\text{SO}_4^{2-}$ ), secondary organic aerosol (SOA), primary aerosol (Prim), sea-salt (SS) and volcanic ash).

The chemical composition of volcanic ash does change with time and for different eruptions. Consequently, the size distribution (e.g., Prata and Grant, 2001) and optical properties of the particles will also vary (different elements have different refractive indices (Pollack et al., 1973)). Therefore, the prediction of their optical properties can be quite challenging. For this investigation, data used were based on measurements performed for the volcanic ash emitted from the Eyjafjallajökull (Schumann et al., 2011). However, the values reported correspond to the period between the 19<sup>th</sup> of April and 18<sup>th</sup> of May 2010, just after the period considered in this analysis. Additionally, the size of the ash particles varies greatly in the plume, both as result of different emissions and from changes during transport. As expected, similar behaviour is also detected for the optical properties. For this reason, when attempting a study of the impact of volcanic ash on satellite observations, it was important to understand how well the ash was characterised in this analysis. At IUP–Bremen, measurements were performed with a CIMEL Sun photometer instrument, early in the morning, on the 16<sup>th</sup> of April (Hoyningen-Huene et al., 2011, submitted). From these, it was possible to derive aerosol phase functions that were then compared to phase function used for the RT calculations. In Figure 4.7, phase functions are presented for ash (in coarse mode) alone, and the ones used in the RT calculations, for the 16<sup>th</sup> of April, in Bremen: one for the aerosol plume at the surface level; and another at 4.5 km where the concentration of ash was high. The phase function of the aerosol plume at 4.5 km shows the dominance of scattering by ash at this altitude over the other aerosol types. The comparison of these different scattering angular distributions is important because the one derived from the measurements does not correspond to ash alone but rather to a mixture of atmospheric particles. In addition, at the time of the measurements, the amount of volcanic ash above Bremen was

quite high in the early hours of the day but decreased in the late morning (i.e., at the time of the satellite overpass). The phase function derived from measurements is very similar to the one used for the surface level, with some differences identified for high scattering angles. The similarity between the phase functions brings confidence to the approach taken. In addition, in the previous chapter, it was shown that only large differences in phase functions have an impact on the AMF values. Therefore, the accuracy and representativeness of the results obtained in this study should not depend much on high precision of this setting alone.

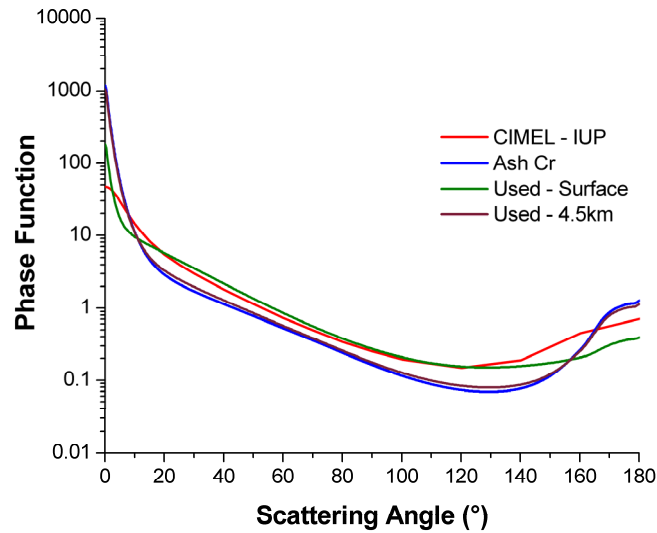


Figure 4.7 Comparison between the phase function of ash used in the SCIATRAN calculations and the one derived from measurements performed at IUP - Bremen with the CIMEL instrument on the morning of 16<sup>th</sup> of April 2010 (data provided by W. Hoyningen-Huene).

As illustrated in Figure 4.7, the phase functions  $p(\theta)$ , i.e., the Legendre expansion coefficients, calculated for each aerosol type were mixed for each of the model layers. This combination of the scattering functions was done according to equation (4.1) that takes into account the amount of each aerosol type present at a certain height:

$$p(\theta) = \frac{\sum_i v_i k_{scat,i} p_i(\theta)}{\sum_i v_i k_{scat,i}} \quad (4.1)$$

where  $i$  corresponds to the aerosol type,  $v$  corresponds to volume mixing ratio, and  $k_{scat}$  is the scattering coefficient. Examples of the resulting phase functions are presented in Figure 4.8 below, for the 16<sup>th</sup> of April 2010, above Berlin, at different layers, for the two scenarios where aerosol is considered.

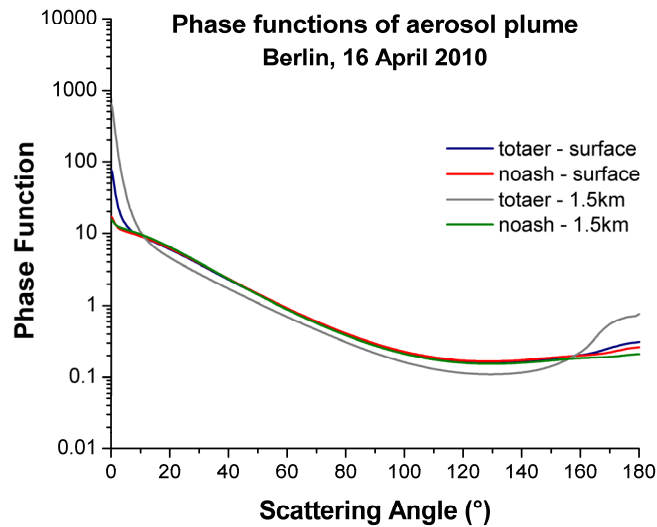


Figure 4.8 Example of phase functions used in the SCIATRAN calculations for the mixture of all aerosol types (totaer) and the case without ash (noash). Data taken for Berlin, on the 16<sup>th</sup> of April, at surface level, where the fraction of ash was small in comparison to the remaining aerosol types, and at 1.5 km, where the contribution of ash was the highest.

From this figure it becomes obvious how the presence of ash can change the scattering functions of the aerosol plume. The phase function for a mixture of all aerosol types, at 1.5 km (where the presence of ash was more significant) is the one showing a higher deviation from the remaining ones. At surface level, the phase functions for the scenarios with and without ash are almost identical.

### 4.3 Impact of volcanic ash on NO<sub>2</sub> AMFs

From the sensitivity study presented in the previous chapter, it became evident that an aerosol plume present in the atmosphere at the time of satellite measurements can influence the observations in different ways. These induced changes can be summarised in two main effects: shielding the trace gas or enhancing the sensitivity of the measurements.

A promising procedure to consider the aerosol in the retrieval of tropospheric NO<sub>2</sub> vertical columns is based on the application of model data that would provide more dynamic information. However, such data usually does not provide information on a regular basis for sporadic and extreme events, with large emission of aerosol. It is therefore important to understand how these situations might affect the retrieved columns. Degradation of the quality of satellite-derived products has been previously

documented and linked to the presence of volcanic ash in the atmosphere. Dahlback et al. (1994) found, from a sensitivity study, that total ozone measured by TOMS was affected by the Pinatubo aerosol. In addition, the radiative transfer calculations also demonstrated that total ozone derived from ground-based measurements performed by a Brewer spectrophotometer at Sodankylä, Finland, may have been underestimated by up to 30% when the aerosol effect was disregarded. Furthermore, also the measurements from surface properties were affected by the particles emitted during the Pinatubo eruption. Studies have reported too low NDVI retrieved from AVHRR observations (Jeyaseelan and Thiruvengadachari, 1993; Vermote et al., 1997). Likewise, site measurements of sea-surface temperature around New Zealand have evidenced that the AVHRR product was providing too cold temperatures for these locations during the last months of 1991 and beginning of the following year (Sutton and Chiswell, 1995).

The focus of this study was not to understand how an aerosol plume influences the sensitivity of the measurements, but rather to investigate how the observations are affected in extraordinary events, such as a volcanic eruption. For this, three different scenarios were created:

- A (noaer) – with no aerosol in the radiative transfer calculations,
- B (totaer) – where the contribution from all the aerosol types, in the model, was considered for the determination of optical properties of the plume,
- C (noash) – with similar characteristics to the previous, but excluding the contribution of the volcanic ash.

In this way, it was possible to determine how the AMF values were affected by the presence of ash within the aerosol simulated. In the following sections, the AMFs obtained for the different scenarios are presented for the domain of the study. In addition, a more detailed analysis is presented, where the vertical distribution and optical properties for specific locations are taken into consideration, in an attempt to understand what factors exactly are responsible for the observed differences of the AMFs. Although the radiative transfer calculations were executed for two wavelengths, here only the results obtained for 437.5 nm will be presented.

### 4.3.1 AMF variation for different scenarios

The ash cloud advected from the Icelandic volcano reached Europe on the night from the 15<sup>th</sup> to the 16<sup>th</sup> of April 2010. The dispersion of the plume changed rapidly in time and the ash amount was very different from place to place. The tropospheric NO<sub>2</sub> AMFs are dependent on aerosol properties and on its optical depth, i.e., the AOD. Therefore, considering the values of AOD presented in Figure 4.5, it was presumed that noticeable differences of the AMFs for the various scenarios would be clearly identifiable. However, this was not the case because several factors changed in these calculations,

namely the NO<sub>2</sub> profiles, and other aerosol properties. In addition, it is important to highlight that the AOD for the volcanic ash was quite small in the region of the study, with maxima of 0.22 - 0.24 on the 16<sup>th</sup> of April in the area of the border between the Netherlands and Germany, and also at the North Sea close to the coast of Norway (see Figure 4.5). The maximum of 0.24 is a low value compared to measurements performed on these days. Examples of observations are the ash AOD of 0.7, at 500 nm, measured in the AERONET station in Leipzig (Ansmann et al., 2010), and 0.34 (layer 2.2 - 3.2 km), at 532 nm, registered in Munich (Wiegner et al., 2011). Nevertheless, for the data used in this analysis, the ash AOD corresponds to ~84% of the total AOD for those locations, which is a significant fraction for ash alone. Moreover, the AOD values were compared with measurements performed at AERONET stations in Hamburg, Cabauw and Paris, during the time period considered in this analysis. With the exception of Cabauw on the 16<sup>th</sup> of April, for all the other sites, the AODs derived from the model output were much lower than the measured daily averages (measurements for the 9:00 to 11:00 UTC were not available for day 16). The largest difference was found in Hamburg: 0.45 measured optical depth, at 440 nm, and 0.07 used in the RT calculations, at 437.5 nm. The lower AOD values determined from the EURAD model data might be related to model settings, and the complexity of simulating such an event. In addition, it can, to some extent, be explained by a lower amount of aerosol present in the atmosphere at one of the hours considered for this study, while the measurements are performed at a later stage with a different aerosol plume above the stations. Additionally, as it will be explained later, the hypothesis assumed for particle-mixing (external mixture), might result in an underestimation of AOD. This factor can be relevant for the conclusions of this study, since the low AODs are most likely the main explanation for the very similar AMFs obtained for the different scenarios. According to the results from the sensitivity study previously performed (see chapter 3), the impact of aerosol on the AMFs is linked to the amount of aerosol present at the time of the measurements. The greatest (and more significant) changes in the NO<sub>2</sub> AMFs were always observed for high AODs, i.e., 0.5 and/or 0.9. Therefore, it was not surprising to find once more that, for low aerosol load, the sensitivity of the measurements is not considerably affected.

In Figure 4.9 below, the results of the RT calculations are presented for the 16<sup>th</sup> of April. No evident difference was found between the AMFs for scenarios A and B, except for some small regions, e.g., Northern Germany, where a decrease of the AMF values was registered. However, when comparing A and C, these differences were not observed, which indicated that the variation of the AMF found between the scenarios with and without aerosol was caused by the presence of ash. The changes of the AMFs were not evident for the results obtained for the days 17 and 18 of April (see Figure 4.10 and Figure 4.11, respectively). On those days, the presence of ash was quite reduced and the similar values in scenarios B and C suggested that the variation of the AMFs was not caused by volcanic ash, but by other aerosol types. This effect was more pronounced on the 18<sup>th</sup> of April, in the area of the English

Channel. This was the day where the highest differences between the scenarios with and without aerosol were found, e.g., AMF of 0.856, for scenario A, decreased to 0.735, for scenario B (minima values of each scenario).

The findings above mentioned are confirmed by ratios between the AMFs obtained for the three scenarios. These ratios are presented in Figure 4.12, Figure 4.13 and Figure 4.14, respectively, clearly showing the regions where the aerosol has influenced the radiative transfer calculation. The highest ratios between scenarios A and B were found for the days 16 (max. 1.13) and 18 of April (max. 1.17). However, when analysing the next two figures, it becomes clear that the changes found on each day were caused by different types of aerosol: a ratio of 1.11 between scenario C and B can be attributed to the presence of ash, on the 16<sup>th</sup> (from Figure 4.14), and 1.13 ratio from scenario A and B, on the 18<sup>th</sup> (from Figure 4.13). It is surprising to see that the highest difference of the AMF does not occur at the same location where the maximum AOD of 0.24 is observed, but where AOD values of ash were 0.23 and 0.22. This is a clear indication of the complexity of nature of the variations of AMFs, which results from the interplay of different factors. The ratio between scenarios C and B illustrates the contribution of ash to the variation of the AMFs. The similarity between these values and the volcanic ash AOD maps (Figure 4.5) is remarkable, indicating that the presence of volcanic ash has affected the satellite measurements of tropospheric NO<sub>2</sub> columns, although only to a small extent. From the AMF figures, the impact of the ash on these values is not immediately obvious, however, the ratios showed clearly where the ash plume has influenced the radiative transfer calculations. The observed AMF changes revealed that there was an overall decrease of the values (ratios > 1, with a few exceptions not related to ash) from the scenarios without to the cases with aerosol. This finding corresponds to what was previously denoted as aerosol shielding effect.

### 4.3.2 Scenarios and results for specific locations

The AMF maps offer a general overview of what can happen in the presence of aerosol. However, as it was already demonstrated in the previous chapter, to completely understand what the source of the variation is, it becomes important to consider several aspects. Not only is essential to look into the optical properties of the aerosol, but also consider the vertical distribution of NO<sub>2</sub> and aerosol, and, particularly for this case, the ash. Therefore, various locations across Europe (several in Germany) were selected for a more detailed analysis (see Figure 4.15). This selection was carried out according to several factors, attempting coverage of different possible profiles for trace gas and aerosol, as well as assuring the presence and absence of ash on the different days. An example is Cabauw that, unlike the remaining ones, is not a large city but a remote area affected by the transport of pollution from other Dutch cities. In addition, lidar and AERONET stations are located at this site which allows for a comparison of aerosol scenario definitions.

## Impact of volcanic ash on NO<sub>2</sub> AMFs

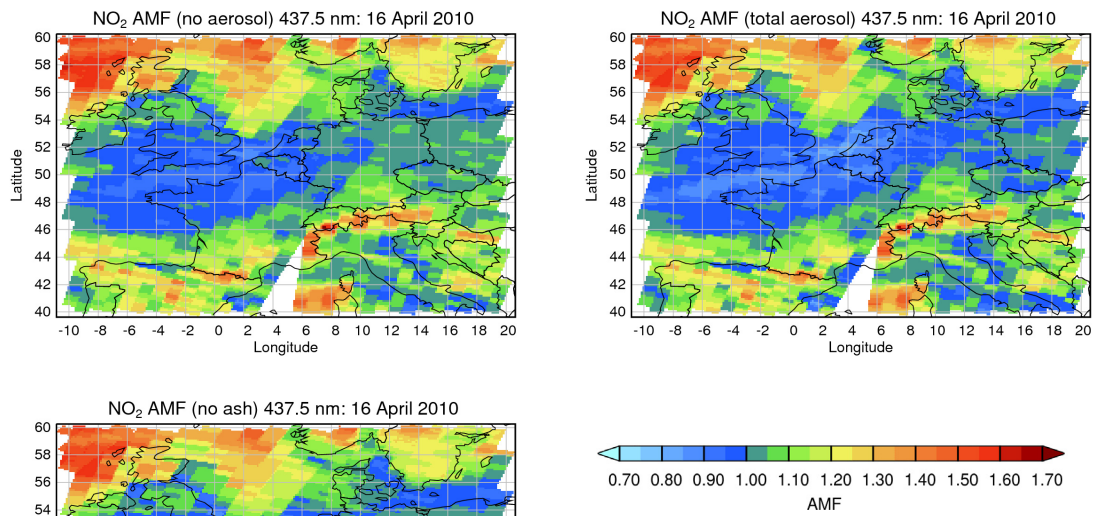


Figure 4.9 NO<sub>2</sub> AMF for the 16<sup>th</sup> of April 2010, plotted for overpass time of GOME-2. AMFs were determined with EURAD model output and calculated for 3 scenarios: (A) no aerosol, (B) total aerosol, (C) all aerosol types except for ash.

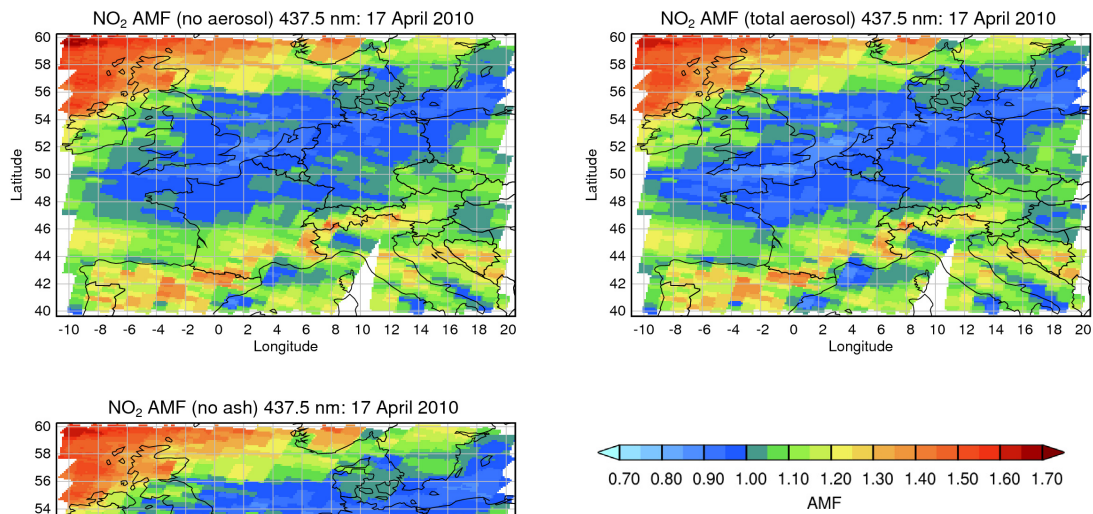


Figure 4.10 NO<sub>2</sub> AMF for the 17<sup>th</sup> of April 2010, plotted for overpass time of GOME-2. AMFs were determined with EURAD model output and calculated for 3 scenarios: (A) no aerosol, (B) total aerosol, (C) all aerosol types except for ash.

## Case study – Eyjafjallajökull eruption

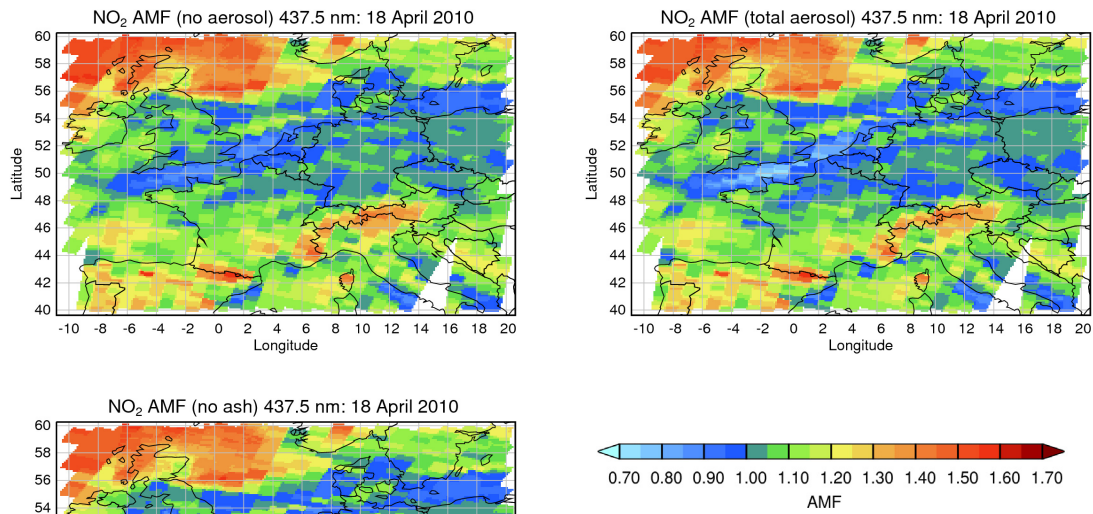


Figure 4.11 NO<sub>2</sub> AMF for the 18<sup>th</sup> of April 2010, plotted for overpass time of GOME-2. AMFs were determined with EURAD model output and calculated for 3 scenarios: (A) no aerosol, (B) total aerosol, (C) all aerosol types except for ash.

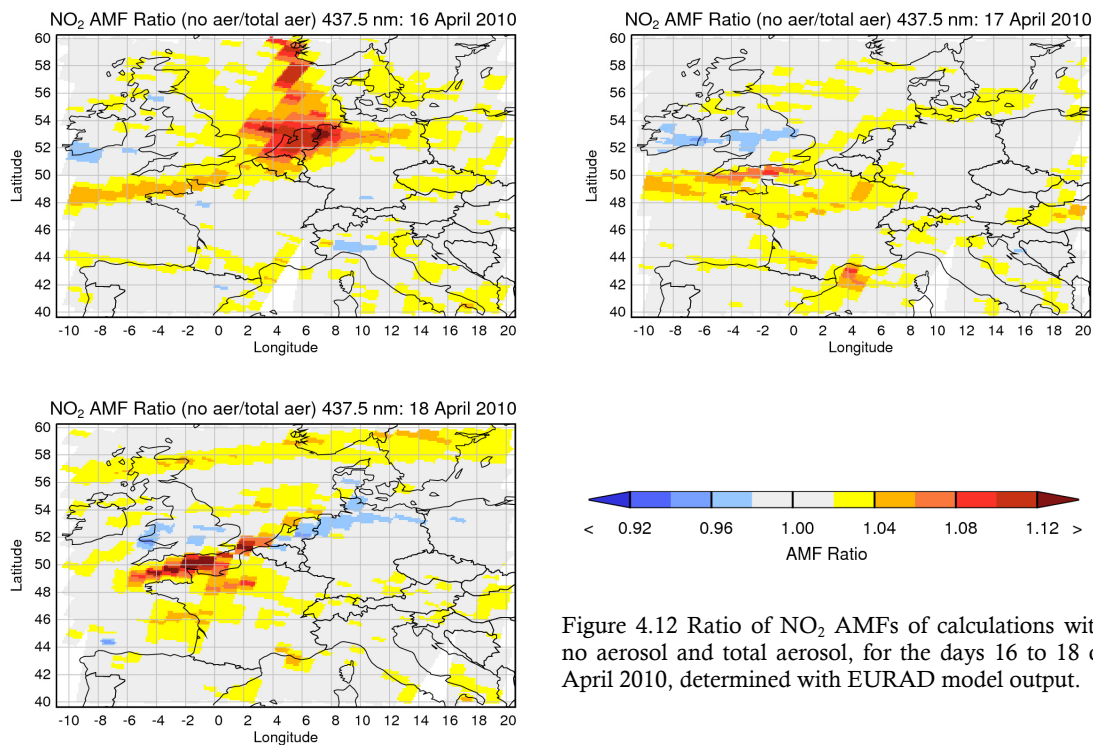


Figure 4.12 Ratio of NO<sub>2</sub> AMFs of calculations with no aerosol and total aerosol, for the days 16 to 18 of April 2010, determined with EURAD model output.

## Impact of volcanic ash on NO<sub>2</sub> AMFs

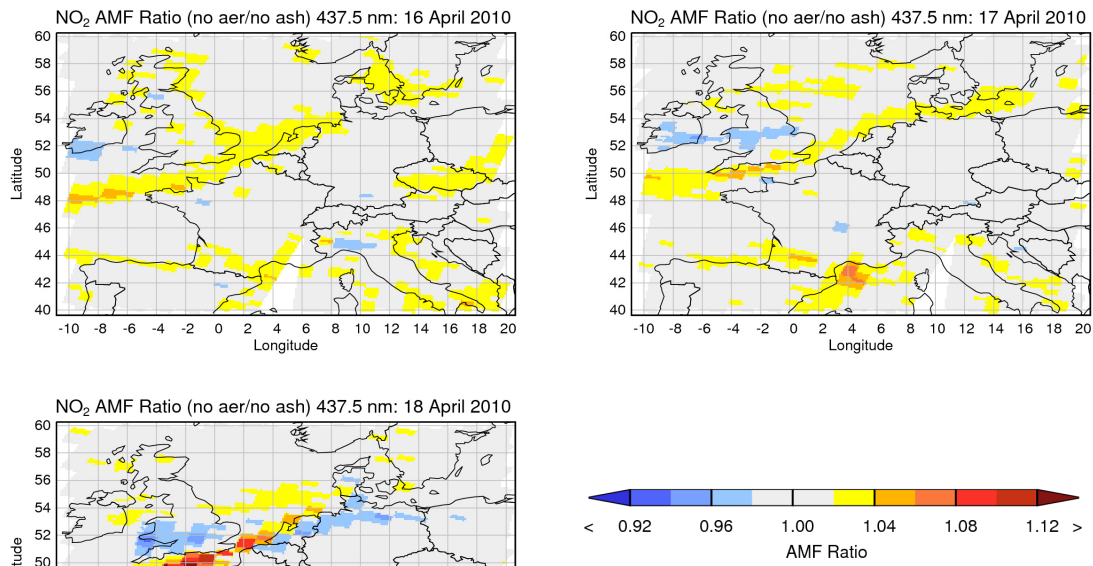


Figure 4.13 Ratio of NO<sub>2</sub> AMFs of calculations with no aerosol and all aerosol except ash, for the days 16 to 18 of April 2010, determined with EURAD model output.

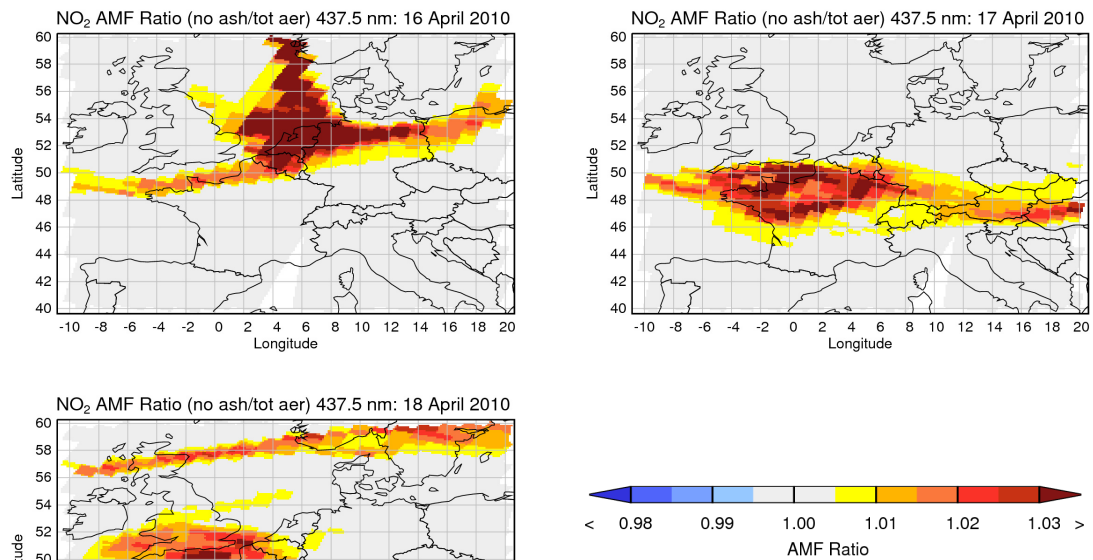


Figure 4.14 Ratio of NO<sub>2</sub> AMFs of calculations with no ash and total aerosol, for the days 16 to 18 of April 2010, determined with EURAD model output. (Note the different colour scale from the previous figures.)

## Case study – Eyjafjallajökull eruption

The trace gas and aerosol profiles were extracted from the SCIATRAN input files, and the AODs and SSA values calculated. These variables, the AMFs for the different scenarios and their ratios are presented in Table 4.4, Table 4.5 and Table 4.6, for the days 16 to 18 of April, respectively.

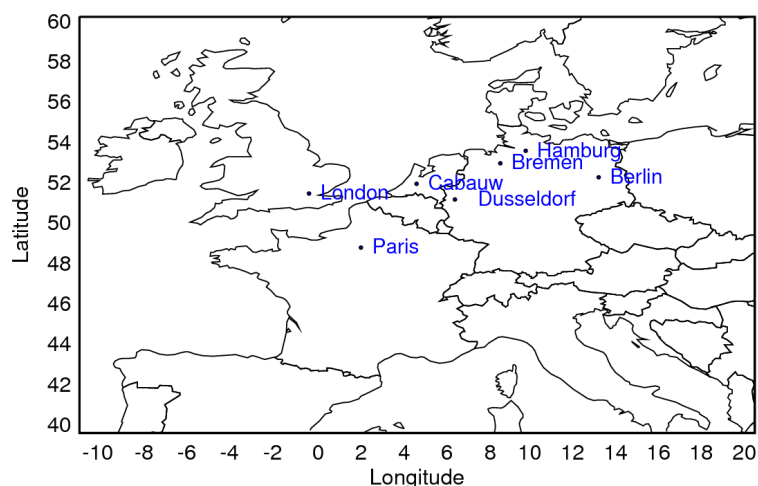


Figure 4.15 Selected locations for a detailed analysis of the effect of ash on the  $\text{NO}_2$  AMFs.

The different scenarios presented in Figure 4.16, Figure 4.17 and Figure 4.18 provide an overview on various possible situations in terms of aerosol and trace gas distribution. For the majority of the cases, the  $\text{NO}_2$  was concentrated close to the surface, within the lowest kilometre. On most of the days and locations, the high volume mixing ratios were fairly constant up to a certain height when a sharp decrease was observed, indicating well mixed boundary layers. Two different profiles are presented for the aerosol, in function of total extinction of the plume and extinction of the volcanic ash. For the selected locations, the great fraction of the ash was located above the  $\text{NO}_2$ . However, on the 18<sup>th</sup> it was possible to see that the ash aerosol presented an almost homogeneous distribution from surface to 5 km (or even higher), for the sites of Cabauw, London and Paris. It is also interesting to observe that the profile of total extinction (corresponding to all aerosol types) was similar to the  $\text{NO}_2$  vertical distribution with exception of those layers where ash was present. As mentioned above, the main focus of this study was not to analyse the impact of an aerosol plume (i.e., total mixture) on the satellite observations, but mainly the influence by volcanic ash. Nevertheless, it is important to note that those profiles might have contributed to an enhancement of the  $\text{NO}_2$  close to the surface. This was clearly what occurred, for example, on the 18<sup>th</sup> of April in Bremen, Hamburg and Cabauw, where the values of the ratios between scenario A and B were smaller than 1 (see Table 4.6). In addition, the shielding effect of ash standing above the  $\text{NO}_2$  can, in other occasions, be compensated by the multiple scattering closer to the surface. It has been observed before (see results of scenario L in

previous chapter) that the combination of the two effects often results in an overall modest change of the tropospheric NO<sub>2</sub> AMF.

From the three days considered, the most interesting, for this study, is certainly the 16<sup>th</sup> of April when the amount of ash was highest above Europe. Several conclusions can be drawn when analysing the profiles and results presented in Table 4.4. The most significant impact on the NO<sub>2</sub> AMF was detected on the 16<sup>th</sup> of April for Cabauw, Bremen and Hamburg, where the volcanic ash caused a decrease of the AMFs of 7.9%, 5.0% and 2.1%, respectively. For Hamburg, it is also important to point out that the magnitude of the AMF change induced by ash was similar to that caused by the remaining aerosol types. Yet, the optical depth of ash alone was only 0.03 compared to the 0.05 of all other aerosol types. This factor highlights once again the importance of the different characteristics of aerosol in the radiative transfer calculations. The situation observed for Düsseldorf is also a good example for this case, where the AMFs obtained were comparable for the three scenarios. Still, the total aerosol load (0.12) was higher than what was predicted for Hamburg (0.07). The potential shielding caused by the ash layer standing above the NO<sub>2</sub> (with AOD of 0.04 and a peak at ~6.5 km) may have been partly cancelled by enhancement of the measurement sensitivity due to a large amount of aerosol mixed with the trace gas (AOD of ~0.03 in the first 500 m). The results obtained on all sites considered, for the days 17 and 18 of April, do not show a significant variation of the AMFs related to the volcanic ash, with the exception of London and Paris. Focusing on the last mentioned day, the results obtained for London are quite exceptional. If on the one hand, a 3.7% reduction of the AMF was observed because of the ash, on the other hand, when comparing the scenarios A (no aerosol) and C (no ash), the AMF increased from 1.018 to 1.034. This is once more a good example of how the interaction of the various aerosol types with the radiation can derive different consequences. In Paris, for both days, the ash has reduced the AMFs by ~2%. However, while on the 17<sup>th</sup> this reduction was higher than the effect of the other aerosol types, on the 18<sup>th</sup> the opposite was verified.

As it was demonstrated in the previous chapter, also the absorbing properties of the aerosol are influencing the AMF values. A column averaged SSA was obtained by the following equation:

$$SSA(\lambda) = \sum_l \left( SSA_l \cdot \frac{k_{ext,l}}{\sum_l k_{ext,l}} \right) \quad (4.2),$$

where  $SSA_l$  and  $k_{ext,l}$  are, respectively, the determined single scattering albedo and extinction coefficients for a layer  $l$  in the profile. As it is possible to see from the values in the tables below, the aerosol mixture for these locations was generally highly absorbing. The lowest SSA for the total mixture (0.70) obtained for Paris on the 17<sup>th</sup>, and the highest scattering aerosol plume (0.90) observed on the 18<sup>th</sup> in the atmosphere above Bremen and Hamburg. Such values are in accordance to values reported from previous studies, as for example SSA values for China, derived from ground and

## Case study – Eyjafjallajökull eruption

satellite measurements, presented by Lee et al. (2007). Unfortunately, AERONET inversion products that might provide SSA values were not available for the relevant time period of this event. In addition, it is interesting to see that the presence of ash did not affect much this property.

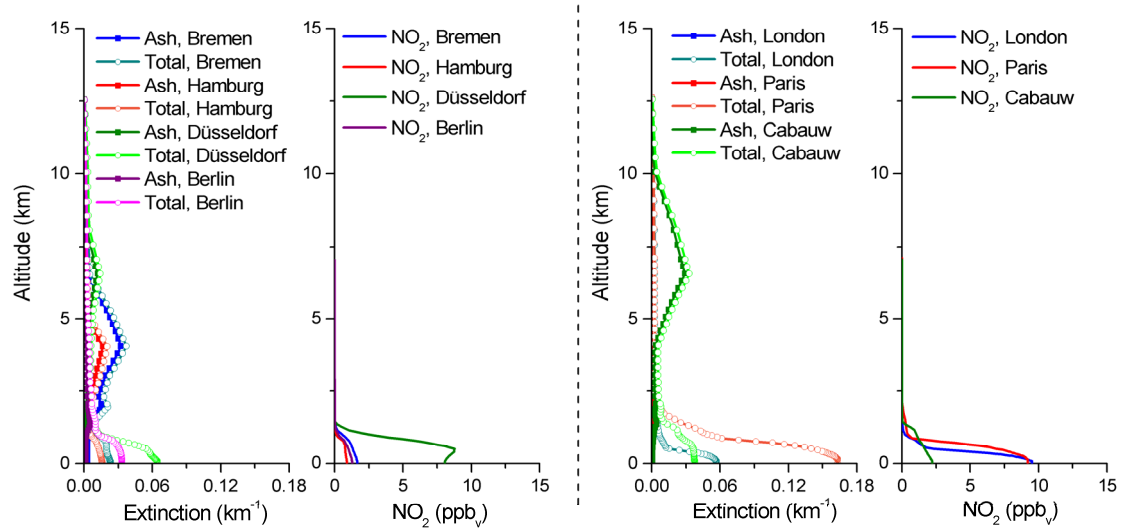


Figure 4.16 NO<sub>2</sub> and aerosol (total aerosol (open circles) and ash (filled squares)) vertical profiles for selected European locations, on the 16<sup>th</sup> of April 2010.

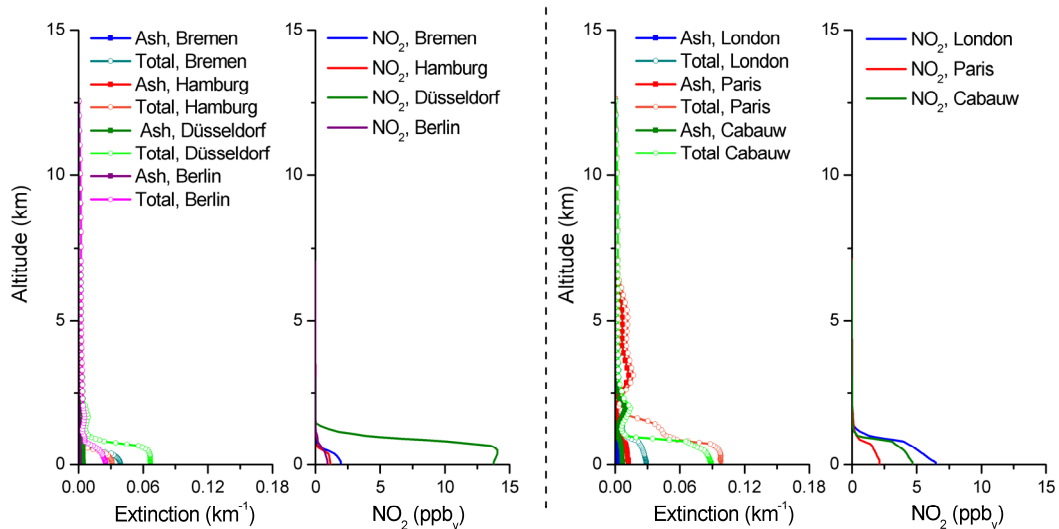


Figure 4.17 NO<sub>2</sub> and aerosol (total aerosol (open circles) and ash (filled squares)) vertical profiles for selected European locations, on the 17<sup>th</sup> of April 2010.

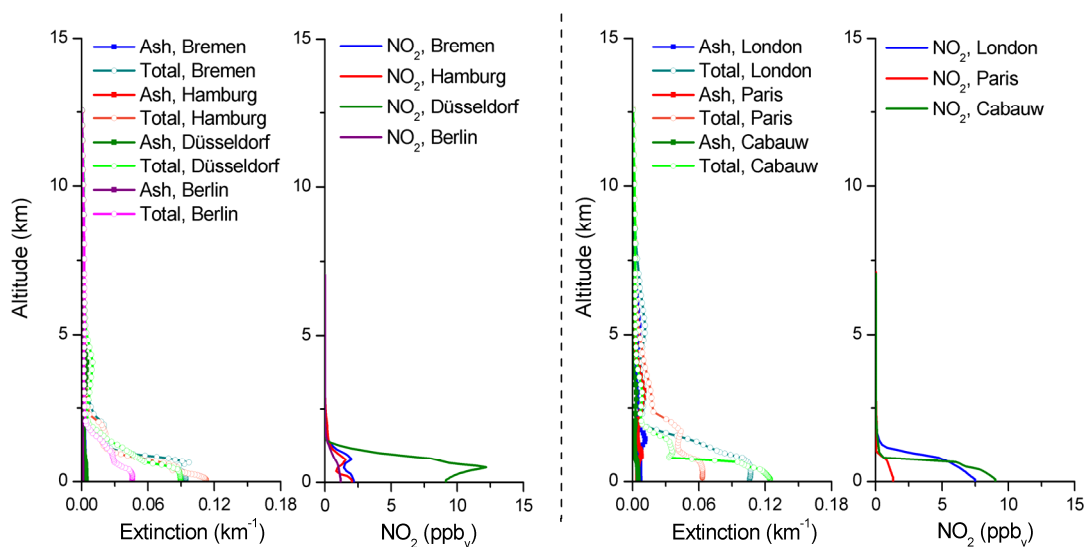


Figure 4.18 NO<sub>2</sub> and aerosol (total aerosol (open circles) and ash (filled squares)) vertical profiles for selected European locations, on the 18<sup>th</sup> of April 2010.

### 4.3.3 Aerosol mixing state assumptions

The analysis performed considered only dry aerosol, i.e., an external mixture of different aerosol types excluding the water content of the aerosol. This approximation leads to uncertainties in the results. However, considering the purpose of the analysis presented, the conclusions achieved are still significant, showing how the tropospheric NO<sub>2</sub> AMF changes in the presence of volcanic aerosol. Still, a short discussion on alternative approaches will be explored in this section.

Different hypotheses exist to represent aerosol mixing states: external mixing, homogenous internal mixing, and core-shell mixing (e.g., Péré et al., 2009). For the latter, particles are considered to have several layers corresponding to different species, the primary insoluble aerosol (the core) and soluble species (the shell). The internal homogenous mixing allows a good characterisation of wet particles when dealing with hydrophilic species. On the other hand, when considering an external mixture, each aerosol type is treated separately and phase functions, extinction and scattering coefficients determined for each of those. All approaches have their associated uncertainties because approximations are necessary to define how the particles are mixed together and what the changes are in the optical properties and in the size distribution of the aerosol. It is known that the atmospheric particles interact and bind together, not existing, thus, entirely in a pure external mixing state.

Case study – Eyjafjallajökull eruption

Table 4.4 Optical characteristics of aerosol layers and results, for different locations, on the 16<sup>th</sup> of April, 2010: total aerosol optical depth (AOD) (all aerosol types considered in the mixture) and for ash alone; single scattering albedo (SSA) for the case with all aerosol types and that without ash; airmass factor (AMF) for the three scenarios considered, no aerosol (noaer), all aerosol (totaer), all aerosol except for ash (noash); and ratios of the different AMFs.

Location	AOD		SSA		AMF			Ratios		
	Total	Ash	totaer	noash	noaer	totaer	noash	noaer/totaer	noaer/noash	noash/totaer
Bremen	0.15	0.11	0.83	0.82	1.021	0.953	1.001	1.07	1.02	1.05
Hamburg	0.07	0.03	0.82	0.82	1.019	0.979	1.000	1.04	1.02	1.02
Berlin	0.07	0.01	0.73	0.72	1.016	0.993	1.004	1.02	1.01	1.01
Düsseldorf	0.12	0.04	0.86	0.87	0.951	0.924	0.936	1.03	1.02	1.01
Cabauw	0.23	0.17	0.85	0.85	0.982	0.891	0.961	1.10	1.02	1.08
London	0.05	0.00	0.79	0.79	0.935	0.916	0.916	1.02	1.02	1.00
Paris	0.15	0.00	0.71	0.71	0.923	0.897	0.897	1.03	1.03	1.00

## Impact of volcanic ash on NO<sub>2</sub> AMFs

Table 4.5 Optical characteristics of aerosol layers and results, for different locations, on the 17<sup>th</sup> of April, 2010: total aerosol optical depth (AOD) (all species considered in the mixture) and for ash alone; single scattering albedo (SSA) for the case with all aerosol types and that without ash; air mass factor (AMF) for the three scenarios considered, no aerosol (noaer), all aerosol (totaer), all aerosol except for ash (noash); and ratios of the different AMFs.

Location	AOD		SSA			AMF			Ratios	
	Total	Ash	totaer	noash	noaer	totaer	noash	noaer/totaer	noaer/noash	noash/totaer
Bremen	0.05	0.00	0.86	0.86	0.955	0.946	0.947	1.01	1.01	1.00
Hamburg	0.05	0.00	0.81	0.81	0.935	0.920	0.921	1.02	1.02	1.00
Berlin	0.04	0.00	0.77	0.77	0.975	0.964	0.965	1.01	1.01	1.00
Düsseldorf	0.08	0.01	0.87	0.87	0.957	0.950	0.953	1.01	1.00	1.00
Cabauw	0.05	0.00	0.86	0.87	0.958	0.956	0.958	1.00	1.00	1.00
London	0.05	0.00	0.85	0.85	0.962	0.937	0.937	1.03	1.03	1.00
Paris	0.16	0.04	0.70	0.69	0.990	0.965	0.981	1.03	1.01	1.02

## Case study – Eyjafjallajökull eruption

Table 4.6 Optical characteristics of aerosol layers and results, for different locations, on the 18<sup>th</sup> of April, 2010: total aerosol optical depth (AOD) (all species considered in the mixture) and for ash alone; single scattering albedo (SSA) for the case with all aerosol types and that without ash; air mass factor (AMF) for the three scenarios considered, no aerosol (noaer), all aerosol (totaer), all aerosol except for ash (noash); and ratios of the different AMFs.

Location	AOD		SSA			AMF			Ratios	
	Total	Ash	totaer	noash	noaer	totaer	noash	noaer/totaer	noaer/noash	noash/totaer
Bremen	0.13	0.01	0.90	0.90	1.061	1.084	1.087	0.98	0.98	1.00
Hamburg	0.12	0.00	0.90	0.90	1.077	1.110	1.111	0.97	0.97	1.00
Berlin	0.07	0.00	0.84	0.84	1.024	1.027	1.027	1.00	1.00	1.00
Düsseldorf	0.13	0.01	0.88	0.88	0.987	0.982	0.989	1.01	1.00	1.01
Cabauw	0.18	0.01	0.79	0.79	0.980	1.008	1.010	0.97	0.97	1.00
London	0.20	0.04	0.83	0.83	1.018	0.997	1.034	1.02	0.98	1.04
Paris	0.15	0.03	0.85	0.86	0.979	0.906	0.920	1.08	1.06	1.02

However, a homogenous internal mixing state does not correspond to reality either, as the level of mixture between the different species is not identical, but rather involving complex processes that change the chemical composition of the aerosol (e.g., reaction between NH<sub>4</sub><sup>+</sup>, NO<sub>3</sub><sup>-</sup> and SO<sub>4</sub><sup>2-</sup>). Furthermore, the interaction between soluble and insoluble species (e.g., black carbon or dust particles) is still not well understood. A study presented by Lesins and colleagues (2002) has revealed that considering pure aerosol modes as an external mixture can result in high overestimations of both AOD and SSA. On the other hand, recently, Péré et al. (2010) shows that the AOD values are not highly affected by the approach taken, whereas the SSA is very sensitive to mixing state assumption. Thus, it is difficult to understand how the results of this study are influenced by the method selected to represent the mixture of several aerosol species.

In the EURAD model, a combination of external and internal mixing is assumed, defining sulphates, nitrates, ammonium, and sea-salt, in the Aitken and accumulation modes, as soluble species (E. Friese, personal communication, Jun. 2011). The remaining aerosol types are insoluble and in a state of external mixing. For the internally mixed particles, the refractive indices and densities of the pure species, in each size bin, are weighted (usually by volume). In this way, the new the refractive index and density reflect the chemical and optical properties of a mixture. These values would then be used to determine phase functions, extinction and scattering coefficients of an aerosol mixture. A pure external mixture was assumed in the analysis described above because the application of this method is highly demanding at computational level. It is important to highlight that several approaches have been found in the literature consulted (Fassi-Fihri et al., 1997; Tombette et al., 2008; Péré et al., 2010; 2011d), with general recommendations for an application of internal mixture, but no agreement on the error induced by the external mixing state. Furthermore, it is also not clear which species should be mixed in each state and what is the best method to determine the properties of the mixture. From the species considered in the analysis performed, volcanic ash is among the hydrophobic aerosol. Since, the main goal of this study was to determine the impact of this specific aerosol type on the retrieval of tropospheric NO<sub>2</sub>, a large impact on the conclusions achieved is not expected. Nevertheless, it is important to stress that other aerosol species are potentially more affected by the treatment of particle-mixing, which may induce more significant changes in the results.

As it was described above, by assuming an external mixing state, the phase functions, the extinction and scattering coefficients were determined separately for each aerosol type. In this way, the water content of aerosol would have to be considered as an extra aerosol type, assuming atmospheric water particles added to the total aerosol. A test was performed, for small parts of the domain, assuming a water refractive index of  $1.34 - i2.0E-9$  and density 1.0 g/cm<sup>3</sup> (Péré et al., 2010). As it can be expected, the addition of more particles (water in this case) will increase the total extinction, i.e., leading to higher AOD. The difference for pure sulphate and pure water particles was verified and

found to be less than a factor of 2 in extinction, with a smaller value for the latter (N. Schutgens, personal communication, Aug. 2011). Hence, it was surprising to notice that for the new mixture, in most of the region analysed, the AOD obtained was often above 0.5, reaching values as high as 3.5 (see Figure 4.5 with previous total AOD without water particles). These are quite unrealistic values caused by very high mass concentrations of water in accumulation mode at some locations. It can only be speculated that such high values correspond to clouds rather than aerosol, and that further investigations are required to understand exactly how the water content provided in the model output should be accounted for.

The diameter of dry particles is another parameter that will also be affected by the commonly denoted relative humidity effect, i.e., growth of the particle due to water uptake. In general, in the present analysis, the temporal and spatial variation of the aerosol size distribution was not considered, once more because of the time required for the calculations. In addition, the CTM provides only median diameters for each aerosol mode, instead of size distribution for different aerosol types. Using such values would, in part, denote that the size of all species changes similarly, whether they are soluble or not. In the calculations carried out, the size distribution of each aerosol mode was defined according to the initial conditions of the model. Examining the radii obtained from the model output, it is possible to identify several profiles where, for the same location, the size of particles was overestimated at certain altitudes, but also underestimated in different layers. The analysis of the equations introduced in section 2.4 helps to understand how the modification of the size distribution will affect the extinction and scattering coefficients. Both the number density and cross section values are affected by the radius of the particle. In the former, the variation can be easily predicted: an increase in size results in a decrease of the number density. The more complex situation occurs with the extinction and scattering cross section values, because these are not only dependent on the geometrical area of the particle, but also on the respective efficiencies. The dependency of these two parameters to the particle's size is neither linear, nor regular and, in addition, it is based on the refractive index (several examples are provided in the literature consulted (van de Hulst, 1981; Liou, 2002; Kokhanovsky, 2008)). The extinction and scattering coefficients might vary greatly for a certain model point, but, in the total column, small changes could be verified due to a compensation of over- and underestimation of radii at different altitudes. In addition, for the radiative transfer calculations, the prediction of impact in the tropospheric NO<sub>2</sub> AMFs is even more complex. As it was demonstrated in chapter 3, the AMF is dependent on the relative vertical distribution of NO<sub>2</sub> and aerosol. This means that errors at some layers can be more significant than at other altitudes where, for example, few aerosol and/or no NO<sub>2</sub> exist. Additionally, the size of the aerosol affects the extinction and single scattering albedo differently, and these two properties do not affect the radiative transfer in the same manner. Therefore, a deep study is required to truly understand the influence of the aerosol size distribution in the results. This would involve the calculation of new extinction and

scattering coefficients, for each aerosol type, at each model point, which, in practice, is a similar method to the internal mixing approach, requiring long calculations.

Finally, it is important to highlight, that independently of the approach taken, uncertainties exist in the aerosol chemical composition, as well as in the mass and size distribution simulated by the CTM and these are more relevant for the conclusions achieved. Furthermore, the refractive indices used for secondary organic aerosol and primary aerosol are coarse approximations, as these categories include many different aerosol species with distinct optical properties. The approach taken here was necessary because the time required for more precise calculations was a significant limitation. However, the assumption of external mixture might not be the most relevant source of uncertainty in the analysis presented. This study highlights how, currently, it is still difficult and complex to consider the application of model data in the retrieval of vertical columns from satellite measurements. In the future, priority should be set in understanding and defining a best methodology to derive aerosol optical properties from simulated mass concentrations, and understand the uncertainties involved in each assumption.

## 4.4 Summary

The main goal of this analysis was to understand how a plume of volcanic ash can affect the satellite observations of tropospheric pollution. The volcanic eruption of Eyjafjallajökull in the spring of 2010 was an ideal event for this study. The ash cloud from this volcano has caused the shutdown of the European airspace and, thus, the evolution of this incident was followed closely, day by day. Several model simulations were available, and measurements were performed at many ground stations across Europe (near and far away from the source), and also from flights. The information necessary to set scenarios in the radiative transfer model SCIATRAN 3.1 could be taken from the datasets produced with such a wide coverage of the several stages of the eruption. The calculations presented here were carried out using data based on CTM output. The NO<sub>2</sub> and aerosol concentrations were simulated by the EURAD model from the Rhenish Institute for Environmental Research. Data used in this study were produced by a specific run focusing on this eruption, where several adaptations were done to include volcanic ash in the simulations. This included an adjustment of the amount of particles emitted to values from in-situ measurements, and the definition of the injection heights done according to reports from VAAC and the Icelandic Meteorological Office. The model NO<sub>2</sub> vertical distributions (up to 7 km) were interpolated onto a finer grid. Additionally, the aerosol mass concentration profiles were converted into extinction

## Validation of NO<sub>2</sub> model output

---

coefficients, as well as single scattering albedo values, and also interpolated onto the same altitudes as the trace gas. Finally, phase functions for each aerosol type were calculated and mixed to define the scattering angular distribution of the aerosol plume. With all this information it was possible to run the RT model and determine tropospheric NO<sub>2</sub> airmass factors that characterise the satellite measurement sensitivity. The region of focus of the study was Central Europe, where pollution levels are higher, during the period of 16<sup>th</sup> to 18<sup>th</sup> of April 2010. To differentiate the impact of ash from the remaining aerosol types it was necessary to consider three different scenarios: no aerosol existing in the atmosphere (A); all the aerosol types mixed in the plume (B); and the representation of the aerosol if the eruption had not occurred (C).

The results from this analysis indicate that the NO<sub>2</sub> closer to the surface was shielded from the satellite observations. In practice, this means that the vertical columns derived from the measured slant columns might be underestimated if the presence of ash is not accounted for in the retrieval process. The changes of the AMFs between the scenarios were quite small, with maxima of 13% on the 16<sup>th</sup>, and 16% on the 18<sup>th</sup> of April. Moreover, the impact of ash is only a fraction of this percentage, with the highest ratio between scenarios C and B being 1.11 and registered for day 16. This is according to expectations considering the low AOD values found. In fact, the ash cloud was not visible by the naked eye which already indicated that the effects verified would probably be small. Nevertheless, considering the conclusions from the previous chapter, it is important to point out that such an effect could be considerably larger if the AOD of ash plume was higher. There have been previous volcanic eruptions where a much greater amount of ash was produced and transported across the globe, e.g., the Mount Pinatubo (Ansmann et al., 1997) or Kasatochi eruptions (Hoffmann et al., 2010). In such events, the effect of the ash might have been of higher relevance. For the period during which the present study was developed, it was noticed that the AOD values were quite high, reaching a maximum of 1.19, but only in the (geographical) areas closer to the volcano. Nevertheless, the results obtained highlight the importance of applying the correct aerosol settings to retrieve accurate trace gas vertical columns. From this analysis it was possible to conclude that the presence of ash has led to an overall decrease of the tropospheric NO<sub>2</sub> AMF values.

The effects caused by the overall aerosol were not analysed in detail. However, it was possible to observe AMF changes similar to what has been already found with the sensitivity analysis presented in the previous chapter. On the 18<sup>th</sup> of April, high ratios between the AMFs from scenarios without and with aerosol were attributed to other aerosol types. It is also for this day that both reductions and increases of AMFs are detected from the results of selected locations across Europe. The enhancement of the AMFs was mostly attributed to aerosol mixed with the trace gas in the lowest kilometre. On the other hand, the decrease of measurement sensitivity was verified for situations

## Summary

---

where aerosol, which was predominantly composed of ash, stands above the trace gas, shielding it from the satellite observations.

This study has illustrated the complexity of accounting for the aerosol presence in the atmosphere in the retrieval of trace gas vertical columns from satellite measurements. The high variability of aerosol distribution, in time and space, and its changing properties, are challenges that complicate the implementation of a systematic correction of the measured slant columns. The interaction of atmospheric particles with radiation needs to be considered in the AMF calculations, and CTMs are potential tools to provide information regarding the measurement conditions. Nevertheless, the results of radiative transfer calculations that use model data, as it was exemplified with this study, are closely linked to the accuracy of the CTM simulations. The reproduction of atmospheric aerosol (spatial distribution, amount, size distribution) is a difficult task which many CTMs are not yet able to successfully put in practice. For such unusual events, as volcanic eruptions, there is still place for much improvement. Uncertainties in the model output will be reflected in conclusions achieved, implying that, in reality, effects could have been larger, with satellite observations affected, to a higher degree, by the ash emitted from the Eyjafjallajökull eruption. Nevertheless, it is important to emphasise that the model data used was generated with special settings for this specific eruption, and data is provided in high spatial and temporal resolution. In addition, the determination of optical properties from mass concentrations involves several assumptions and complex computations that might yield high uncertainties. In this analysis an important limitation was the computation time required for a more precise method that could probably, reproduce conditions closer to reality.

It is also important to highlight that exceptionally high aerosol loads are not exclusively originating from volcanic eruptions. Desert dust events and biomass burning are also phenomena responsible for high emissions of particulate matter. Some of the plumes can be transported above pollution hot-spots (e.g., China and Central Europe) and might, then, interfere with the satellite observations. The Russian fires in the summer of 2010 were devastating, caused by long period of drought and the very high temperatures of that season. Several people died because of the intense smog events and thick smoke near the surface in Moscow was reported for several days. If such a smoke was causing visibility impairment within a few meters, it is highly probable that an impact on the satellite measurements has been also verified. With the necessary information available, i.e., aerosol properties and their vertical distribution, available on global level and appropriate resolution, the impact of these episodes can also be analysed. Chemical transport models are potential source of information, providing datasets for trace gas and aerosol. Nonetheless, there are still some limitations to overcome, like the long computational time required to use this data in the radiative transfer calculations. Still, if this data can be employed, global air pollution trends would be determined with higher levels of confidence assuring that the satellite observations and their retrieved products are as accurate as possible.

# 5

## Validation of NO<sub>2</sub> model output

Growing evidence of harmful effects of atmospheric pollution on human health and the apprehension towards climate change due to a fast increase of anthropogenic emissions, have led to the creation of several protocols, such as the Convention on Long-Range Transboundary Air Pollution (CLTRAP, from 1979), the Montreal Protocol (in force since 1989), the United Nations Framework Convention on Climate Change (UNFCCC, in force since 1994) or the Kyoto protocol (initially adopted in 1997). Major environmental concerns have been addressed in these treaties aiming at a reduction of emissions. Policies and strategies are developed and sustainable targets defined so that the impact of air pollution on ecosystems can be minimised.

Measurements performed at ground-based stations became essential to monitor the air quality and compliance with the defined emission targets. These were, for a long time, the most convenient options (and often the only) to measure the concentrations of gases and aerosol in the air. But soon it became clear that these point measurements could not be representative of large areas. In addition, the higher atmosphere is not characterised by such measurements, which becomes an important disadvantage when analysing, for example, the ozone hole evolution. Radiosondes and aircraft measurements became the obvious alternative, but their potential is limited as the measurements are constrained to a certain altitude region and will not provide global atmospheric characterisation. Satellite measurements are an ideal alternative to fill this gap. Surveying the Earth from above and performing observations in remote areas, where otherwise one would not be able to

assess trace gas concentrations, is a convenient method to derive global maps of atmospheric pollution.

Chemical transport models (CTMs) have evolved significantly and are, nowadays, very useful tools applied for air quality predictions at different scales (e.g., street canyon, local, regional, global). As exemplified in the previous chapters, model output can be used to define the *a priori* settings required for retrieval of satellite measurements. However, satellite data are useful to validate the simulation outputs in order to identify and improve possible flaws and, in some occasions, assimilated into models to adjust the simulations. This chapter will explore some of the problems usually found in model schemes when comparing the simulation results to satellite observations.

### 5.1 The GEMS project

We are in a new era of near real-time information and raised public awareness on air pollution and its harmful impact on human health. These concerns have driven the creation of initiatives like the Global Monitoring for Environment and Security (GMES), a joined project from the European Commission and the European Space Agency. GMES's main goal is to provide environmental information to the community by establishing an accessible dataset that combines different and complementary observations from ground-based, airborne and space-based systems. This type of project is innovative as it is not only science-oriented, but rather directed to be a public service, i.e., user oriented. On the one hand, the goal is to supply data to scientists and policymakers (to monitor atmospheric pollution or analyse long-term pollution trends), on the other hand, the objective is also to keep information on air quality accessible to the population in general. These were the circumstances motivating the creation of the GEMS (Global and regional Earth-system (atmosphere) Monitoring using Satellite and in-situ data) project. More than thirty project partners (from several countries) started working on GEMS in 2005 with funds from the European Commission as part of its Sixth Framework Programme. In the GEMS timeline, several of the proposed tasks were successfully completed. With its pioneering service, the project was a success (although with some goals not achieved), and the MACC (Monitoring Atmospheric Composition and Climate) project started directly after (June 2009) as a follow up. This project joins the work of the GEMS and PROMOTE (ESA-funded GMES Service Element), and aims to implement a fully operational atmosphere monitoring system with fast response to needs and requirements from users. The services provided (at the project homepage <http://www.gmes-atmosphere.eu/>) are grouped

into four main themes: European Air Quality, Global Atmospheric Composition, Climate, and UV and Solar Energy.

GEMS goals were mostly based on those already defined in the GMES initiative, yet, in practical terms, the GEMS project aimed at creating an integrated model system for greenhouse gases, aerosol and reactive gases within the ECMWF Integrated Forecasting System (IFS). The concept of these projects is based on the overarching area of chemical weather forecast, where operational air quality models are coupled with numerical weather prediction models, in an attempt to simulate the feedback mechanism between atmospheric composition and meteorological phenomena. The project was divided into four main thematic elements: greenhouse gases (GHG), reactive gases (GRG), aerosol (AER), and regional air-quality (RAQ). This project aimed at building a fully integrated monitoring and forecasting system, combining both observational data sources and state-of-the-art models (Hollingsworth et al., 2008). In that way, a more complete and consistent method became available to determine global atmospheric composition, with focus on the European region. The final goal was to bring together three global components interacting on one common system, although during the initial stage these were still treated separately. The forecast results were provided on a near real-time basis but, in parallel, a retrospective analysis was also carried out to allow a more complete interpretation of evolution of sources and sinks of gases and aerosol. As already mentioned, the resulting products were made available to the public to be used in different areas. The data is useful for the assessment of long-term trends, determination of pollution events of long-range transport (especially from the global data), and can also serve as support on scientific field campaigns. Furthermore, the regional air quality modellers are potential users of the global model output that provides chemical fields at the boundaries of model domains.

The validation exercise presented in this thesis was part of the work developed within the GRG subgroup and, therefore, the remaining groups and their activities will not be explored. The GRG subproject was focused on the setup of a pre-operational data assimilation system for the reactive gases. This was done by coupling of three CTMs - MOCAGE, MOZART and TM5 – with the Integrated Forecast System (IFS) from ECMWF. In addition, the CTMs were also run in off-line mode. Global forecast of tropospheric and stratospheric distributions of ozone (O<sub>3</sub>), nitrogen dioxide (NO<sub>2</sub>), carbon monoxide (CO), formaldehyde (HCHO), and sulphur dioxide (SO<sub>2</sub>) was achieved. Additionally, reanalysis products were also part of the main outcome from this subgroup. Data assimilation was successfully achieved in the GEMS timeline for O<sub>3</sub> and CO. The assimilation of NO<sub>2</sub>, SO<sub>2</sub>, and HCHO observations was performed only for particular time periods.

The initially planned full implementation of the model schemes in the IFS system was not carried out. As an alternative, an easier method (also a quicker solution) was employed by using external

coupling software (OASIS 4, <https://verc.enes.org/models/software-tools/oasis>) to run a coupled system of IFS and a CTM, allowing also for a high flexibility in the choice of chemistry scheme. In this system, the meteorology is taken from the IFS, which was responsible for the computation of the transport of the reactive gases. On the other hand, the deposition processes, injection heights or chemical conversions of chemical species were taken from the CTM processor. The complete description of models and the GEMS Integrated System setup, e.g., time and spatial resolutions, can be found at Flemming et al. (2009) and references therein.

Quality assessment was a major concern during the execution of the project and extensive validation of the resulting products was performed on a regular basis by comparing the model output to data from various independent observation sources. These included not only ground-based networks (e.g., EMEP, GAW), but also measurements performed from aircraft (e.g., MOZAIC) and satellite (e.g., SCIAMACHY, MOPITT) instruments. Through this way, it was possible to assess the model performances and identify problematic areas that needed improvements in the model schemes. Furthermore, the evaluation of the standalone runs was useful to determine if the problems identified in the coupled system derived either from the CTM itself or were introduced by the coupled setup. Within the GEMS project (and later in the following MACC), SCIAMACHY data retrieved at the IUP-Bremen was used to validate the results from different runs (of the several model setups). In the following sections, part of this work is presented with focus on the evaluation of the NO<sub>2</sub> from standalone runs from MOZART and TM5. This analysis demonstrates how the model limitations could be detected from the evaluation exercise and later corrected in the following model versions. A more detailed description can be found in the GEMS Final report (2010).

## 5.2 Chemical Transport Models (CTMs)

A great amount of different model versions were created during the GEMS project. This was the result of the continuous improvement of the CTMs, and partly stimulated by the outcome of regular validation of the global models. It is therefore important to summarise here the timeline dealing with these changes and consequent feedbacks on model output. The complete model description can be found in the GEMS Final report (2010). Here, only a general overview is presented, with focus on the definitions that: a) were identified as source of problems for inconsistent results and b) influence (and to some extent limit) the comparison with satellite data (e.g., the coarse model spatial resolution). Furthermore, the description will also be focused on the settings for the

standalone runs. As mentioned above, the forecast and reanalysis modes were set up as coupled systems. All runs were validated against SCIAMACHY data. However, as the present thesis focuses on the role of satellite measurements in the process of model validation, the results, obtained for the validation of the many versions available of standalone runs, are useful (and sufficient) examples for that exercise. The model setups for MOZART and TM5 were different in some aspects and a general overview of each of the models schemes is given in the following sections.

### 5.2.1 MOZART

The MOZART (Model for Ozone And Related Tracers) version used in GEMS is a global CTM based on the MOZART-3 model code (Kinnison et al., 2007) (hereafter denoted by MOZART only). In the GEMS project, MOZART was not only used for standalone runs but also in reanalysis and forecast mode, coupled with the IFS.

The horizontal resolution of the model is 1.875° x 1.875° and the vertical domain included 60 hybrid sigma layers, from the surface up to 0.1 hPa. The model outputs were saved at 1h intervals. The meteorology parameterisation was taken from ECMWF fields and the chemical solver was based on the MOZART-tracer model. Mixing rates of 115 species were simulated from the surface to the mesosphere and the system of chemical reactions incorporated 71 photolysis reactions, 223 gas phase reactions and 21 heterogeneous reactions (see Kinnison et al., 2007 for more details). From the initial chemical scheme, 37 gas phase reactions were updated according to the recommendations of JPL-06 (Sander et al., 2006). A relevant outcome of this change is the decrease 10-20% of the reaction rates in the CO + OH. The model included physical parameterisations for the usual processes of advection, convective transport, boundary layer mixing, wet and dry deposition. The detailed explanation of each of these settings is out of the scope of this research and further information can be found in the GEMS Final report (2010).

The evolution of MOZART into different versions is presented in Figure 5.1 with remarks on the major changes that were implemented. V10 was the latest version for the standalone runs and it was run for the years 2003 and 2004. The new GEMS/GRG emission inventory data, provided on a monthly basis, was used for anthropogenic sources. This dataset was basically a merge of the RETRO (for year base of 2000) and REAS inventories. Nevertheless, for the eastern Asian inventory, the seasonality was kept from the RETRO version. The NO<sub>x</sub> emissions from ships in RETRO were scaled to totals from Corbett and Koehler (2003) (implemented from V7 onwards). Information for emissions of other chemical compounds was taken from different sources: EDGAR2 for the NH<sub>3</sub>; EDGAR-FT2000 for the SO<sub>2</sub> from anthropogenic sources and GEIA for the

volcanic SO<sub>2</sub> emissions; and the records of Kloster et al. (2005) for the DMS. In addition, the wildfire emissions were taken from GFEDv2 and confined to the lowest MOZART level. The initial model version used this dataset on a monthly basis, but, from V7 onwards, these input data were improved and values for 8 day periods were used instead. Aircraft emissions of NO<sub>x</sub> and CO are also included in the model (Horowitz et al., 2003). Lightning produced NO<sub>x</sub> follows the parameterisation of Price et al. (1997) that accounts for the distribution of convective clouds. The changes from the initial version to the very last one (including upgrades and bug fixes) resulted in an increase of about 17% of total NO<sub>x</sub> emissions. The top of the model (as in altitude) from previous versions was higher (including mesosphere) than the one used in GEMS and, therefore, the upper boundary fluxes were initially erroneous. A zero flux for some species was implemented for V7. In addition, the results from V1 had also indicated a wrong initialisation of species in the stratosphere and the integration of data from BASCOE (<http://bascoe.oma.be/>) was the solution found to correct for this problem.

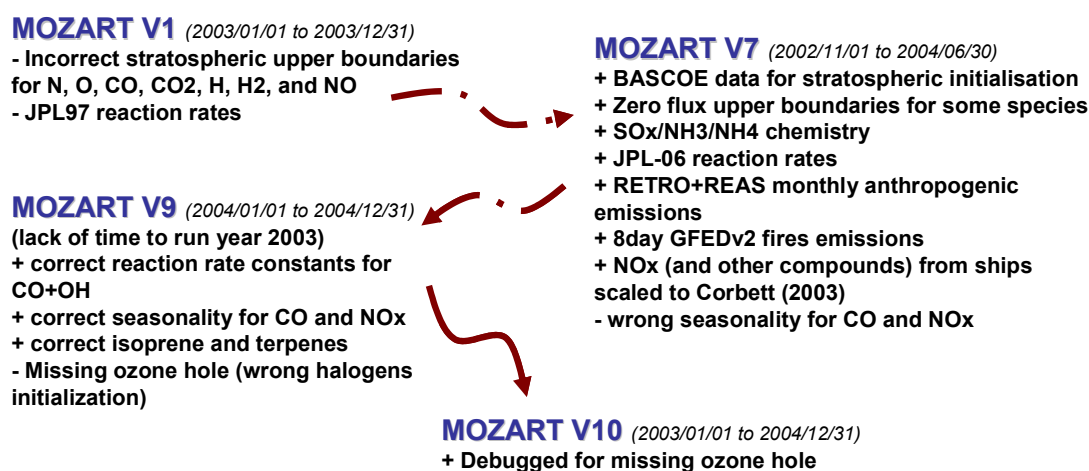


Figure 5.1 Scheme of different MOZART versions analysed and the respective time period of the available results. The changes in each of the versions are noticed: (+) for the improvements and (-) for the problems identified or old settings that were later changed.

## 5.2.2 TM5

TM5 (Tracer Model 5, version KNMI-cy3-GEMS) is a global CTM, developed in a cooperation of several institutes, with parameterisations similar to the TM3 version (Dentener et al., 2003). As for MOZART, the analysis of TM5 presented in the current document is focused on the standalone runs. Unfortunately, for the different versions available there is no output for the same time period.

## Validation of NO<sub>2</sub> model output

---

While for V7 data were available for the year 2003, for V9 and V10 the output only exists for 2004 (and just the summer months in the case of V9). This limited, to some extent, the detailed comparison between the results from different versions, but a general overview was still possible and will be presented below (see Figure 5.2).

The horizontal resolution of this model is 2° x 3° (latitude x longitude) and the vertical resolution the same as in MOZART: 60 hybrid sigma layers, from the surface up to 0.1 hPa. As for all the models included in the GEMS project, the meteorology parameterisation was derived from the ECMWF operational forecast data. More details for advection schemes, convective mass flux (that was changed from 2003 data to 2004), vertical diffusion, deposition fluxes, and photolysis scheme can be found in the GEMS Final report (2010). A modified CBM-IV scheme by Houweling et al. (1998) was the basis for the chemistry, and the reaction rates considered (from JPL-03 (Sander et al., 2003)) have been updated following at the present time the JPL-06 recommendations (Sander et al., 2006). This model accounted for 55 individual tracers, where 39 were transported and the remaining 16 not. It is important to point out that the components that were part of the nitrogen oxides (such as NO, NO<sub>2</sub>, NO<sub>3</sub>, HNO<sub>4</sub>, N<sub>2</sub>O<sub>5</sub>) were only evaluated in the chemical scheme and the transport in the model dealt with NO<sub>x</sub> as a whole. In addition, HNO<sub>3</sub> and PAN are chemical species also included in the transports scheme. The NO<sub>2</sub> validated here is the amount determined after the chemistry processes. A final step of vertical mixing employed in the model scheme is not applied to the NO<sub>2</sub> alone but rather to the NO<sub>x</sub>. This approach would be more problematic for validation of model output with surface measurements, however, because this evaluation was done to tropospheric and stratospheric columns this factor was not highly relevant for the conclusions taken. To account for the variation of injection heights, in TM5, most of the emissions were released in the lowest two model layers. Relevant exceptions are the anthropogenic NO<sub>x</sub> which is injected in the first four layers, and the biogenic emissions distributed at a surface level. Furthermore, in the latest versions, the biomass burning emissions were injected up to 6000 m (previous version considered 2000 m). Another important characteristic of the TM5 is the fact that for the stratosphere the same tropospheric chemistry scheme is used. TM5 is rather a troposphere-focused model, which means that simple assumptions are made for the upper layers. Further details on the climatologies employed for O<sub>3</sub> and HNO<sub>3</sub> (relevant for the NO<sub>2</sub> concentrations) can be found in the GEMS Final report (2010) and Huijnen et al. (2010b).

V10 was the latest version for the standalone runs of this model and its anthropogenic emissions applied were based on the GEMS inventories, i.e., a combination of RETRO for 2000, and the enhanced emissions over China and South-East Asia originating from the REAS inventory. In previous versions (up to V9), the CO and NO<sub>x</sub> emissions retained for the biofuel emissions (and also biomass burning) were based on the EDGAR V3 emission inventory for 1995. These were later

removed in the model version V10, because they were already included in the RETRO inventory. Further information on the datasets used for aircraft and shipping emissions can be found at Huijnen et al. (2010b). The biomass burning emissions based on GFEDv2 (van der Werf et al., 2006) specific for the year of the run are used on 8 day period time resolution. Emissions of biogenic sources were derived from GEIA (Global Emissions Inventory Activity, Guenther et al., 1995) and the ORCHIDEE model (Lathière et al., 2006). NO<sub>x</sub> production from lightning was calculated using a linear relationship between lightning flashes and convective precipitation, with a total annual production of approximately 5 Tg(N)/yr. As it was mentioned in the MOZART description, SO<sub>2</sub>, NH<sub>3</sub> or DMS emission values were missing for the GEMS inventories setup and were taken from different sources as described in the GEMS Final report (2010) and Huijnen et al. (2010b).

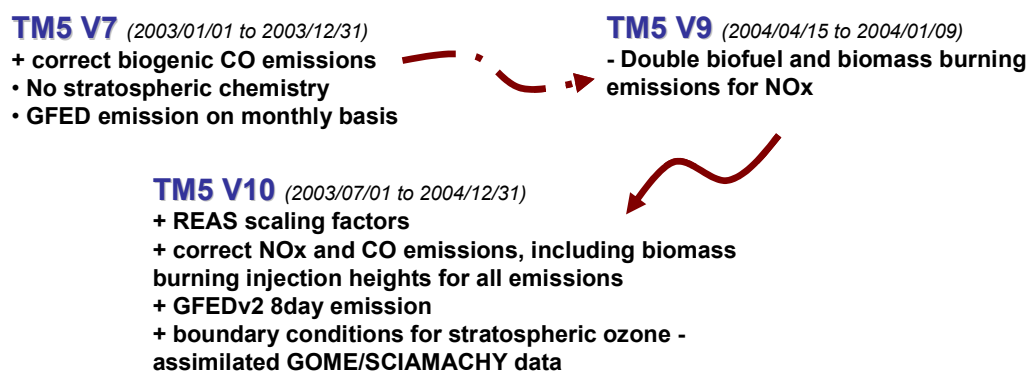


Figure 5.2 Scheme of different TM5 versions analysed and the respective time period of the available results. The changes in each of the versions are noticed: (+) for the improvements and (-) for the problems identified or old settings that were later changed.

## 5.3 Description of evaluation method

### 5.3.1 Data treatment

The NO<sub>2</sub> model outputs, i.e., stratospheric and tropospheric columns, from MOZART and TM5 were analysed for the years of 2003 and 2004. Since the two datasets (simulations and measurements) were quite different, a direct comparison of the original data was not feasible. Adaptation of spatial and temporal resolutions, with matching of datasets, was required to assure consistency of the values compared.

The retrieval of satellite data was already explained in section 2.6. Here, SCIAMACHY total and tropospheric NO<sub>2</sub> vertical columns (hereafter referred to as columns only) will be used to validate the model output.

### a) Time interpolation of model data to the satellite overpass

The first step consisted in selecting, from the model data, the output for the satellite overpass time (approx. 10:00 solar local time (LT)). When the model output was available on an hourly basis (like for the MOZART data), no major transformations were required and the values used were very close to the original ones. However, this was not the case for TM5, which provided only global 3-hour output. In this case, UTC hours used by the model had to be first converted into LT, which were then interpolated to the corresponding satellite overpass time. Since the NO<sub>2</sub> daily cycle does not present a linear variation this approximation will introduce some erroneous values, predominantly evident for the stratospheric data (see for example Figure 5.16 below).

### b) From model layers to stratospheric and tropospheric columns

Satellite measurements provide NO<sub>2</sub> vertical columns. On the other hand, the models offer NO<sub>2</sub> volume mixing ratios per layer. Therefore, the MOZART and TM5 results were integrated into tropospheric and stratospheric vertical columns, as it is illustrated in Figure 5.3. From this figure it becomes evident the large difference between the NO<sub>2</sub> amount at high altitudes and in the layers closer to the surface.

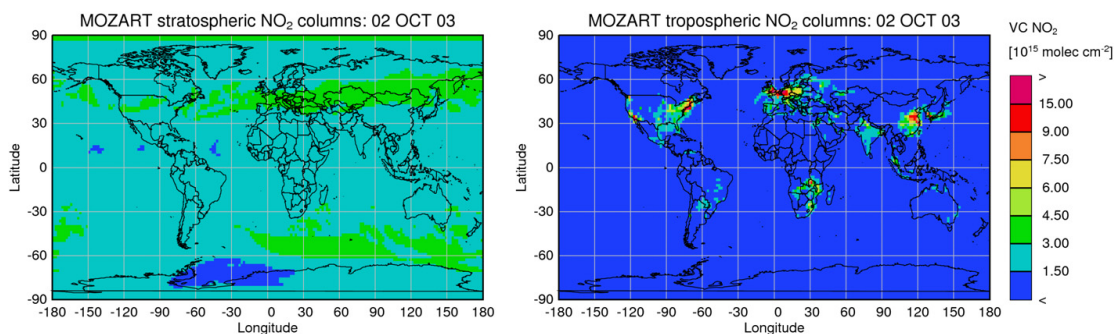


Figure 5.3 One day (2<sup>nd</sup> October 2003) of NO<sub>2</sub> data from model output (MOZART V10 in this example) separated into stratospheric (left) and tropospheric columns (right).

For the separation of the stratosphere and troposphere, a latitude dependent tropopause height was used from Santer et al. (2003). This simplistic approximation of the boundary between the lower layers of the atmosphere does not fully represent its inter-annual variability or spatial variations (see further information on the tropopause in chapter 2). The incorrect tropopause height might lead to

inaccurate attribution of the  $\text{NO}_2$  to either the tropospheric or stratospheric column. Still, in the typical tropopause region, the  $\text{NO}_2$  concentrations are very low (see chapter 2) and, therefore, the impact of this approximation on the results can be neglected. In addition, the accurate determination of daily global tropopause height is a complex process that involves many uncertainties. For these reasons, the use of an averaged estimation of this height was a good approach for this exercise.

### c) Re-gridding satellite data into model resolution

As described in the previous section, the spatial resolutions of the models were different and coarser than the standard SCIAMACHY product ( $0.125^\circ \times 0.125^\circ$ ). Thus, the daily satellite measurements were re-gridded in the correspondent model resolution:  $1.875^\circ \times 1.875^\circ$  for MOZART, and  $2^\circ \times 3^\circ$  for TM5, the model versions analysed in the present thesis. In this process, the average of all valid SCIAMACHY grid boxes within one model grid box was taken without applying any area weighting, i.e., all satellite data are considered as long as part of it is located within the model box.

As it is possible to see from Figure 5.4, this process resulted in loss of information from the satellite measurements. The hot-spots for the  $\text{NO}_2$  columns were averaged when a larger grid was considered and the exact locations of major point sources could not be identified (see for example the region of China where the high values are not observed whatsoever in the coarser grid and the maximum registered is  $\sim 2.00 \times 10^{16}$  instead of  $\sim 5.00 \times 10^{16}$ ). On the other hand, the coarser grid also improved the coverage of measurements. This occurs because the bigger grid boxes include the average of small boxes (within that area), even if only one measurement was available for such a large area. However, this means that locations without available measurements the  $\text{NO}_2$  tropospheric columns were still represented, which might result in some incorrect values for certain locations. Nevertheless, this can also be perceived as an advantage for this specific evaluation exercise because less model data was excluded in the following step.

### d) Matching of available satellite data

A last required process was to select the model data according to the existing satellite data, ensuring that both datasets consisted of data for the same days at the same locations. This is mostly important because SCIAMACHY data are not available on a daily global coverage. As explained in section 2.7, the global coverage would be obtained, in optimal conditions, every 6 days (assuming that, for example, no orbit will be missing due to technical issues). Moreover,  $\text{NO}_2$  tropospheric columns are only determined for clear sky pixels, i.e., cloud fraction smaller than 20% according to the FRESCO dataset (Koelemeijer et al., 2001, 2002). This led to the exclusion of some measurement pixels, a situation that occurs with higher incidence in the winter periods. Additionally, the retrieval is not performed over very bright surfaces that cannot be easily

## Validation of NO<sub>2</sub> model output

distinguished from clouds. Thus, a recurrent lack of values over some regions is verified, e.g., for Greenland, Antarctica or the Arctic (which in the case of the NO<sub>2</sub> is not so problematic since these are fairly clean regions). For this reason, the daily model data previously selected for the overpass time were then matched to the available SCIAMACHY data already converted in the model resolution (an example can be seen in Figure 5.5). Hence, in this evaluation exercise, only a small fraction of the model data was in fact used. Given that for some regions data were systematically excluded in some months, this might have resulted in an artificial bias that needs to be accounted for in the analysis of results.

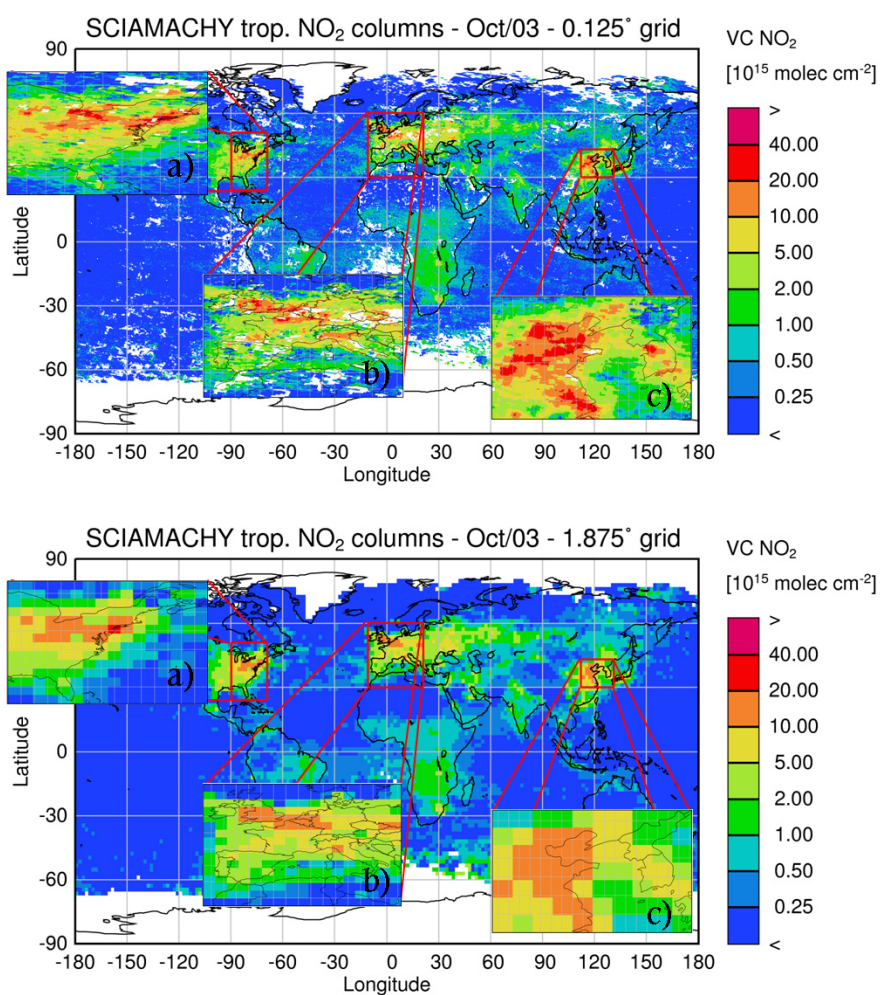


Figure 5.4 Monthly average (October 2003) of tropospheric NO<sub>2</sub> vertical columns for SCIAMACHY. Differences illustrated for fine (0.125°, top) and coarse (1.875°, bottom) spatial resolution. Three regions characterised by high anthropogenic emissions are amplified: a) USA, b) Europe and c) China.

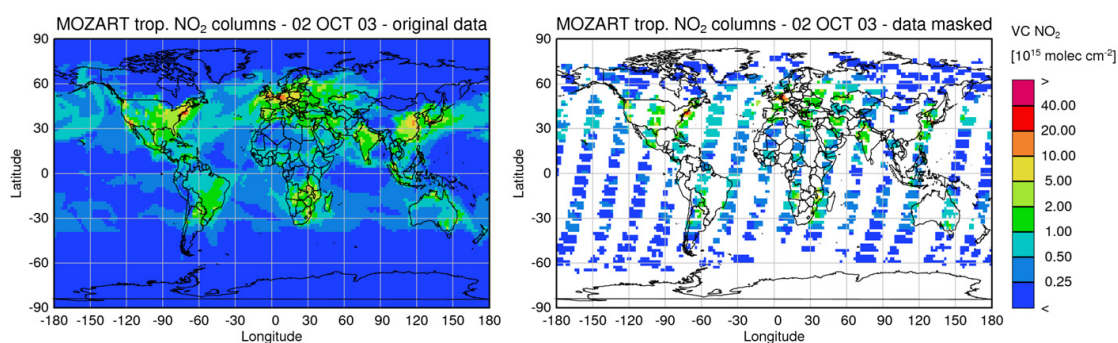


Figure 5.5 One day (2<sup>nd</sup> October 2003) of tropospheric NO<sub>2</sub> vertical columns from model output (MOZART V10 in this example) in its original format (left) and after the masking with SCIAMACHY available measurements (right) on the same day.

Nevertheless it is important to mention that the analysis was not performed on a daily basis but rather with monthly averages, assuring predominantly the global spatial coverage.

### e) Additional adaptations

After performing all those steps, the two datasets were finally consistent and the model output could be evaluated against the satellite measurements. Still, it is important to notice that the SCIAMACHY stratospheric columns are in fact total columns. While, the model data was divided into tropospheric and stratospheric NO<sub>2</sub> columns, the (current) retrieval method of trace gas columns from satellite measurements does not truly separate the NO<sub>2</sub> amount in the stratosphere from what remains below in the troposphere. Therefore, the amount considered here as stratospheric includes a weighted part of the tropospheric NO<sub>2</sub>. Nevertheless, this contribution is relatively small, especially over unpolluted regions as is the case of the Pacific region used as reference sector, i.e., 140°W to 180°W (or 180° to 220°). For the remaining regions, the use of stratospheric airmass factor (AMF) would discard part of the tropospheric NO<sub>2</sub> amount. The sensitivity of the measurements decreases to the lower atmosphere. Since this is not accounted for in the AMF used, the contribution of the lower NO<sub>2</sub> to the total columns is rather small. Furthermore, as no cloud screening is performed for the stratospheric data, all the tropospheric NO<sub>2</sub> below the clouds is not included in the total column values either. Still, as it will be explained below, the following model evaluation was focused on the reference sector region only. In the following sections, satellite measured stratospheric columns will be labelled as total columns to facilitate the distinction from the model stratospheric columns as, in fact, the two values do not strictly correspond to the same amount.

### 5.3.2 Data comparison - methods

Throughout the GEMS project, several methods were used to validate the NO<sub>2</sub> columns, and some of those are presented in the following sections. In a first step, 2D global maps of monthly (not presented) and/or 3 month averages allowed for a preliminary qualitative interpretation of the overall results. In addition, several regions were selected according to their relevance for NO<sub>x</sub> emissions, and monthly averages were determined for those. These regions are shown in Figure 5.6 below. For the evaluation of the stratosphere, the study regions considered corresponded to different latitude bands for the commonly named reference sector: 140°W to 180°W. This was done in order to minimise the contribution of tropospheric NO<sub>2</sub> to the total columns and guarantee that the same columns from model and measurements were being compared. The division in latitude bands would not be sensible for the troposphere where the spatial variation is more accentuated. The tropospheric regions were selected according to their representativeness of the regions, characterised by either anthropogenic sources (polluted regions) or biomass burning events. The study of the NO<sub>2</sub> time series provided useful insights on the temporal variations included in the model schemes.

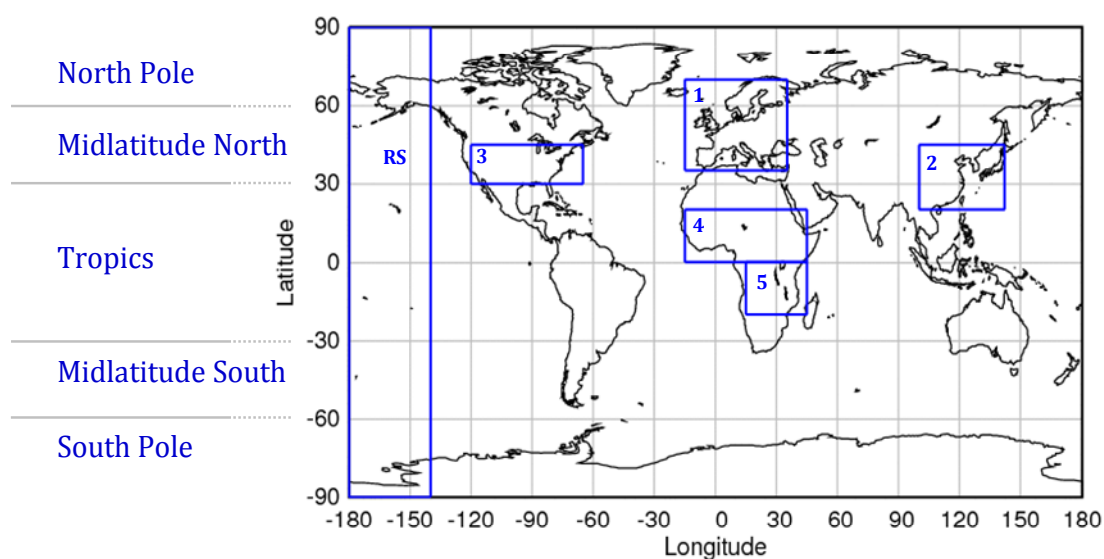


Figure 5.6 Regions selected for the evaluation of NO<sub>2</sub>. Stratospheric regions correspond to latitude bands (named in the left side of the figure) in the reference sector region (RS). Tropospheric regions are represented on the map: 1) Europe, 2) East-Asia, 3) US, 4) Northern Africa (henceforth North-Africa) and 5) Southern Africa (henceforth South-Africa). Regions 1-3 correspond to polluted places and 4-5 to typical biomass burning areas.

## Description of evaluation method

---

For the tropospheric regions only data over land was considered when calculating the monthly averages. The very low values over the oceanic regions would have biased the comparison and, therefore, the evaluation of the tropospheric columns was restricted to the location of the main NO<sub>2</sub> emission sources. This selection also excluded high values that are occasionally measured over water due to long-range transport events.

Monthly averages were good measures for an initial assessment of the model performance. With these it was possible to assess if the amount of NO<sub>2</sub> simulated by the model was close to the satellite measurements. Furthermore, a spatial correlation coefficient was also used to determine exactly how the data over such large regions would compare between measurements and simulations. Scatter plots (and the determination of slope and offset between the two datasets) are also valuable tools to evaluate the model results. These allow for a more detailed analysis on the quantitative level to determine exactly where the model is under- or overestimating the NO<sub>2</sub> columns measured. Moreover, an approach based on skill scores was also developed within the GEMS project. These metrics varied between 0 and 1 (bad to good model performance, respectively) and were based on a normalised bias (between model and observation) determined with the averages at certain location. The scores were especially useful since model performance could be quickly determined. The main objective would be to calculate a single score that would illustrate how the model simulations compare to the satellite measurements. This was a novel approach that evolved throughout the project according to identified problems. A drawback of this method was for example the challenge to find validation regions that would be representative of different trace gases knowing that, for example, the hot-spots of NO<sub>2</sub> and HCHO are quite different. For the case where, in the selected regions, the trace gas concentrations are low, both the model and measurements, a good model performance would be established. However, this interpretation might conceal flaws over other regions where important sources are located. The use of a single score in such a situation would certainly not be the ideal approach. Furthermore, it was found that these values were often too influenced by factors like data availability. In some occasions this would lead to contradictory conclusions when comparing the monthly maps or considering the score values. The deep evaluation of model output based on the scatter plots and/or skill scores is beyond the purpose of the work presented here and will, therefore, not be explored in detail. The seasonal trends and the correlation values provide a good example of what can be done and are sufficient to identify the main current problems of CTMs. Further information on the remaining methods and its results can be found in the GEMS Final report (2010).

## 5.4 Results: Comparison with independent satellite data

Model validation is an important assessment of the accuracy of simulations and allows for an identification of weak points that can later be improved and/or corrected. Nevertheless, a comparison of model results with satellite data can also highlight phenomena that are still not completely understood and, thus, not fully expressed in the model schemes. Furthermore, consistent and systematic differences between satellite and model simulations that are not easily explained can also indicate regions and/or events where the satellite retrieval method of vertical columns still requires improvement. Here, an attempt is made not only to compare and validate the model results with the satellite observations, but also to understand and explore the reasons for the differences found.

Stratospheric NO<sub>2</sub> columns are expected to be fairly constant over the same latitude and a systematic annual variability is frequently observed. The poles are an exception of such behaviour where the concentrations also vary according to polar vortex formation and its characteristics. As it was explained in the introductory chapters, the formation and destruction of NO<sub>2</sub> in the stratosphere involves several reactions and these mechanisms are rather complex (see section 2.3 for more details). Nevertheless, it is possible to say that the main source of NO<sub>x</sub> in the stratosphere is the uplifted N<sub>2</sub>O that yields NO, from the reaction with oxygen atom in exciting state. The NO is later converted to NO<sub>2</sub>. The dynamics in the stratosphere is a rather important factor regulating the distribution of trace gases. This is highly important also for the polar vortex and a correct simulation of this feature becomes essential for good model results, at least in near-polar regions.

The analysis of the tropospheric data is more complex than the stratosphere output, since different source regions and types of emissions need to be considered. In the lower layer of the atmosphere, the NO<sub>x</sub> has a shorter lifetime than in higher altitudes (van Noije et al., 2006, and references therein), and concentrations of this trace gas vary considerably in time and space. The tropospheric columns are very much dependent on the location of main sources of this trace gas (e.g., fossil fuel combustion processes and biomass burning). In addition, long-range transport of NO<sub>2</sub> (e.g., from the US to Europe) in the upper troposphere is also observed in the satellite measurements. The large urban areas and industrial sectors are, normally, hot-spots easily identified, and sometimes it is also possible to recognise single large power plants that are isolated from other sources (e.g., Four Corners coal-fired power plant in New Mexico, USA, or the Highveld region in South Africa). Emission factors combined with data from emission inventories are, to a large extent, the key model parameters in the simulation of NO<sub>2</sub>. In addition, the chemistry scheme is also important, especially

in the troposphere, where this trace gas presents a strong daily cycle and its concentrations are highly influenced by the atmospheric composition (see section 2.3 for details on the tropospheric chemistry of  $\text{NO}_2$ ). Biomass burning emissions can be considered as natural sources although, often, the burning of large areas of crops after the harvesting season is a traditional agricultural practice in many cultures. Good examples of large emissions of  $\text{NO}_x$  from fires observed from satellite are the large savannah fires in Central Africa (see Figure 2.5 depicting the fire counts from MODIS observations). With a regular occurrence, a large area of the northern region close to the tropics burns in the end/beginning of the year, alternating in the summer months with the southern region. This phenomenon is observed systematically every year and these regions are large sources of  $\text{NO}_2$  easily identified in the maps of satellite measurements. Furthermore, regions like Amazonia or Indonesia are also detected in certain months that are characteristic for biomass burning season. Emissions from fires are largely dependent on the type of vegetation burned (e.g., Brasseur, 2003) and, therefore, it is essential that surface type is correctly considered in the models. Furthermore, emission factors from fires and conversion rates between, for example, VOCs and  $\text{NO}_x$  are still rather unknown for these situations due to their high variability from scene to scene. All these factors combined make the simulation of biomass burning emissions a great challenge. The integration of different products and databases globally available has been a good advantage for the models involved in the GEMS project.

### 5.4.1 MOZART

As pointed out before, during the GEMS project there were several versions for MOZART standalone (offline) runs. Newer versions were often the result of the validation exercises. The analysis of different simulations allowed for the interpretation of the impact of model parameterisation on the  $\text{NO}_2$  fields. A good example is the stratospheric definition and how much the results changed according to the dataset used for initialisation variables, or impact of different emission inventories in the tropospheric columns.

The selected 3 month averages of stratospheric  $\text{NO}_2$  determined by different MOZART versions, presented in Figure 5.7 and Figure 5.8, illustrate how the model has changed during the extent of the GEMS project. While, for the year 2003, the initial version of MOZART V1 did not perform well, the standalone V7 shows stratospheric  $\text{NO}_2$  fields that agree nicely with the satellite data (spatially and temporally). The problematic simulation of the stratosphere in the initial version (extremely high values in the high latitude regions in the winter periods of the Polar Regions) was in part related to wrong upper boundaries of the species and incorrect stratospheric chemistry.

## Validation of NO<sub>2</sub> model output

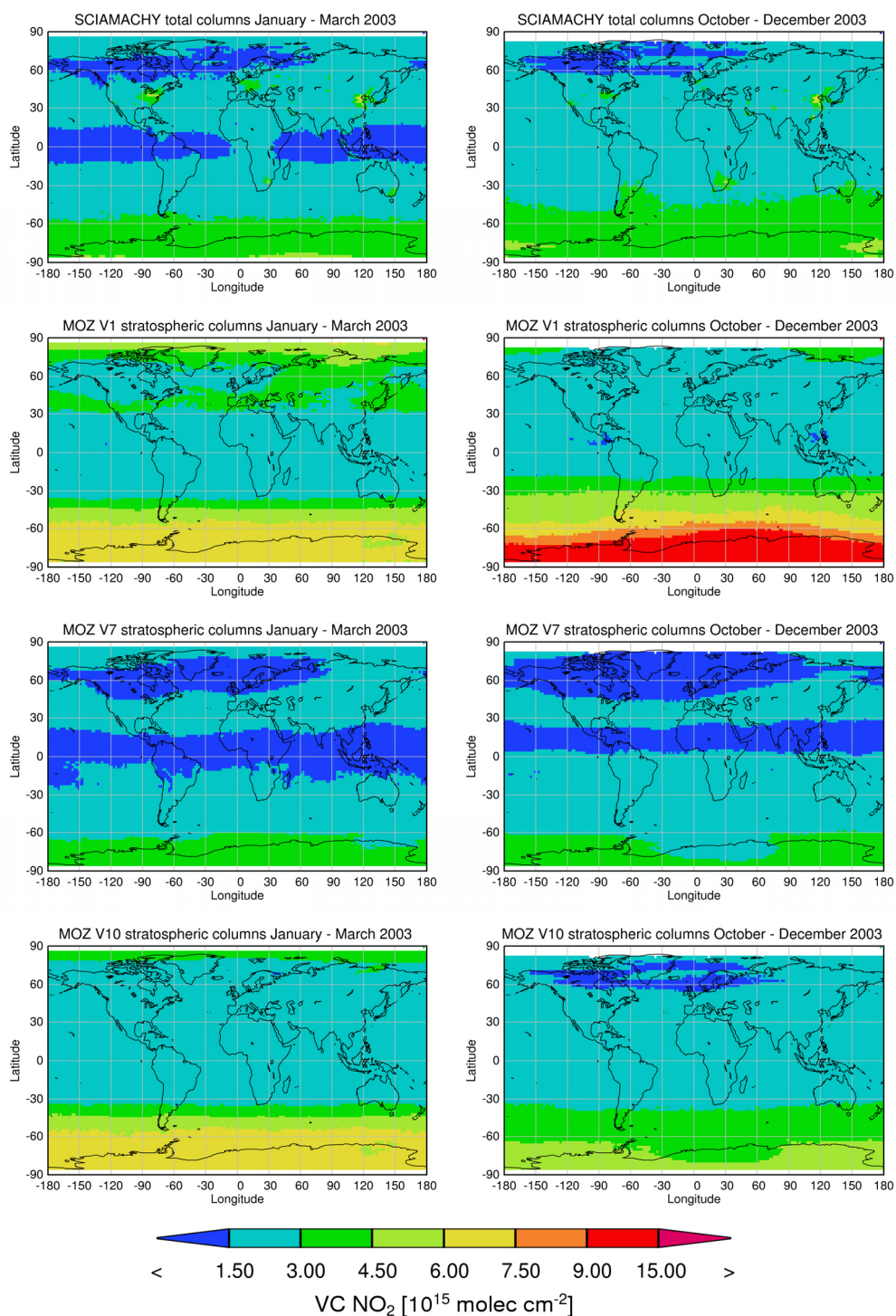


Figure 5.7 Three month averages of global total NO<sub>2</sub> columns measured by SCIAMACHY (top) and stratospheric columns determined by (from second of the top to bottom) MOZART V1, V7 and V10, for the periods of January – March (left) and October – December (right) of the year 2003.

## Results: Comparison with independent satellite data

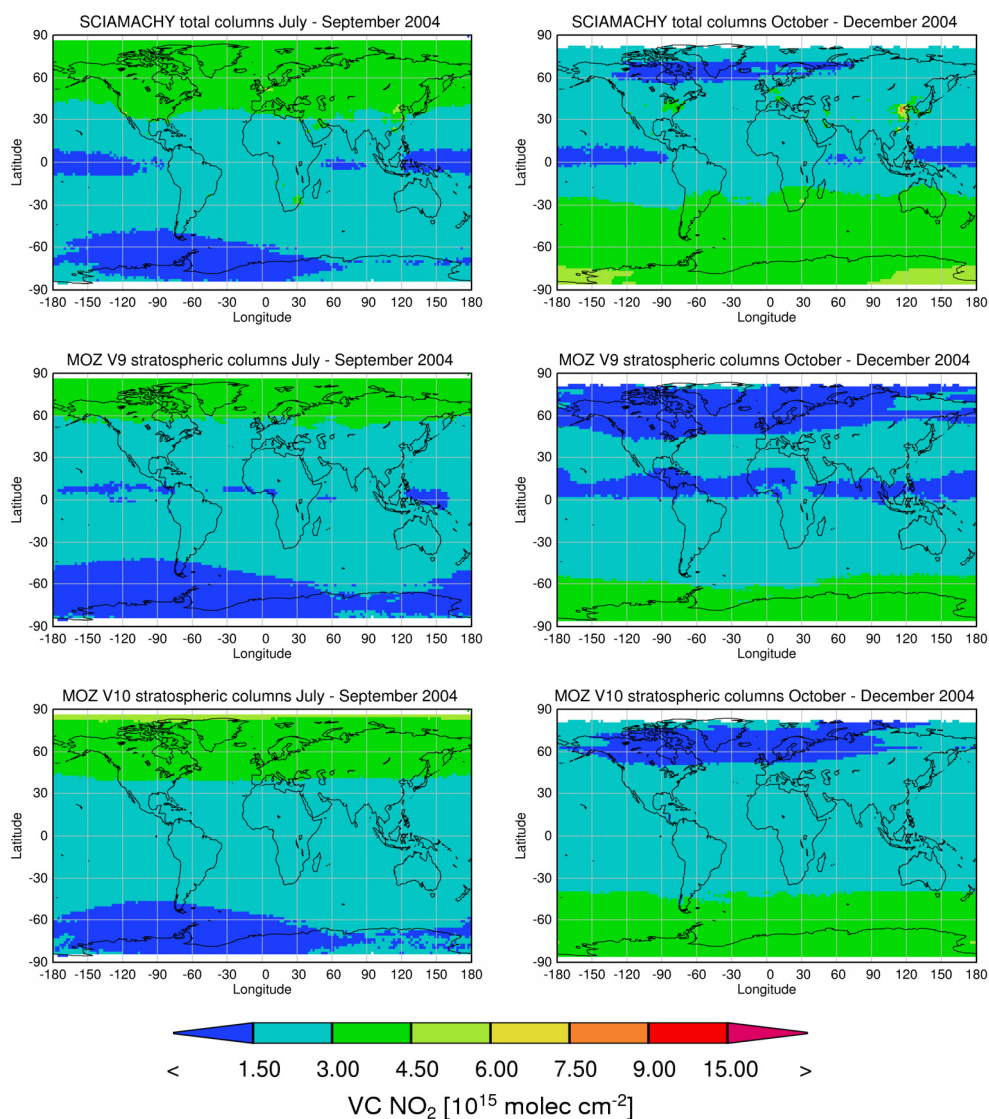


Figure 5.8 Three month averages of global total NO<sub>2</sub> columns measured by SCIAMACHY (top) and stratospheric columns determined by MOZART V9 (middle) and V10 (bottom), for the periods of July – September (left) and October – December (right) of the year 2004.

The lack of simulated ozone depletion in this layer for the year 2003 is also an indication of erroneous settings that influence both species. This was corrected for the following versions. The latest version V10 is a peculiar case, since in 2003 from January to August the NO<sub>2</sub> columns in the stratosphere are often overestimated by a factor of 2 when compared to the satellite measurements. On the other hand, for the year 2004 both model versions (V9 and V10) have very good results with only a slight overestimation in the winter months, in the tropics regions, for the version V10 (the output for the other versions were simulated only for specific case scenarios on the summer of 2004). It becomes then essential to emphasise that the results of V10 show a general decrease (up to

## Validation of NO<sub>2</sub> model output

57% in May in the Northern Polar Region) in the stratospheric NO<sub>2</sub> from 2003 to 2004. However, this trend is not observed by the satellite, and such differences can be better identified in the seasonality curves in Figure 5.9. Here it is quite evident the great improvement from recent versions compared to V1. Even with the overestimation of the satellite values in some months of 2003, the latest version provides an overall best agreement.

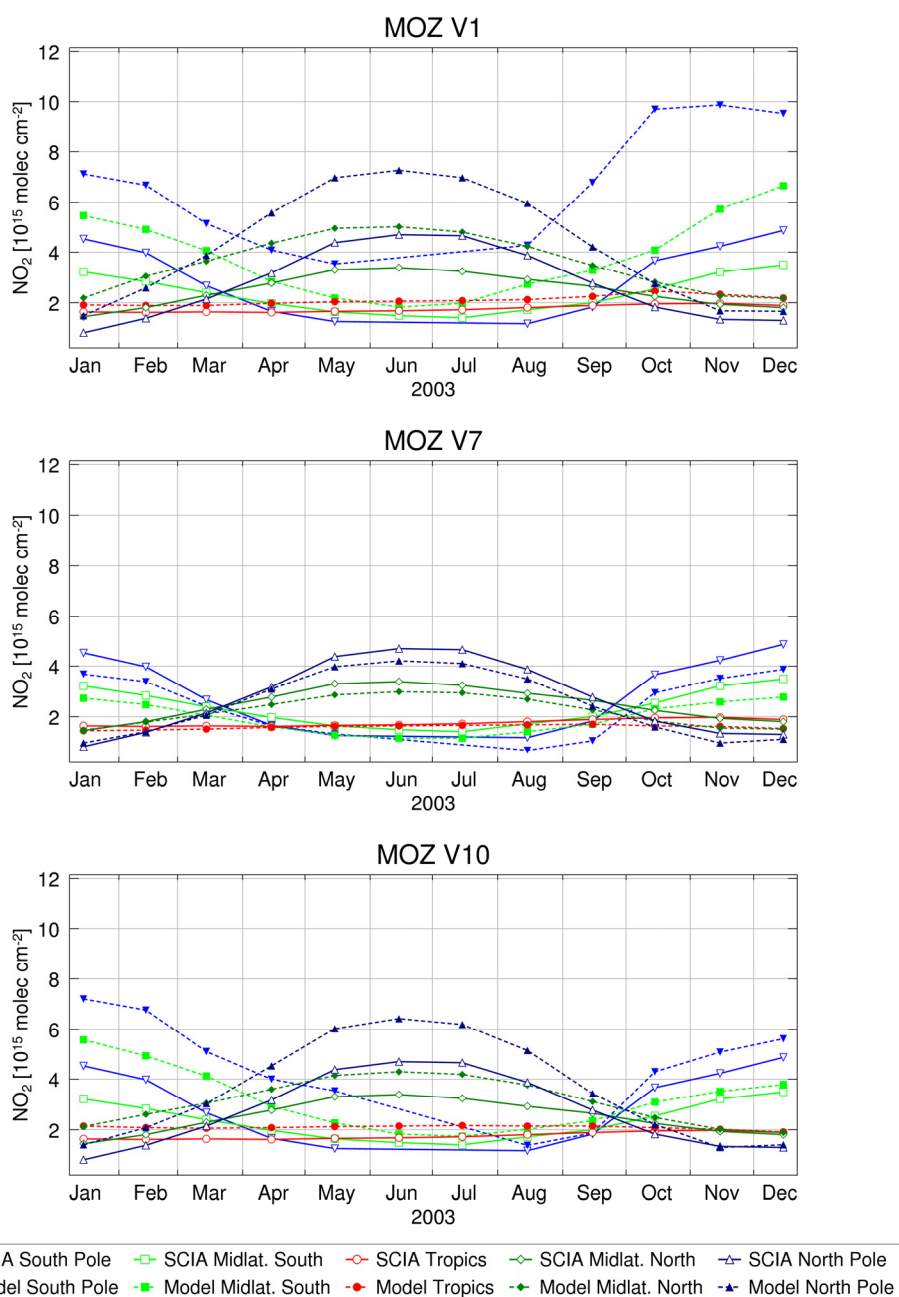


Figure 5.9 Seasonality curves for the year 2003 of total NO<sub>2</sub> columns measured by SCIAMACHY (open symbols) and stratospheric columns determined by MOZART V1 (top), V7 (middle) and V10 (bottom). Monthly averages determined for the selected regions as defined in Figure 5.6.

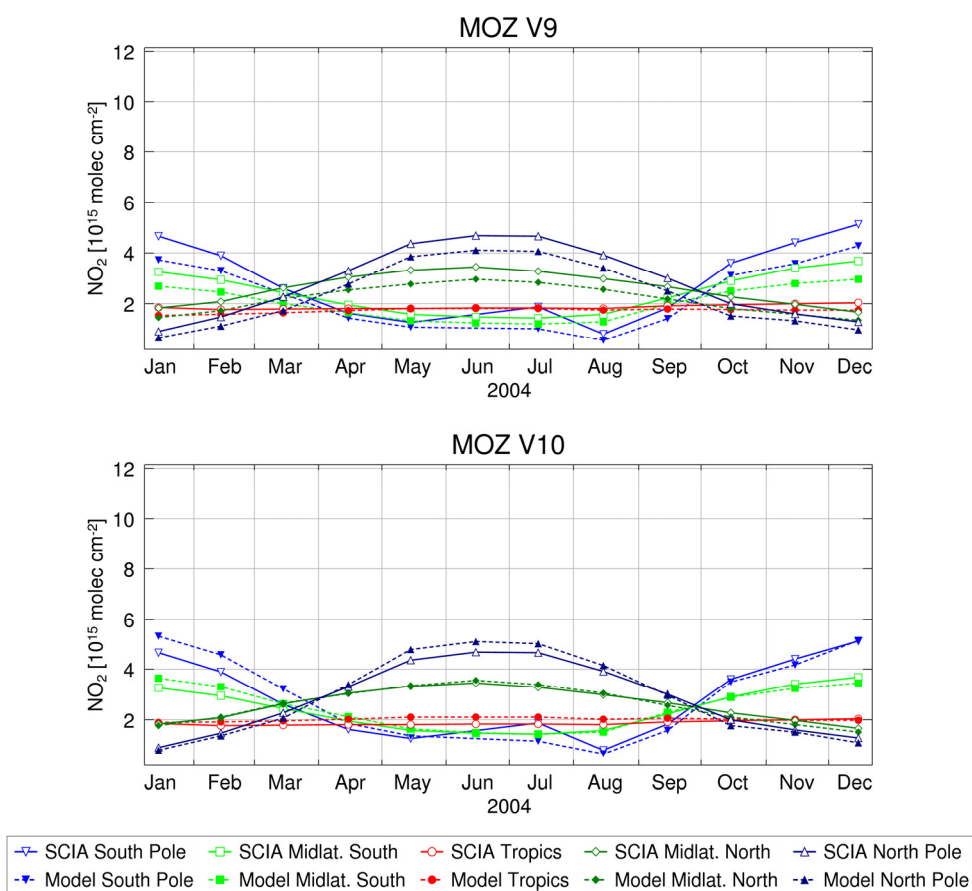


Figure 5.10 Seasonality curves for the year 2004 of total  $\text{NO}_2$  columns measured by SCIAMACHY (open symbols) and stratospheric columns determined by MOZART V9 (top) and V10 (bottom). Monthly averages determined for the selected regions as defined in Figure 5.6.

As mentioned earlier, the analysis of tropospheric data is more complex than for the stratosphere. The high variability observed in time and space is often related to the location of sources and short lifetime of  $\text{NO}_2$ . These factors are determinant for the correct model simulations. From the figures below it is possible to observe that above polluted regions, the modelled tropospheric  $\text{NO}_2$  columns are usually similar to the satellite measurements. MOZART V1 is once more the exception since it underestimates, throughout the year, by far, the  $\text{NO}_2$  over regions like the US, Europe or East-Asia. The subsequent adjustments performed in the chemistry scheme (e.g., the reaction rates and constants) might explain the observed improvements. Nevertheless, for East-Asia, this error was partly attributed to the combination of inaccurate emission inventories that did not reflect the rapid population growth and consequent development and increase of industrial activities.

## Validation of NO<sub>2</sub> model output

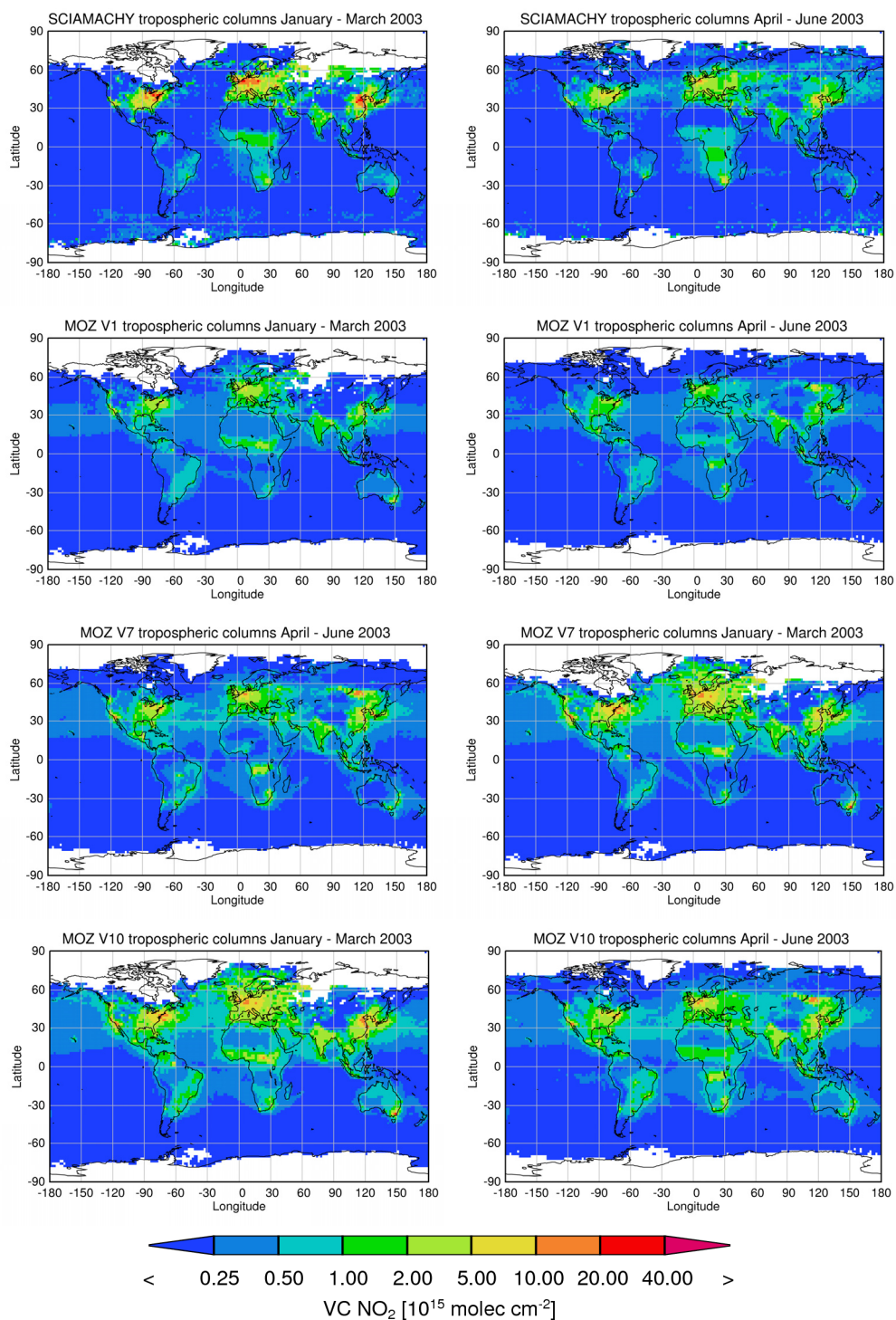


Figure 5.11 Three month averages of global tropospheric NO<sub>2</sub> columns measured by SCIAMACHY (top) and determined by (from second of top to bottom) MOZART V1, V7 and V10, for the periods of January – March (left) and April – June (right) of the year 2003.

## Results: Comparison with independent satellite data

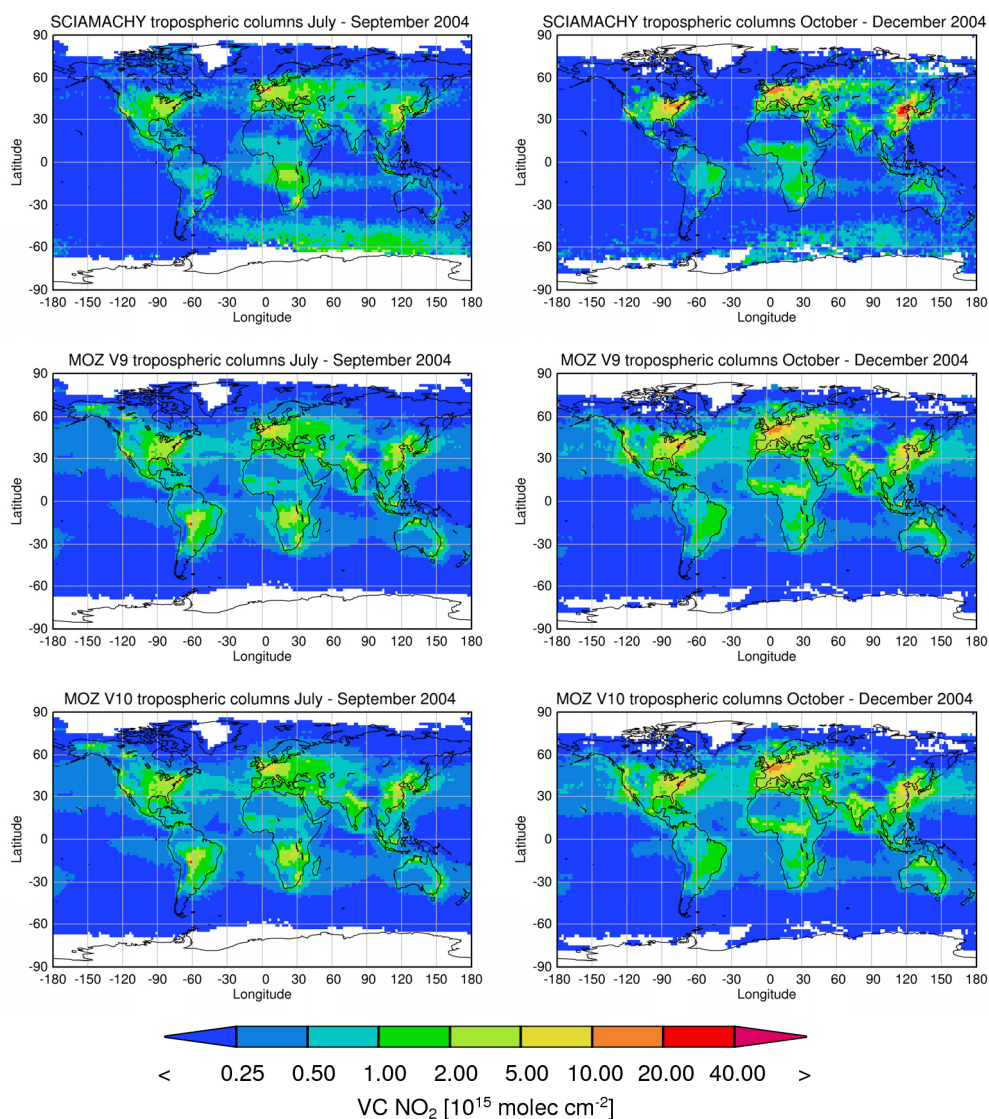


Figure 5.12 Three month averages of global tropospheric  $\text{NO}_2$  columns measured by SCIAMACHY (top) and determined by MOZART V9 (middle) and V10 (bottom), for the periods of July – September (left) and October – December (right) of the year 2004.

In V7, the introduction of up-to-date emission values for East-Asia, from the REAS inventory, resulted in a more reasonable model output in this region. In the following versions, the seasonality for CO and  $\text{NO}_x$  was corrected in the model scheme and better agreement was found between simulations and measurements. Nevertheless, for the winter periods, the differences between model results and observations remained quite high. If the longer lifetime of  $\text{NO}_2$ , in this season, is not correctly represented in the model scheme, then the  $\text{NO}_2$  concentrations will be too low in the simulations. In addition, also the emission inventory might underestimate the  $\text{NO}_2$  emissions for the winter time. On the other hand, in the period of November 2003 to February 2004 (and again in the end of 2004) all versions (with the exception of V1) overestimate the  $\text{NO}_2$  in Europe which is quite

## Validation of NO<sub>2</sub> model output

unexpected. Once more, outdated emission inventories can be a possible explanation for this feature. Opposite to what was observed for East-Asia, in Europe the data used did not follow the decreasing trend in this region prompted by the implementation of environmental legislation that forced the reduction of emissions. In addition, the high emission values attributed ships might contribute, in part, to such overestimation. The differences pointed out above are more clearly observed in the seasonality plots presented in Figure 5.14 and Figure 5.15. To a certain degree, this difference could be linked to incorrect SCIAMACHY columns caused by errors in the retrieval process. It is known that East-Asia is an extremely polluted region and the aerosol load is frequently very high (Streets et al., 2009). As it was illustrated in the previous chapters, currently, the influence of the aerosol to the radiation that reaches the satellite is not fully described in the retrieval method. However, since these effects are rather complex, it is difficult to predict if the measured tropospheric columns are under- or overestimated. Furthermore, during the winter periods, the satellite measurements are scarcer because of increased cloud cover. Also, the sensitivity of the measurements to the NO<sub>2</sub> close to the surface is smaller in this period due to the low Sun.

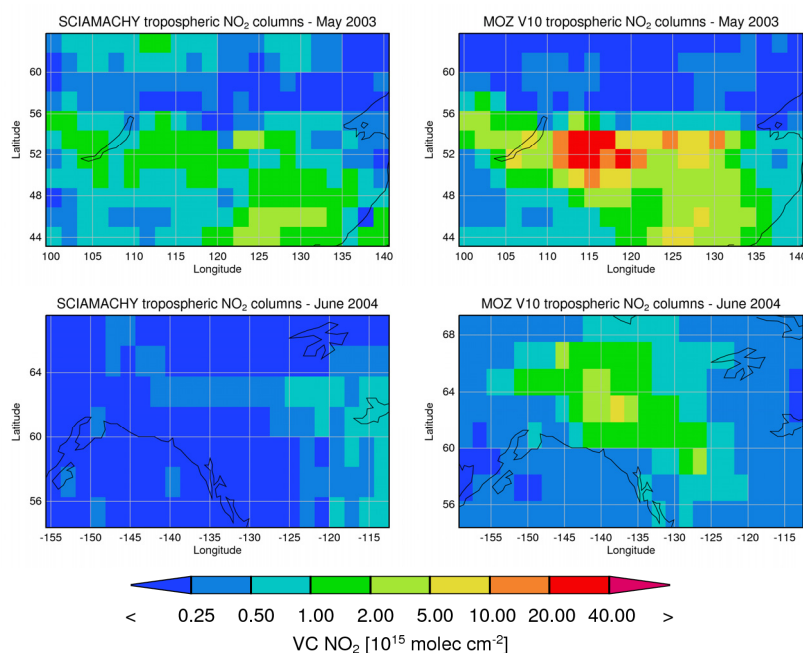


Figure 5.13 Monthly averages of tropospheric NO<sub>2</sub> columns measured by SCIAMACHY (left) and determined by MOZART V10 (right) for two different case studies: Siberia fires – May 2003 (top) and, Alaska fires – June 2004 (bottom).

As mentioned above, a dominant natural source of NO<sub>2</sub> is the burning savannah in central Africa. The figures above highlight a general tendency of overestimation of the NO<sub>2</sub> for wildfire events. The exception is, for 2003, the MOZART V1, which was able to simulate the right order of magnitude

over the regions in Africa. However,  $\text{NO}_2$  in the following versions was overestimated. Figure 5.13 illustrates such discrepancy between the satellite data and the results of latest model version (V10) for two major events of boreal fires: in the region of Siberia in May 2003, and Alaska in June 2004. This type of fires is typical for its smouldering combustion and low content of nitrogen which leads to low  $\text{NO}_x/\text{CO}$  emission ratios. Furthermore, a rapid conversion to PAN might explain why, in the satellite observations, almost no  $\text{NO}_2$  is measured in these regions. The model simulations are much higher probably because of an incorrect parameterisation of the facts above mentioned. Differences are also found for other types of fires in South America, in 2004, and central Africa, for both years. This is in fact quite unexpected since from V7 onwards the emission dataset was changed from a monthly based to 8 day period which should have reflected as an improvement on the simulations. However, apart from this, other modifications in the chemistry scheme and reaction rates, namely those for  $\text{CO} + \text{OH}$ , can also be a reason for an increase of  $\text{NO}_2$ , when, e.g., limiting the formation of  $\text{HNO}_3$ . Furthermore,  $\text{NO}_2$  from tropical fires is normally present in higher altitudes (due to pyroconvective lofting) which might not be well described in the model simulations. On the other hand, the differences found might also be related to some uncertainties in the retrieved vertical columns. In the case of fires, it is difficult to predict the vertical distribution of trace gas and particles, and how the sensitivity of the measurements would be influenced. The results presented in the previous chapters have shown that higher plumes of highly absorbing aerosol can shield the trace gas below. Thus, when this is not accounted for in the retrieval, the  $\text{NO}_2$  columns might be underestimated. Conversely, many particles mixed with the trace gas will enhance the scattering of the light.

As expected, the last two versions V9 and V10 present very similar results for the tropospheric  $\text{NO}_2$ . The  $\text{NO}_2$  values in the lower atmospheric layer were not so influenced by this update because the difference between those two versions is mostly related to the stratospheric parameterisations.

### 5.4.2 TM5

In this section, the evaluation of results from the TM5 standalone runs is presented for the year 2003 with V7 run, and 2004 with V9 (only the summer period), and V10.

The stripes appearing at high latitudes in the Southern hemisphere in the stratospheric TM5 maps, in Figure 5.16 below, are an artefact caused by the processing of the model data, as explained in section 5.3.1. The strong variation in stratospheric  $\text{NO}_2$  chemistry with time is not fully compensated with a linear interpolation applied to the 3-hour TM5 fields, and the sharp differences in values for different satellite orbits become more visible.

## Validation of NO<sub>2</sub> model output

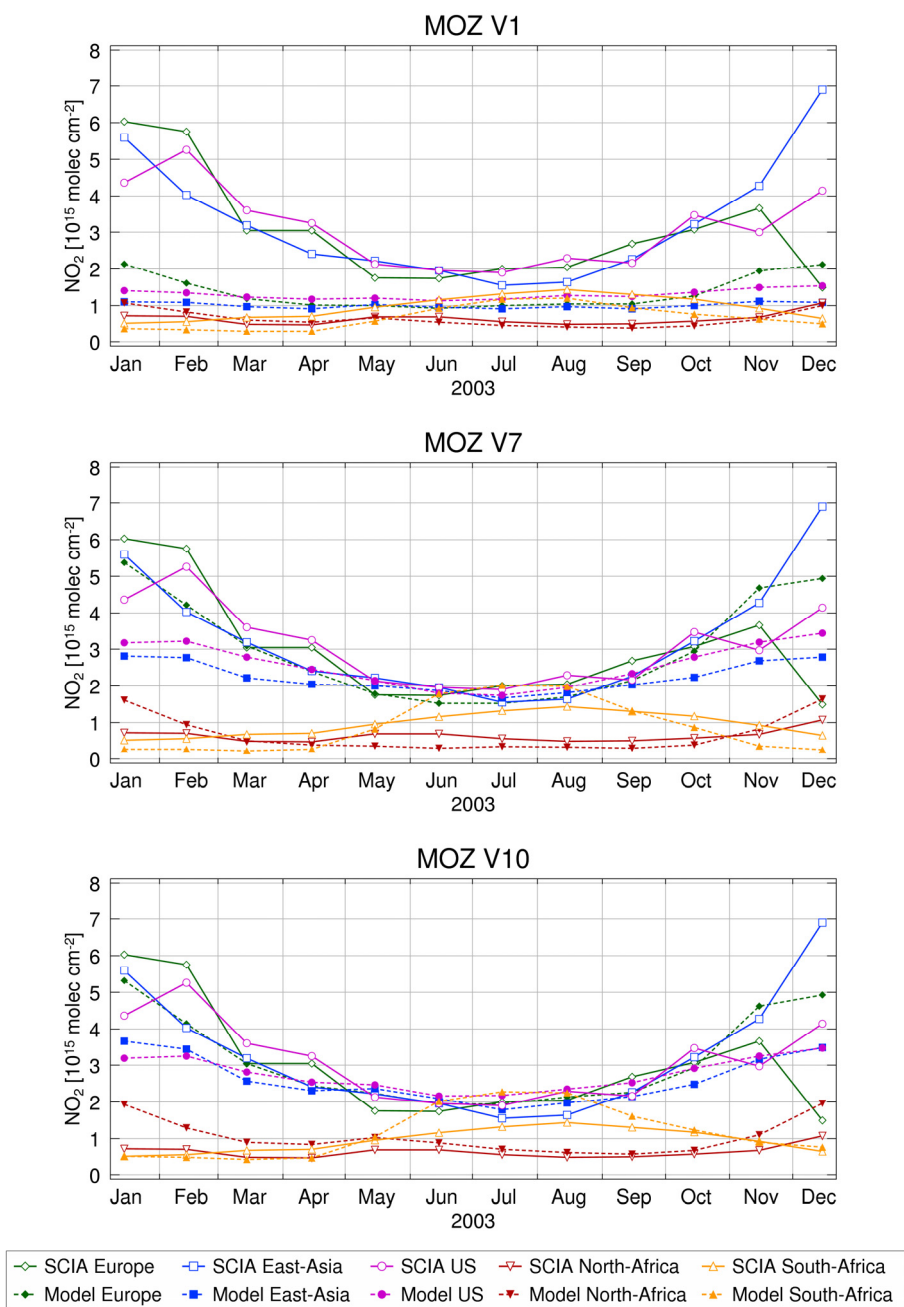


Figure 5.14 Seasonality curves for 2003 of tropospheric NO<sub>2</sub> columns measured by SCIAMACHY (open symbols) and determined by MOZART V1 (top), V7 (middle) and V10 (bottom). Monthly averages determined for the selected regions as defined in Figure 5.6.

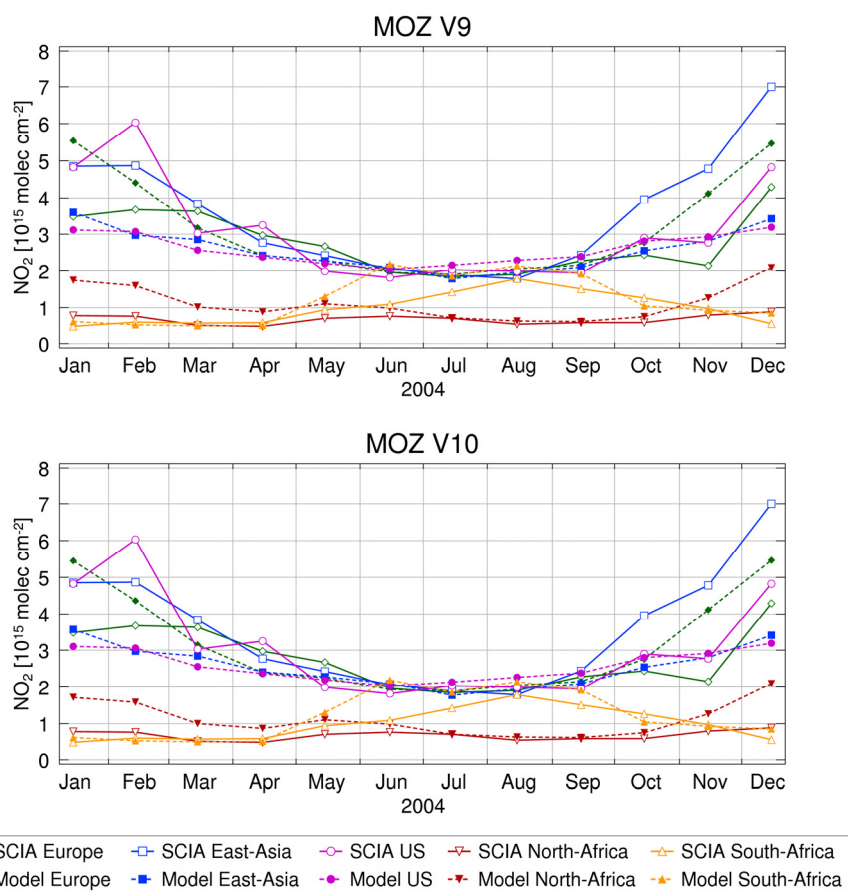


Figure 5.15 Seasonality curves for 2004 of tropospheric  $\text{NO}_2$  columns measured by SCIAMACHY (open symbols) and determined by MOZART V9 (top) and V10 (bottom). Monthly averages determined for the selected regions as defined in Figure 5.6.

The differences found for the stratospheric product from TM5 V7 are highlighted for the second half of the year 2003 (see Figure 5.16). At high latitudes, the  $\text{NO}_2$  values from satellite are lower than the modelled ones and the opposite is observed in the tropics. The succeeding versions that provided data for the year 2004 were able to simulate slightly better the  $\text{NO}_2$  over the high latitude regions (see Figure 5.17). However, the latest version V10 overestimates the stratospheric  $\text{NO}_2$  over the South Pole region, especially in the second half of 2004. This is not surprising considering that the model is not focussed on the stratosphere, and the chemistry scheme in this layer is the same as for the troposphere. Furthermore, the concentrations in the Polar regions are dependent on many other factors related to dynamics of the polar vortex and ozone hole occurrence. Therefore, bearing this in mind, the results are quite good but also highlight the importance of correct  $\text{NO}_2$  chemistry scheme in the higher atmosphere. The seasonal trends of TM5 output for the years 2003 and 2004 (Figure 5.18) illustrate the similarity between the different model versions. The South Pole values are overestimated by V7 and V10 in the winter period (local summer) and this maximum appears to be

## Validation of NO<sub>2</sub> model output

shifted by 1-2 months. The remaining stratospheric columns are in general good with only a remark necessary for the low seasonality observed in mid-latitudes.

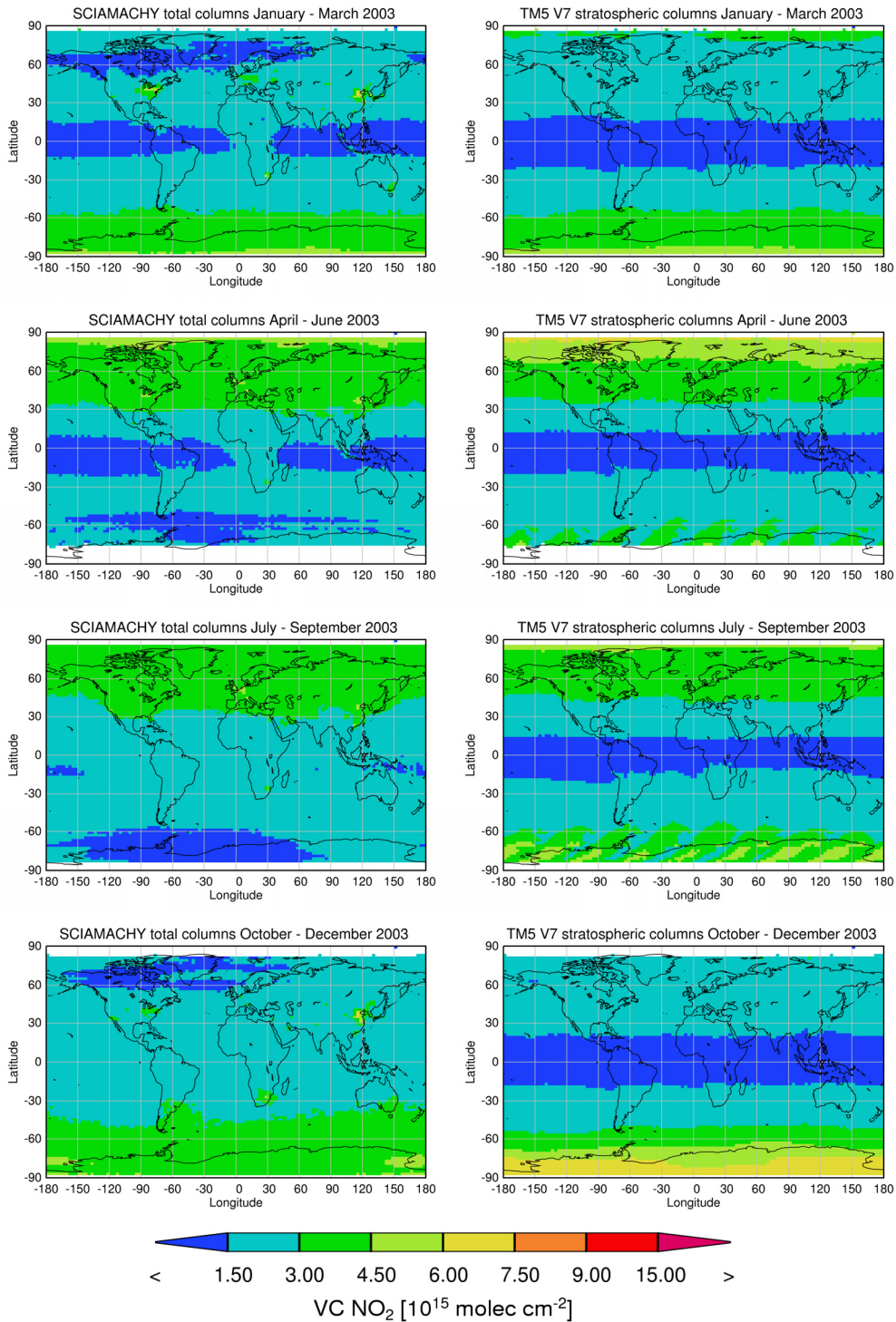


Figure 5.16 Three month averages of global total NO<sub>2</sub> columns measured by SCIAMACHY (left) and stratospheric columns determined by TM5 V7 (right) for the year 2003.

## Results: Comparison with independent satellite data

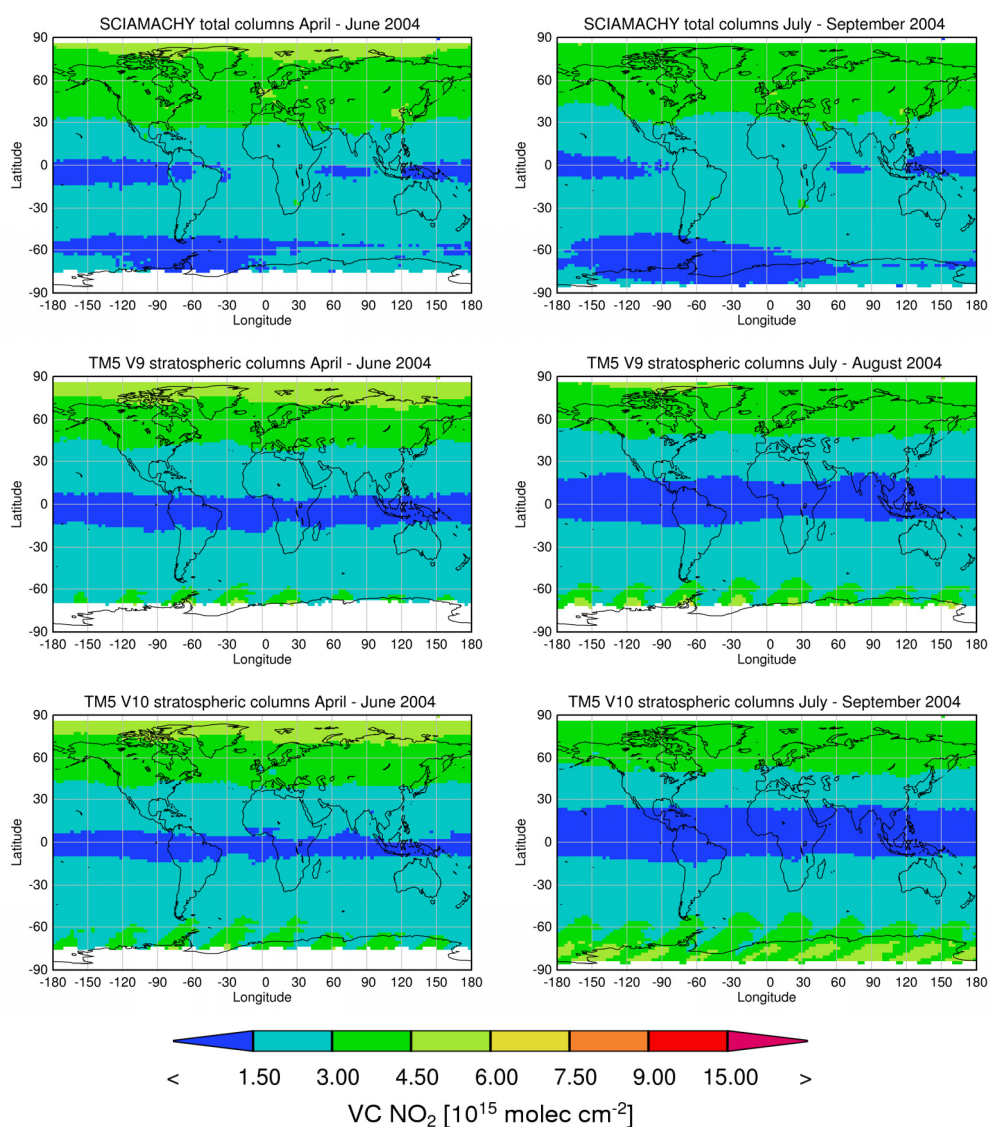


Figure 5.17 Three month averages of global total NO<sub>2</sub> columns measured by SCIAMACHY (top) and stratospheric columns determined by TM5 V9 (middle) and V10 (bottom) for the periods of April – June (left) and July – September (right) of the year 2004 (except V9 with data only for July and August).

The evaluation of tropospheric NO<sub>2</sub> yielded by the TM5 V7 demonstrated that the model output was too low over anthropogenic source regions, such as Europe, China or the US. This was corrected in later versions with the inclusion of a more up-to-date emission inventory for the East-Asia region, the REAS dataset. Furthermore, as illustrated in Figure 5.2, NO<sub>x</sub> and CO emissions were also corrected. Consequently, the results from V10 are more similar to the satellite measurements. Nevertheless, as it was observed for MOZART, during the winter period, the NO<sub>2</sub> columns observed for East-Asia are still higher than the modelled values. This may be on the

## Validation of NO<sub>2</sub> model output

account of weak seasonality implemented in the TM5 scheme, but also due to extremely low values from the emission inventories. Nevertheless, the opposite occurs for Europe in the months of January and December where the model output is slightly higher than the measurements. For the biomass burning regions, a systematic over- or underestimation of the NO<sub>2</sub> column was not verified.

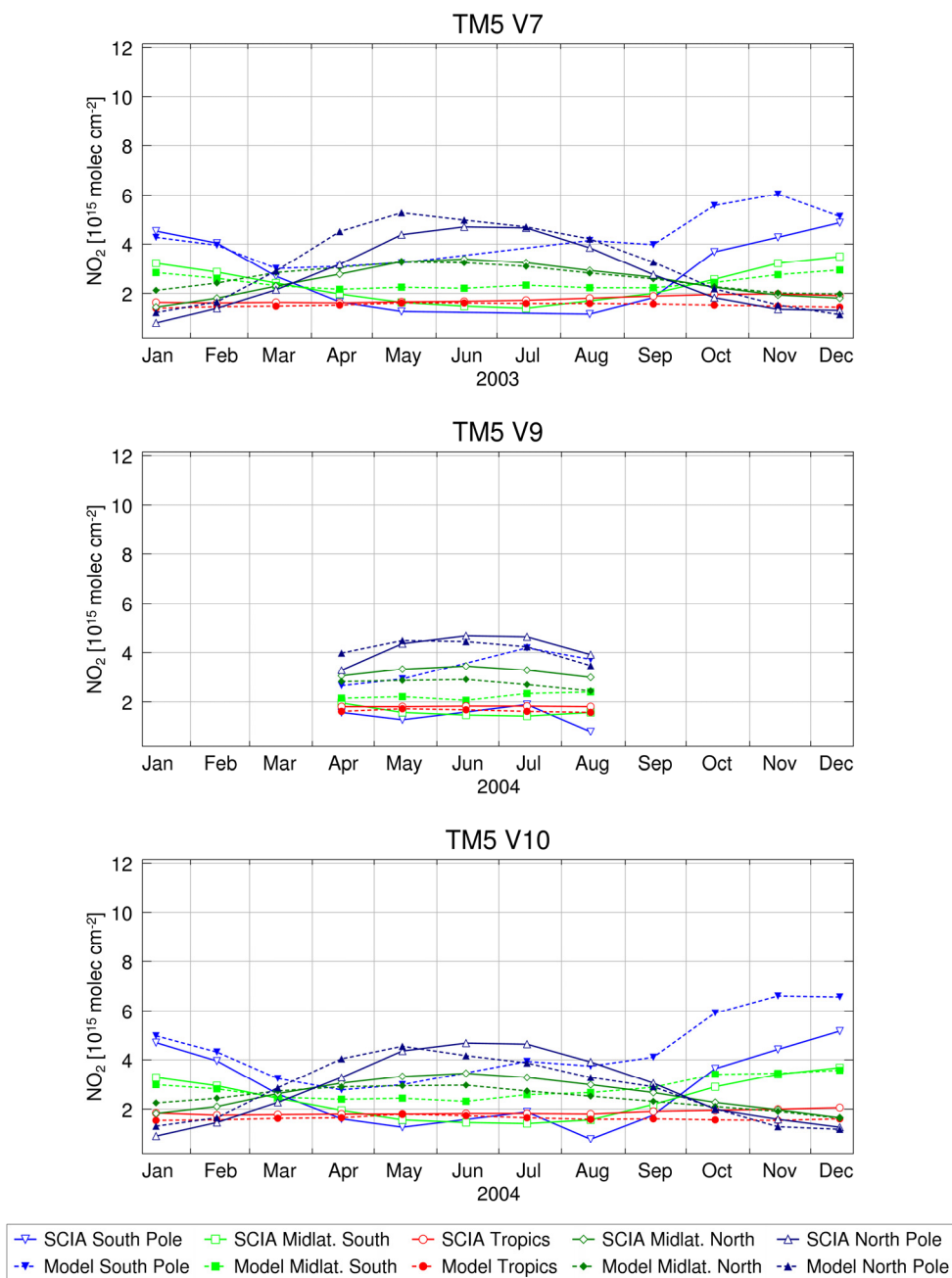


Figure 5.18 Seasonality curves for 2003 (top) and 2004 (middle and bottom) of total NO<sub>2</sub> columns measured by SCIAMACHY (open symbols) and stratospheric columns determined by TM5 V7 (top), V9 (middle with data only for April - August 2004) and V10 (bottom). Monthly averages determined for the selected regions as defined in Figure 5.6.

## Results: Comparison with independent satellite data

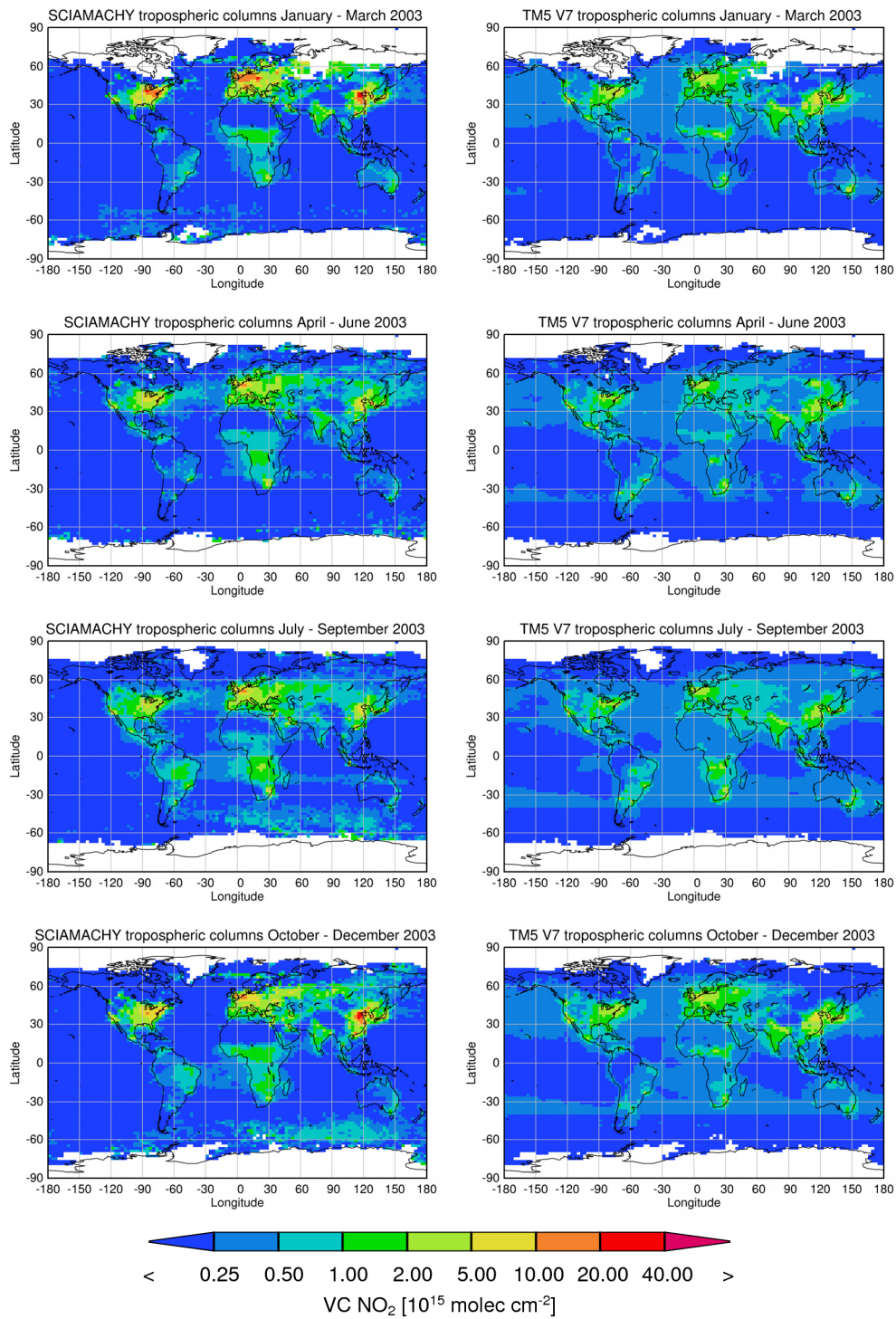


Figure 5.19 Three month averages of global tropospheric NO<sub>2</sub> columns measured by SCIAMACHY (left) and determined by TM5 V7 (right) for the year 2003.

## Validation of NO<sub>2</sub> model output

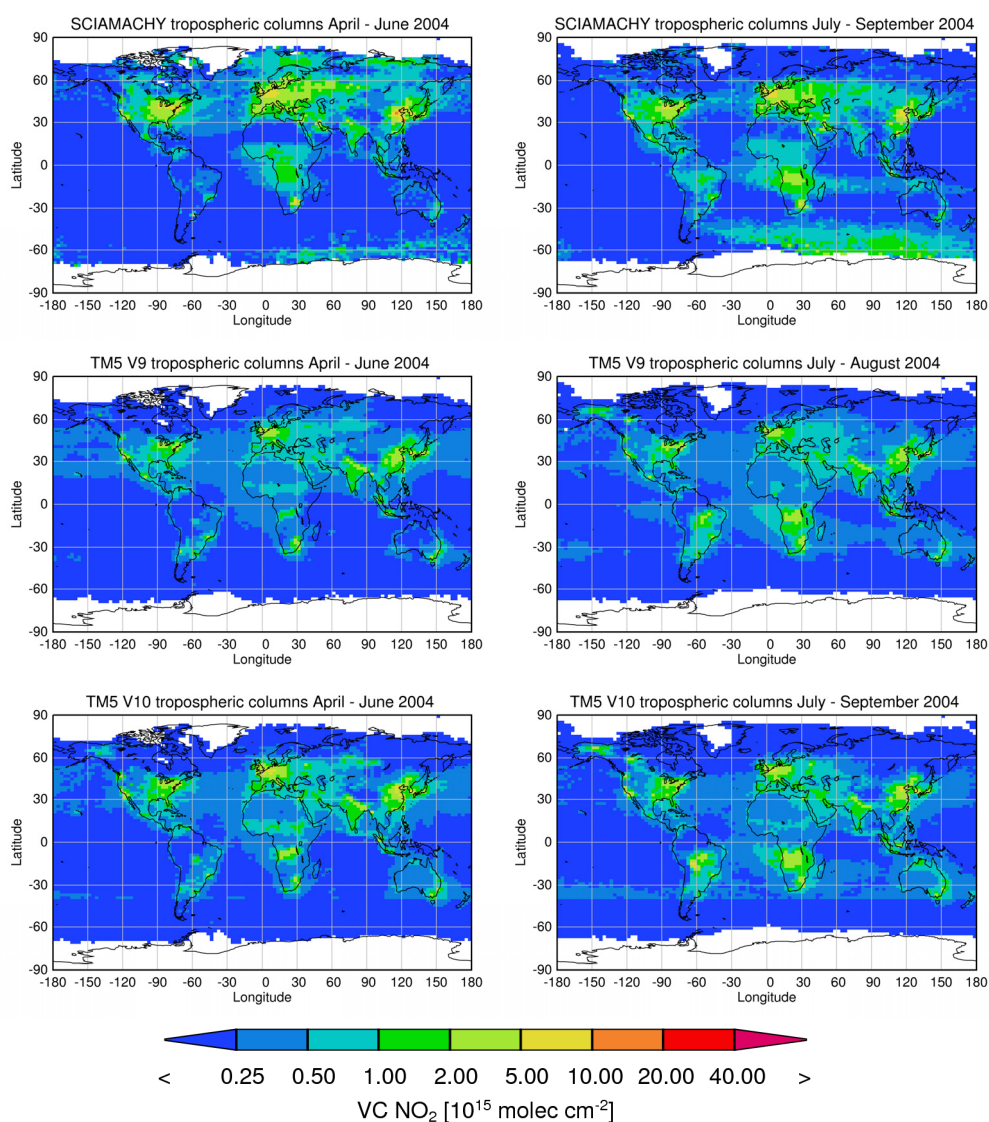


Figure 5.20 Three month averages of global tropospheric NO<sub>2</sub> columns measured by SCIAMACHY (top) and determined by TM5 V9 (middle) and V10 (bottom) for the periods of April – June (left) and July – September (right) of the year 2004 (except V9 with data only for July and August).

The period of July-September is a good example where both occurrences were verified. While in 2003 the simulated NO<sub>2</sub> columns are too small over South America and central Africa, in the following year the model predicts high NO<sub>2</sub> emissions in the Alaska region which are not detected by the satellite (see Figure 5.21). It seems that TM5 overestimates the emissions from boreal fires and underestimates those of tropical biomass burning events (except for the last months of 2004 in V10). The source of the problem could not be easily identified. It is also surprising to see that the output from V9, which erroneously used doubled emissions from biomass burning sources,

## Results: Comparison with independent satellite data

compares nicely to the satellite measurements for such events, while the TM5 V10 results for those regions are still higher than the satellite measurements. From the seasonality trends in Figure 5.22, it is also possible to observe that, for this version, while in the beginning of the year 2004 the model underestimates the NO<sub>2</sub> columns in the North-Africa region, the opposite is registered for the month of December. The simulations of emissions from biomass burning events in the year 2004 with V10 are affected by different assumptions. In the months of January and February no GFED data was considered in the model, which might explain the underestimation of the fires in the North-Africa region. Furthermore, the definition of injection height was improved in May. This change will lead to modifications of the model output because, as explained in chapter 2, the NO<sub>2</sub> chemistry is highly dependent on the temperature which decreases with height. While from March to May the emissions were considered in the two lowest layers of the model, for the remaining months the biomass burning emissions are injected up to 6000 m. This might explain the low values in the months of March to May and, from then onwards, higher NO<sub>2</sub> columns than those measured by SCIAMACHY. Nevertheless, the differences in the monthly averages are quite small and the seasonality is well reproduced in these regions (see Figure 5.22). In general, for the biomass burning regions, the results are better than those produced by MOZART runs. However, because of the many factors involved in these simulations, and the several changes performed in the TM5 configuration, it is difficult to point out what exactly became an advantage in terms of model scheme and what might be the source of erroneous results.

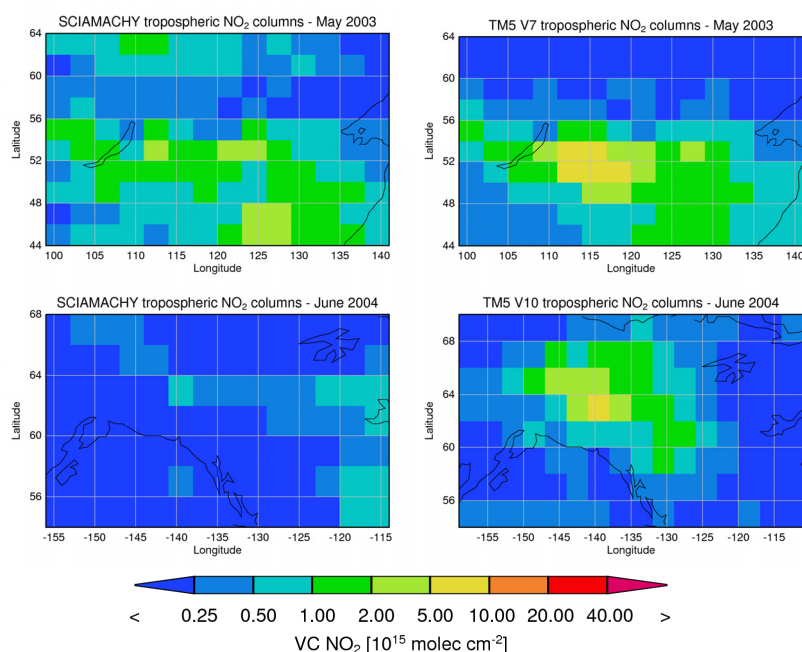


Figure 5.21 Monthly averages of tropospheric NO<sub>2</sub> columns measured by SCIAMACHY (left) and determined by TM5 V7 and V10 (right top and bottom, respectively) for two different case studies: Siberia fires – May 2003 (top) and, Alaska fires – June 2004 (bottom).

## Validation of NO<sub>2</sub> model output

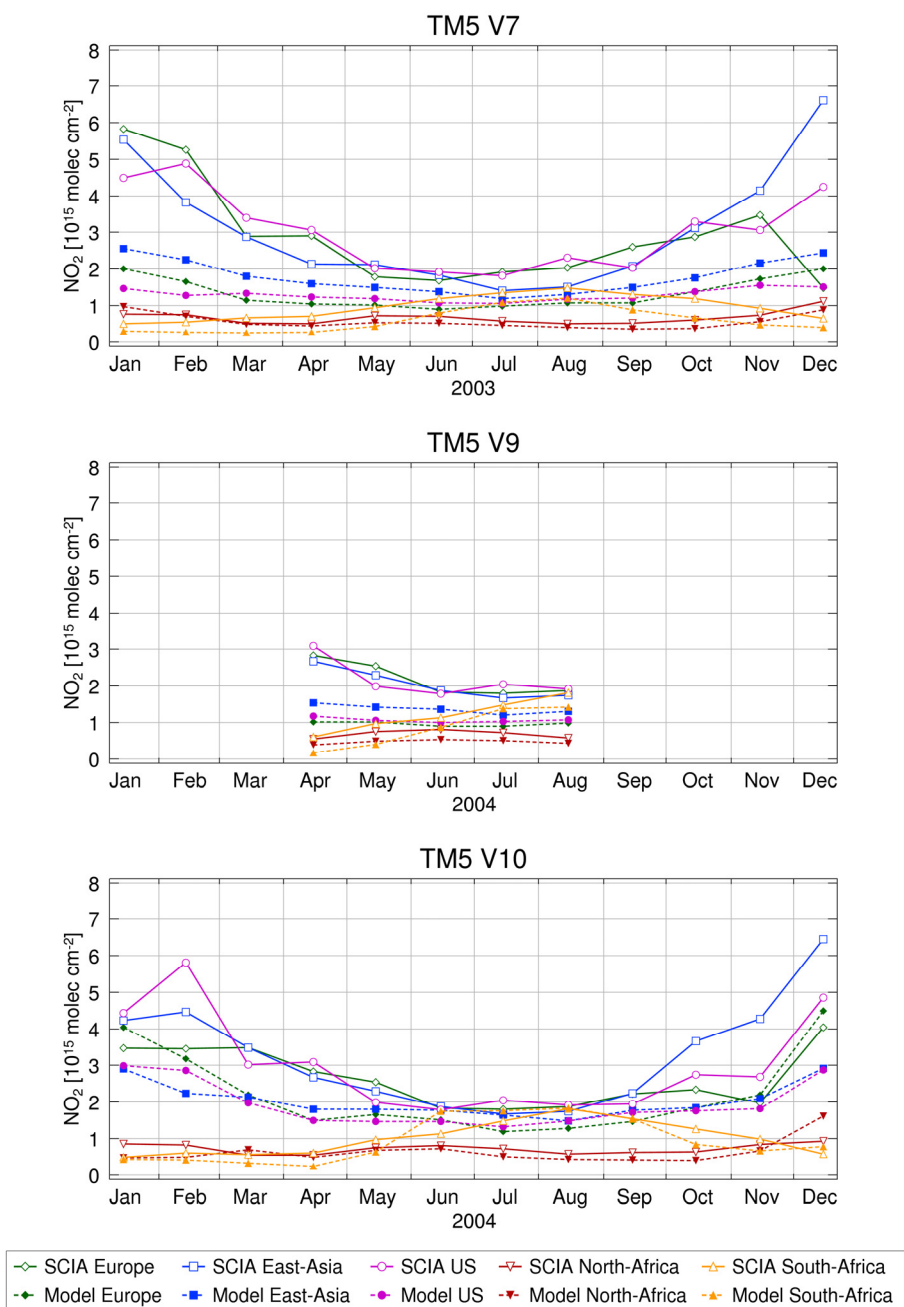


Figure 5.22 Seasonality curves of tropospheric NO<sub>2</sub> columns measured by SCIAMACHY (open symbols) and determined by TM5 V7 (top) for the year 2003, and V9 (middle, with data only for April – August 2004) and V10 (bottom) for the year 2004. Monthly averages determined for the selected regions as defined in Figure 5.6

## 5.5 Quantitative analysis

As introduced in section 5.3.2, the evaluation of the models included also several approaches of quantitative analysis. An objective of this chapter is to exemplify how the satellite data can be useful to validate models and identify flaws that can later be corrected. For that reason, the complete validation exercise will not be presented. From the seasonal plots presented in the previous section, it was possible to compare the modelled and measured monthly averages of stratospheric and tropospheric columns, for certain regions. Here, the spatial correlation values (i.e., correlation of values from the gridded maps) will be provided for some of the model versions already analysed. The magnitude of the columns is not evaluated here. The correlations were determined for the monthly averages and are helpful to determine the accordance between the location of emissions simulated by the model and the observations. That is to say, that a good correlation value will denote that, for a certain region, the model did simulate the high/low values as it is observed by the satellite. The tables below are also colour coded to help a visualisation of the results. Green/blue correspond to very good results and orange/red spot the worse simulations. A point by point comparison was also performed but the extensive results will not be included in the analysis presented here.

From the values determined, a first prominent observation is that in general, better correlation values are obtained for the regions characterised by anthropogenic emissions (Europe, East-Asia, and US). This is consistent with the findings from the previous section, where the major differences between model output and measurements were found for the biomass burning regions. Only for a few exceptional cases the correlation value is below 0.5. In fact, for the latest version of TM5 (Table 5.5), the lowest value obtained is 0.7, which leads to the conclusion that emission inventories used in this model are quite good and sources are well represented. With the implementation of legislation for air quality control, it became progressively necessary to keep up-to-date records of existing anthropogenic sources, especially in modernised societies and developed countries. The challenge in the modelling exercise is still to assess the exact emissions and predict correctly the trend of such sources as often the inventories employed are only available for past years. A more complex simulation is presented when focusing on the biomass burning events. The monthly correlations for North-Africa and South-Africa regions are usually below 0.5, with a maximum obtained of 0.7 for some months. This observation indicates that while the models do a fairly good job simulating the fire event and reproducing the amount of NO<sub>2</sub> emitted in these regions (see for example the TM5 results from Figure 5.22), they still fail to determine the exact location of the burning area at the time of the satellite measurements. This suggests that if, on the one hand, emission inventories for anthropogenic sources are mostly correct in identifying the location of the main sources, on the other hand, such accurate datasets for fires are hard to produce as these occurrences are not easily predicted nor registered. In addition, unlike

industrial and urban sources, wildfire events and their evolution are dependent on many natural conditions that are quite complex to implement in a model scheme. A new method including satellite observations of fire events helps to include most of the fire occurrences registered. However, this information is still incomplete in regard to, for example, type of fire, intensity and height of plume (that will influence the transport of the trace gases for example). Therefore, the follow up of such an event is still a challenging task for some models. Nevertheless, for MOZART V10 a great improvement from 2003 (Table 5.2) to 2004 (Table 5.4) is registered. When comparing the different model versions, the general improvement becomes evident, i.e., from MOZART V1 (Table 5.1) to V10 (Table 5.2 and Table 5.4), and TM5 V7 (Table 5.3) to V10 (Table 5.5). However, for the latter, the quality of simulations in the biomass burning regions presents a clear decline.

It is interesting to observe differences (and large in some cases) between the two models, even though many aspects in the model schemes are similar, e.g., vertical resolution, meteorology fields, most of the emission inventories considered. Part of these differences may be related to the different chemistry schemes, but also the horizontal resolution contributes to a better comparison to the satellite observations. Coarser resolution leads to loss of detail of hot-spot emissions, producing smoother fields that might result in improved correlations. This artificial effect was also verified by Huijnen et al. (2010a) that compared tropospheric NO<sub>2</sub> simulated by various regional air quality models (included in the GEMS project) and global CTMs, TM5 and MOZART-IFS (not analysed in this thesis), with OMI observations. The authors have found overall better correlations for the global models that are run in a coarser grid. Therefore, caution is necessary when comparing directly the results of MOZART and TM5, two models that have different spatial resolutions. Albeit this difference, from the correlation coefficients obtained, one can assert that, for the polluted regions, TM5 demonstrates a better performance in comparison to the MOZART versions. However, the results for the typical biomass burning (high contrast between very low and high correlations) were very similar for both models. The first months of 2004 where TM5 obtains very low results is an exception for comparable results.

## 5.6 Summary

SCIAMACHY measurements of NO<sub>2</sub> were used to validate the results of different chemical transport models. The work presented in this chapter was part of the main validation exercise of the models MOZART and TM5 that were integrated in the GRG (Global Reactive Gases) working group of the

## Summary

European GEMS (Global and regional Earth-system (atmosphere) Monitoring using Satellite and in-situ data) project.

Table 5.1 Monthly correlation coefficients between tropospheric NO<sub>2</sub> columns measured by SCIAMACHY and simulated by MOZART V1 for the year 2003 for several regions as defined in Figure 5.6.

	Europe	East-Asia	US	N-Africa	S-Africa
Jan	0.6	0.7	0.6	0.7	0.3
Feb	0.7	0.6	0.5	0.6	0.5
Mar	0.8	0.7	0.8	0.5	0.3
Apr	0.9	0.7	0.7	0.5	0.3
May	0.9	0.7	0.8	0.5	0.5
Jun	0.8	0.8	0.7	0.6	0.7
Jul	0.8	0.6	0.7	0.5	0.7
Aug	0.8	0.6	0.7	0.4	0.6
Sep	0.9	0.7	0.7	0.1	0.6
Oct	0.9	0.6	0.7	0.3	0.7
Nov	0.8	0.6	0.7	0.7	0.5
Dec	0.5	0.7	0.7	0.7	0.3

Table 5.2 Monthly correlation coefficients between tropospheric NO<sub>2</sub> columns measured by SCIAMACHY and simulated by MOZART V10 for the year 2003 for several regions as defined in Figure 5.6.

	Europe	East-Asia	US	N-Africa	S-Africa
Jan	0.6	0.9	0.7	0.6	0.3
Feb	0.6	0.7	0.5	0.6	0.4
Mar	0.8	0.8	0.8	0.5	0.3
Apr	0.9	0.8	0.7	0.5	0.3
May	0.9	0.8	0.8	0.5	0.4
Jun	0.8	0.8	0.6	0.5	0.6
Jul	0.8	0.6	0.6	0.3	0.6
Aug	0.8	0.7	0.7	0.3	0.5
Sep	0.9	0.8	0.7	0.0	0.5
Oct	0.9	0.8	0.7	0.4	0.7
Nov	0.8	0.8	0.7	0.6	0.5
Dec	0.4	0.8	0.7	0.7	0.4

## Validation of NO<sub>2</sub> model output

Table 5.3 Monthly correlation coefficients between tropospheric NO<sub>2</sub> columns measured by SCIAMACHY and simulated by TM5 V7 for the year 2003 for several regions as defined in Figure 5.6.

	Europe	East-Asia	US	N-Africa	S-Africa
Jan	0.8	0.8	0.9	0.7	0.5
Feb	0.8	0.8	0.6	0.6	0.5
Mar	0.9	0.8	0.9	0.3	0.6
Apr	0.9	0.7	0.9	0.3	0.1
May	0.9	0.8	0.9	0.4	0.4
Jun	0.9	0.7	0.9	0.5	0.7
Jul	0.9	0.7	0.9	0.5	0.7
Aug	0.9	0.7	0.9	0.2	0.7
Sep	0.9	0.8	0.7	0.1	0.6
Oct	0.9	0.8	0.9	0.3	0.7
Nov	0.9	0.8	0.8	0.6	0.6
Dec	0.7	0.8	0.8	0.7	0.6

Table 5.4 Monthly correlation coefficients between tropospheric NO<sub>2</sub> columns measured by SCIAMACHY and simulated by MOZART V10 for the year 2004 for several regions as defined in Figure 5.6.

	Europe	East-Asia	US	N-Africa	S-Africa
Jan	0.6	0.8	0.8	0.7	0.4
Feb	0.7	0.8	0.7	0.6	0.4
Mar	0.8	0.6	0.8	0.6	0.1
Apr	0.9	0.8	0.7	0.6	0.3
May	0.8	0.8	0.8	0.6	0.6
Jun	0.8	0.8	0.7	0.7	0.7
Jul	0.8	0.7	0.7	0.5	0.7
Aug	0.9	0.7	0.7	0.3	0.7
Sep	0.9	0.8	0.6	0.4	0.7
Oct	0.9	0.8	0.7	0.5	0.6
Nov	0.8	0.8	0.7	0.7	0.5
Dec	0.6	0.8	0.7	0.6	0.2

## Summary

Table 5.5 Monthly correlation coefficients between tropospheric NO<sub>2</sub> columns measured by SCIAMACHY and simulated by TM5 V10 for the year 2004 for several regions as defined in Figure 5.6.

	Europe	East-Asia	US	N-Africa	S-Africa
<b>Jan</b>	0.7	0.9	0.8	0.3	0.1
<b>Feb</b>	0.8	0.9	0.9	0.3	0.0
<b>Mar</b>	0.9	0.7	0.9	0.4	0.2
<b>Apr</b>	0.9	0.9	0.9	0.4	0.2
<b>May</b>	0.9	0.9	0.9	0.3	0.6
<b>Jun</b>	0.9	0.9	0.8	0.4	0.7
<b>Jul</b>	0.8	0.9	0.8	0.2	0.7
<b>Aug</b>	0.9	0.8	0.9	0.1	0.7
<b>Sep</b>	0.9	0.9	0.7	0.1	0.8
<b>Oct</b>	0.9	0.8	0.8	0.5	0.7
<b>Nov</b>	0.8	0.9	0.7	0.6	0.4
<b>Dec</b>	0.8	0.9	0.8	0.7	0.2

In the current study, the analysis presented was focused on the standalone versions (offline runs), but the reanalysis and forecast runs (CTMs coupled with IFS from ECMWF) have also been evaluated. Satellite data is useful to determine how good the model simulations are, and to recognise some of their main problems. The purpose of the validation exercise with SCIAMACHY data was accomplished and this has contributed to the identification of model flaws, that could be rectified during the extent of the GEMS project, and later implemented for the follow up project – MACC (Monitoring Atmospheric Composition and Climate).

Both datasets (model and satellite) had to be adjusted so that they could be compared. The satellite data was regridded in the same resolution of each of the models, and the model data interpolated to the overpass time of SCIAMACHY. The volume mixing ratios provided for the 60 layers were then separated and integrated into stratospheric and tropospheric vertical columns. In a last step, the model output was selected according to the availability of the satellite data, so that comparisons were done only where both measurements and simulations exist.

The latest versions of both the MOZART and TM5 models were able to simulate well the stratospheric fields, albeit the existing differences between the model designs: MOZART has a full stratospheric chemistry scheme, while TM5, for this atmospheric layer, is mostly based on data from climatologies. Some differences were still observed in several months but, overall, the agreement

between measurements and model output is quite good. It is important to highlight that this was a great improvement from the initial results, which had the tendency to overestimate the stratospheric NO<sub>2</sub>, partly because the models failed to simulate the ozone depletion in this layer.

The simulation of tropospheric NO<sub>2</sub> proved to be a more complex and difficult task due to the high spatial and temporal variability of its concentration. In general, it is possible to say that the model results were often too low over polluted regions and too high over biomass burning regions. These findings are in accordance with the conclusions drawn by van Noije et al. (2006), where tropospheric NO<sub>2</sub> simulated by multi-model ensemble was compared to GOME data for the year 2000. The main sources of NO<sub>2</sub> are correctly identified in the model simulations, but there seems to be still some improvement required in the chemistry scheme for this compound. Furthermore, the use of more up-to-date emission inventories would probably lead to more accurate predictions over urban and/or industrial areas. In East-Asia, the satellite has measured a strong increasing trend of air pollution for the past years (Richter et al., 2005). Unfortunately, in the present analysis, only 2003 and 2004 were considered (the years available from the standalone model runs) which limits the comparison to recent trends. The GEMS emission inventory included the REAS up-to-date emissions for this region, yet, the models failed to predict the high tropospheric NO<sub>2</sub> columns. This problem is more relevant in the winter months which might indicate a problem related to seasonality of emissions or reproduction of NO<sub>2</sub> lifetime. On the other hand, overestimation for Europe is also found in some months, which might be related to too high emissions from ships. It is difficult to explain the reason for the differences observed for the biomass burning regions. NO<sub>2</sub> from fires is not easily represented in models because each fire is a very unique event and the emissions depend on several aspects, e.g., type of fuel, combustion temperature, and injection height. The incorrect model simulations of tropospheric NO<sub>2</sub> in these cases might, on the one hand, be related to wrong values predicted for CO and OH and/or wrong NO<sub>x</sub>/CO emission ratio. On the other hand, the source of the problem may be the chemistry scheme that fails to reproduce the rapid conversion of NO<sub>2</sub> to other compounds, e.g., PAN or HNO<sub>3</sub>, in these specific situations.

The comparison with satellite data is especially useful in order to identify hot-spots as main source-regions, and also to observe the variation of columns throughout the year. However, if one attempts to perform a deep quantitative analysis, satellite data are not always the best choice for model validation. The limitations are mostly related to the uncertainties still associated with the method to retrieve vertical columns (as illustrated in the previous chapters). The determination of NO<sub>2</sub> tropospheric columns requires assumptions on many levels that will determine the value of retrieved vertical columns. The correction of the stratospheric fraction within the total columns, for example, is something still to be improved. When models, as the MOZART or TM5, perform well on a daily basis, these data can be used to determine exactly how much NO<sub>2</sub> is in each atmospheric layer.

## Summary

---

Another example of uncertainty in satellite data is the case of the aerosol and its influence on the measurements (*via* interaction with radiation) which is still rather unknown and not well accounted for in the retrieval. The approaches to improve the aerosol assumptions and the consequent variation of results were already discussed in detail in the previous chapters, where model data was also identified as a potential source of information. An alternative to the validation performed here, is the use of averaging kernels that would reduce the bias caused by uncertainties in the retrieved tropospheric columns.

# 6

## Conclusions and outlook

The present thesis focused on the influence of aerosol on satellite measurements and the way this has an impact on the retrieval of tropospheric NO<sub>2</sub> vertical columns. The particulate matter present in the atmosphere will interact with radiation and, in that way, influence the sensitivity of satellite observations. The main goal of this work was to identify key factors of the radiative transfer calculations, assessing as well how much aerosol can affect the values of the retrieved tropospheric NO<sub>2</sub> vertical column.

### **Sensitivity study to determine key factors in the calculation of tropospheric NO<sub>2</sub> AMF**

In a sensitivity study, air mass factors were determined with the SCIATRAN radiative transfer model for a large number of different aerosol scenarios. In those, the NO<sub>2</sub> profiles were changed together with aerosol size distribution, optical properties and its vertical distribution. The findings of this study reveal that, in order to upgrade the current satellite data products, improved knowledge is still required on surface reflectance, vertical profiles of trace gas and aerosol, and particles' properties. The AMF values were found to increase by 90% when the surface reflectance was increased from 0.01 to 0.1, a value that can be higher in different circumstances. This means that, because sunlight is more efficiently reflected by brighter surfaces, the measurement sensitivity will be enhanced, and tropospheric NO<sub>2</sub> vertical columns can be overestimated if an excessively dark surface is considered. In addition, the factors identified as pivotal in the determination of NO<sub>2</sub> columns were the relative vertical distribution of aerosol and NO<sub>2</sub>, and the scattering/absorption properties of the particles, i.e., the aerosol optical depth (AOD) and single scattering albedo (SSA). The size of the particles

## Conclusions and outlook

---

determines (together with other parameters) the phase function of an aerosol plume, leading to some differences in the AMFs when the size distributions of aerosol considered represent either coarse or fine aerosol particles. However, this impact is only relevant for large variations of sizes.

Overall, the presence of particulate matter in the atmosphere, at the time of satellite measurements, will affect the observations mainly in two contrasting ways: enhancement of measurement sensitivity or decrease of AMFs. Aerosol mixed with the trace gas, even if not at the full extension of the layer, will, by means of increased effective albedo and multiple scattering, enhance the NO<sub>2</sub> signal. This is often observed at urban scenarios, where aerosol and NO<sub>2</sub> can be mixed together in the same layer. The combination of NO<sub>2</sub> profiles from CHIMERE model output and data from aerosol measurements, for these locations, showed that the presence of particulate matter does not influence the observations much: the AMFs varied only by ~7% on average. This moderate impact could be explained by a balance between enhancement and reduction of the signal because the aerosol is both mixed within and above the NO<sub>2</sub> layer. On the other hand, any aerosol layer that lies above the trace gas (e.g., long-range transport of desert dust, volcanic eruptions, or fire smoke) will act as a shield, decreasing the sensitivity of the measurements. If this impact is not accounted for, the computed NO<sub>2</sub> vertical columns will be too small. From the cases analysed, the impact on AMF is highly dependent on the scenario considered. Such impact can lead to reductions as high as ~62%, when an elevated smoke layer with AOD = 1.05 stands above NO<sub>2</sub> existing close to the surface.

### **Impact of volcanic ash on the satellite observations of tropospheric NO<sub>2</sub>**

In a next step, it was important to understand how the sensitivity study findings would compare to real situations, on a wider temporal and spatial scale. The event selected was the volcanic eruption of Eyjafjallajökull that took place during the spring of 2010. NO<sub>2</sub> and aerosol data from the chemical transport model EURAD were used in the radiative transfer model to investigate the influence of volcanic ash in the satellite observations. The results showed a slight change of the tropospheric NO<sub>2</sub> AMFs. It was possible to conclude that the presence of ash has led to an overall decrease of the measurement sensitivity, with a maximum reduction of 13%. This indicates that the vertical columns derived from the measured slant columns might be underestimated if the presence of ash is not accounted for in the retrieval process. This moderate impact of ash on the tropospheric NO<sub>2</sub> AMFs is according to expectations due to the low AODs derived from the model output. However, as it was illustrated in this thesis, the impact of aerosol in the AMF values could be considerably larger if the AOD of ash was higher. Furthermore, it is important to mention that the conclusions of this study are not only dependent on the model's accuracy but also on the approach taken to derive the aerosol optical properties from the provided mass concentrations. Refractive indices, densities and size distribution are characteristics that will influence the extinction and scattering coefficients of the aerosol. These are not yet well defined for all aerosol types included in the model output. An

## Conclusions and outlook

---

additional limitation of this approach is the time required for the computation of optical properties of internally mixed particles, where the water content is considered and spatial and temporal variation of size distribution.

### **Validation of MOZART and TM5 models with satellite observations**

SCIAMACHY measurements of stratospheric and tropospheric NO<sub>2</sub> were used to validate two chemical transport models globally: MOZART and TM5. The performed evaluation exercise allowed an assessment of the model simulations' quality, and identification of flaws that could be rectified during the extent of the GEMS project. The latest versions of both MOZART and TM5 were able to simulate well the stratospheric fields, with small differences found only for some months. This was the outcome of continuous improvement, from an initial overestimation of the stratospheric NO<sub>2</sub>, which could, to some extent, be explained by the incorrect simulation the ozone depletion in this layer. On the other hand, the simulation of tropospheric NO<sub>2</sub> columns showed to be more complex. In general, the NO<sub>2</sub> predicted by the model for areas characterized by anthropogenic pollution is too low, especially in the winter period, and too high in the biomass burning regions. In fact, this is a common problem for several CTMs, as it was also identified in the study by van Noije et al. (2006). The emission values used as input seem to be a weakness in the models, together with the parameterisation assumed for the seasonal variations. The hot-spots of NO<sub>2</sub> are identified, but the magnitude of tropospheric amounts is not well predicted. Up-to-date emission inventories that follow the decreasing trends in developed countries, and the fast rising emission values from other nations, such as China, may be a solution for this issue. In addition, it was concluded that some improvements are necessary in the chemistry schemes so that interactions between NO<sub>2</sub> and several other compounds are well simulated. This would be especially relevant for the biomass burning simulations, where the representation of NO<sub>2</sub> emissions cannot be easily generalised. For these cases, incorrect NO<sub>x</sub>/CO emission ratios or very slow conversion of NO<sub>2</sub> into other compounds, e.g., PAN or HNO<sub>3</sub>, were identified as weak points to be improved. Nevertheless, high uncertainties are still associated to model simulations of biomass burning events because of unknown characteristics of individual fires (e.g., fuel type, combustion temperature, or burning area).

### **Outlook**

The study presented did not consider cases that are representative of highly polluted scenes, as those of megacities, where, for example, AOD can be much higher than 0.9. Thus, in order to allow a better understanding of the aerosol's influence in the measured NO<sub>2</sub> columns in those particular locations, further analysis is still required. Furthermore, the complexity of considering aerosol in the retrieval process of trace gas columns from satellite measurements has been demonstrated in this thesis. The high spatial and temporal variability of aerosol distribution and its changing properties, are challenges

## Conclusions and outlook

---

that difficult the implementation of a systematic correction of its influence on the conversion of slant to vertical columns. It is also important to keep in mind that high loads of aerosol are not only registered in urban and/or industrial areas, but also during volcanic eruptions, desert dust storms, or wild fires. These are sporadic events, with unpredictable emissions, that can be transported over large distances and, therefore, cannot be considered in retrievals using static aerosol corrections. Future operational retrievals should be able to deal with the interaction between particles and radiation in all possible cases. This can only be achieved if the necessary information (i.e., aerosol properties and their vertical distribution) is readily available, with suitable spatial and temporal resolutions, when the satellite data are processed. In this way, global distributions of trace gases, namely tropospheric NO<sub>2</sub>, and air pollution trends can be determined with higher levels of confidence, assuring high accuracy of satellite observations and the retrieved products.

Chemical transport models are potential providers of these datasets, but resources and computational time are still constraints to achieve results with the desired accuracy. Once models, as MOZART or TM5, are able to achieve good results on a daily basis and at high resolution, these data can be employed to derive AMFs with radiative transfer models. However, using model data as source of information for measurement conditions will create a strong link between the precision of the CTM simulations and the accuracy of the retrieved columns. Atmospheric aerosol (spatial distribution, amount, size distribution, etc) is not yet successfully simulated in many CTMs on a regular basis, especially when dealing with sporadic events, such as volcanic eruptions or biomass burning. Furthermore, the use of model data is also complicated by the complex conversion of mass concentrations of several aerosol species (dealt differently in each CTM) into optical properties. Models serve the purpose of decision making and that demands fast response, as it was the case to predict the dispersion the ash plume during the volcanic eruption. However, these are also needed on high accuracy, two requirements that are not always easily combined. This explains in part how fast simulation results, on high resolution and good accuracy, are not always readily available to serve the purpose of satellite retrievals.

Simultaneous measurements of trace gas and aerosol properties from space, already achieved with some instruments, would be an alternative to the use of model data. However, while this is not put in place, a synergistic approach can be the alternative by combining data from two instruments, e.g., using AOD from MERIS in the retrieval of NO<sub>2</sub> from SCIAMACHY (both instruments flying on the ENVISAT platform). Another, promising approach is the extension of what was done in this study: a combination of satellite (e.g., MODIS, MISR, CALIPSO) and ground-based measurements (e.g., from AERONET and EARLINET networks) with model predictions, when those are available in a suitable resolution. In addition, a methodology can be designed to use O<sub>4</sub> measurements to determine aerosol properties and vertical distribution, similar to what is done for ground-based techniques

## Conclusions and outlook

---

(Wagner et al., 2004). The  $O_2-O_2$  absorption bands at 477 nm are modified in the presence of clouds and can, therefore, be used to determine the cloud fraction and pressure (Acarreta et al., 2004), a method already applied in the retrieval of OMI data (Boersma et al., 2011). A combination of several datasets here mentioned might be the solution to derive the aerosol information necessary for the retrieval of trace gas columns from satellite measurements.

It is also important to highlight that the findings of this investigation have demonstrated that, in the AMF calculations, it is not only the aerosol that influences the results, but also the trace gas profile and surface properties. The exact shape of the  $NO_2$  profile in different locations is still rather unknown, which makes the use of typical profiles as *a priori* assumptions a complex approach. Data from ground-based observations as, for example, those of MAX-DOAS instruments (Wagner et al., 2004; Wittrock et al., 2004) show potential to provide simultaneous measurements of trace gas and aerosol profiles in the lower troposphere. Additionally, alternative techniques have been employed to assess the vertical distribution of  $NO_2$ , as it is the case of lidar measurements performed by Volten et al. (2009), or, more recently, Sluis and colleagues (2010) that have developed an  $NO_2$  sonde that provides tropospheric profiles. The application of such measurements, together with model results have shown to improve satellite retrievals (Hains et al., 2010) and should, therefore, be used for revised *a priori* datasets in the near future. Static climatological assumptions that are often applied can be replaced by more up-to-date data that are more suitable to describe the measurement conditions. Through this method, spatial and temporal variability can be accounted for, improving the retrieval algorithm for tropospheric  $NO_2$  columns.

As exemplified in this thesis, satellite observations can be used to validate CTM output. However, the accuracy of the satellite data will influence the interpretation of the results regarding the quality of the model simulations. Therefore, updating the retrieval method with improved stratospheric correction for tropospheric slant columns and more accurate AMFs will also benefit model validation. Moreover, the use of averaging kernels in the validation of model output might be an alternative to consider. Since these reflect the sensitivity of satellite observations to different heights, the evaluation exercise will not be affected by the systematic biases caused by *a priori* assumptions on the satellite retrieval method (Eskes and Boersma, 2003).



# Appendix

Within the chapter 5, the output of the chemical transport models MOZART and TM5 was validated against SCIAMACHY observations of stratospheric and tropospheric NO<sub>2</sub>. The spatial correlation values were determined for all model versions considered in this analysis, but only the most relevant were presented in the chapter above. Here there results for the remaining versions are provided. The correlations were determined for the monthly averages and for regions as defined in Figure 5.6. The tables below are also colour coded to help a visualisation of the results: green/blue for the very good results and orange/red spot the worse simulations.

## a) 2003

Table A.1 Monthly correlation coefficients between tropospheric NO<sub>2</sub> columns measured by SCIAMACHY and simulated by MOZART V7 for the year 2003 for several regions as defined in Figure 5.6.

	Europe	East-Asia	US	N-Africa	S-Africa
Jan	0.6	0.9	0.7	0.6	0.2
Feb	0.6	0.7	0.5	0.6	0.5
Mar	0.8	0.8	0.8	0.4	0.4
Apr	0.9	0.8	0.7	0.3	0.3
May	0.9	0.8	0.8	0.2	0.4
Jun	0.8	0.8	0.6	0.2	0.6
Jul	0.8	0.6	0.6	0.5	0.6
Aug	0.8	0.7	0.7	0.3	0.5
Sep	0.9	0.8	0.7	0.1	0.4
Oct	0.9	0.8	0.7	0.3	0.6
Nov	0.7	0.8	0.7	0.6	0.2
Dec	0.4	0.8	0.7	0.7	0.2

## Appendix

### b) 2004

Table A.2 Monthly correlation coefficients between tropospheric NO<sub>2</sub> columns measured by SCIAMACHY and simulated by MOZART V9 for the year 2004 for several regions as defined in Figure 5.6.

	Europe	East-Asia	US	N-Africa	S-Africa
Jan	0.6	0.8	0.8	0.7	0.4
Feb	0.7	0.8	0.7	0.6	0.4
Mar	0.8	0.6	0.8	0.6	0.1
Apr	0.9	0.8	0.7	0.6	0.3
May	0.8	0.8	0.8	0.6	0.6
Jun	0.8	0.8	0.7	0.7	0.7
Jul	0.8	0.7	0.7	0.5	0.7
Aug	0.9	0.7	0.7	0.3	0.7
Sep	0.9	0.8	0.6	0.4	0.7
Oct	0.9	0.8	0.7	0.5	0.6
Nov	0.8	0.8	0.7	0.7	0.5
Dec	0.6	0.8	0.7	0.6	0.2

Table A.3 Monthly correlation coefficients between tropospheric NO<sub>2</sub> columns measured by SCIAMACHY and simulated by TM5 V9 for the year 2004 for several regions as defined in Figure 5.6.

	Europe	East-Asia	US	N-Africa	S-Africa
Jan	-	-	-	-	-
Feb	-	-	-	-	-
Mar	-	-	-	-	-
Apr	0.9	0.8	0.8	0.2	0.3
May	0.9	0.8	0.9	0.3	0.6
Jun	0.9	0.8	0.9	0.5	0.7
Jul	0.9	0.8	0.9	0.5	0.7
Aug	0.9	0.7	0.8	0.3	0.8
Sep	-	-	-	-	-
Oct	-	-	-	-	-
Nov	-	-	-	-	-
Dec	-	-	-	-	-

# 7

## References

- U.S. standard atmosphere (1976), U.S. Government Printing Office, Washington, D.C., 1976.
- OASIS webpage: <https://verc.enes.org/models/software-tools/oasis>, 2011a.
- AeroCom initiative: <http://dataipsl.ipsl.jussieu.fr/AEROCOM/>, 2011b.
- Merriam Webster dictionary: <http://www.merriam-webster.com/dictionary/>, access: March, 2011, 2011c.
- MM5 webpage: <http://www.mmm.ucar.edu/mm5/mm5-home.html>, 2011d.
- Acarreta, J. R., De Haan, J. F., and Stammes, P.: Cloud pressure retrieval using the O<sub>2</sub>-O<sub>2</sub> absorption band at 477 nm, *J. Geophys. Res.*, 109, D05204, doi:10.1029/2003jd003915, 2004.
- Ackermann, I. J., Hass, H., Memmesheimer, M., Ebel, A., Binkowski, F. S., and Shankar, U.: Modal aerosol dynamics model for Europe: development and first applications, *Atmos. Environ.*, 32, 17, 2981-2999 pp, doi:10.1016/s1352-2310(98)00006-5, 1998.
- Adachi, K., Chung, S. H., and Buseck, P. R.: Shapes of soot aerosol particles and implications for their effects on climate, *J. Geophys. Res.*, 115, D15, doi:10.1029/2009jd012868, 2010.
- Aitchison, J., and Brown, A. C.: *The Lognormal Distribution*, Cambridge Univ. press, London, 1957.
- Akimoto, H.: Global Air Quality and Pollution, *Science*, 302, 5651, 1716-1719 pp, doi:10.1126/science.1092666, 2003.
- Allen, M., Lunine, J. I., and Yung, Y. L.: The Vertical Distribution of Ozone in the Mesosphere and Lower Thermosphere, *J. Geophys. Res.*, 89, D3, 4841-4872 pp, doi:10.1029/JD089iD03p04841, 1984.
- Glossary of Meteorology: <http://amsglossary.allenpress.com/glossary>, access: 27 June 2011.

## References

---

- Amiridis, V., Balis, D. S., Kazadzis, S., Bais, A., Giannakaki, E., Papayannis, A., and Zerefos, C.: Four-year aerosol observations with a Raman lidar at Thessaloniki, Greece, in the framework of European Aerosol Research Lidar Network (EARLINET), *J. Geophys. Res.*, 110, D21, 1-12 pp, doi:10.1029/2005jd006190, 2005.
- Ångström, A.: On the atmospheric transmission of Sun radiation and on dust in the air, *Geogr. Ann.*, 11156-166 pp, 1929.
- Ansmann, A., Mattis, I., Wandinger, U., Wagner, F., Reichardt, J., and Deshler, T.: Evolution of the Pinatubo Aerosol: Raman Lidar Observations of Particle Optical Depth, Effective Radius, Mass, and Surface Area over Central Europe at 53.4°N, *Journal of the Atmospheric Sciences*, 54, 22, 2630-2641 pp, doi:10.1175/1520-0469(1997)054<2630:EOTPAR>2.0.CO;2, 1997.
- Ansmann, A., Bösenberg, J., Chaikovsky, A., Comerón, A., Eckhardt, S., Eixmann, R., Freudenthaler, V., Ginoux, P., Komguem, L., Linné, H., Márquez, M. A. L., Matthias, V., Mattis, I., Mitev, V., Müller, D., Music, S., Nickovic, S., Pelon, J., Sauvage, L., Sobolewsky, P., Srivastava, M. K., Stohl, A., Torres, O., Vaughan, G., Wandinger, U., and Wiegner, M.: Long-range transport of Saharan dust to northern Europe: The 11–16 October 2001 outbreak observed with EARLINET, *J. Geophys. Res.*, 108, D24, 2003.
- Ansmann, A., Baars, H., Tesche, M., Müller, D., Althausen, D., Engelmann, R., Pauliquevis, T., and Artaxo, P.: Dust and smoke transport from Africa to South America: Lidar profiling over Cape Verde and the Amazon rainforest, *Geophys. Res. Lett.*, 36, 11, doi:10.1029/2009gl037923, 2009.
- Ansmann, A., Tesche, M., Groß, S., Freudenthaler, V., Seifert, P., Hiebsch, A., Schmidt, J., Wandinger, U., Mattis, I., Müller, D., and Wiegner, M.: The 16 April 2010 major volcanic ash plume over central Europe: EARLINET lidar and AERONET photometer observations at Leipzig and Munich, Germany, *Geophys. Res. Lett.*, 37, 13, doi:10.1029/2010gl043809, 2010.
- Arimoto, R., Kim, Y. J., Kim, Y. P., Quinn, P. K., Bates, T. S., Anderson, T. L., Gong, S., Uno, I., Chin, M., Huebert, B. J., Clarke, A. D., Shinozuka, Y., Weber, R. J., Anderson, J. R., Guazzotti, S. A., Sullivan, R. C., Sodeman, D. A., Prather, K. A., and Sokolik, I. N.: Characterization of Asian Dust during ACE-Asia, *Global and Planetary Change*, 52, 1-4, 23-56 pp, doi:10.1016/j.gloplacha.2006.02.013, 2006.
- Arola, A., Lindfors, A., Natunen, A., and Lehtinen, K. E. J.: A case study on biomass burning aerosols: effects on aerosol optical properties and surface radiation levels, *Atmos. Chem. Phys.*, 74257–4266 pp, doi:10.5194/acp-7-4257-2007, 2007.
- AWI press release 5 April 2011: [http://www.awi.de/en/news/press\\_releases/](http://www.awi.de/en/news/press_releases/), access: 15 April 2011, 2011.
- Baklanov, A.: Chemical weather forecasting: a new concept of integrated modelling, *Adv. Sci. Res.*, 423-27 pp, doi:10.5194/asr-4-23-2010, 2010.
- Balis, D. S., Amiridis, V., Zerefos, C., Gerasopoulos, E., Andreae, M., Zanis, P., Kazantzidis, A., Kazadzis, S., and Papayannis, A.: Raman lidar and sunphotometric measurements of aerosol optical properties over Thessaloniki, Greece during a biomass burning episode, *Atmos. Environ.*, 37, 32, 4529-4538 pp, doi:10.1016/s1352-2310(03)00581-8, 2003.

## References

---

- Beirle, S., Platt, U., Glasow, R. v., Wenig, M., and Wagner, T.: Estimate of nitrogen oxide emissions from shipping by satellite remote sensing, *Geophys. Res. Lett.*, 31, 18, 1-4 pp, 2004.
- Beirle, S., Salzmann, M., Lawrence, M. G., and Wagner, T.: Sensitivity of satellite observations for freshly produced lightning NO<sub>x</sub>, *Atmos. Chem. Phys.*, 9, 3, 1077-1094 pp, doi:10.5194/acp-9-1077-2009, 2009.
- Beirle, S., Huntrieser, H., and Wagner, T.: Direct satellite observation of lightning-produced NO<sub>x</sub>, *Atmos. Chem. Phys.*, 10, 22, 10965-10986 pp, doi:10.5194/acp-10-10965-2010, 2010a.
- Beirle, S., Kühl, S., Puškite, J., and Wagner, T.: Retrieval of tropospheric column densities of NO<sub>2</sub> from combined SCIAMACHY nadir/limb measurements, *Atmos. Meas. Tech.*, 3, 1, 283-299 pp, doi:10.5194/amt-3-283-2010, 2010b.
- Berk, A., Bornstein, L. S., and Robertson, D. C.: MODTRAN: A moderate resolution model for LOWTRAN 7, Spectral Sciences, Inc., Burlington, MA, GL-TR-89-C122, 1989.
- Bézy, J.-L., Delwart, S., and Rast, M.: MERIS – a new generation of ocean colour sensor onboard ENVISAT, *ESA Bull.*, 10348–56 pp, 2000.
- BASCOE website: <http://bascoe.oma.be/>, 2011.
- Boersma, K. F., Eskes, H. J., and Brinksma, E. J.: Error analysis for tropospheric NO<sub>2</sub> retrieval from space, *J. Geophys. Res.*, 109, D4, 1-20 pp, 2004.
- Boersma, K. F., Eskes, H. J., Veefkind, J. P., Brinksma, E. J., van der A, R. J., Sneep, M., van den Oord, G. H. J., Levelt, P. F., Stammes, P., Gleason, J. F., and Bucseles, E. J.: Near-real time retrieval of tropospheric NO<sub>2</sub> from OMI, *Atmos. Chem. Phys.*, 7, 8, 2103-2118 pp, doi:10.5194/acp-7-2103-2007, 2007.
- Boersma, K. F., Jacob, D. J., Eskes, H. J., Pinder, R. W., Wang, J., and van der A, R. J.: Intercomparison of SCIAMACHY and OMI tropospheric NO<sub>2</sub> columns: Observing the diurnal evolution of chemistry and emissions from space, *J. Geophys. Res.*, 113, D16S26, 1-14 pp, 2008.
- Boersma, K. F., Eskes, H. J., Dirksen, R. J., van der A, R. J., Veefkind, J. P., Stammes, P., Huijnen, V., Kleipool, Q. L., Sneep, M., Claas, J., Leitão, J., Richter, A., Zhou, Y., and Brunner, D.: An improved tropospheric NO<sub>2</sub> column retrieval algorithm for the Ozone Monitoring Instrument, *Atmos. Meas. Tech. Discuss.*, 4, 2, 2329-2388 pp, doi:10.5194/amtd-4-2329-2011, 2011.
- Bohren, C. F., and Huffman, D. R.: Absorption and scattering of light by small particles, A Wiley-Interscience publication, Wiley, 1983.
- Bohren, C. F., and Clothiaux, E. E.: Fundamentals of atmospheric radiation: an introduction with 400 problems, Physics textbook, Wiley-VCH, 2006.
- Bovensmann, H., Burrows, J. P., Buchwitz, M., Frerick, J., Noël, S., Rozanov, V. V., Chance, K. V., and Goede, A. P. H.: SCIAMACHY: Mission Objectives and Measurement Modes, *Journal of the Atmospheric Sciences*, 56, 2, 127-150 pp, doi:doi:10.1175/1520-0469(1999)056<0127:SMOAMM>2.0.CO;2, 1999.
- Brasseur, G. P.: Atmospheric chemistry in a changing world: an integration and synthesis of a decade of tropospheric chemistry research; the international global atmospheric chemistry project of

## References

---

- the International Geosphere-Biosphere Programme, Global change - the IGBP series, Springer, 2003.
- Brasseur, G. P., and Solomon, S.: *Aeronomy of the middle atmosphere: chemistry and physics of the stratosphere and mesosphere*, 3., rev. and enl. ed., Atmospheric and oceanographic sciences library; 32, Springer, 2005.
- Bucsela, E. J., Celarier, E. A., Wenig, M. O., Gleason, J. F., Veefkind, J. P., Boersma, K. F., and Brinksma, E. J.: Algorithm for NO<sub>2</sub> vertical column retrieval from the ozone monitoring instrument, *IEEE Trans. Geosci. Remote Sensing*, 44, 4, 1245-1258 pp, doi:10.1109/TGRS.2005.863715, 2006.
- Burrows, J. P., Hölzle, E., Goede, A. P. H., Visser, H., and Fricke, W.: *SCIAMACHY - Scanning Imaging Absorption Spectrometer for Atmospheric Cartography*, *Acta Astronautica*, 35, 7, 445-451 pp, 1995.
- Burrows, J. P., Buchwitz, M., Eisinger, M., Rozanov, V., Weber, M., Richter, A., and Ladstaetter-Weissenmayer, A.: The Global Ozone Monitoring Experiment (GOME): Mission concept and first scientific results, *J. Atmos. Sci.*, 56151-171 pp, 1999.
- Burrows, J. P., Platt, U., and Borrell, P., Eds.: *The Remote Sensing of Tropospheric Composition from Space, Physics of Earth and Space Environments*, Springer, 2011.
- Callies, J., Corpaccioli, E., Eisinger, M., Hahne, A., and Lefebvre, A.: GOME-2 – MetOp's Second Generation Sensor for Operational Ozone Monitoring, *ESA Bulletin*, 102, 2000.
- Carvalho, A., Monteiro, A., Ribeiro, I., Tchepel, O., Miranda, A. I., Borrego, C., Saavedra, S., Souto, J. A., and Casares, J. J.: High ozone levels in the northeast of Portugal: Analysis and characterization, *Atmos. Environ.*, 44, 8, 1020-1031 pp, 2010.
- Chang, D., Song, Y., and Liu, B.: Visibility trends in six megacities in China 1973–2007, *Atmospheric Research*, 94, 2, 161-167 pp, doi:10.1016/j.atmosres.2009.05.006, 2009.
- Chapman, S.: A theory of the upper atmospheric ozone, *Memoirs of the Royal Meteorological Society*, 3, 26, 103 pp, 1930.
- Chazette, P., Randriamiarisoa, H., Sanak, J., Couvert, P., and Flamant, C.: Optical properties of urban aerosol from airborne and ground-based in situ measurements performed during the Etude et Simulation de la Qualité de l'air en Ile de France (ESQUIF) program, *J. Geophys. Res.*, 110, D2, 1-18 pp, doi:10.1029/2004jd004810, 2005.
- Chen, D., Zhou, B., Beirle, S., Chen, L. M., and Wagner, T.: Tropospheric NO<sub>2</sub> column densities deduced from zenith-sky DOAS measurements in Shanghai, China, and their application to satellite validation, *Atmos. Chem. Phys.*, 9, 11, 3641-3662 pp, doi:10.5194/acp-9-3641-2009, 2009.
- Cheng, M. T., and Tsai, Y. I.: Characterization of visibility and atmospheric aerosols in urban, suburban, and remote areas, *The Science of The Total Environment*, 263, 1-3, 101-114 pp, doi:10.1016/s0048-9697(00)00670-7, 2000.
- Corbett, J. J., and Koehler, H. W.: Updated emissions from ocean shipping, *J. Geophys. Res.*, 108, D20, 4650-4654 pp, 2003.

## References

---

- Crutzen, P.: A discussion of the chemistry of some minor constituents in the stratosphere and troposphere, *Pure and Applied Geophysics*, 106, 1, 1385-1399 pp, doi:10.1007/bf00881092, 1973.
- Crutzen, P. J., and Stoermer, E. F.: The “Anthropocene”, *IGBP Newsletter*, 41, 2000.
- Dahlback, A., Rairoux, P., Stein, B., Del Guasta, M., Kyrö, E., Stefanutti, L., Larsen, N., and Braathen, G.: Effects of stratospheric aerosols from the Mt. Pinatubo eruption on ozone measurements at Sodankylä, Finland in 1991/92, *Geophys. Res. Lett.*, 21, 13, 1399-1402 pp, doi:10.1029/93gl02895, 1994.
- Damoah, R., Spichtinger, N., Forster, C., James, P., Mattis, I., Wandinger, U., Beirle, S., Wagner, T., and Stohl, A.: Around the world in 17 days – hemispheric-scale transport of forest fire smoke from Russia in May 2003, *Atmos. Chem. Phys.*, 4, 1311–1321 pp, doi:10.5194/acp-4-1311-2004, 2004.
- Dentener, F., van Weele, M., Krol, M., Houweling, S., and van Velthoven, P.: Trends and inter-annual variability of methane emissions derived from 1979-1993 global CTM simulations, *Atmos. Chem. Phys.*, 3, 1, 73-88 pp, doi:10.5194/acp-3-73-2003, 2003.
- Dubovik, O., Holben, B., Eck, T. F., Smirnov, A., Kaufman, Y. F., King, M. D., Tanré, D., and Slutsker, I.: Variability of absorption and optical properties of key aerosol types observed in worldwide locations, *J. Atmos. Sci.*, 59, 590–608 pp, 2002.
- Eck, T. F., Holben, B. N., Reid, J. S., O'Neill, N. T., Schafer, J. S., Dubovik, O., Smirnov, A., Yamasoe, M. A., and Artaxo, P.: High aerosol optical depth biomass burning events: A comparison of optical properties for different source regions, *Geophys. Res. Lett.*, 30, 20, doi:10.1029/2003gl017861, 2003.
- Eck, T. F., Holben, B. N., Reid, J. S., Sinyuk, A., Hyer, E. J., O'Neill, N. T., Shaw, G. E., Vande Castle, J. R., Chapin, F. S., Dubovik, O., Smirnov, A., Vermote, E., Schafer, J. S., Giles, D., Slutsker, I., Sorokine, M., and Newcomb, W. W.: Optical properties of boreal region biomass burning aerosols in central Alaska and seasonal variation of aerosol optical depth at an Arctic coastal site, *J. Geophys. Res.*, 114, D11, doi:10.1029/2008jd010870, 2009.
- EDGAR-EU: Emission Database for Global Atmospheric Research (EDGAR), Joint Research Centre (JRC)/Netherlands Environmental Assessment Agency (PBL), release version 4.0, <http://edgar.jrc.ec.europa.eu>, 2009.
- Elbern, H., Schmidt, H., and Ebel, A.: Variational data assimilation for tropospheric chemistry modeling, *J. Geophys. Res.*, 102, D13, 15967-15985 pp, doi:10.1029/97jd01213, 1997.
- ESA: Eyjafjallajökull (Iceland), April 2010, [http://ew.eo.esa.int/web/guest/events/-/journal\\_content/56\\_INSTANCE\\_QCx4/10122/16460?showFull=true&area=Volcanoes%20events](http://ew.eo.esa.int/web/guest/events/-/journal_content/56_INSTANCE_QCx4/10122/16460?showFull=true&area=Volcanoes%20events), ESA, access: 2010
- Eskes, H. J., and Boersma, K. F.: Averaging kernels for DOAS total-column satellite retrievals, *Atmos. Chem. Phys.*, 3, 1285–1291 pp, 2003.
- Evans, M. J., Shallcross, D. E., Law, K. S., Wild, J. O. F., Simmonds, P. G., Spain, T. G., Berrisford, P., Methven, J., Lewis, A. C., McQuaid, J. B., Pilling, M. J., Bandy, B. J., Penkett, S. A., and Pyle, J. A.: Evaluation of a Lagrangian box model using field measurements from EASE (Eastern Atlantic Summer Experiment) 1996, *Atmos. Environ.*, 34, 23, 3843-3863 pp, 2000.

## References

---

- Fassi-Fihri, A., Suhre, K., and Rosset, R.: Internal and external mixing in atmospheric aerosols by coagulation: Impact on the optical and hygroscopic properties of the sulphate-soot system, *Atmos. Environ.*, 31, 10, 1393-1402 pp, doi:10.1016/s1352-2310(96)00341-x, 1997.
- Flemming, J., Inness, A., Flentje, H., Huijnen, V., Moinat, P., Schultz, M. G., and Stein, O.: Coupling global chemistry transport models to ECMWF's integrated forecast system, *Geosci. Model Dev.*, 2, 2, 253-265 pp, doi:10.5194/gmd-2-253-2009, 2009.
- Friese, E., and Ebel, A.: Temperature Dependent Thermodynamic Model of the System  $H^+ - NH_4^+ - Na^+ - SO_4^{2-} - NO_3^- - Cl^- - H_2O$ , *The Journal of Physical Chemistry A*, 114, 43, 11595-11631 pp, doi:10.1021/jp101041j, 2010.
- Fu, T.-M., Jacob, D. J., Palmer, P. I., Chance, K., Wang, Y. X., Barletta, B., Blake, D. R., Stanton, J. C., and Pilling, M. J.: Space-based formaldehyde measurements as constraints on volatile organic compound emissions in east and south Asia and implications for ozone, *J. Geophys. Res.*, 112, D6, doi:10.1029/2006jd007853, 2007.
- Geiger, H., Barnes, I., Bejan, I., Benter, T., and Spittler, M.: The tropospheric degradation of isoprene: an updated module for the regional atmospheric chemistry mechanism, *Atmos. Environ.*, 37, 11, 1503-1519 pp, doi:10.1016/s1352-2310(02)01047-6, 2003.
- GEMS-team: A Monitoring and Forecasting System for Atmospheric Composition - Final report of the GEMS project, 2010.
- Gerasopoulos, E., Andreae, M. O., Zerefos, C. S., Andreae, T. W., Balis, D., Formenti, P., Merlet, P., Amiridis, V., and Papastefanou, C.: Climatological aspects of aerosol optical properties in Northern Greece, *Atmos. Chem. Phys.*, 3, 6, 2025-2041 pp, doi:10.5194/acp-3-2025-2003, 2003.
- Gloudemans, A. M. S., Schrijver, H., Hasekamp, O. P., and Aben, I.: Error analysis for CO and CH<sub>4</sub> total column retrievals from SCIAMACHY 2.3  $\mu$ m spectra, *Atmos. Chem. Phys.*, 8, 14, 3999-4017 pp, doi:10.5194/acp-8-3999-2008, 2008.
- Goede, A. P. H., Aarts, H. J. M., van Baren, C., Burrows, J. P., Change, K. V., Hoekstra, R., Hölzle, E., Pitz, W., Schneider, W., Smorenburg, C., Visser, H., and de Vries, J.: SCIAMACHY instrument design, *Adv. Space Res.*, 11, 3, 243-246 pp, doi:10.1016/0273-1177(91)90427-1, 1991.
- Gottwald, M., and Bovensmann, H., Eds.: SCIAMACHY - Exploring the Changing Earth's Atmosphere, Earth and Environmental Science, Netherlands, Springer, 2011.
- Guenther, A., Hewitt, C., Erickson, D., Fall, R., Geron, C., Graedel, T., Harley, P., Klinger, L., Lerdau, M., McKay, W., Pierce, T., Scholes, B., Steinbrecher, R., Tallamraju, R., Taylor, J., and Zimmerman, P.: A global model of natural volatile organic compound emissions, *J. Geophys. Res.*, 100, D5, 8873-8892 pp, 1995.
- Gutro, R.: NASA Observes Ash Plume of Icelandic Volcano, <http://www.nasa.gov/topics/earth/features/iceland-volcano-plume-archive1.html>, NASA's Goddard Space Flight Center, access: 2010
- Hains, J. C., Boersma, K. F., Kroon, M., Dirksen, R. J., Cohen, R. C., Perring, A. E., Bucsel, E., Volten, H., Swart, D. P. J., Richter, A., Wittrock, F., Schoenhardt, A., Wagner, T., Ibrahim, O. W., Roozendael, M. v., Pinardi, G., Gleason, J. F., Veefkind, J. P., and Levelt, P.: Testing

## References

---

- and improving OMI DOMINO tropospheric NO<sub>2</sub> using observations from the DANDELIONS and INTEX-B validation campaigns, *J. Geophys. Res.*, 115, D5, 1-20 pp, 2010.
- Hamonou, E., Chazette, P., Balis, D., Dulac, F., Schneider, X., Galani, E., Ancellet, G., and Papayannis, A.: Characterization of the vertical structure of Saharan dust export to the Mediterranean basin, *J. Geophys. Res.*, 104, D18, 22257-22270 pp, doi:10.1029/1999JD900257, 1999.
- Han, L., Zhuang, G., Cheng, S., and Li, J.: The mineral aerosol and its impact on urban pollution aerosols over Beijing, China, *Atmos. Environ.*, 41, 35, 7533-7546 pp, doi:10.1016/j.atmosenv.2007.05.046, 2007.
- Harrison, R. M., Ed. *Understanding our environment: An introduction to environmental chemistry and pollution*, Royal Society of Chemistry, 1999.
- Hass, H.: *Description of the EURAD Chemistry Transport Model version 2 (CTM2)*, Mitteilungen aus dem Institut für Geophysik und Meteorologie der Universität zu Köln, 1991.
- Hass, H., van Loon, M., Kessler, C., Stern, R., Matthijssen, J., Sauter, F., Zlatev, Z., Langner, J., Foltescu, V., and Schaap, M.: *Aerosol modelling: results and intercomparison from European Regional-scale modelling systems*, Special Report EUROTRAC -2 ISS, Garmisch Partenkirchen., 2003.
- He, Q., Li, C., Mao, J., Lau, A. K.-H., and Chu, D. A.: Analysis of aerosol vertical distribution and variability in Hong Kong, *J. Geophys. Res.*, 113, D14, doi:10.1029/2008jd009778, 2008.
- Heckel, A., Kim, S. W., Frost, G. J., Richter, A., Trainer, M., and Burrows, J. P.: Influence of under-sampled a priori data on tropospheric NO<sub>2</sub> satellite retrievals, *Atmos. Meas. Tech. Discuss.*, 4, 2, 1893-1934 pp, doi:10.5194/amtd-4-1893-2011, 2011.
- Hewitt, C. N., and Jackson, A. V.: *Atmospheric science for environmental scientists*, Wiley-Blackwell, 2009.
- Hilboll, A., Richter, A., Rozanov, A., and Burrows, J. P.: Retrieval of tropospheric NO<sub>2</sub> columns from SCIAMACHY using combined measurements from limb and nadir geometries, *Atmos. Meas. Tech.*, 2011, to be submitted.
- Hild, L., Richter, A., Rozanov, V., and Burrows, J. P.: Air mass factor calculations for GOME measurements of lightning-produced NO<sub>2</sub>, *Adv. Space Res.*, 29, 11, 1685-1690 pp, doi:10.1016/s0273-1177(02)80014-x, 2002.
- Hodzic, A., Chepfer, H., Vautard, R., Chazette, P., Beekmann, M., Bessagnet, B., Chatenet, B., Cuesta, J., Drobinski, P., Goloub, P., Haefelin, M., and Morille, Y.: Comparison of aerosol chemistry transport model simulations with lidar and Sun photometer observations at a site near Paris, *J. Geophys. Res.*, 109, D23, doi:10.1029/2004jd004735, 2004.
- Hodzic, A., Vautard, R., Chepfer, H., Goloub, P., Menut, L., Chazette, P., Deuzé, J. L., Apituley, A., and Couvert, P.: Evolution of aerosol optical thickness over Europe during the August 2003 heat wave as seen from CHIMERE model simulations and POLDER data, *Atmos. Chem. Phys.*, 6, 1853-1864 pp, 2006.

## References

---

- Hoffmann, A., Ritter, C., Stock, M., Maturilli, M., Eckhardt, S., Herber, A., and Neuber, R.: Lidar measurements of the Kasatochi aerosol plume in August and September 2008 in Ny-Ålesund, Spitsbergen, *J. Geophys. Res.*, 115, doi:10.1029/2009jd013039, 2010.
- Holben, B. N., Eck, T. F., Slutsker, I., Tanré, D., Buis, J. P., Setzer, A., Vermote, E., Reagan, J. A., Kaufman, Y. J., Nakajima, T., Lavenu, F., Jankowiak, I., and Smirnov, A.: AERONET - A Federated Instrument Network and Data Archive for Aerosol Characterization, *Remote Sensing of Environment*, 66, 1, 1-16 pp, doi:10.1016/s0034-4257(98)00031-5, 1998.
- Hollingsworth, A., Engelen, R. J., Textor, C., Benedetti, A., Boucher, O., Chevallier, F., Dethof, A., Elbern, H., Eskes, H., Flemming, J., Granier, C., Kaiser, J. W., Morcrette, J. J., Rayner, P., Peuch, V. H., Rouil, L., Schultz, M. G., Simmons, A. J., and the GEMS consortium: Toward a Monitoring and Forecasting System for Atmospheric Composition: The GEMS Project, *Bull. Amer. Meteor. Soc.*, 891147-1164 pp, 2008.
- Honoré, C., Rouil, L., Vautard, R., Beekmann, M., Bessagnet, B., Dufour, A., Elichegaray, C., Flaud, J.-M., Malherbe, L., Meleux, F., Menut, L., Martin, D., Peuch, A., Peuch, V.-H., and Poisson, N.: Predictability of European air quality: Assessment of 3 years of operational forecasts and analyses by the PREV'AIR system, *J. Geophys. Res.*, 113, D04301, 1-19 pp, 2008.
- Horowitz, L. W., Walters, S., Mauzerall, D. L., Emmons, L. K., Rasch, P. J., Granier, C., Tie, X., Lamarque, J.-F., Schultz, M. G., Tyndall, G. S., Orlando, J. J., and Brasseur, G. P.: A global simulation of tropospheric ozone and related tracers: Description and evaluation of MOZART, version 2, *J. Geophys. Res.*, 108, D24, 2003.
- Houweling, S., Dentener, F., and Lelieveld, J.: The impact of nonmethane hydrocarbon compounds on tropospheric photochemistry, *J. Geophys. Res.*, 103, D9, 10673-10696 pp, doi:10.1029/97jd03582, 1998.
- Hoyningen-Huene, W. v., Schlundt, C., Vountas, M., Yoon, J., Istomina, L. G., Kokhanovsky, A. A., and Burrows, J. P.: Retrieval of volcanic ash cloud properties from Eyjafjallajökull eruption in spring 2010, *Atmospheric Research, Special Issue*, 2011, submitted.
- Hu, R.-M., Martin, R. V., and Fairlie, T. D.: Global retrieval of columnar aerosol single scattering albedo from spacebased observations, *J. Geophys. Res.*, 112, D02204, doi:10.1029/2005JD006832, 2007.
- Huijnen, V., Eskes, H. J., Poupkou, A., Elbern, H., Boersma, K. F., Foret, G., Sofiev, M., Valdebenito, A., Flemming, J., Stein, O., Gross, A., Robertson, L., D'Isidoro, M., Kioutsioukis, I., Friese, E., Amstrup, B., Bergstrom, R., Strunk, A., Vira, J., Zyryanov, D., Maurizi, A., Melas, D., Peuch, V. H., and Zerefos, C.: Comparison of OMI NO<sub>2</sub> tropospheric columns with an ensemble of global and European regional air quality models, *Atmos. Chem. Phys.*, 10, 7, 3273-3296 pp, doi:10.5194/acp-10-3273-2010, 2010a.
- Huijnen, V., Williams, J., van Weele, M., van Noije, T., Krol, M., Dentener, F., Segers, A., Houweling, S., Peters, W., de Laat, J., Boersma, F., Bergamaschi, P., van Velthoven, P., Le Sager, P., Eskes, H., Alkemade, F., Scheele, R., Nédélec, P., and Pätz, H. W.: The global chemistry transport model TM5: description and evaluation of the tropospheric chemistry version 3.0, *Geosci. Model Dev.*, 3, 2, 445-473 pp, doi:10.5194/gmd-3-445-2010, 2010b.

## References

---

- Husar, R. B., Prospero, J. M., and Stowe, L. L.: Characterization of tropospheric aerosols over the oceans with the NOAA advanced very high resolution radiometer optical thickness operational product, *J. Geophys. Res.*, 102, D14, 16889-16909 pp, doi:10.1029/96jd04009, 1997.
- IPCC: Climate Change 2001: Synthesis Report. A Contribution of Working Groups I, II, and III to the Third Assessment Report of the Intergovernmental Panel on Climate Change, Cambridge, United Kingdom; New York, N.Y., USA, 398 pp, 2001.
- IPCC: Climate Change 2007: Synthesis Report. Contribution of Working Groups I, II and III to the Fourth Assessment Report of the Intergovernmental Panel on Climate Change, Geneva, Switzerland, 104 pp, 2007.
- Jacob, D. J.: Introduction to Atmospheric Chemistry, Princeton University Press, Princeton, New Jersey, USA, <http://acmg.seas.harvard.edu/people/faculty/djj/book/index.html>, 1999.
- Jacobson, M. Z.: Fundamentals of atmospheric modeling, 2. ed., Cambridge Univ. Press, 2005.
- Jaeglé, L., Steinberger, L., Martin, R. V., and Chance, K.: Global partitioning of NO sources using satellite observations: Relative roles of fossil fuel combustion, biomass burning and soil emissions, *Faraday Discussions*, 130407-423 pp, 2005.
- Jenkin, M. E., and Clemitshaw, K. C.: Ozone and other secondary photochemical pollutants: chemical processes governing their formation in the planetary boundary layer, *Atmos. Environ.*, 34, 16, 2499-2527 pp, doi:10.1016/s1352-2310(99)00478-1, 2000.
- Jeyaseelan, A. T., and Thiruvengadachari, S.: Suspected Mt. Pinatubo aerosol impact on the NOAA AVHRR NDVI over India, *International Journal of Remote Sensing*, 14, 3, 603 - 608 pp, 1993.
- Kahn, R. A., Li, W. H., Moroney, C., Diner, D. J., Martonchik, J. V., and Fishbein, E.: Aerosol source plume physical characteristics from space-based multiangle imaging, *J. Geophys. Res.*, 112, D11, D11205 pp, doi:10.1029/2006jd007647, 2007.
- Kang, S. M., Polvani, L. M., Fyfe, J. C., and Sigmond, M.: Impact of Polar Ozone Depletion on Subtropical Precipitation, *Science*, doi:10.1126/science.1202131, 2011.
- Keeling, C. D., Piper, S. C., Whorf, T. P., and Keeling, R. F.: Evolution of natural and anthropogenic fluxes of atmospheric CO<sub>2</sub> from 1957 to 2003, *Tellus B*, 63, 1, 2010.
- Kim, S.-W., Heckel, A., McKeen, S. A., Frost, G. J., Hsie, E.-Y., Trainer, M. K., Richter, A., Burrows, J. P., Peckham, S. E., and Grell, G. A.: Satellite-observed U.S. power plant NO<sub>x</sub> emission reductions and their impact on air quality, *Geophys. Res. Lett.*, 33, 22, 1-5 pp, 2006.
- King, M. D., Kaufman, Y. J., Menzel, W. P., and Tanre, D.: Remote-Sensing of Cloud, Aerosol, and Water-Vapor Properties from the Moderate Resolution Imaging Spectrometer (MODIS), *IEEE Trans. Geosci. Remote Sensing*, 30, 1, 2-27 pp, 1992.
- Kinnison, D. E., Brasseur, G. P., Walters, S., Garcia, R. R., Marsh, D. R., Sassi, F., Harvey, V. L., Randall, C. E., Emmons, L., Lamarque, J. F., Hess, P., Orlando, J. J., Tie, X. X., Randel, W., Pan, L. L., Gettelman, A., Granier, C., Diehl, T., Niemeier, U., and Simmons, A. J.: Sensitivity of chemical tracers to meteorological parameters in the MOZART-3 chemical transport model, *J. Geophys. Res.*, 112, D20, 1-24 pp, 2007.

## References

---

- Kleipool, Q. L., Dobber, M. R., de Haan, J. F., and Levelt, P. F.: Earth surface reflectance climatology from 3 years of OMI data, *J. Geophys. Res.*, 113, D18, D18308 pp, doi:10.1029/2008jd010290, 2008.
- Kloster, S., Feichter, J., Maier-Reimer, E., Six, K. D., Stier, P., and Wetzzel, P.: DMS cycle in the marine ocean-atmosphere system - a global model study, *Biogeosciences Discussions*, 21067-1126 pp, 2005.
- Kneizys, F. X., Robertson, D. C., Abreu, L. W., Acharya, P., Anderson, G. P., Rothman, L. S., Chetwynd, J. H., Selby, J. E. A., Shettle, E. P., Gallery, W. O., Berk, A., Clough, S. A., and Bernstein, L. S.: *The MODTRAN 2/3 Report and LOWTRAN 7 MODEL*, Ontar Corporation, North Andover, M.A., 1996.
- Koelemeijer, R. A., Homan, C., and Matthijsen, J.: Comparison of spatial and temporal variations of aerosol optical thickness and particulate matter over Europe, *Atmos. Environ.*, 40, 27, 5304-5315 pp, doi:10.1016/j.atmosenv.2006.04.044, 2006.
- Koelemeijer, R. B. A., Stammes, P., Hovenier, J. W., and Haan, J. F. d.: A fast method for retrieval of cloud parameters using oxygen A band measurements from the Global Ozone Monitoring Experiment, *J. Geophys. Res.*, 106, D4, 3475-3490 pp, doi:10.1029/2000jd900657, 2001.
- Koelemeijer, R. B. A., Stammes, P., Hovenier, J. W., and Haan, J. F. d.: Global distributions of effective cloud fraction and cloud top pressure derived from oxygen A band spectra measured by the Global Ozone Monitoring Experiment: Comparison to ISCCP data, *J. Geophys. Res.*, 107, D12, 2002.
- Koelemeijer, R. B. A., Haan, J. F. d., and Stammes, P.: A database of spectral surface reflectivity in the range 335-772 nm derived from 5.5 years of GOME observations, *J. Geophys. Res.*, 108, D2, 2003.
- Kokhanovsky, A. A.: *Aerosol optics: light absorption and scattering by particles in the atmosphere*, Springer praxis books in environmental sciences, Springer, 2008.
- Kokhanovsky, A. A., and Rozanov, V. V.: Retrieval of NO<sub>2</sub> vertical columns under cloudy conditions: A sensitivity study based on SCIATRAN calculations, *Atmospheric Research*, 93, 4, 695-699 pp, doi:10.1016/j.atmosres.2009.01.022, 2009.
- Konovalov, I. B., Beekmann, M., Burrows, J. P., and Richter, A.: Satellite measurement based estimates of decadal changes in European nitrogen oxides emissions, *Atmos. Chem. Phys.*, 8, 10, 2623-2641 pp, doi:10.5194/acp-8-2623-2008, 2008.
- Krueger, A., Walter, L., Bhartia, P., Schnetzler, C., Krotkov, N., Sprod, I., and Bluth, G.: Volcanic sulfur dioxide measurements from the total ozone mapping spectrometer instruments, *J. Geophys. Res.*, 100, D7, 14057-14076 pp, 1995.
- Kukkonen, J., Balk, T., Schultz, D. M., Baklanov, A., Klein, T., Miranda, A. I., Monteiro, A., Hirtl, M., Tarvainen, V., Boy, M., Peuch, V. H., Poupkou, A., Kioutsioukis, I., Finardi, S., Sofiev, M., Sokhi, R., Lehtinen, K., Karatzas, K., San José, R., Astitha, M., Kallos, G., Schaap, M., Reimer, E., Jakobs, H., and Eben, K.: Operational, regional-scale, chemical weather forecasting models in Europe, *Atmos. Chem. Phys. Discuss.*, 11, 2, 5985-6162 pp, doi:10.5194/acpd-11-5985-2011, 2011.

## References

---

- Kulkarni, P. S., Bortoli, D., Salgado, R., Antón, M., Costa, M. J., and Silva, A. M.: Tropospheric ozone variability over the Iberian Peninsula, *Atmos. Environ.*, 45, 1, 174-182 pp, 2011.
- Labonne, M., Bréon, F.-M., and Chevallier, F.: Injection height of biomass burning aerosols as seen from a spaceborne lidar, *Geophys. Res. Lett.*, 34, 11, 1-5 pp, 2007.
- Lamarque, J. F., Kiehl, J. T., Hess, P. G., Collins, W. D., Emmons, L. K., Ginoux, P., Luo, C., and Tie, X. X.: Response of a coupled chemistry-climate model to changes in aerosol emissions: Global impact on the hydrological cycle and the tropospheric burdens of OH, ozone, and NO<sub>x</sub>, *Geophys. Res. Lett.*, 32, 16, doi:10.1029/2005gl023419, 2005.
- Lathièrre, J., Hauglustaine, D. A., Friend, A. D., De Noblet-Ducoudré, N., Viovy, N., and Folberth, G. A.: Impact of climate variability and land use changes on global biogenic volatile organic compound emissions, *Atmos. Chem. Phys.*, 6, 8, 2129-2146 pp, doi:10.5194/acp-6-2129-2006, 2006.
- Lawrence, M. G., Hov, Ø., Beekmann, M., Brandt, J., Elbern, H., Eskes, H., Feichter, H., and Takigawa, M.: The Chemical Weather, *Environmental Chemistry*, 2, 1, 6-8 pp, doi:http://dx.doi.org/10.1071/EN05014, 2005.
- Lee, C., Martin, R. V., Donkelaar, A. v., O'Byrne, G., Krotkov, N., Richter, A., Huey, L. G., and Holloway, J. S.: Retrieval of vertical columns of sulfur dioxide from SCIAMACHY and OMI: Air mass factor algorithm development, validation, and error analysis, *J. Geophys. Res.*, 114, D22, 1-20 pp, 2009.
- Lee, K. H., Li, Z., Wong, M. S., Xin, J., Wang, Y., Hao, W.-M., and Zhao, F.: Aerosol single scattering albedo estimated across China from a combination of ground and satellite measurements, *J. Geophys. Res.*, 112, D22, doi:10.1029/2007jd009077, 2007.
- Leitão, J., and Soares, J.: Influência da estrutura vertical da atmosfera na qualidade do ar, Diploma Thesis, Environmental Engineer, Aveiro University, Aveiro, Portugal, 2004.
- Leitão, J., Richter, A., Vrekoussis, M., Kokhanovsky, A., Zhang, Q. J., Beekmann, M., and Burrows, J. P.: On the improvement of NO<sub>2</sub> satellite retrievals – aerosol impact on the air mass factors, *Atmos. Meas. Tech.*, 3, 2, 475-493 pp, doi:10.5194/amt-3-475-2010, 2010.
- Lesins, G., Chylek, P., and Lohmann, U.: A study of internal and external mixing scenarios and its effect on aerosol optical properties and direct radiative forcing, *J. Geophys. Res.*, 107, D10, doi:10.1029/2001jd000973, 2002.
- Leue, C., Wenig, M., Wagner, T., Klimm, O., Platt, U., and Jähne, B.: Quantitative analysis of NO<sub>x</sub> emissions from Global Ozone Monitoring Experiment satellite image sequences, *J. Geophys. Res.*, 106, D6, 5493-5505 pp, 2001.
- Liou, K.-N.: An introduction to atmospheric radiation, 2. ed., International geophysics series; 84, Academic Press, 2002.
- M., M., Friese, E., Ebel, A., Jakobs, H. J., Feldmann, H., Kessler, C., and Piekorz, G.: Long-term simulations of particulate matter in Europe on different scales using sequential nesting of a regional model, *Int. J. Environm. and Pollution*, 22, 1-2, 108-132 pp, 2004.

## References

---

- Mårtensson, E. M., Nilsson, E. D., de Leeuw, G., Cohen, L. H., and Hansson, H. C.: Laboratory simulations and parameterization of the primary marine aerosol production, *J. Geophys. Res.*, 108, D9, 4297 pp, doi:10.1029/2002jd002263, 2003.
- Martin, R. V., Chance, K., Jacob, D. J., Kurosu, T. P., Spurr, R. J. D., Bucsela, E., Gleason, J. F., Palmer, P. I., Bey, I., Fiore, A. M., Li, Q., Yantosca, R. M., and Koelemeijer, R. B. A.: An improved retrieval of tropospheric nitrogen dioxide from GOME, *J. Geophys. Res.*, 107, D20, doi:10.1029/2001jd001027, 2002.
- Martin, R. V., Jacob, D. J., Chance, K., Kurosu, T. P., Palmer, P. I., and Evans, M. J.: Global inventory of nitrogen oxide emissions constrained by space-based observations of NO<sub>2</sub> columns, *J. Geophys. Res.*, 108, D17, doi:10.1029/2003JD003453, 2003.
- Martonchik, J. V., Diner, D. J., Crean, K., and Bull, M.: Regional aerosol retrieval results from MISR, *IEEE Trans. Geosci. Remote Sens.*, 401520-1531 pp, 2002.
- Mastin, L. G.: A user-friendly one-dimensional model for wet volcanic plumes, *Geochem. Geophys. Geosyst.*, 8, 3, Q03014 pp, doi:10.1029/2006gc001455, 2007.
- Mattis, I., Ansmann, A., Müller, D., Wandinger, U., and Althausen, D.: Dual-wavelength Raman lidar observations of the extinction-to-backscatter ratio of Saharan dust, *Geophys. Res. Lett.*, 29, 9, 2002.
- Mattis, I., Ansmann, A., Müller, D., Wandinger, U., and Althausen, D.: Multiyear aerosol observations with dual-wavelength Raman lidar in the framework of EARLINET, *J. Geophys. Res.*, 109, D13203, 1-15 pp, doi:10.1029/2004JD004600, 2004.
- Memmesheimer, M., Tippke, J., Ebel, A., Hass, H., Jakobs, H. J., and Laube, M.: On the use of EMEP emission inventories for European scale air pollution modelling with the EURAD model, EMEP workshop on photooxidant modelling for long range transport in relation to abatement strategies, Berlin 1991, 307-324 pp, 1991.
- Mie, G.: Beiträge zur Optik trüber Medien, speziell kolloidaler Metallösungen, *Annalen der Physik*, Johann Ambrosius Barth, Leipzig, 377-445 pp, 1908.
- Mishchenko FORTRAN codes: <http://www.giss.nasa.gov/staff/mmishchenko/brf/>, access: October 2009.
- Mishchenko, M. I., Lacis, A. A., Carlson, B. E., and Travis, L. D.: Nonsphericity of dust-like tropospheric aerosols: Implications for aerosol remote sensing and climate modeling, *Geophys. Res. Lett.*, 22, 9, 1077-1080 pp, doi:10.1029/95gl00798, 1995.
- Monahan, E. C., Spiel, D. E., and Davidson, K. L.: A model of marine aerosol generation via whitecaps and wave disruption, in: *Oceanic Whitecaps*, edited by: Monahan, E. C., and Niocaill, G. M., D. Reidel, Norwell, MA, 167 - 174, 1986.
- Mora, S. J. D., Harrison, R. M., Graham, M. C., Farmer, J. G., Monks, P. S., Pulford, I. D., Halsall, C. J., and Harris, R. M.: *Principles of environmental chemistry*, edited by: Harrison, R. M., Royal Society of Chemistry, 2007.
- Müller, D., Mattis, I., Wandinger, U., Ansmann, A., Althausen, D., Dubovik, O., Eckhardt, S., and Stohl, A.: Saharan dust over a central European EARLINET-AERONET site: Combined

## References

---

- observations with Raman lidar and Sun photometer, *J. Geophys. Res.*, 108, D12, doi:10.1029/2002JD002918, 2003.
- Müller, D., Mattis, I., Wandinger, U., Ansmann, A., Althausen, D., and Stohl, A.: Raman lidar observations of aged Siberian and Canadian forest fire smoke in the free troposphere over Germany in 2003: Microphysical particle characterization, *J. Geophys. Res.*, 110, D17, 1-16 pp, 2005.
- Munro, R., Eisinger, M., Anderson, C., Callies, J., Corpaccioli, E., Lang, R., Lefebvre, A., Livschitz, Y., and Perez Albinana, A.: GOME-2 on MetOp: From in-orbit verification to routine operations, EUMETSAT Meteorological Satellite Conference, Helsinki, Finland, 12–16 June 2006 pp, 2006.
- Murayama, T., Sugimoto, N., Uno, I., Kinoshita, K., Aoki, K., Hagiwara, N., Liu, Z., Matsui, I., Sakai, T., Shibata, T., Arai, K., Sohn, B.-J., Won, J.-G., Yoon, S.-C., Li, T., Zhou, J., Hu, H., Abo, M., Iokibe, K., Koga, R., and Iwasaka, Y.: Ground-based network observation of Asian dust events of April 1998 in east Asia, *J. Geophys. Res.*, 106, D16, 18345-18359 pp, 2001.
- Murayama, T., Masonis, S. J., Redemann, J., Anderson, T. L., Schmid, B., Livingston, J. M., Russell, P. B., Huebert, B., Howell, S. G., McNaughton, C. S., Clarke, A., Abo, M., Shimizu, A., Sugimoto, N., Yabuki, M., Kuze, H., Fukagawa, S., Maxwell-Meier, K., Weber, R. J., Orsini, D. A., Blomquist, B., Bandy, A., and Thornton, D.: An intercomparison of lidar-derived aerosol optical properties with airborne measurements near Tokyo during ACE-Asia, *J. Geophys. Res.*, 108, D23, 2003.
- Murayama, T., Müller, D., Wada, K., Shimizu, A., Sekiguchi, M., and Tsukamoto, T.: Characterization of Asian dust and Siberian smoke with multi-wavelength Raman lidar over Tokyo, Japan in spring 2003, *Geophys. Res. Lett.*, 31, L23103, doi:10.1029/2004gl021105, 2004.
- NASA: MODIS/TERRA 1 Degree gridded MODIS active fire, <http://disc.sci.gsfc.nasa.gov/neespi/data-holdings/mod14cm1.shtml>, NASA, access: January, 2011, 2011
- Nickovic, S., Kallos, G., Papadopoulos, A., and Kakaliagou, O.: A model for prediction of desert dust cycle in the atmosphere, *J. Geophys. Res.*, 106, D16, 18113-18129 pp, doi:10.1029/2000jd900794, 2001.
- Noxon, J.: Stratospheric NO<sub>2</sub>, 2. Global Behavior, *J. Geophys. Res.*, 84, C8, 5067-5076 pp, 1979.
- Noxon, J. F.: Stratospheric NO<sub>2</sub> in the Antarctic winter, *Geophys. Res. Lett.*, 5, 12, 1021-1022 pp, doi:10.1029/GL005i012p01021, 1978.
- Nuß, J. H.: Verbes serungen des troposphärischen NO<sub>2</sub>-Retrievals aus GOME- und SCIAMACHY-Daten, PhD thesis, IUP-Bremen, University of Bremen, Bremen, Germany, 2005.
- Oltmans, S., Lefohn, A., Harris, J., Galbally, I., Scheel, H., Bodeker, G., Brunke, E., Claude, H., Tarasick, D., and Johnson, B.: Long-term changes in tropospheric ozone, *Atmos. Environ.*, 40, 17, 3156-3173 pp, doi:10.1016/j.atmosenv.2006.01.029, 2006.
- Péré, J. C., Mallet, M., Bessagnet, B., and Pont, V.: Evidence of the aerosol core-shell mixing state over Europe during the heat wave of summer 2003 by using CHIMERE simulations and AERONET inversions, *Geophys. Res. Lett.*, 36, L09807, doi:10.1029/2009gl037334, 2009.

## References

---

- P  r  , J. C., Mallet, M., Pont, V., and Bessagnet, B.: Evaluation of an aerosol optical scheme in the chemistry-transport model CHIMERE, *Atmos. Environ.*, 44, 30, 3688-3699 pp, doi:10.1016/j.atmosenv.2010.06.034, 2010.
- P  rez, C., Nickovic, S., Baldasano, J. M., Sicard, M., Rocadenbosch, F., and Cachorro, V. E.: A long Saharan dust event over the western Mediterranean: Lidar, Sun photometer observations, and regional dust modeling, *J. Geophys. Res.*, 111, D15, doi:10.1029/2005jd006579, 2006.
- Petersen, G. N.: A short meteorological overview of the Eyjafjallaj  kull eruption 14 April–23 May 2010, *Weather*, 65, 8, 203-207 pp, doi:10.1002/wea.634, 2010.
- Pitts, J. N., and Finlayson-Pitts, B. J.: Chemistry of the upper and lower atmosphere: theory, experiments, and applications, Academic Press, 2000.
- Platt, U., and Stutz, J.: Differential Optical Absorption Spectroscopy, Springer, Heidelberg, 2008.
- Pollack, J. B., Toon, O. B., and Khare, B. N.: Optical properties of some terrestrial rocks and glasses, *Icarus*, 19, 3, 372-389 pp, doi:10.1016/0019-1035(73)90115-2, 1973.
- Poole, L. R., Winker, D. M., Pelon, J. R., and McCormick, M. P.: CALIPSO: global aerosol and cloud observations from lidar and passive instruments, SPIE's 9th International Symposium on Remote Sensing, Agia Pelagia, Crete, Greece, 23-27 Sep 2002, 419-426 pp, 2003.
- Popp, C., Wang, P., Brunner, D., Stammes, P., Zhou, Y., and Grzegorski, M.: MERIS albedo climatology for FRESCO+ O<sub>2</sub> A-band cloud retrieval, *Atmos. Meas. Tech.*, 4, 3, 463-483 pp, doi:10.5194/amt-4-463-2011, 2011.
- Prata, A. J., and Grant, I. F.: Retrieval of microphysical and morphological properties of volcanic ash plumes from satellite data: Application to Mt Ruapehu, New Zealand, *Quarterly Journal of the Royal Meteorological Society*, 127, 576, 2153-2179 pp, doi:10.1002/qj.49712757615, 2001.
- Price, C., Penner, J., and Prather, M.: NO<sub>x</sub> from lightning 1. Global distribution based on lightning physics, *J. Geophys. Res.*, 102, D5, 5929-5941 pp, doi:10.1029/96jd03504, 1997.
- Ravishankara, A. R., Daniel, J. S., and Portmann, R. W.: Nitrous Oxide (N<sub>2</sub>O): The Dominant Ozone-Depleting Substance Emitted in the 21st Century, *Science*, 326, 5949, 123-125 pp, doi:10.1126/science.1176985, 2009.
- Rayleigh, L.: On the transmission of light through an atmosphere containing many small particles in suspension, and on the origin of the blue of the sky, *Phil. Mag.*, 41447-454 pp, 1899.
- Richter, A., and Burrows, J. P.: Retrieval of Tropospheric NO<sub>2</sub> from GOME Measurements Adv. Space Res., 291673-1683 pp, 2002.
- Richter, A., Burrows, J. P., Nusz, H., Granier, C., and Niemeier, U.: Increase in tropospheric nitrogen dioxide over China observed from space, *Nature*, 437, 7055, 129-132 pp, doi:10.1038/nature04092, 2005.
- Richter, A., Begoin, M., Hilboll, A., and Burrows, J. P.: An improved NO<sub>2</sub> retrieval for the GOME-2 satellite instrument, *Atmos. Meas. Tech.*, 4, 1, 1147-1159 pp, doi:10.5194/amt-4-1147-2011, 2011.
- Rozanov, A., Rozanov, V., Buchwitz, M., Kokhanovsky, A., and Burrows, J. P.: SCIATRAN 2.0 - A new radiative transfer model for geophysical applications in the 175-2400 nm spectral region, *Adv. Space Res.*, 36, 5, 1015-1019 pp, doi:10.1016/j.asr.2005.03.012, 2005.

## References

---

- Rozanov, V. V., Diebel, D., Spurr, R. J. D., and Burrows, J. P.: GOMETRAN: A radiative transfer model for the satellite project GOME, the plane-parallel version, *J. Geophys. Res.*, 102, D14, 16683-16695 pp, doi:10.1029/96jd01535, 1997.
- Rozanov, V. V., and Rozanov, A. V.: Differential optical absorption spectroscopy (DOAS) and air mass factor concept for a multiply scattering vertically inhomogeneous medium: theoretical consideration, *Atmos. Meas. Tech.*, 3, 3, 751-780 pp, doi:10.5194/amt-3-751-2010, 2010.
- Rozanov, V. V., Rozanov, A. V., Kokhanovsky, A. A., and Burrows, J. P.: Radiative transfer through terrestrial atmosphere and ocean: software package SCIATRAN, *Journal of Quantitative Spectroscopy & Radiative Transfer*, to be submitted, 2011.
- Russell, A. G., and Milford, J. B.: Atmospheric Modeling, in: Kirk-Othmer Encyclopedia of Chemical Technology, John Wiley & Sons, Inc., 2000.
- Salomonson, V. V., Barnes, W. L., Maymon, P. W., Montgomery, H. E., and Ostrow, H.: MODIS - Advanced Facility Instrument for Studies of the Earth as a System, *IEEE Trans. Geosci. Remote Sensing*, 27, 2, 145-153 pp, 1989.
- Sander, S. P., Friedl, R. R., Ravishankara, A. R., Golden, D. M., Kolb, C. E., Kurylo, M. J., Huie, R. E., Orkin, V. L., Molina, M. J., Moortgat, G. K., and Finlayson-Pitts, B. J.: Chemical Kinetics and Photochemical Data for Use in Atmospheric Studies - Evaluation Number 14, JPL, NASA, JPL Publication 02-25, 2003.
- Sander, S. P., Friedl, R. R., Ravishankara, A. R., Golden, D. M., Kolb, C. E., Kurylo, M. J., Molina, M. J., Moortgat, G. K., Keller-Rudek, H., Finlayson-Pitts, B. J., Wine, P. H., Huie, R. E., and Orkin, V. L.: Chemical Kinetics and Photochemical Data for Use in Atmospheric Studies - Evaluation Number 15, JPL, NASA, JPL Publication 06-2, 2006.
- Santer, B. D., Sausen, R., Wigley, T. M. L., Boyle, J. S., AchutaRao, K., Doutriaux, C., Hansen, J. E., Meehl, G. A., Roeckner, E., Ruedy, R., Schmidt, G., and Taylor, K. E.: Behavior of tropopause height and atmospheric temperature in models, reanalyses, and observations: Decadal changes, *J. Geophys. Res.*, 108, D1, 2003.
- Schell, B., Ackermann, I. J., Hass, H., Binkowski, F. S., and Ebel, A.: Modeling the formation of secondary organic aerosol within a comprehensive air quality model system, *J. Geophys. Res.*, 106, D22, 28275-28293 pp, doi:10.1029/2001jd000384, 2001.
- Schmidt, H., Derognat, C., Vautard, R., and Beekmann, M.: A comparison of simulated and observed ozone mixing ratios for summer of 1998 in western Europe, *Atmos. Environ.*, 35, 6277-6297 pp, 2001.
- Schumann, U., Weinzierl, B., Reitebuch, O., Schlager, H., Minikin, A., Forster, C., Baumann, R., Sailer, T., Graf, K., Mannstein, H., Voigt, C., Rahm, S., Simmet, R., Scheibe, M., Lichtenstern, M., Stock, P., Rüba, H., Schäuble, D., Tafferner, A., Rautenhaus, M., Gerz, T., Ziereis, H., Krautstrunk, M., Mallaun, C., Gayet, J. F., Lieke, K., Kandler, K., Ebert, M., Weinbruch, S., Stohl, A., Gasteiger, J., Groß, S., Freudenthaler, V., Wiegner, M., Ansmann, A., Tesche, M., Olafsson, H., and Sturm, K.: Airborne observations of the Eyjafjalla volcano ash cloud over Europe during air space closure in April and May 2010, *Atmos. Chem. Phys.*, 11, 5, 2245-2279 pp, doi:10.5194/acp-11-2245-2011, 2011.

## References

---

- Seinfeld, J. H., and Pandis, S. N.: Atmospheric chemistry and physics: from air pollution to climate change, 2. ed., Wiley, 2006.
- Sierk, B., Richter, A., Rozanov, A. A., Savigny, C. v., Schmoltner, A. M., Buchwitz, M., Bovensmann, H., and Burrows, J. P.: Retrieval and monitoring of atmospheric trace gas concentrations in nadir and limb geometry using the space-borne SCIAMACHY instrument, *Environmental Monitoring and Assessment*, 120, 1-3, 65-77 pp, doi:10.1007/s10661-005-9049-9, 2006.
- Sioris, C. E., Kurosu, T. P., Martin, R. V., and Chance, K.: Stratospheric and tropospheric NO<sub>2</sub> observed by SCIAMACHY: first results, *Adv. Space Res.*, 34, 4, 780-785 pp, doi:10.1016/j.asr.2003.08.066, 2004.
- Sluis, W. W., Allaart, M. A. F., Peters, A. J. M., and Gast, L. F. L.: The development of a nitrogen dioxide sonde, *Atmos. Meas. Tech.*, 3, 6, 1753-1762 pp, doi:10.5194/amt-3-1753-2010, 2010.
- Solomon, S., Portmann, R. W., Sanders, R. W., Daniel, J. S., Madsen, W., Bartram, B., and Dutton, E. G.: On the role of nitrogen dioxide in the absorption of solar radiation, *J. Geophys. Res.*, 104, D10, 12047-12058 pp, doi:10.1029/1999jd900035, 1999.
- Stull, R. B.: An introduction to the boundary layer meteorology, Kluwer Academic Publishers, Dordrecht, The Netherlands, 1988.
- Sutton, P. J. H., and Chiswell, S. M.: Effect of volcanic aerosols on satellite-derived sea surface temperatures around New Zealand, *New Zealand Journal of Marine and Freshwater Research*, 30, 1, 105 - 113 pp, 1995.
- Thomas, W., Erbertseder, T., Ruppert, T., Roozendael, M. V., Verdebout, J., Balis, D., Meleti, C., and Zerefos, C.: On the Retrieval of Volcanic Sulfur Dioxide Emissions from GOME Backscatter Measurements, *Journal of Atmospheric Chemistry*, 50, 3, 295-320 pp, doi:10.1007/s10874-005-5544-1, 2005.
- Tombette, M., Chazette, P., Sportisse, B., and Roustan, Y.: Simulation of aerosol optical properties over Europe with a 3-D size-resolved aerosol model: comparisons with AERONET data, *Atmos. Chem. Phys.*, 8, 23, 7115-7132 pp, doi:10.5194/acp-8-7115-2008, 2008.
- van de Hulst, H. C.: Light scattering by small particles, Unabridged and corr. republ. of the work orig. publ. in 1957, New York ed., Dover, 1981.
- van der A, R. J., Eskes, H. J., Boersma, K. F., van Noije, T. P. C., Van Roozendael, M., De Smedt, I., Peters, D. H. M. U., and Meijer, E. W.: Trends, seasonal variability and dominant NO<sub>x</sub> source derived from a ten year record of NO<sub>2</sub> measured from space, *J. Geophys. Res.*, 113, D4, D04302 pp, doi:10.1029/2007jd009021, 2008.
- van der Werf, G. R., Randerson, J. T., Giglio, L., Collatz, G. J., Kasibhatla, P. S., and Arellano Jr, A. F.: Interannual variability in global biomass burning emissions from 1997 to 2004, *Atmos. Chem. Phys.*, 6, 11, 3423-3441 pp, doi:10.5194/acp-6-3423-2006, 2006.
- van Noije, T. P. C., Eskes, H. J., Dentener, F. J., Stevenson, D. S., Ellingsen, K., Schultz, M. G., Wild, O., Amann, M., Atherton, C. S., Bergmann, D. J., Bey, I., Boersma, K. F., Butler, T., Cofala, J., Drevet, J., Fiore, A. M., Gauss, M., Hauglustaine, D. A., Horowitz, L. W., Isaksen, I. S. A., Krol, M. C., Lamarque, J. F., Lawrence, M. G., Martin, R. V., Montanaro, V., Müller, J. F., Pitari, G., Prather, M. J., Pyle, J. A., Richter, A., Rodriguez, J. M., Savage, N.

## References

---

- H., Strahan, S. E., Sudo, K., Szopa, S., and van Roozendaal, M.: Multi-model ensemble simulations of tropospheric NO<sub>2</sub> compared with GOME retrievals for the year 2000, *Atmos. Chem. Phys.*, 6, 10, 2943-2979 pp, doi:10.5194/acp-6-2943-2006, 2006.
- VanCuren, R. A.: Asian aerosols in North America: Extracting the chemical composition and mass concentration of the Asian continental aerosol plume from long-term aerosol records in the western United States, *J. Geophys. Res.*, 108, D20, doi:10.1029/2003jd003459, 2003.
- Vasilkov, A. P., Joiner, J., Oreopoulos, L., Gleason, J. F., Veefkind, P., Bucsele, E., Celarier, E. A., Spurr, R. J. D., and Platnick, S.: Impact of tropospheric nitrogen dioxide on the regional radiation budget, *Atmos. Chem. Phys.*, 9, 17, 2009.
- Velders, G. J. M., Granier, C., Portmann, R. W., Pfeilsticker, K., Wenig, M., Wagner, T., Platt, U., Richter, A., and Burrows, J. P.: Global tropospheric NO<sub>2</sub> column distributions: Comparing three-dimensional model calculations with GOME measurements, *J. Geophys. Res.*, 106, D12, 12643-12660 pp, doi:10.1029/2000jd900762, 2001.
- Vermote, E., Saleous, N. E., Kaufman, Y. J., and Dutton, E.: Data pre-processing: Stratospheric aerosol perturbing effect on the remote sensing of vegetation: Correction method for the composite NDVI after the Pinatubo eruption, *Remote Sensing Reviews*, 15, 1, 7 - 21 pp, 1997.
- Volten, H., Brinksma, E. J., Berkhout, A. J. C., Hains, J., Bergwerff, J. B., Van der Hoff, G. R., Apituley, A., Dirksen, R. J., Calabretta-Jongen, S., and Swart, D. P. J.: NO<sub>2</sub> lidar profile measurements for satellite interpretation and validation, *J. Geophys. Res.*, 114, D24301, doi:10.1029/2009jd012441, 2009.
- Wagner, T., Dix, B., Friedeburg, C. v., Frieß, U., Sanghavi, S., Sinreich, R., and Platt, U.: MAX-DOAS O<sub>4</sub> measurements: A new technique to derive information on atmospheric aerosols — Principles and information content, *J. Geophys. Res.*, 109, D22205, doi:10.1029/2004jd004904, 2004.
- Wagner, T., Burrows, J. P., Deutschmann, T., Dix, B., von Friedeburg, C., Frieß, U., Hendrick, F., Heue, K. P., Irie, H., Iwabuchi, H., Kanaya, Y., Keller, J., McLinden, C. A., Oetjen, H., Palazzi, E., Petritoli, A., Platt, U., Postlyakov, O., Pukite, J., Richter, A., van Roozendaal, M., Rozanov, A., Rozanov, V., Sinreich, R., Sanghavi, S., and Wittrock, F.: Comparison of box-air-mass-factors and radiances for Multiple-Axis Differential Optical Absorption Spectroscopy (MAX-DOAS) geometries calculated from different UV/visible radiative transfer models, *Atmos. Chem. Phys.*, 7, 7, 1809-1833 pp, doi:10.5194/acp-7-1809-2007, 2007.
- Wallace, J. M., and Hobbs, P. V.: *Atmospheric science: an introductory survey*, 2. ed., International geophysics series; 92, Elsevier, 2006.
- Wang, K., Dickinson, R. E., and Liang, S.: Clear sky visibility has decreased over land globally from 1973 to 2007, *Science*, 323, 5920, 1468-1470 pp, doi:10.1126/science.1167549, 2009.
- Wang, P., Richter, A., Bruns, M., Rozanov, V. V., Burrows, J. P., Heue, K. P., Wagner, T., Pundt, I., and Platt, U.: Measurements of tropospheric NO<sub>2</sub> with an airborne multi-axis DOAS instrument, *Atmos. Chem. Phys.*, 5, 2, 337-343 pp, doi:10.5194/acp-5-337-2005, 2005.
- Warneck, P.: *Chemistry of the natural atmosphere*, 2. ed., International geophysics series; 71, Academic Press, 2000.

## References

---

- Wayne, R. P., Barnes, I., Biggs, P., Burrows, J. P., Canosa-Mas, C. E., Hjorth, J., Le Bras, G., Moortgat, G. K., Perner, D., Poulet, G., Restelli, G., and Sidebottom, H.: The nitrate radical: Physics, chemistry, and the atmosphere, *Atmospheric Environment. Part A. General Topics*, 25, 1, 1-203 pp, doi:10.1016/0960-1686(91)90192-a, 1991.
- Wayne, R. P.: *Chemistry of atmospheres: an introduction to the chemistry of the atmospheres of earth, the planets, and their satellites*, 3., reprint. ed., Oxford Univ. Press, 2006.
- Wenig, M., Köhl, S., Beirle, S., Bucsela, E., Jähne, B., Platt, U., Gleason, J., and Wagner, T.: Retrieval and analysis of stratospheric NO<sub>2</sub> from the Global Ozone Monitoring Experiment, *J. Geophys. Res.*, 109, D4, 1-11 pp, 2004.
- WHO: Air quality guidelines for particulate matter, ozone, nitrogen dioxide and sulfur dioxide, Global update 2005 - Summary of risk assessment, WHO, 2006a.
- WHO: Air quality guidelines for particulate matter, ozone, nitrogen dioxide and sulfur dioxide, Global update 2005, WHO Regional Publications, European Series, edited by: WHO, WHO, 2006b.
- Wiegner, M., Gasteiger, J., Groß, S., Schnell, F., Freudenthaler, V., and Forkel, R.: Characterization of the Eyjafjallajökull ash-plume: Potential of lidar remote sensing, *J. Phys. Chem. Earth*, in press, doi:10.1016/j.pce.2011.01.006, 2011.
- Winker, D. M., Pelon, J. R., and McCormick, M. P.: The CALIPSO mission: spaceborne lidar for observation of aerosols and clouds, Hangzhou, China 2003, 1-11 pp,
- Wittrock, F., Oetjen, H., Richter, A., Fietkau, S., Medeke, T., Rozanov, A., and Burrows, J. P.: MAX-DOAS measurements of atmospheric trace gases in Ny-Alesund - Radiative transfer studies and their application, *Atmos. Chem. Phys.*, 4955–966 pp, 2004.
- WMO: Antarctic Ozone Bulletin No 4 / 2010, 2010a.
- WMO: Scientific assessment of ozone depletion: 2010 - Global Ozone Research and Monitoring Project, National Oceanic and Atmospheric Administration, National Aeronautics and Space Administration, United Nations Environment Programme, World Meteorological Organization and European Commission, No. 52, 2010b.
- Wuebbles, D. J.: Nitrous Oxide: No Laughing Matter, *Science*, 326, 5949, 56-57 pp, doi:10.1126/science.1179571, 2009.
- Zhang, L., Cao, X., Bao, J., Zhou, B., Huang, J., Shi, J., and Bi, J.: A case study of dust aerosol radiative properties over Lanzhou, China, *Atmos. Chem. Phys.*, 10, 9, 4283-4293 pp, doi:10.5194/acp-10-4283-2010, 2010.
- Zhou, J., Yu, G., Jin, C., Qi, F., Liu, D., Hu, H., Gong, Z., Shi, G., Nakajima, T., and Takamura, T.: Lidar observations of Asian dust over Hefei, China, in spring 2000, *J. Geophys. Res.*, 107, D15, 2002.

# Erklärung

Hiermit erkläre ich, dass ich die Arbeit ohne unerlaubte fremde Hilfe angefertigt habe, dass ich weiterhin keine anderen als die angegebenen Quellen und Hilfsmittel benutze und die den benutzten Werken wörtlich oder inhaltlich entnommenen Stellen als solche kenntlich gemacht habe.

Bremen, 01 August 2011

*Joana Leitão Alexandre*

<i>Bjartar vonir rætast</i>	<i>(Bright hopes come true)</i>
<i>Er við göngum bæinn</i>	<i>(as we walk downtown)</i>
<i>Brosum og hlæjum glaðir</i>	<i>(smiling and laughing)</i>
<i>Vinátta og þreyta mætast</i>	<i>(as friendship and exhaustion collide)</i>
<i>Höldum upp á daginn</i>	<i>(we celebrate)</i>
<i>Og fögnum tveggja ára bið</i>	<i>(a two year wait)</i>

*Sigur Rós: Ágætis Byrjun*

# Acknowledgements

I am indebted to Prof. John Burrows for the opportunity of doing a PhD, and for including me in the group of fantastic scientists working at IUP. I would like to thank you for your good advice, and insight into this delicate business of atmospheric sciences.

I am thankful to Prof. Otto Schrems who kindly accepted to review this manuscript, being the second examiner and dedicating his time to evaluate my work.

Doing a PhD is not an easy task and one should never go through it alone. I was lucky to be part of the “DOAS group” at IUP-Bremen and have fantastic colleagues with whom I have shared more than 4 years of working days. Achim, the three Andreas, Anja, Annette, Enno, Folkard, Frank, Henning, Matthias, Mihalis, Katsuyuki, Sebastian, Stefan and Sven, I thank you all of you for making the work a much easier mission. Special gratitude goes to:

- Andreas Richter, the steering wheel of this research, he has help me to keep focus on the work that had to be done and often reminded me of being pleased for what had been already achieved.
- Andreas Hilboll and Heckel, and Achim, the software providers, without whom I would have never been able to get where I am, three great colleagues and friends that shared the fun in SCIATRANing. A special thanks to Andreas Hilboll, whom has also proof-read great part of this manuscript, and has given me everlasting support, sharing the frustrating and happy times during this long journey.
- Anja Schönhardt, a dear friend, whom has been always there next to me (not only in the office) whenever needed. To her I owe (at least partially) this time at IUP... the opening of the door and much more... these years will never be forgotten.
- Mihalis who shared with me the feeling of outcasts including in a fantastic working group, and a friend who has helped me in many ways.
- Folkard has not only kept my computer running in the many occasions that it almost failed me, but it has also provided good advice for this thesis.
- Sebastian Dikty has given useful insight for my work and has always been ready to chip in.

The results presented in this thesis were only possible thanks to the collaboration with many other great scientists. I am grateful for the help, fruitful advices, data provided, for sharing some of your busy times with me, and, above all, for the support given:

- M. Beekman and Q. J. Zhang for the NO<sub>2</sub> CHIMERE data;
- H. Elbern and E. Friese for the NO<sub>2</sub> and aerosol EURAD data;
- C. Kittaka and D. Winker for the CALIPSO aerosol data;
- A. Kokhanovsky, W. von Hoyningen Huene that were always available to answer my endless questions concerning the mysterious world of aerosol;
- M. Mishchenko for the FORTRAN code spher.f, the basis of so many calculations in this work;
- A. and V. Rozanov that have attended to my restless questions and issues with SCIATRAN;
- J. C. Pére whom, although not knowing me, has helped much in understanding the complex business of aerosol simulations;
- N. Schutgens, a friend with a great mind, a first-class scientist, that guided me when I felt at lost in a sea of particles;
- All the GEMS and MACC GRG team(s) members for the many good years of work, with special thanks to Olaf and Vincent for the many discussions on the CTMs MOZART and TM5.

I thank my family for their support during these past years, for their continuous believe that I would succeed, and for their constant motivation. I am lucky to have such a mom and dad that help me become the person whom I am today. Above all, I my deepest admiration goes to my true soul mate, my sister, who has been there with me, all the time, even if we are more than thousand km apart. She has given me strength all these past 4 years when I, as the oldest, should have been the stronger.

Last, but certainly not least, there is an army of friends spread around the world that are precious to me, and show(ed) me that the world can be a good place, that there is hope, and that this is all worth it. To Joana, the other *me*, I send a big tight hug for all this life of shared experiences. To Charles, I say “Merci” for your friendship, for understanding me and constant aid in all those times the hell seemed to come loose. To Alex and Cristina, two great minds in this business, I say “Obrigada” for all the enlightenment granted. A big “Obrigadinha” also to Carla whom has always managed to keep my spirits high. To Mariska and Bas I say “Dank je wel” for putting this effort of mine into perspective when I (almost) lost track. To Katinka, Johannes, Juliane, Philine and Tobias I say “Dankeschön” for all the memorable times in Bremen, for putting up with my peculiar (and not always easy) mood, helping the days go by with bliss, for reminding that there is life beyond work. To Jaaee I say “Dhanyawaad” for her constant joy, for showing me that dreams can come true, for sharing her good vibes. To Luca I say “Grazie mille” for many things, but above all for being my dope supplier with frequent the donut delivers that make any bad day to be heaven!

*Obrigada a todos por tornarem isto possível!*